



PROCEEDING

OF

UIE 2021

XIX International UIE Congress on Evolution and
New Trends in Electrothermal Processes

Congress is supported by



ampere europe asc.

www.ampereeurope.org



Organizing Committee

Prof. Ivo Doležel, Chairman

Prof. Jiří Kožený, Chairman

Assoc. Prof. Václav Kotlan, Local Organizer

Assoc. Prof. David Rot, Local Organizer

Dr. Lenka Šroubová, Secretariat

Faculty of Electrical Engineering, University of West Bohemia, Czech Republic

Industrial partners presentation

Václav Pavlovec, CEO, JUNKER Industrial Equipment s.r.o., OTTO JUNKER – GROUP
Transistor Technology for Induction Melting Furnaces

Stanislav Němeček, CEO, RAPTECH s.r.o.
Benefits and Properties of Tools Processed by Laser Beam

Transistor technology for induction melting furnaces

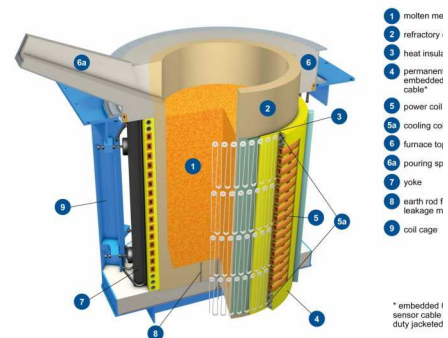
UIE congress 2021, 1.-3.2021, Pilsen, CZ

Václav Pavlovec, Dr.techn.-Dipl.-Ing. Dipl.-Wirt.Ing., CEO, JUNKER Industrial Equipment s.r.o., OTTO JUNKER - GROUP

Boskovice, CZ, vaclav.pavlovec@otto-junker.com

1. Introduction to induction melting furnaces

A modern coreless induction furnace is shown in picture 1. It melts metal (“charge”) by the means of electric energy – alternating current. The charge works as the core of the coil (wound copper profile). The energy transfer to the core happens by “iron losses” their main sources being eddy currents and (for ferromagnetic materials) magnetic hysteresis and finally anomalous losses.



Picture 1

2. The road from the net frequency melting furnace to modern transistor technology

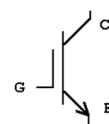
Initially induction melting furnaces were relatively simple devices, as long as they used net frequency (50/60Hz) – while modern furnaces use medium frequency which ranges from 250 Hz to a high kHz range. All that was needed on the supply side were transformers to adjust the voltage.

These net frequency MF had a few disadvantages, mainly the need to maintain a minimum level of molten material through the whole melting process (modern medium frequency furnaces can be emptied completely) and a very intense stirring effect on the molten metal, which is under certain conditions not desirable.

Therefore medium frequency furnaces were introduced. They require additionally a frequency converter that increases the frequency from 50/60 Hz. Such a device consists of a rectifier part and an inverter. Originally both the rectifier and the inverter were equipped with thyristors. Thyristors, once they are conducting, cannot be switched off actively. This results in an unfavorable behavior in the supply network, the thyristor frequency converter together with an inductive load showing low power factors (ideal $\text{pf} = 1.0$) – utilities typically charge additional costs to commercial customers who have a power factor below some limit, which is typically 0.9 to 0.95. To eliminate this disadvantage transistors were introduced in the inverter part of the frequency converter.

3. IGBT – insulated gate bipolar transistors and their advantages

IGBT (symbol see picture 2) are designed to switch on and off very rapidly, therefore they are very well suited for industrial control systems. That is why they are the prime choice for the application in frequency converters for medium frequency induction melting furnaces, especially in the critical inverter part. Because in the crucial parameters (voltage rating, current rating) they surpass other transistor types (power bipolars and MOSFETS) they are used despite their higher price.



Picture 2

4. Comparison between thyristor and IGBT inverters

IGBT allow to reach constantly a much better power factor (0.99-1.0). They are also more reliable (self-protective) and allow for a simpler cooling setup, because they are suited for indirect cooling.

5. Experience from use, reliability, examples of installations

IGBT are being used in a few hundreds OTTO JUNKER induction furnaces and the results are very satisfactory. The reliability is outstanding and the behavior in the network makes it possible to avoid additional costs charged by the utility company under all circumstances.

BENEFITS AND PROPERTIES OF TOOLS PROCESSED BY LASER BEAM

Němeček Stanislav

RAPTECH s.r.o., U Vodárny 473, 330 08 Zruč-Senec, Czech Republic,

Corresponding author: nemecek@raptech.cz

Laser hardening brings a great increase in part life and it is an industry-proven process, typically used for hardening of moulds, gears, shafts etc. It was mainly the recent advancement of diode lasers that turned it into a competitive process. The contribution describes the nature of residual stresses, the influence on hardness, tribological lifetime and fatigue properties of such parts. Investigations have to be performed in order to gain a comprehensive knowledge about effects on microstructure, hardness, surface properties of treated materials. This contribution contains results of a partial studies of laser hardening and cladding in industrial practice at RAPTECH company.

INTRODUCTION

Laser hardening and cladding offers short processing times and appreciable cost savings, as well as capabilities to accommodate almost any geometry, and control the depths and widths of the treated surfaces. In addition, laser processed surfaces exhibit additional beneficial properties when compared to conventionally hardened surfaces. These include differences in tribological, fatigue, and corrosion behavior, specifically an improved wear life, fatigue and corrosion resistance.

Sheet forming dies for automotive industry may serve as a good example in this context. The car body consists of about 300 components, which represent a demand for about 750 pairs of press dies (progressive dies, punching and trimming dies). Car manufacturers launch about 120 new car models every year. Based on that number, the cost estimate for die making is 12 billion euro every year. Laser hardening of rounded and shearing edges may double the number of parts formed.

Differences in surface hardening technologies

In **flame hardening**, the depth of heating is given by the relative speed of the flame movement across the surface. The efficiency of heat transfer to the material is poor and the surrounding surfaces become heated as well. As a result, the dwell time required for austenitizing increases, the grains in the material coarsen, and their boundaries may become burnt. The surface also develops a layer of oxides. In this process, the uniformity and control of temperature are limited and inaccurate. In induction hardening, the heat generated depends on electric resistance and current. The depth of heating is given by the frequency of the power source. The lower the frequency, the shallower is the hardening depth. Even with high-frequency induction heating, however, heating takes several seconds.

In **flame hardening**, as well as in **induction hardening**, the heating stage must be followed by sufficiently rapid cooling (using a water spray or polymer solution). There is an ever-present risk that steam and a vapor blanket may form during cooling, which would retard the heat removal rate and prevent the surface from hardening. Similar to the heat-affected zone in weld joints, there is a deep transition zone beneath the hardened layer. This is the zone in which the elevated temperature, though insufficient for hardening, has caused some changes in the matrix of the parent metal. Unfortunately, these changes are typically for the worse.

In **laser treatment**, the austenitizing temperature must be achieved in the surface, as with the other techniques. However, thanks to rapid heating rates of thousands of degrees per second, the resulting transitional heat-affected zone is very thin.

The maximum laser hardened depth is approximately 2 mm, depending on the heat conductivity of the material. The hardening depth can be controlled by the speed of the beam movement and by the temperature. To improve control, the process is typically monitored using a pyrometer linked to the laser source and operated by robot. By regulating the power input, this control loop can maintain a fixed surface temperature, thus providing uniform hardness and

preventing local melting.

In the heating step, austenitizing temperature, that is, a temperature above Ac3, must be achieved in the surface layer of steel. Rapid heating with a laser beam is one of the factors which minimize the distortion of the part heated. As the material around the laser spot remains cold, it does not expand, and the distortion does not occur. Another difference from the other surface hardening techniques lies in the heat removal mechanism which is based on self-quenching. It involves rates of several thousand °C/sec. There is no need for cooling the surface using a liquid supplied from outside because the interior of the part remains cold and absorbs the heat by conduction at a sufficient rate (i.e., cooling by convection). One can therefore assume that phase transformation begins from within the part and the surface is the last to cool down.

Laser beam hardening is much more favorable to the material in terms of crack susceptibility than other techniques. The steep thermal gradient from quenching causes severe (tensile) stresses which lead to surface crack initiation. In laser hardening, however, the cooling process begins by heat removal to the cold interior of the workpiece. The temperatures thus equalize gradually from within the part. This minimizes the resulting stresses and eliminates cracking.

Laser cladding is increasingly being used to repair molds and dies. As with hardening, the method is non-invasive and minimally affects the structure around the weld. It even allows you to create 3D structures, similar to additive manufacturing. Molds with a size of centimeter to a few meters and a weight of tens of tons can be repaired. The service life of tools repaired in this way is even longer than with original tools produced by machining and heat treatment, probably due to the fine-grained homogeneous microstructure.

Continuous wave laser sources are preferred for laser hardening applications. The most widely used systems rely on diode or fiber lasers. Surfaces of experimental specimens were laser treated using the facilities of the RAPTECH company, 3kW high power diode laser from LaserLine GmbH with a dual-channel pyrometer for temperature measurement. The optical head is installed on FANUC robot, see figure below.



ACKNOWLEDGMENT

This contribution presents results of the project Additec TH03020130, supported by Technological Agency of Czech Republic.

REFERENCES

1. Fiedler L., Monitoring of Wear and Dynamic Impact Loading of Laser Surface Hardened Steels. Bachelor thesis, University of West Bohemia, 2012.

List of congress papers

Valters Dzelme, Andris Jakovics and Egbert Baake <i>Liquid metal layer dynamics in transverse alternating magnetic field</i>	12
Imants Kaldre and Andris Bojarevics <i>Directional solidification of metallic alloys and composites under electromagnetic interaction</i>	14
Reinis Baranovskis, Didzis Berenis, Ilmars Grants, Andris Bojarevics and Toms Beinerts <i>New contactless aluminum degassing system - GalSn model experiments with a numerical study</i>	16
Yuliya Pleshivtseva, Ilya Levin, Bernard Nacke, Martin Ennen and Alexander Nikanorov <i>Time-Optimal Feedback System with Identifier to Control Induction Heating Process</i>	18
Alexandr Ivanov, Vladimir Bukanin and Alexei Zenkov <i>Simulation Problems of Internal Inductors</i>	20
Alexandr Ivanov, Vladimir Bukanin, Alexei Zenkov, Valentin Vologdin and Vladislav Vologdin <i>A New Approach to Induction Heating Control</i>	22
Sean Muyskens and Robert Goldstein <i>Physical Simulation of Soft Magnetic Composite Impeder Performance for use in Induction Tube Welding Systems</i>	24
Ulrich Lüdtkke and Andreas Löhlein <i>Temperature and flow distribution of liquid metal fin in refractory of induction crucible furnaces</i>	26
Mihails Birjukovs, Pavel Trtik, Anders Kaestner, Jevgenijs Telicko, Jan Hovind, Dariusz Jakub Gawryluk, Imants Bucenieks, Knud Thomsen and Andris Jakovics <i>Dynamic Neutron Imaging of Argon Bubble Flow in Liquid Gallium in Horizontal or Vertical Magnetic Field</i>	28
Patrick Rochala, Alexander Fröhlich, Martin Kroll and Verena Kräusel <i>A inductive joining technology for production of hybrid material composites</i>	30
Pablo Guillén, Héctor Sarnago, Óscar Lucía and José Miguel Burdío <i>Efficiency-Oriented Comparison of Modulation Strategies of a Multi-Output ZVS Resonant Inverter for Domestic Induction Heating</i>	32
Alexander Nikanorov, Yulia Pleshivtseva, Anton Popov, Marco Baldan and Bernard Nacke <i>Optimal programmed control of mass induction heating with guaranteed quality</i>	34
Mario Perez-Tarragona, Héctor Sarnago, Óscar Lucía and José M. Burdío <i>PFC Rectifier for High Power Quality and High Efficiency Domestic Induction Heating Appliances</i>	36

Martin Kroll, Wladimir Ebel, Peter Birnbaum, Jonas Gruner and Verena Kräusel <i>Electro-thermo-mechanical simulation of the longitudinal HFI-welding process of carbon steel tubes</i>	38
Sergej Belik <i>Development of high-performance air heater based on an inductively heated packed bed</i>	40
Amar Al-Obaidi, Martin Kroll and Verena Kräusel <i>FEM Simulation of Hot Single Point Incremental Forming Assisted by Induction Heating</i>	42
Mihails Birjukovs, Juris Vencels, Juhani Kataja and Peter Raback <i>Microwave Heating of Water in a Rectangular Waveguide: Validating EOF-Library Against COMSOL Multiphysics and Existing Data</i>	44
Nikolay Khrenkov <i>Load capacity of cables insulated materials of high thermal conductivity</i>	46
Bernard Nacke and Marco Baldan <i>Induction tempering of surface hardened components</i>	48
Jan Hrbek, Bence Mészáros, Mykhaylo Paukov and Martin Kudláč <i>Density of the System Al₂O₃-ZrO₂ in a Liquid Phase</i>	50
Jerzy Barglik, Adrian Smagór and Albert Smalcerz <i>Electrical Efficiency of Induction Contour Hardening Systems</i>	52
Guillaume Wasselynck, HUU-Kien Bui, Antoine Pierquin, Didier Trichet, Gérard Berthiau, Banda Kane, Javad Fouladagar and Abdoulaye Ba <i>Welding of Carbon Fibers Composite by Induction Heating</i>	54
Martin Ennen, Egbert Baake and Igor Niedzwiecki <i>Tailored Heating Of Billets For Hot Forming Using An Induction Heating Approach</i>	56
Mattia Guglielmi, Marco Baldan, Egbert Baake and Martin Schulze <i>Influence of Double-Frequency Lorentz Force Component in Modeling Electromagnetic Stirring of Molten Metals</i>	58
Igor Sokolov, Evgeniy Shvydkiy and Gennady Losev <i>Liquid metal flow generating by unsymmetric traveling magnetic field</i>	60
Sergejs Pavlovs, Andris Jakovics and Alexander Chudnovsky <i>Melt Electro-vortex Flow in DC EAF Model with Two Bottom Electrodes in Axial Magnetic Field</i>	62
Matteo Lazzarin, Michele Forzan and Fabrizio Dughiero <i>Thermal behaviour of synthetic countertop used as cooker surface over induction hobs</i>	64

Sergio Lupi, Michele Forzan, Paolo Di Barba, Maria Evelina Mognaschi and Elisabetta Sieni <i>Optimal Synthesis of Dual Frequency Transverse Flux Induction Heating of Metal Strips</i>	66
Maxim Khatsayuk, Viktor Demidovich and Viktor Timofeev <i>The destruction model of cylindrical billet's hard shell during heating and melting by internal heat sources</i>	68
Stefan Schubotz <i>Research of multicentric ring coils in comparison to classic ring coils</i>	70
Alexander Antipin and Vasiliy Frizen <i>Investigation of the induction heating spherical bodies dispersed in the continuous load inductor stove</i>	72
Yuriy Perevalov and Victor Demidovich <i>Induction heat treatment of large rolls with two independent power sources</i>	74
Jonas Kimme, Josephine Zeisig, Alexander Fröhlich and Verena Kräusel <i>Technology development for manual laser cladding of high-alloy tool steels with simultaneous inductive preheating for crack prevention</i>	76
Ervīns Blumbergs, Janis Freibergs, Eriks Platacis, Mihails Majorovs and Vera Serga <i>Model experiments using slag during CdO recovery</i>	78
Patrick Rochala, Christian Hofmann, Martin Kroll, Maik Wiemer and Verena Kräusel <i>Chip-level bonding for microelectronic components by induction sintering of micro structured Ag particles</i>	80
Yuriy Perevalov, Victor Demidovich and Ivan Vegera <i>Advanced Induction Heat Treatment Systems of Pipes</i>	82
Vasiliy Frizen, Ivan Smolyanov, Fedor Tarasov and Salavat Fatkullin <i>Refined Model of Induction Heater Taken into Account Static Characteristics of Inverter</i>	84
Koen Van Reusel <i>Exposure to electromagnetic fields produced by industrial processes</i>	86
Francois Bay, Jesus Oswaldo Garcia, Jose Alves and Julien Barlier <i>Error analysis in finite element modelling of induction heating processes</i>	88
Ivan Smolyanov, Evgeny Shmakov and Juris Vencels <i>Numerical Approaches to Analyzing of MHD Processes Occuring to Induction Pump</i>	90
Alexander Lepeshkin, Alexander Kuvaldin and Stepan Lepeshkin <i>Investigation of Heating of Rotating Disks in an Electromagnetic Field Using Strong Permanent Magnets</i>	92

Evgeniy Shmakov, Ivan Smolyanov and Juris Vencels <i>Calculation Fluid Dynamic of Induction Pump Using Open Source Software</i>	94
Marina Rashevskaya, German Lipinskiy and Alexey Kulikov <i>Applicability of calculation methods of minimum and maximum short circuit currents in grid with voltage up to 1 kV</i>	96
Tareq Eddir, Robert Goldstein and Robert Haun <i>Investigating the Benefit of Soft Magnetic Composite Inserts on Energy Efficiency in Cold Wall Billet Casters Using Computer Simulation</i>	98
Pablo García Michelena, Xabier Chamorro Sanchez, Emilio Ruiz Reina and Nuria Herrero Dorca <i>Multiphysical modelling and validation of VIM for Inconel 718 heating and melting</i>	100
Andrey Zhurkin, Sergey Nekhamin, Michael Pogrebisskiy and Irina Martynova <i>AC arc electrical load model for new power supply analysis</i>	102
Eduard Vinter, Mikhail Pervukhin and Viktor Timofeev <i>Numerical simulation of conduction refining of molten aluminum in the casting launder</i>	104
Malvine Strakova, Vadims Geza, Mihails Scepaniskis and Alvis Eimuss <i>Computer Simulation of Steel Microstructure Composition for Induction Hardening of a Splined Shaft for Various Cooling Rates</i>	106
Suraj Murali, Christian Bothen, Srivijay Manjunath, Ebrahim Bagheri, Mohamed Loukil, Daniel Pelikan, Kristiaan Pelckmans and Dragos Dancila <i>Energy Efficient Solid-State Microwave Curing of Carbon Fiber Reinforced Composites</i>	108
Ivan Smolianov, Vaclav Kotlan and Ivo Dolezel <i>Approaches to Modernize Induction Heater for Purpose of Heat Treatment of Titanium Alloys</i>	110
Jakub Jirinec, Michal Knedlik and David Rot <i>Possibilities of Using an Energy Surplus of Photovoltaic Power Plants</i>	112
Jakub Jiřinec, Lenka Raková and David Rot <i>Controlled Ventilation of Interior Spaces Using a Central Recuperation Unit</i>	114
David Rot, Michal Knedlik, Jakub Jirinec, Jiri Hajek, Jiri Kozeny and Antonin Podhrazky <i>Cost reduction opportunities in induction surface hardening processes for smaller diameter cylindrical loads</i>	116
Vaclav Kotlan, Roman Hamar, Karel Slobodnik and Ivo Dolezel <i>Modeling of temperature patterns and hardness of surfaces obtained by additive technique</i>	118
Jan Kohout and Lenka Sroubova <i>Modeling of the heat transfer in the switchboard cabinet</i>	120

Liquid metal layer dynamics in transverse alternating magnetic field

Valters Dzelme
Institute of Numerical Modelling
University of Latvia
Riga, Latvia
valters.dzelme@lu.lv

Andris Jakovics
Institute of Numerical Modelling
University of Latvia
Riga, Latvia
andris.jakovics@lu.lv

Egbert Baake
Institute of Electrotechnology
Leibniz University of Hanover
Hanover, Germany
baake@etp.uni-hannover.de

Abstract—We study liquid metal layer edge instability in transverse alternating magnetic field, both experimentally and numerically. An inductor is located along one of the layer edges. We find experimentally that liquid metal surface oxidation leads to almost static edge pattern unlike non-oxidized case where wavy oscillations of the edge are observed. In both cases, numerical modelling is a complicated and time-consuming matter, especially due to three-dimensional nature of the phenomena. Nevertheless, preliminary 3D simulations are in a qualitative agreement to experiments.

Index Terms—magnetohydrodynamics, liquid metal, instability

I. INTRODUCTION

Medium- to high-frequency magnetic fields are often used in electromagnetic processing of materials - heating and melting. In some technologies, such as cold crucible induction melting, the liquid metal can semi-levitate - it is supported by a solid base from the bottom but is completely repelled from the crucible side walls by electromagnetic forces. [1] In the case of liquid metal electromagnetic semi-levitation, if the melt layer is relatively thin, so that surface tension and contact line dynamics play an important role, different free surface instabilities have been observed in the past, such as gallium drop oscillations and rotation [2]. The phenomena have been studied theoretically [3], explaining the main causes of the edge pinch instability where some small edge perturbations are amplified by the magnetic field line concentration. Numerical modelling of such dynamic free surface effects, due to the complexity of physics involved and simulation time requirements, has not been done.

In this work, we study thin liquid metal layer edge instability near a high-frequency inductor. Experimental work involves studying the edge instability depending on inductor current, frequency, as well as layer thickness. Additionally, the effect of liquid metal free surface oxidation on the dynamics is assessed. Numerical work involves fully coupled 3D simulations, at this stage trying to achieve at least qualitative agreement to experimental observations.

This work is partially supported by the ERDF project No. 1.1.1.1/18/A/108 "Development of numerical modelling approaches to study complex multi-physical interactions in electromagnetic liquid metal technologies".

II. EXPERIMENTAL SETUP

Experiments were done at the Institute of Electrotechnology, Leibniz University of Hanover in Germany. The setup is shown in Fig.1. The melt is gallium or galinstan (we did experiments with both), the container is acrylic, inductor is a water-cooled copper tube. The inductor is connected to a 100 kW power generator and during the experiments frequencies of 3 to 5 kHz and currents of 1 to 3 kA were used. Melt dimensions are 200 mm along the inductor edge, 100 mm in direction normal to inductor and thickness is from 4 to 11 mm.

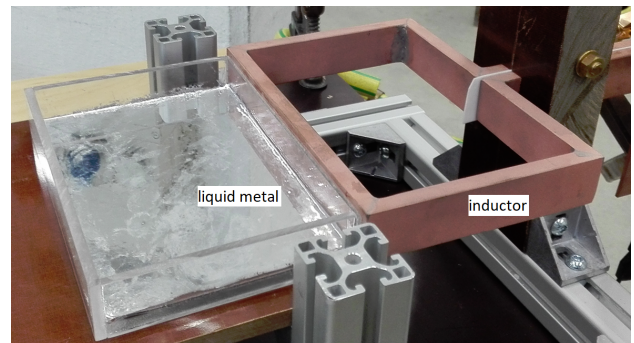


Fig. 1. Experimental setup.

III. NUMERICAL MODEL

The problem is multi-physical and coupled - electromagnetic force induces fluid flow and deforms liquid metal surface and the electromagnetic field depends on the liquid metal volume shape. Numerical approaches to solve such problems have been developed in the past [4] using external coupling between commercial tools for electromagnetics and fluid flow. Recently developed EOF-Library [5] allows efficient coupling of free open-source tools Elmer [6] (electromagnetics, finite element method) and OpenFOAM [7] (fluid flow, finite volume method). These tools have been verified against simulations with commercial software [8]. In this work, we use the open-source tools.

The numerical model consists of two parts - electromagnetics model (part of the inductor near the melt, melt volume and some air around) and two-phase fluid flow model (only

the melt domain with some air above it). Elmer solves steady electromagnetics in frequency domain, OpenFOAM solves two-phase flow using the Volume of Fluid method [9] for free surface capturing and $k-\omega$ SST model [10] for turbulence.

IV. RESULTS

The most representative results out of all experiments and simulations are shown in Fig.2 and Fig.4 (experiments) and Fig.3 and Fig.5 (simulations), with only the region near the inductor shown. Note that in the case of non-oxidized surface, the edge pattern was fluctuating, whereas the oxidized melt was almost static apart from some small fluctuations perhaps due to turbulent bulk flow. Clearly, the metal surface oxidation plays an important role in the pattern formation. Similar effect has been observed in [2], where the effect of oxidation was explained as a formation of a "crust" which not only changes the surface tension coefficient but also reduces the mobility of the liquid-solid contact line. We observed that, in the case of smallest thickness used in experiments (4 mm), the oxide layer could even support the deformed melt shape - it remained so even after switching off the inductor current.



Fig. 2. Oxidized galinstan free surface shape in experiments; melt thickness 4 mm, current 1500 A, frequency 5330 Hz.



Fig. 3. "Oxidized" galinstan free surface shape in simulations; melt thickness 4 mm, current 760 A, frequency 5330 Hz.



Fig. 4. Non-oxidized galinstan free surface shape in experiments; melt thickness 11 mm, current 2585 A, frequency 4270 Hz.

The simulations don't really consider the oxidation but we model the effect as a modified contact angle - in the non-oxidized case it is large (experimental estimation is around 150 degrees) and for oxidized melt it is small (estimation of around 30 degrees). Such approximation, of course, is not ideal and we cannot obtain the melt support only by the oxide crust that we observed experimentally. Nevertheless, the preliminary simulations are in a qualitative agreement to experiments.



Fig. 5. "Non-oxidized" galinstan free surface shape in simulations; melt thickness 11 mm, current 2585 A, frequency 4270 Hz.

V. CONCLUSIONS

The liquid metal free surface edge near a high-frequency inductor can assume different shapes depending on oxidation, field intensity, layer thickness etc. Since the phenomena are three-dimensional, numerical modelling is very time-consuming. Simplified preliminary simulations using coupled open-source tools are in a qualitative agreement to experimental observations. More precise mathematical models are necessary to account for the oxide layer effects on surface tension and contact line dynamics. More experiments are planned in near future to obtain data in a wider range of the parameter space considered (layer thickness, current and frequency etc).

REFERENCES

- [1] K. Pericleous, V. Bojarevics, G. Djambazov, R.A. Harding, M. Wickins, Experimental and numerical study of the cold crucible melting process, *Applied Mathematical Modelling*, Vol. 30, 2006, pp. 1262-1280
- [2] K. Spragg, S. Letout, R. Ernst, A. Sneyd, Y. Fautrelle, Instabilities in electromagnetic quasilevitation, *Physical Review E*, Vol. 89, 2014, 053014
- [3] J. Priede, J. Etay, Y. Fautrelle, Edge pinch instability of liquid metal sheet in a transverse high-frequency ac magnetic field, *Physical Review E*, Vol. 73, 2006, 066303
- [4] S. Spitan, E. Baake, B. Nacke, A. Jakovics, Numerical Modeling of Free Surface Dynamics of Melt in an Alternate Electromagnetic Field. Part II: Conventional Electromagnetic Levitation, *Metallurgical and Materials Transactions B*, Vol. 47, 2016
- [5] J. Vencels, P. Raback, V. Geza, EOF-Library: Open-source Elmer FEM and OpenFOAM coupler for electromagnetics and fluid dynamics, *SoftwareX*, Vol. 9, pp. 68-72, 2019
- [6] <https://www.csc.fi/web/elmer>
- [7] <https://openfoam.org>
- [8] J. Vencels, A. Jakovics, V. Geza, Simulation of 3D MHD with free surface using open-source EOF-Library: levitating liquid metal in an alternating electromagnetic field, *Magnetohydrodynamics*, Vol. 53, 2017, pp. 643-652
- [9] J. Heyns, O. Oxtoby, Modelling surface tension dominated multiphase flows using the VOF approach, 6th European Conference on Computational Fluid Dynamics, 2014
- [10] F. R. Menter, Two-Equation Eddy-Viscosity Turbulence Models for Engineering Applications, *AIAA Journal*, Vol. 32, pp. 1598-1605, 1994

Directional solidification of metallic alloys and composites under electromagnetic interaction

Imants Kaldre
University of Latvia
Institute of Physics
Riga, Latvia
imants.kaldre@lu.lv

Andris Bojarevics
University of Latvia
Institute of Physics
Riga, Latvia
andris.bojarevics@lu.lv

Abstract— In this work metallic alloys with particle inclusions has been directionally solidified under electromagnetic interaction. Applied magnetic field and electric current creates melt flow which has impact on solidification structure and properties of the alloy. There are various effects taking place under electromagnetic fields during solidification. For different materials different effects can be dominant. In this work aim is to investigate aluminum alloys. Test experiments using low temperature alloys are presented as well. Experimental results are explained by analytical and numerical models.

Keywords— Aluminum alloys, Metal matrix composites, Directional solidification, electromagnetic ultrasound

I. INTRODUCTION

Solidification of metallic alloy is a complicated multiphysical process where numerous physical processes take part and influence each other in different ways. Structure of the metal or alloy is also significantly affected by heat and solute transport in the liquid melt in the vicinity of the solidification interface and in the mushy zone during solidification process. At low solidification velocity larger grains are forming and their size depends on temperature gradient along the solidification interface and solidification velocity. This relation is well known and studied. If electromagnetic force is present, then situation can be different.

Application of magnetic fields can be additional mechanism to affect and create convection in the liquid melt and mushy zone of metallic alloy. Combined alternating (AC) and static (DC) magnetic fields has been used to affect microstructure and impurity transport of the metallic alloys and metal matrix composites. DC magnetic field creates thermoelectromagnetic convection and melt flow perpendicular to magnetic field leading to anisotropic material structure [1]. Electric current and DC electromagnetic interaction has been studied showing that electromagnetic vibrations is one of the methods to disperse particles and refine grain structure of the metallic alloys.

II. METAL MATRIX COMPOSITES

Dielectric particles in metal matrix can significantly improve some of metal properties, like mechanical strength, thermal properties and radiation absorption properties. Particles added to liquid metal tend to form agglomerates due to Van der Waals forces and electromagnetic separation between metal and particles or their ensembles. Dispersion of these agglomerates is a technical challenge which limits the

production of these materials in larger quantities. Electromagnetically induced vibrations is one of the means how to disperse particles contactlessly. In previous works it has been shown that combined AC and DC magnetic fields can create sufficiently high-pressure amplitude to disperse particles in some metals [2]. Application of AC and DC magnetic fields during directional solidification can be an effective approach to refine grain structure and to disperse particles.

III. EXPERIMENT

Directional solidification has been widely used to study solidification characteristics and its dependence on various external parameters. In this work series of experiments has been done by directionally solidifying SnBi and SnPb alloys. Principal scheme of experimental setup is shown in Fig.1. Metal is filled in corundum tube. Tube is pulled by programmable step motor through the AC coil which melts the sample and water-cooled heat exchanger. Solidification interface remains at fixed location between the coil and heater. DC magnetic field is provided by external permanent magnet assembly. Directionally solidified samples are then investigated by optical microscopy and EDX spectroscopy to visualize particle distribution.

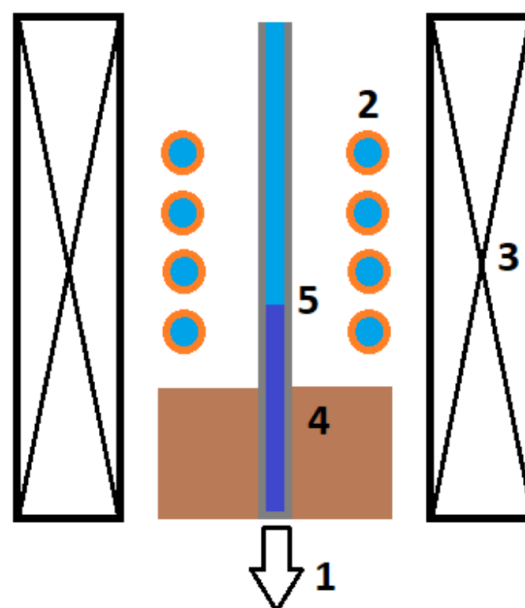


Figure 1. Scheme of the experimental setup: 1) Programmable pulling motor, 2) AC inductor, 3) DC magnet, 4) Cooler, 5) Solidification interface

Experimental setup allows us to achieve up to 0.6 T DC magnetic field, while AC magnetic field at 50 Hz frequency is 0.05 T. We use solidification velocities from 10 $\mu\text{m/s}$ to 1 mm/s. Effect of electromagnetic vibrations under various magnetic fields are solidification velocity has been studied. However, result interpretation is difficult, because there are not always direct link between solidified microstructure and melt flow during solidification.

CONCLUSIONS

Electromagnetic effects can have significant impact on the solidification structure and impurity distribution. Results of these experiments show that superimposed AC and DC magnetic fields can be used to affect the melt flow near the solidification interface during directional solidification and to refine the grain structure, and to improve particle dispersion.

ACKNOWLEDGMENT

This work is supported by PostDoc Latvia Postdoctoral research grant « Electromagnetic methods for metal matrix nano-composite production » No. 1.1.1.2/VIAA/2/18/264

REFERENCES

- [1] I. Kaldre, Y. Fautrelle, J. Etay, A. Bojarevics, L. Buligins, "Influence on the macrosegregation of binary metallic alloys by thermoelectromagnetic convection and electromagnetic stirring combination," *Journal of Crystal Growth*, Vol. 402, pp. 230-233, 2014.
- [2] I. Kaldre, A. Bojarevičs, I. Grants, T. Beinerts, M. Kalvāns, M. Milgrāvis, G. Gerbeth, "Nanoparticle dispersion in liquid metals by electromagnetically induced acoustic cavitation," *Acta Materialia*, Vol. 118, pp. 253-259, 2016.

New contactless aluminum degassing system - GaInSn model experiments with a numerical study

Reinis Baranovskis
Institute of Physics
University of Latvia
Riga, Latvia
reinis.baranovskis@lu.lv

Didzis Berenis
Institute of Physics
University of Latvia
Riga, Latvia
didzis.berenis@lu.lv

Ilmars Grants
Institute of Physics
University of Latvia
Riga, Latvia
ig@sal.lv

Andris Bojarevics
Institute of Physics
University of Latvia
Riga, Latvia
andris.bojarevics@lu.lv

Toms Beinerts
Institute of Physics
University of Latvia
Riga, Latvia
toms.beinerts@lu.lv

Abstract—Molten aluminum in metallurgy environment collects hydrogen from ambient air and water vapor thus after crystallization causing porosity. Therefore hydrogen concentration must be reduced below a certain threshold before the final metal product is made. The most common way is gas purging when inert gas is injected in the melt which absorbs dissolved hydrogen and leaves the metal through the free surface. The existing methods need a mechanical contact with hot and chemically aggressive aluminum which leads to higher maintenance costs. We propose a novel contactless degassing method which uses electromagnetic forces to drive the flow and split the injected inert gas bubbles. Numerical analysis is used to study permanent magnet driven flows and to optimize the degassing process. The problem is solved by coupling OpenFoam for hydrodynamic calculations and Elmer for electromagnetic calculations. According to them, the most promising design is chosen for GaInSn experimental scale model (see Fig. 1). In experiments the velocity field and the developed pressure in different operating regimes has been obtained and later compared to the numerical model. Results show that the iron yokes can be used as a cost effective tool for magnetic flux concentrators even on rotating permanent magnet machinery providing at least a 30 % pressure increase. Overall, the system can achieve large velocities which when scaled to industrial sized setup would be sufficient for the argon dissipation to take place. The developed pressure head is high enough to lift aluminum several meters, allowing device to be integrated in a manufacturing line.

Index Terms—Aluminum degassing, MHD modelling, GaInSn experiment, Permanent magnet pump, Bubble flow

I. INTRODUCTION

In industrial processes aluminum inevitably dissolves hydrogen from air and water vapor present in environment. Dissolved hydrogen causes porosity even in trace amounts and that leads to worse mechanical properties [5]. Therefore degassing is a necessary step in most aluminum manufacturing operations. Here we propose a novel degassing system based on inert gas injection. Classically a rotary gas impeller is used [3] but here metal is driven by electromagnetic forces. A rotating permanent magnet system in a contactless way can achieve a rapid and turbulent flow in which the gas is injected. Empirically, gas purging studies have shown for best degassing efficiency bubble sizes should be refined to size around 2 – 3 mm [4] since smaller bubbles rise slower and have larger surface/ volume ratio. Analysis of mechanically stirred water [2] show that Reynolds number of at least $2 \cdot 10^4$

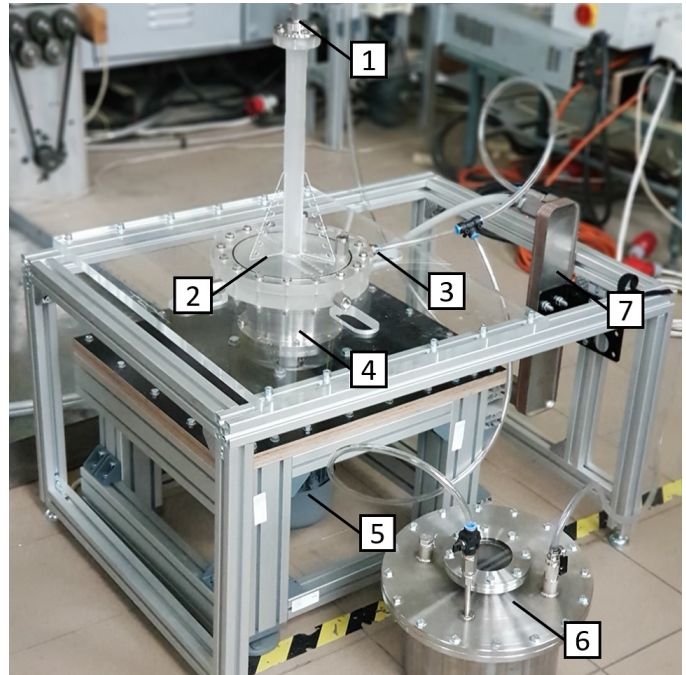


Fig. 1. GaInSn experimental model. The lower frame holds the rotating permanent magnet. The top structure contains the metal reservoir, a cooling loop and a vertical loop for pressure head. 1 - inlet 2 - plexiglass vessel for GaInSn; 3 - outlet; 4 - permanent magnet rotor; 5 - electric motor; 6 - GaInSn storage; 7 - heatsink

is necessary for bubble breakup of that size to take place. One of the challenges is to have a flow that maximizes argon bubble rising time to improve degassing efficiency since hydrogen trapping by inert gas bubbles is a physical process. Flow that meets these constraints is achieved by using permanent magnet dipole stirrer under the volume of molten metal. Compared to inductors rotating permanent magnet machinery is more efficient in generating low frequency magnetic field due to absence of Joule losses in coil. We have shown that with permanent magnet stirrer it is possible to achieve metal velocities up to 4 m/s in GaInSn alloy in size relevant for industrial processes [1]. In this paper we analyze and optimize a specific stirring setup (see figure 1) which differs other rotating permanent magnet machines because of the magnetic

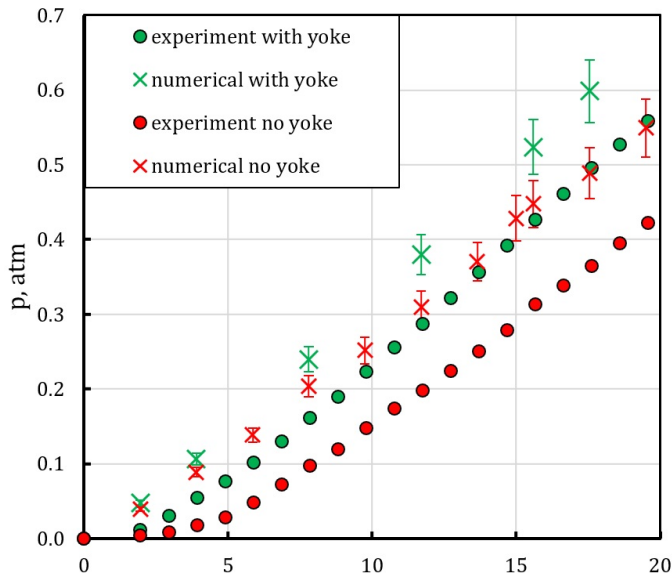


Fig. 2. Pressure in outlet as a function of magnet rotation speed. No flow rate.

field configuration used.

II. RESULTS AND DISCUSSION

Both pressure and velocity is measured at various magnetic field rotation frequencies. Since it essentially is a dipole field its rotational frequency is the same as permanent magnet's. In figure 2 cases with and without yokes are compared experimentally and numerically. It is shown experimentally that pressure with yoke is 32 % higher at the fastest of tested configurations and difference in numerical calculations is 22 %. Discrepancy might be explained by combination of inaccuracies both in numerical model and experiment. Numerical model accuracy depend on used material properties e.g. viscosity and electrical conductivity which for GaInSn are known only to two significant digits. Experimentally biggest error is brought by uncertainty of distance between magnet and liquid metal since magnetic field decays rapidly from surface and force is proportional to magnetic field squared. Overall pressure head of 884 mm GaInSn (or 0.55 atm) is a good result because when the degassing unit is up-scaled it would be able to lift aluminum multiple meters if the device is also used as a pump for molten aluminum transport.

Tangential velocity in multiple radial positions is presented in figure 3 where experimental, numerical and magnetic field velocities are compared. Firstly, a maximum velocity in numerical calculations is observed at radial position $R = 4.5 \text{ cm}$ and in experiment in position $R = 3.8 \text{ cm}$. At first it seems counter-intuitive since the velocity of traveling magnetic field is proportional to radius $v = \omega R$ so a larger velocity is expected near the outer wall. Just as unexpected is the fact that in the cases of low rotational frequency it is observed that the fluid as fast as the magnetic field in region close to center. That means magnetic field in that region is even slowing down the flow. Both of these findings can be explained

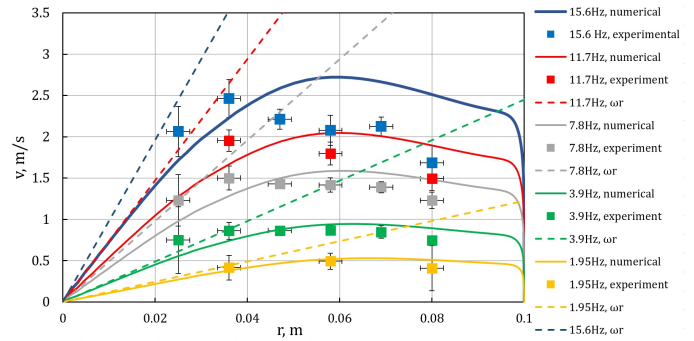


Fig. 3. Flow profiles at different magnet rotation frequencies. Lines represent numerical calculations, squares are experimental measurements and dashed lines are ωr - velocity of magnetic field at given radius.

by inward transfer of impulse moment by radial flow. Overall velocities in range of 2.0 to 2.5 m/s are reached with 15.6 Hz rotational frequency. Considering GaInSn physical properties it corresponds to fully turbulent flow with $Re = 5 \cdot 10^5$. Higher rotational frequencies are not measured due to the limitations of the UDV system in which further measurements were not convincing.

III. CONCLUSION

Iron yokes can be used as a cost effective tool for magnetic flux concentrators even on rotating permanent magnet machinery. In this setup it provides at least a 30 % pressure increase which means more intensive flow or ability to use less magnetic material for same hydrodynamic performance. Overall system can achieve large velocities which when scaled to industrial sized setup would be sufficient for the argon dissipation to take place. Developed pressure head is high enough to lift aluminum several meters. Velocity profiles show maximum velocity closer to the center than expected and flow near center as fast as velocity of traveling magnetic field. These finding can be explained by inward momentum transfer with radial flow. A sophisticated numerical model has been developed which solves permanent magnet driven turbulent flows with at least 25 % accuracy for mean velocity.

REFERENCES

- [1] T. Beinerts, A. Bojarevičs, I. Buceniēks, Y. Gelfgat, and I. Kaldre. Use of permanent magnets in electromagnetic facilities for the treatment of aluminum alloys. *Metallurgical and Materials Transactions B*, 47(3):1626–1633, Jun 2016.
- [2] B. O. Hasan. Experimental study on the bubble breakage in a stirred tank. part 1. mechanism and effect of operating parameters. *Int. J. Multiphase Flow*, 97:94 – 108, 2017.
- [3] E. Mancilla, W. Cruz-Méndez, I. E. Garduño, C. González-Rivera, M. A. Ramírez-Argáez, and G. Ascanio. Comparison of the hydrodynamic performance of rotor-injector devices in a water physical model of an aluminum degassing ladle. *Chemical Engineering Research and Design*, 118:158 – 169, 2017.
- [4] G. K. Sigworth, E. M. Williams, and D. C. Chesonis. *Gas Fluxing of Molten Aluminum: An Overview*, pages 65–70. Springer International Publishing, Cham, 2016.
- [5] D. E. J. Talbot. Effects of hydrogen in aluminium, magnesium, copper, and their alloys. *International Metallurgical Reviews*, 20(1):166–184, 1975.

Time-Optimal Feedback System with Identifier to Control Induction Heating Process

Yuliya Pleshivtseva
Samara State Technical University
Samara, Russia
yulia_pl@mail.ru

Ilya Levin
Samara State Technical University
Samara, Russia
levin.is@samgtu.ru

Bernard Nacke
Leibniz Universität Hannover
Hannover, Germany
nacke@etp.uni-hannover.de

Martin Schulze
Leibniz Universität Hannover
Hannover, Germany
schulze@etp.uni-hannover.de

Alexander Nikanorov
Leibniz Universität Hannover
Hannover, Germany
nikanorov@etp.uni-hannover.de

Abstract — The goal of the paper is to show a possible solution of time-optimal control problem applied to the induction heating process when the information about process parameters is not precisely known. In order to solve this problem a special method to construct time-optimal closed-loop control system was suggested. The identifier of unknown parameters is integrated in the implemented optimal control system. The proposed method is approved by numerical FLUX&Matlab simulation and experimental results.

Keywords— induction heating, time-optimal control, interval uncertainties, feedback control systems.

I. INTRODUCTION

One of the central and most complex problems in modern control theory is to synthesize control algorithms and control systems under almost always existing conditions of uncertainty of industrial process characteristics primarily due to the inaccurate knowledge of its parameters and the action of uncontrolled external disturbances. In application to induction heating systems, the information about such parameters of the processes as initial temperature and heat loss, is usually not fixed, and only the intervals of their possible values variation are known. From engineering point of view the other important factor is necessity to obtain as simple control algorithm as possible to be implemented in practice. In order to achieve this goal the synthesis of time-optimal control system with identifier of uncertain parameters in the loop is required. The paper considers the developed procedure to solve this problem.

II. THE PROCEDURE OF STRUCTURAL-PARAMETRIC SYNTHESIS OF TIME-OPTIMAL FEEDBACK CONTROL SYSTEM

The process of static induction heating of cylindrical billet with interval uncertainty of initial temperature and heat loss values is considered. The temperature distribution $T(r, l, t)$ along axial $r \in [0, R]$ and radial $l \in [0, L]$ directions within the heated cylindrical billet considered as an axially symmetrical temperature field (fig. 1). For electromagnetic and temperature field analysis the non-linear two-dimensional numerical model developed in FLUX software has been used [1]. The parameters of induction heating system are shown in table I. The value of inductor voltage U is selected as a control input constrained by condition $0 \leq U \leq U_{\max}$.

An optimization problem could be formulated in the following form. It is required to obtain a desired temperature T^* with maximum heating accuracy ε_0 using two-stage time optimal control U^* (fig. 2) in minimal process time t_{end} under

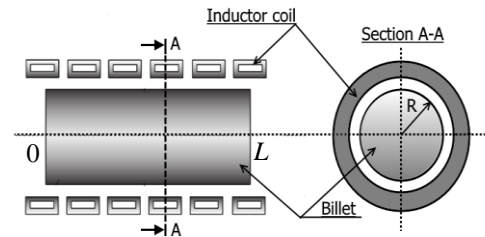


Fig. 1. Geometry of induction heating system

condition of interval uncertainty of the initial temperature T_0 and heat loss α values: $T_0 \in [T_{0\min}, T_{0\max}]$, $\alpha \in [\alpha_{\min}, \alpha_{\max}]$. A final temperature distribution is considered along radial coordinate in the central cross-section of the billet (fig. 1, cross-section A-A).

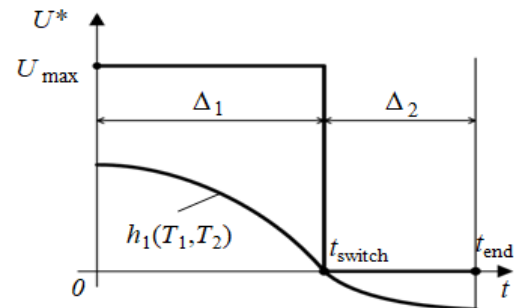


Fig. 2. Time-optimal control with two intervals of durations Δ_1 and Δ_2

The goal is to design an optimal control algorithm with feedback that provides a solution to the given problem.

First step is to synthesize deterministic optimal control system with the fixed values of initial temperature $T_{0\text{av}}$ and heat loss α_{av} .

The solution of this problem is an optimal control algorithm that can be written in the following form:

$$U^*(T_1(t), T_2(t)) = U_{\max}/2 \times (1 + \text{sign}h_1(T_1(t), T_2(t))). \quad (1)$$

Here $h_1(T_1(t), T_2(t))$ is switching function depended on the current values of measured temperatures at two selected points within the cross-section A-A of the billet:

$$h_1(T_1, T_2) = \rho_1(T^* - \varepsilon_0 - T_1(t)) + \rho_2(T^* - \varepsilon_0 - T_2(t)). \quad (2)$$

The points of measurement are located on the edge $T_1(t) = T(R,t)$ and at the center of the billet $T_2(t) = T(0,t)$; ρ_1, ρ_2 are feedback coefficients that could be obtained along with the maximum heating accuracy ε_0 after a solution of time-optimal control problem for open loop system is found [2]. Switching from one control stage to another happens when the sign of a switching function changes (fig. 2).

On the next step the identification of the uncertain process parameters T_0 and α can be done using special function that represents the dependence of unknown parameters on the results of measurements. In the considered case this function is formulated as the dependence $F(T_1(t_{\text{fix}}), T_2(t_{\text{fix}}))$ on the temperatures measured in the center $T_1(t_{\text{fix}})$ and on the surface $T_2(t_{\text{fix}})$ at the time t_{fix} which can be chosen arbitrarily within the heating time interval Δ_1 . The procedure of approximation of this function described in [3].

Final step is integration of identifier $F(T_1(t_{\text{fix}}), T_2(t_{\text{fix}}))$ with the previously obtained algorithm (1) in order to provide a correction of the feedback coefficients ρ_1, ρ_2 in (2). Obtained control algorithm with identifier could be implemented as a program for industrial controller or as a module for control system software. The measurement in selected points could be done with temperature sensors.

III. RESULTS

In order to test time optimal feedback control system with identifier in the loop computer simulation is used. Simulation procedure is divided into following steps. First, the solution of optimal program control problem is found using Matlab in order to obtain optimal parameters of control algorithm (Δ_1, Δ_2 and ε_0). Then the temperature distribution is imported from FLUX to Matlab software. After that it is possible to calculate feedback and identifier's correction coefficients and run simulation in Simulink. The results of computer simulation of time optimal feedback control system of induction heating of cylindrical billet with identifier in the loop are shown on fig. 3, 4. The results demonstrate a good coincidence with the optimal program control solution ($\Delta_1 = 1825$ sec., $\Delta_2 = 162$ sec., $\varepsilon_0 = 1.8^\circ\text{C}$) when the difference between average and actual value of heat loss α equals to 10 %.

TABLE I. PARAMETERS OF THE INDUCTION HEATING SYSTEM

Parameter	Name	Aluminum billet	Steel billet
		Value	Value
Length of inductor, mm	L_i	1376	80
Number of turns	N	69	5
Distance between inductor and billet, mm	G	50	5
Size of turn, mm	$TW \times TH$	12x16	6x12
Distance between turns, mm	D_t	4	5
Radius of the billet, mm	R	250	50
Length of the billet, mm	L	1000	95
Frequency of current, Hz	f	50	125000
Inductor voltage, V	U_{max}	470	237
Initial temperature, $^\circ\text{C}$	T_0	20	20
Required temperature, $^\circ\text{C}$	T^*	460	500

In order to obtain qualitative characteristics of the optimal control process, the verification of obtained optimal feedback control system without identifier is done by testing the developed algorithm on the existing laboratory installation of the Institute of Electrotechnology of Leibniz

University. The parameters of the process are used only for the experimental case study but not for industrial application.

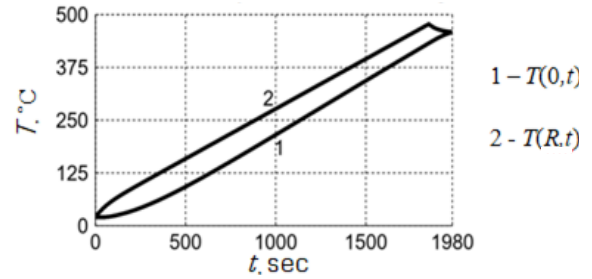


Fig. 3. Time-Temperature history (results of simulation)

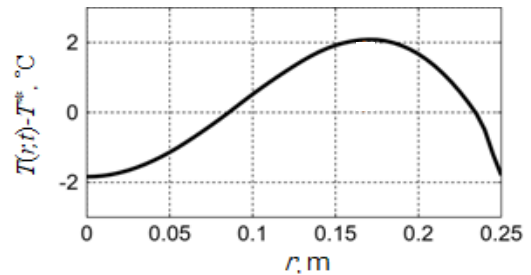


Fig. 4. Final radial temperature distribution in the center cross-section

Parameters and system geometry for a steel billet are shown in table I. In order to calculate feedback coefficients the results of previously obtained optimal control solution were used: $\Delta_1 = 95$ sec., $\Delta_2 = 80$ sec., $\varepsilon_0 = 2^\circ\text{C}$. On fig. 5 the results of this experiment are in good agreement with the obtained solution: the moment of control switching coincides with optimal program control and the final temperatures reach the required value with deviation not more than 4°C .

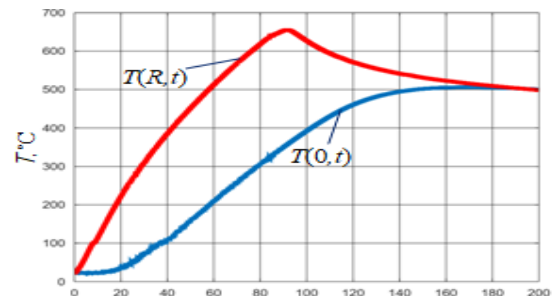


Fig. 5. Time-Temperature history (experimental results)

ACKNOWLEDGMENTS

The work is partly supported by Russian Foundation for Basic Researches (project №19-08-00232).

REFERENCES

- [1] Pleshivtseva Yu., Popov A., Diakonov A., Two-dimensional problem of optimal with respect to typical quality criteria control of through induction heating processes [Dvumernaya zadacha optimalnogo po tipovim kriteriyam kachestva upravleniya protsessom skvoznoho induktsionnogo nagreva]. Vestnik of Samara State Technical University. Technical Sciences Series, 2014. №2(42). pp. 148-163
- [2] Rapoport E., Optimal control systems with distributed parameters [Optimalnoe upravlenie sistemami s raspredelennimi parametrami]. Moscow: Vysshaya Shkola, 2009
- [3] Rapoport E.Y., Levin I.S., Structural-Parametric Synthesis of Time-Optimal Distributed Parameter Control Systems with Interval Uncertainty of the Plant Characteristics, Optoelectronics, Instrumentation and Data Processing. Vol. 51, no. 5. pp. 429-440.2015

Simulation Problems of Internal Inductors

Alexandr Ivanov
St. Petersburg
Electrotechnical University
(LETI)
St. Petersburg, Russia
ANIvanov@etu.ru

Vladimir Bukanin
St. Petersburg
Electrotechnical University
(LETI)
St. Petersburg, Russia
VABukanin@etu.ru

Alexei Zenkov
St. Petersburg
Electrotechnical University
(LETI)
St. Petersburg, Russia
AEZenkov@etu.ru

Abstract—The problems of choosing and calculating the parameters of the internal inductor, the power supply and the necessary matching circuits are considered. A simple analytical method for calculating the electrical parameters of a multi-turn internal inductor with a magnetic core is described. The results of simulating the internal induction heating system are presented, which allow determining the main electrical and heating parameters at the stage of preliminary selection of the design of the induction coil and magnetic concentrator for induction heat treatment.

Keywords—internal inductors, computer simulation, calculation algorithm, ELTA program

I. INTRODUCTION

Some individual induction technologies require the use of internal heating as more efficient than other variants of process. Applications of internal inductors are described by V. Vologdin (1947), F. Kurtis (1950), V. Nemkov et al. (1988) [1-3] and other scientists. Research has also been carried out in recent years by V. Nemkov et al. (2004), V. Bukanin et al. (2005, 2008) [4-6]. They showed an increasing interest in optimizing the parameters of the internal inductor to obtain the maximum efficiency. The developer of the induction installation tries to solve two main problems. The first of them is the choice of the induction system, the parameters of the power supply and the variant of the matching circuit, for example, parallel, series or other compensation circuit, the matching transformer, leads, etc. The second task is to obtain the necessary quality and efficiency of process by optimizing the design of the induction system selected at the first stage. A rational solution can be found using approximate or simple analytical calculation methods at the first design stage and using more accurate numerical methods at the second stage. Induction systems currently in use are discussed below.

A. Hair-pin Internal Inductors

A hairpin inductor (Fig. 1) can heat the hollow part near the coil areas

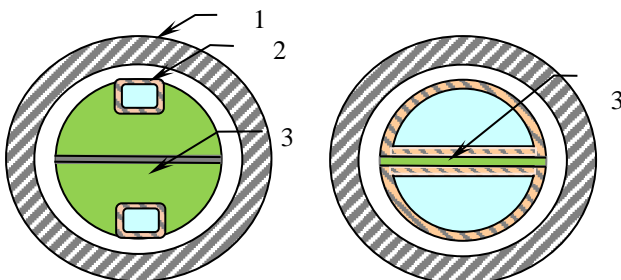


Fig. 1. View of cross-section of a heating system using the hairpin coils (1 – workpiece, 2 – coil, 3 – magnet yoke)

In this case, the inductor or the workpiece should be rotated at a certain speed to ensure uniform heating throughout the surface.

B. Single-turn Internal Inductors

Two types of the single-turn inductors are usually used to heat different workpieces (Fig. 2).

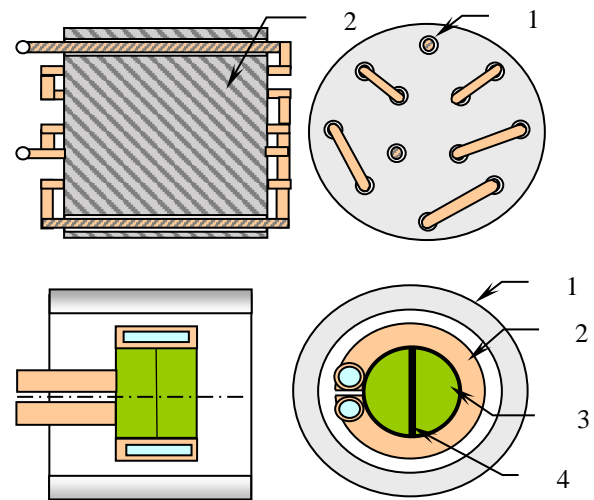


Fig. 2. Examples of single-turn inductors for a forging mold (top) and a hollow cylinder (bottom) (1 – workpiece, 2 – coil, 3 – magnet yoke, 4 – technological gap)

The single-turn cylindrical inductor can be realized both simultaneously and continuously technological process.

II. CALCULATION ALGORITHM

All variants of internal induction systems can be calculated based on the simplified magnetic substitutional circuits and a Total Flux Method (TFM) proposed by V. Nemkov [3]. The equivalent electrical circuitry of the multi-turn inductor with a magnetic core and a return leg is shown in Fig. 3. The two main views of the system are shown in Fig. 4.

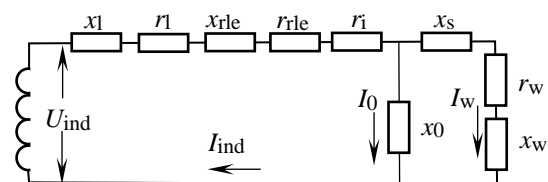


Fig. 3. Electrical schem of the induction system (inductive reactance of leads x_l , return leg x_{rle} , air clearance x_s , reverse closure x_0 , workpiece x_w , active resistance of leads r_l , return leg r_{rle} , coil r_i and workpiece r_w)

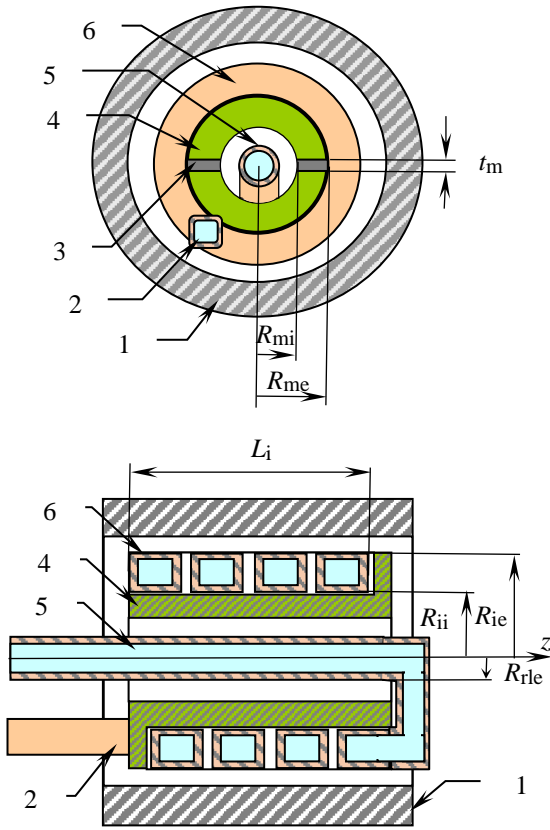


Fig. 4. View of multi-turn induction system (1 – workpiece, 2 – leads, 3 – technological gap, 4 – magnet yoke, 5 – return leg, 6 – coil)

The main problem of calculation in the TFM is the determination of active resistance r_{rle} and inductive reactance x_{rle} of the return leg, as well as reactance of an air clearance x_s and reverse closure x_0 .

The resistance of the return leg r_{rle} (Ohm) can be found using the following formula:

$$r_{rle} = \frac{\rho L_{rle}}{2\pi(R_{rle} - \Delta_{rle}/2)\Delta_{rle}}, \quad (1)$$

where ρ is the resistivity (Ohm·m); L_{rle} is the length (m); R_{rle} is the external radius of the leg (m); Δ_{rle} is the penetration or reference depth (m).

An inductive reactance of the return leg x_{rle} (Ohm) is:

$$x_{rle} = \frac{\omega L_{rle} \mu_0}{2\pi} \left[\ln \frac{R_{ii} + \Delta_{ind}/2}{R_{rle} - \Delta_{rle}/2} + K_m \right], \quad (2)$$

where R_{ii} is internal radius of the inductor (m); K_m is a coefficient of magnetic core.

Other formulae of resistances, inductive reactance's, impedances, power, efficiency, power factor, the induction in the magnetic core, etc. are described and implemented in ELTA program for further analysis and choosing of rational variant, which can provide heating the inner layer of 0.1 cm to the quenching temperature of about 1000...850 °C (Fig. 5).

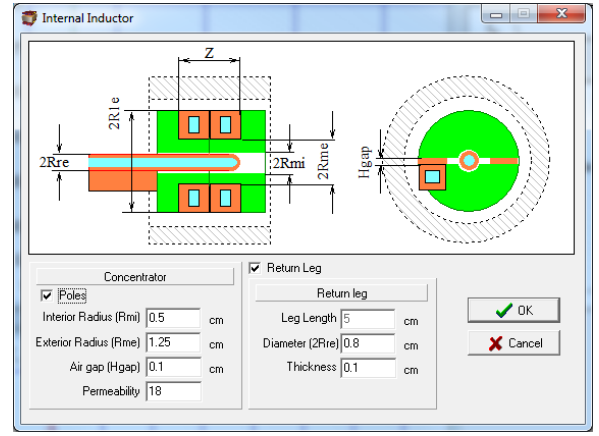


Fig. 5. View of investigated multi-turn induction system

III. RESULTS OF INVESTIGATION AND DISCUSSION

In this section, we will consider two main tasks that need to be solved to optimize the heating by the internal inductor. The first problem is the choice of the concentrator parameters to prevent saturation and overheating of the magnetic material. The second problem is economical, i.e. obtaining minimum energy consumption.

As an example, consider the case of surface hardening of steel 1040 tube to a depth of 0.1 cm. The workpiece has an inner diameter of 4.8 cm, an outer diameter of 5.8 cm and a length of 5.0 cm. The frequency of the power supply is about 70 kHz and varies during the stage. 5 cm long, 4-turn coil is made of copper oval tubing with dimension 1×1 cm and the coil has exterior diameter of 4.5 cm. The return leg is 5 cm long and has an outer diameter of 0.8 cm and a wall thickness of 0.1 cm. There are two sections of leads: 2×12 cm long tube 0.8 cm OD and 20 cm long rectangular busbars 8 cm×0.4 cm. The heating time is 1.0 s. The main electrical parameters of the optimized induction heating are shown in Table I.

TABLE I. ELECTRICAL PARAMETERS DEPENDING ON THE VARIANT

Variant	Electrical parameters					
	U_{ind} V	I_{ind} A	$\cos\phi_{ind}$	η_{ind}	P_{ind} kW	B T
Core no, poles no, return leg yes	247.5	3010	0.170	0.613	127.5	–
Core yes, poles yes, return leg yes	247.1	1552	0.337	0.774	127.5	1.251

REFERENCES

- [1] F. W. Curtis, High-Frequency Induction Heating. McGraw-Hill Book Co., Inc. New York, NY USA, 1950, 380 p.
- [2] V. P. Vologdin, Induction Surface Hardening. Oborongiz, 1947, 292 p.
- [3] V. S. Nemkov and V. B. Demidovich, "Theory and Calculation of Induction Heating Devices," Leningrad: Energoatomizdat, 1988, 280 p. (in Russian)
- [4] V. Nemkov, R. Goldstein, and V. Bukanin, "Optimal Design of Internal Induction Coil," Proc. of the International Symposium on Heating by Electromagnetic Sources. Padua: SDEditorial, pp. 489 – 496, June 2004.
- [5] V.A. Bukanin, D.V. Kuchmasov, A.E. Zenkov and V.S. Nemkov, "Study of Heating by Internal Inductor," Proc. of the International Conference "Actual Problems of Theory and Practice of Induction Heating APIH 05, 2005 (in Russian).
- [6] V.A. Bukanin, V.S. Nemkov and R.S. Goldstein, "Inductors to heat the interior surfaces". Induction heating, No. 5, 2008, pp. 11–17. (in Russian).

A New Approach to Induction Heating Control

Alexandr Ivanov
St. Petersburg
Electrotechnical University
(LETI)
St. Petersburg, Russia
ANIvanov@etu.ru

Vladimir Bukanin
St. Petersburg
Electrotechnical University
(LETI)
St. Petersburg, Russia
VABukanin@etu.ru

Alexei Zenkov
St. Petersburg
Electrotechnical University
(LETI)
St. Petersburg, Russia
AEZenkov@etu.ru

Valentin Vologdin
FREAL&Co Ltd.
St. Petersburg, Russia
valentin@freal.ru

Vladislav Vologdin
FREAL&Co Ltd.
St. Petersburg, Russia
freal@freal.ru

Abstract—A new concept in the implementation of induction heating technologies using smart high-frequency power supplies is described. The smart heating control system consists of a single board industrial computer with built-in ELTA simulation software, several sensors and a visualization system. The real-time heating process is calculated and adjusted according to the required specification. Parameters invisible to sensors, such as the temperature distribution in the heated billet, are calculated and displayed in the process monitoring and documentation system for further analysis of product quality. The results of the study of induction heating systems are presented.

Keywords—induction heating, smart control system, optimization, ELTA program

I. INTRODUCTION

Typically, the induction heating installation of high frequency (HF) consists of the HF power supply, one or more induction coils with the workpiece to be heated, a matching circuit between the power supply and the induction coil(s), and the control system with electrical and temperature sensors. The power supply converts 3-phase 380 V electrical energy of line frequency into single-phase power of frequency 10...440 kHz. The external heating process is controlled by output power, frequency and surface temperature in the HF power supply. DC current and voltage sensors installed after the rectifier allow to determine the power of the power supply. In addition, the power supply has the control and monitoring system for its internal devices.

Problems that are more complex arise when the type of the matching circuit is chosen and its parameters is calculated. The main elements of these matching circuits are the capacitors to compensate for the reactive power of the inductor and the matching transformers to obtain the required voltage at the inductor's input. H. Conrad, et al. (2001) claims that there are two basic schemes of semiconductor converters with the modern MOSFET and IGBT transistors – parallel resonant inverters and series resonant inverters [1]. It is recommended that parallel resonant inverter should be used at low load impedance, low frequency and big power and series inverter – at high load impedance, high frequency and low power. H. Conrad, at al., (2001), C. Hammouma, at al., (2019), A. Attab, at al., (2019) describe that the high frequency installations with solid-state power supplies (for example transistor IGBT-based full bridge series inverter) have series compensation circuits [1, 2, 3]. If the matching circuit includes the transformer, then it is necessary to know

its transformation ratio, approximate efficiency, as well as the voltage drop due to magnetic stray flux and magnetization current.

Typically, a study to optimize the heating process is done in advance, determining the required parameters of the power supply, the heating time for the simultaneous process, the speed of moving for a continuous process, etc. Many optimization criteria are known, the most important of which are obtaining the minimum heating time, the minimum temperature difference in the cross-section of the workpiece, the maximum efficiency of the heating process or some others, described for example by E. Rapoport et al. (2006) [4]. Research on optimization and the creation of new algorithms is constantly ongoing in order to obtain solutions that are more effective by many authors, for example, Yu. Pleshivtseva et al. (2017), P. Di Barba et al. (2014), and many others [5 – 7].

In some industries, the requirement for heating quality is increasing, so innovative approaches are needed to implement induction technologies. Some management systems of product quality have introduced heating control requirements that cannot be identified by sensors and recorded in reporting protocols. Parameters invisible to sensors, such as the temperature distribution in the heated billet, can be calculated and displayed in the process monitoring and documentation system for further analysis of product quality. This requires the use of cyber physical systems with embedded industrial computers and real-time control systems, as described by V. Bukanin et al. (2019) and A. Ivanov et al. (2020) [8, 9].

II. SIMULATION PART OF THE CONTROL SYSTEM

A. Continuous Induction Heating

The results of the real heating process should be documented in the process record for verification in the product quality management system. To meet all the requirements for this, it was necessary to develop a smart control system. The main requirements for this system are preliminary modeling of the continuous heating process, finding the optimal mode for each power supply, adjusting the parameters when conditions change, recording electrical and thermal parameters in the heating protocol. A special application of the program ELTA allows to simulate the process of continuous heating with optimization procedure according to selected criteria. One of the variants for the implementation of the smart control system is shown in Fig. 1. This application may be used in heat tempering, hardening, annealing and forging technologies.

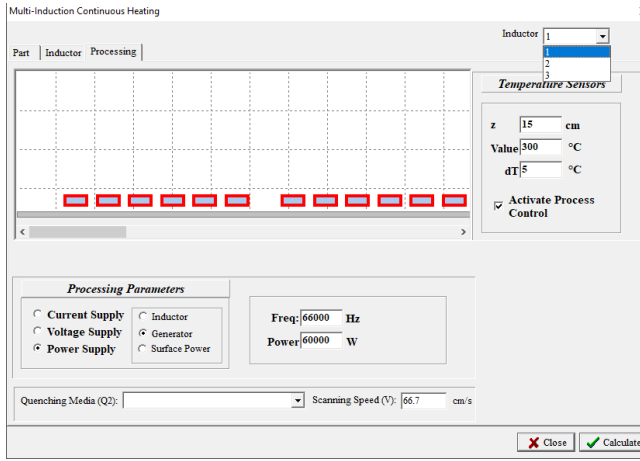


Fig. 1. Window Processing of ELTA application

The main functions of this application are: automatic calculation of the reference value of the output power (voltage/current), real-time calculation and visualization of real temperature profile, real-time temperature control (temperature feedback and power consumption feedback are used).

B. Calculation Algorithm

Operator sets the required temperature on the surface T_{set} and the initial value of the power source S_0 , for example power. ELTA calculates the surface temperature T_{cur} . Then T_{cur} is compared to required temperature range $T \pm \varepsilon$, where ε is the allowed temperature tolerance. If T_{cur} is more than $T + \varepsilon$, the output parameter S decreases and the calculation continues. If T_{cur} is less than $T - \varepsilon$, ELTA will calculate the process with the increased value of output parameter S . If T_{cur} is inside the temperature range $T \pm \varepsilon$, solution is found. This application calculates the integral parameters of the induction coils and temperature profile at the suitable speed for real-time processes, adjusting the parameters of the first and subsequent power supplies to achieve the required temperature, which are programmed and monitored by the temperature sensors. Modification of bisection method is used in ELTA. There are two kinds of this algorithm: the first allows to find required value of generator output parameter S for the required surface temperature and the second one allows to find required value of generator output parameter S for the required temperature difference between surface temperature and point in the internal layer of workpiece [8].

III. FEATURE OF THE CONTROL SYSTEM

A. The Possible Structure of Control System

Several variants for the industrial implementation of the induction heating control system were considered, taking into account the cost, the possibility of the ELTA program, etc. Programmable logical controller (PLC) is the most popular for the control of many manufacturing processes. Typically, PLC is available in almost all control systems of the HF power supply, implementing various functions (Fig. 2). Modular PLC can be used for the induction heating system especially with multiple inductors and power supplies. It includes the central processing unit (CPU) and several additional units. The *Ethernet communication unit* allows to set at the information level the exchange of technological data (*receipts* and *temperature logs*) between the control system and the subject-oriented software ELTA.

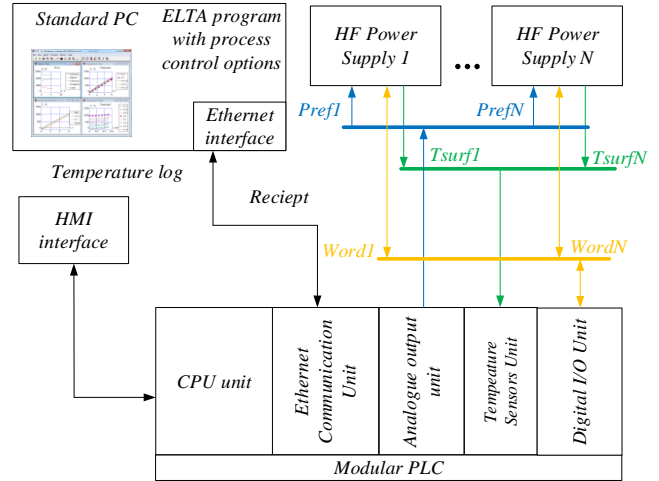


Fig. 2. Structure of the control system for several HF power supplies built on PLC

B. Implementation of Control System

ICO100-839-N3350-2COM-DIO-DC embedded system with Intel® Celeron® N3350, 1.1 GHz 1.1 is one of the most interesting variants that can be completely suitable for solving the problem of optimization and control of the continuous induction heating process. The embedded industrial computer with Windows IoT Enterprise 10 and the ELTA application allows the operator to easily set-up this system to automatically implement technology without further human involvement performing all heating and controlling settings.

REFERENCES

- [1] H. Conrad, Y. Blinov, and S. Dzljev, Modern Solid-State Power supplies for Induction Heating, Proc. of the Intern. Seminar on Heating by Internal Sources, Padua (Italy), HIS-01, pp. 91-98.
- [2] C. Hammouma, H. Zeroug, and A. Attab, Maximum Power Tracking for Frequency Adaptation in Series Resonant Inverter for Induction Hardening Application, Proc. of the Intern. Conference on Heating by Electromagnetic Sources, Padua (Italy), HES-19, pp. 303-308.
- [3] A. Attab, H. Zeroug, and C. Hammouma, A Constant Power Control Using Two Series Resonant Inverters for Metal Induction Heating System, Proc. of the Intern. Symposium Heating by Electromagnetic Sources, Padua (Italy), HES-19, pp. 333-338.
- [4] E. Rapoport, and Yu. Pleshivtseva, Optimal Control of Induction Heating Processes, Boca Raton: CRC Press, 2006, 349 p.
- [5] Pleshivtseva Y., Rapoport E., Nacke B., Nikanorov A., Di Barba P., Forzan M., Lupi S. and Sieni E. (2017), "Design concepts of induction mass heating technology based on multiple criteria optimization", *COMPEL: The Intern. Journal for Computation and Mathematics in Electrical and Electronic Engineering*, 36, 2, pp. 386-400.
- [6] Di Barba, P. (2014), "Basic principles of optimal design of electromagnetic devices and multi-objective optimization", in *ASM Handbook, Volume 4C, Induction Heating and Heat Treatment*, pp. 359-365.
- [7] Di Barba, P., Forzan, M. and Sieni, E. (2014), "Multi-objective design of power inductor: a benchmark problem of inverse induction heating". *COMPEL: The Intern. Journal for Computation and Mathematics in Electrical and Electronic Engineering*, 33(6), pp. 1990-2005.
- [8] V. Bukanin, V. Vologdin, VI. Vologdin Jr., A. Blagirev, A. Homutinnikov, A. Ivanov and A. Zenkov, Control system of smart HF power supply integrated with ELTA program, in Proc. of the Intern. Conference on Heating by Electromagnetic Sources HES-19, Padua, 2019, pp. 73-78.
- [9] A. Ivanov, V. Bukanin, A. Zenkov, V. Vologdin and V. Vologdin, Cyber Physical Systems Integration for Induction Heating Technologies, in Proc. of the 9th Mediterranean conference on embedded computing (MECO), 8-11 JUNE 2020, Budva, Montenegro, pp. 825-828.

Physical Simulation of Soft Magnetic Composite Impeder Performance for use in Induction Tube Welding Systems

Sean Michael Muyskens
Engineering
Fluxtrol Inc.
Auburn Hills, USA
smmuyskens@fluxtrol.com

Robert Charles Goldstein
Engineering
Fluxtrol Inc.
Auburn Hills, USA
rcgoldstein@fluxtrol.com

Abstract— Induction tube welding is used for the continuous production of metallic tubes. These systems often utilize an internal magnetic flux controller (impeder) to improve process efficiency. Significant energy savings and increased productivity have been demonstrated both theoretically and practically when switching from the traditional ferrite impeder core, to one made of a soft magnetic composite (SMC) with high saturation flux density. In order to use SMCs in these systems it is important to balance the greater heat generated in these materials at higher fields with the cooling water available.

A test stand was devised for physical simulation of SMC impeder performance for use in induction tube welding systems. Tests were run to determine the loading and cooling conditions that an impeder core made of SMCs could survive. Additionally, loss estimates based on the rise in temperature from the cooling water were compared with published loss data for the SMCs used. The goal of these tests was to create a design envelope in which impeder cores made of SMCs could survive and validate their use in induction tube welding systems.

Keywords— induction tube welding, soft magnetic composites, induction heating, magnetothermal properties of materials.

I. INTRODUCTION

Inductive welding is a popular method for making tubes used in a variety of industries. Over the past 20-30 years, the industry has been transitioning from tube generators operating at 400 kHz, to solid state generators (either IGBT or MOSFET) which operate at frequencies from 50 kHz to 400 kHz. The availability of high power at lower frequencies has created the opportunity to successfully weld larger tubes with greater wall thicknesses for more demanding applications. At the same time, one of the key components of the system, the impeder, has not changed significantly, which is limiting the production rate or resulting quality of some types of tubing.

Impeders are typically manufactured using a combination of construction elements and ferrite rods or tubes (ferrites). Ferrites have a low saturation flux density which is strongly temperature sensitive, are limited in size availability and are very susceptible to mechanical and thermal shock. The saturation flux density becomes more and more of an issue for lower frequencies, where the desirable flux density for welding is higher. This new situation creates an opportunity to improve the welding system performance using soft magnetic composites (SMCs) [1-3].

With the greater saturation flux density associated with SMCs there is also an increased amount of heat generated that could lead to failure if not properly handled. A test stand was devised for physical simulation of SMC impeder performance for use in induction tube welding systems. Tests were run to determine the loading and cooling conditions that an impeder core made of SMCs could survive. The goal of these tests was to create a design envelope in which impeder cores made of SMCs could survive and validate their use in induction tube welding systems.

II. PHYSICAL SIMULATION

A. Test Stand

In induction tube welding, a steel sheet is formed into the profile of a tube by a series of rollers. As the profile is nearly formed, the edges of the strip form a vee shape, which is referred to as the weld vee. The point at which the vee terminates is often referred to as the apex or touching point. Just past the apex, a set of rollers apply pressure to create a solid-state bond. The size of the rollers depends upon the characteristics of the tube that is being welded. Near the last set of rollers, an induction coil is placed over the tube. Finally, an impeder is placed on the inside of the formed profile that extends from before the induction coil to near the apex. A basic geometry of the system is shown in Fig. 1 [4].

Currents are induced around the body of the strip under the induction coil. As the currents approach the edge of the vee, the currents have three main options for which direction to flow: on the edge towards the apex, on the edge towards the incoming material, or along the inside diameter of the tube. The currents flowing along the edge of the vee are what generates the heat necessary for the solid-state welding process [5].

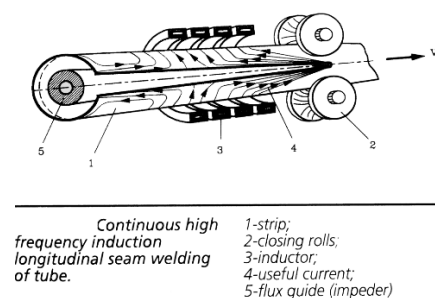


Fig. 1. Basic geometry of tube welding system



Fig. 2. Impeder test stand

While it would be preferable to run tests on a full production line, a much more controllable test stand was constructed to simulate these conditions. The stand can be seen in Fig. 2. The major components are a 25kW PPST induction power supply, a three-turn inductor, impeder casings, and SMC impeder cores. There are also a variety of sensors (Rogowski belt, voltage probe, thermocouples) for measuring electrical parameters of the inductor and inlet and outlet temperature of the cooling water.

Using the electrical parameters for the inductor, a simulation can be run to estimate the loading of the SMC core. Loading and frequency allow for an estimation of losses that can be directly compared to measured loss based on the change in cooling water temperature at steady state. An additional thermal simulation will be run to estimate the temperature in the most heavily loaded portion of the core. This, along with inspection of the impeders between trials will be a good indication of survivability of the impeder in the real system.

B. Trials

To cut down on the number of independent variables, the water inlet will be kept at 40 PSI in each trial, and frequency and power will be adjusted to target the maximum sustainable levels of power density in the core. As the same power densities in the core could be achieved in the core at different power levels and frequencies from the power supply, simulation will be used to target required voltage across the inductor at the resonant frequency of each setup, and power will be adjusted accordingly.

Table 1 show the planned trials where the major variables to be explored include impeder size and material. Each combination of impeder material and size will be run with three different cores at the maximum sustainable power to show repeatability. Each trial will be run for an hour to ensure there are no changes in electrical parameters that may point to degradation of the core.

TABLE I. PLANNED TRIALS

Trials	Impeder Materials	Impeder OD (mm)
1-12	Fluxtrol A	10,12,14,19
13-24	Fluxtrol 75	10,12,14,19
25-36	Ferrotron 559H	10,12,14,19
37-48	Ferrotron 559 Original	10,12,14,19

III. RESULTS

Fig. 3 below shows the operating envelope for Fluxtrol A based on trials run so far. The theoretical functional range was calculated using the simulated max flux density in the core based on the electrical parameters of the inductor recorded during each trial. The measured functional range was created based on measured calorimetric loss inversely calculated to a flux density that would correspond to the loss. As losses and power densities can vary based on frequency and field strength, results in Fig 3. demonstrate the maximum sustainable power density achieved in the core expanded over the full range of potential frequencies and magnetic loading one might expect in induction tube welding systems. This data was gathered using a single 14mm core made from Fluxtrol A and will be expanded with trials run in the other core sizes. Operating envelopes like that seen in Fig. 3 will be created for each SMC material detailed in Table I.

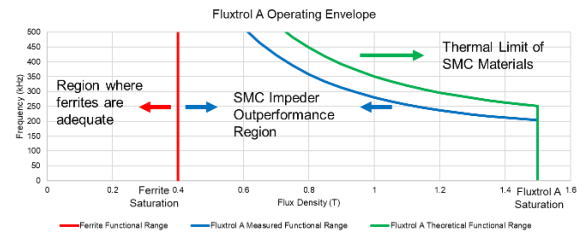


Fig. 3. Fluxtrol A operating envelope

IV. RESULTS

Initial trials using Fluxtrol A 14 mm impeder cores were run at combinations of flux densities and frequencies that significantly exceed the capabilities of ferrites. After 9 hours of use between all trials the core showed little damage caused by heating. The only sign of degradation being a single point where the protective coating had chipped leading to very minor corrosion due to water exposure. Given that there was little to no damage to the cores, the conclusion of these trials is that SMCs are viable for use in induction tube welding systems given they are supplied with sufficient cooling, in this case an inlet at 40PSI. When looking at tube welding cases where the ferrite is saturated, see the ferrite functional range in Fig 3., there is room for improvement when switching to an SMC impeder.

REFERENCES

- [1] Goldstein, R.C. (2014). "Magnetic flux controllers in induction heating and melting." ASM Handbook Volume 4C, 633-645. J. Clerk Maxwell, A Treatise on Electricity and Magnetism, 3rd ed., vol. 2. Oxford: Clarendon, 1892, pp.68-73.
- [2] Nemkov, V. (2008). "Magnetic flux guide for continuous high frequency welding of closed profiles." US Patent Application, US20080308550A1.
- [3] Muyskens, S., Eddir, T. and Goldstein, R. (2019), "Improving induction tube welding system performance using soft magnetic composites", COMPEL - The international journal for computation and mathematics in electrical and electronic engineering, Vol. ahead-of-print No. ahead-of-print. <https://doi.org/10.1108/COMPEL-06-2019-0232>
- [4] Lupi, S., et. al. (1992). Induction Heating Industrial Applications. UIE, "Induction heating" working group, 73
- [5] Scott, P.F. (2014). Key Parameters of High Frequency Welding. A ThermoTool Corp. Publication, <https://thermatool.com/resources/technical-papers/>

Temperature and flow distribution of liquid metal fin in refractory of induction crucible furnaces

Ulrich Lüdtké
Dept. of Electrical Engineering and Information Technology
Technische Universität Ilmenau
Ilmenau, Germany
ulrich.luedtke@tu-ilmenau.de

Andreas Löhlein
Saveway GmbH & Co. KG
Ilmenau, Germany
A.Loehlein@saveway-germany.de

Abstract—The melting process in induction crucible furnaces causes permanent erosion at the refractory. Apart from the fact that liquid metal may infiltrate the refractory, mechanical strains may also cause cracks. Liquid metal can enter the cracks and the metal can penetrate the refractory and reach the water cooled induction coil. If the induction coil is insufficiently cooled by water, it is possible that the hot liquid metal fin melts the copper coil. Should this happen, water would vaporize and produce hydrogen. An explosion with possibly fatal results would occur. Here, we numerically simulate the transient behavior of such a liquid metal fin in the refractory of induction crucible furnaces. We include the description of the boundary conditions, of the materials, of the arrangement, of the simplifications, and of the parameter variations used for the simulations. The results of the numerical simulations will be presented and finally some liquid metal fin characteristics will be interpreted.

Keywords—induction, heating, crucible, temperature, flow, metal, fin, safety

I. INTRODUCTION

The simulated section of the furnace wall (Fig. 1) consists of seven vertical regions. Here we find the furnace wall, the induction coil, and the environment. We assume a liquid melt is in the inner region of the furnace. The crucible wall consists of 60 mm refractory and an electrode panel which is 0.3 mm thick and of layer silicate. The electrode panel is simplified as mica and will be directly glued onto the 20 mm coil grout. The copper coil follows the coil grout after 0.3 mm coil isolation. The coil profile is a rectangular hollow profile with 12 mm x 20 mm edge length and an inner cutout of 6 mm x 14 mm for cooling water. To insulate the coil windings, a 10 mm layer of coil isolation will be used. Air is assumed to be the induction furnace environment. The liquid

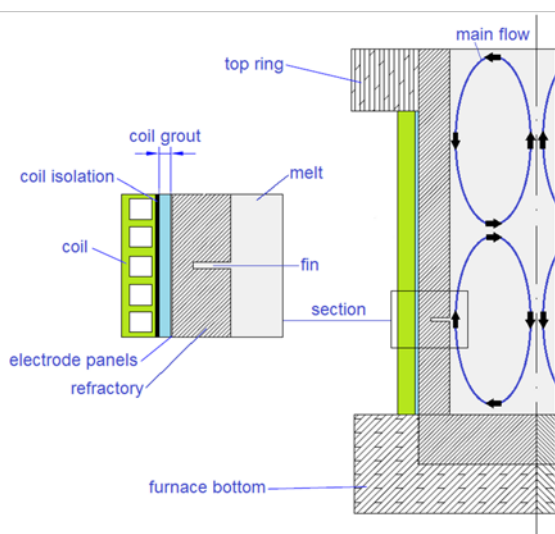


Fig. 1. Location of the section in the induction crucible furnace.

metal fin with 4 mm height is inserted horizontally into the refractory and then different cases are calculated. We expect a strong influence of the melt flow on the heat transfer in the metal fin. Numerical simulations are the only way to obtain information about the heat transfer conditions in these types of metal fins, since the hostile environment of a working furnace makes real measurements impossible.

II. NUMERICAL SIMULATION

Simulating the entire furnace including the necessary environment is exceedingly expensive and time-consuming. Thus, we assume symmetry and we define a section with useful boundary conditions at the boundaries. Fig. 2 shows three coils and the melt with the penetrating fin of the section. Magnetic boundary conditions and thermal boundary conditions for the stationary temperature field calculation will be assumed to respect the symmetry conditions. Inside the crucible we have hot liquid iron with a temperature of 1600°C. In such induction crucible furnaces we find a strong turbulent flow with velocities of 1 meter per second or higher [2]. Normally we find two vortices of melt flow inside an induction crucible furnace. We consider a worst case position for our section where the flow moves vertically from the bottom to the top. For our simplification we use a melt flow velocity of 1 meter per second (Fig. 2). Detailed information about boundary conditions, material properties, and simulation results without metal flow can be found in [1].

ANSYS WORKBENCH is used for the coupled simulation of the electromagnetic field (MAXWELL) together with the flow and temperature field (FLUENT). MAXWELL is used to calculate the heat sources and the time averaged Lorentz forces for FLUENT. It is a one-way coupling, because we assume a constant electrical

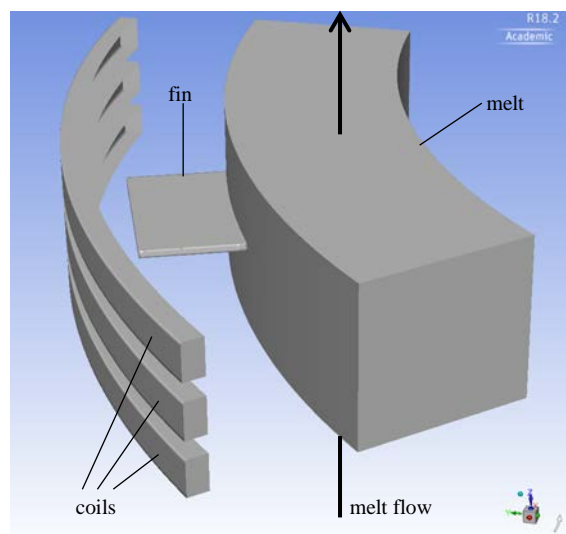


Fig. 2. Section of the wall with coils, and melt with fin.

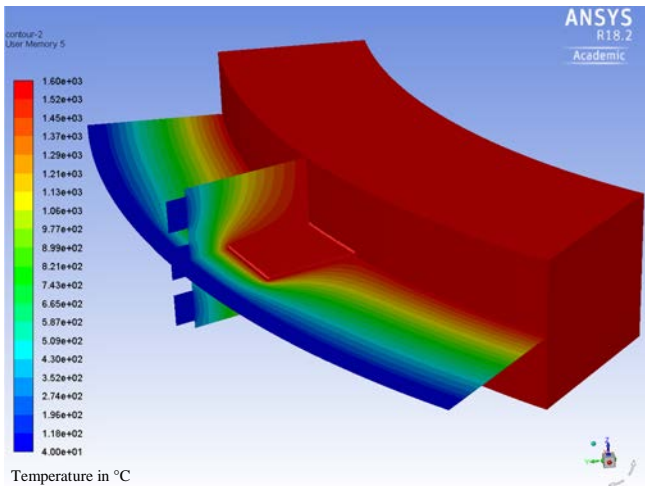


Fig. 3. Temperature distribution of the melt with fin and two cut planes, fin width: 100 mm.

conductivity not depending on temperature. That's why the temperature isn't needed for MAXWELL. ANSYS is able to transfer the heat sources from MAXWELL to FLUENT, but it is not possible to transfer the time averaged Lorentz forces on the WORKBENCH to FLUENT automatically. That's why the coupling must be performed by hand. We use the so called User Defined Functions of FLUENT to save the coordinates of the FLUENT mesh in a file. The powerful MAXWELL field calculator is able to read this coordinate file to calculate the time averaged Lorentz force density and to save the data in a file for FLUENT. Now FLUENT can read and use the Lorentz force density for the flow calculation. To calculate the strong turbulent flow, we chose the Transition SST (4eqn) turbulent model. The Reynolds number has a value of about $4 \cdot 10^6$.

III. RESULTS

The numerical model is able to calculate different fin types under the influence of heat sources and Lorentz forces including the global melt flow in the crucible. In this research we investigate horizontal metal fins with a length of about 60 mm and a thickness of 4 mm. The top of the fin is located near the electrode panel.

A fin width of 100 mm (Fig. 3) leads to a nearly constant temperature distribution in the fin which has the level of the liquid metal in the crucible (1600°C). The temperature at the top of the fin decreases only by about 50 K, which is not to be seen in Fig. 3. This nearly constant temperature distribution in the fin can only be explained by a powerful metal flow in the fin. A detailed view to the flow in the fin shows a velocity up to 1.86 m/s near to the side walls of the fin. This could explain the erosion effect of the refractory. Solid thin horizontal metal fins are occasionally found at the end of the lifetime of the induction crucible furnace in the refractory.

A fin width of 10 mm (Fig. 4) leads to a temperature distribution in the fin which is similar to the temperature of the undisturbed case without fin in the refractory. The metal flow is not able to develop in this small fin. That's why the heat transfer is mainly generated by heat conduction. A detailed view of the flow in the small fin only shows a very small melt flow velocity. This could explain that horizontal small solid fins are not found at the end of the lifetime of the induction crucible furnace in the refractory.

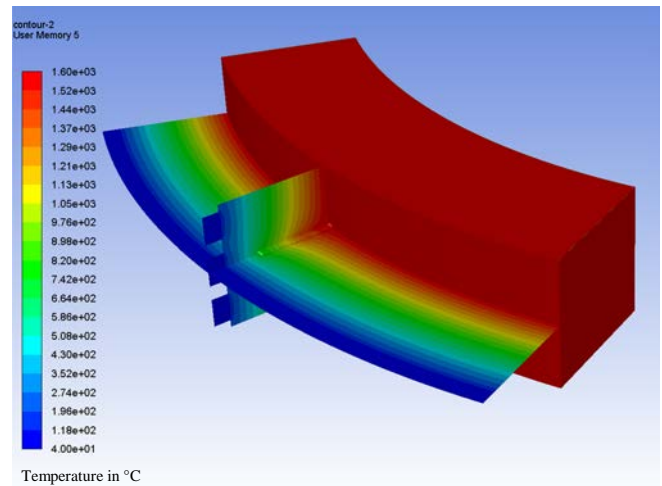


Fig. 4. Temperature distribution of the melt with fin and two cut planes, fin width: 10 mm.

We can change the axial position of the fin in our model by varying the velocity of the vertical melt flow. The position of the section in the middle is an interesting case where we assume the velocity of the main flow is equal to zero. In this case only the Lorentz forces push the flow in the fin, and we get a similar temperature distribution in the metal fin like shown in Fig. 3. Simulation results show that the influence of the velocity of the vertical main flow is low.

IV. CONCLUSIONS

Former numerical investigations [1] of metal fins didn't consider the melt flow. In these cases the heat sources in the metal fin near to the inductor lead to temperatures much higher than 1600°C . From a certain fin width between 10 to 50 mm, flow vortices occur in the fin which lead to an intensive heat transfer and finally to a nearly constant temperature of 1600°C (temperature in the crucible). The conclusion is that the fluid flow can't be neglected in the metal fin.

In this investigation we only use a static contour of the metal fin. But to summarize our findings, we assume that the melt fin needs a minimum width in order to grow into the refractory. If the fin is too narrow the heat transfer is too small. Then the temperature decreases below the melting point and the liquid metal becomes solid. The induced eddy currents are not strong enough to prevent the cooling. Small fins which have a width lower than a certain limit value can't exist.

V. OUTLOOK

Further interesting questions can be investigated using our new coupled simulation model. Open questions are: What happens with the melt fin if it is located vertically? What is the influence of frequency, eddy currents, Lorentz forces and global melt flow on the heating and growing process of the liquid metal fin? Is it possible to simulate the growing process of the metal fin?

REFERENCES

- [1] D. Wandt, U. Lütke, A. Löhlein, Temperature distribution of liquid metal fin in refractory of induction crucible furnaces, heat processing, Induction Technology Reports, 3-2019.
- [2] A. Umbrashko, E. Baake, B. Nacke, A. Jacovics, Modeling of the turbulent flow in induction furnaces, Metallurgical and materials transactions, Volume 37B, 2006, pp.831-838.

Dynamic Neutron Imaging of Argon Bubble Flow in Liquid Gallium in Horizontal or Vertical Magnetic Field

Mihails Birjukovs
Institute of Numerical Modelling
University of Latvia
Riga, Latvia
mihails.birjukovs@lu.lv

Jevgenijs Telicko
Institute of Numerical Modelling
University of Latvia
Riga, Latvia

Imants Buceniekš
Institute of Physics
University of Latvia
Salaspils, Latvia

Pavel Trtik
Research with Neutrons and Muons
Paul Scherrer Institut
Villigen, Switzerland
pavel.trtik@psi.ch

Jan Hovind
Research with Neutrons and Muons
Paul Scherrer Institut
Villigen, Switzerland

Knud Thomsen
Research with Neutrons and Muons
Paul Scherrer Institut
Villigen, Switzerland

Anders Kaestner
Research with Neutrons and Muons
Paul Scherrer Institut
Villigen, Switzerland

Dariusz Jakub Gawryluk
Research with Neutrons and Muons
Paul Scherrer Institut
Villigen, Switzerland

Andris Jakovics
Institute of Numerical Modelling
University of Latvia
Riga, Latvia

Abstract — This paper details the results of the latest dynamic neutron imaging experiments with magnetohydrodynamic argon bubble chain flow in liquid gallium. We perform parameter space mapping for our model system by imaging bubble flow without and with applied static horizontal or vertical magnetic field over a range of gas flow rates and reproduce the experiments numerically.

Keywords — neutron imaging, liquid metal, bubble flow, magnetic field, computational fluid dynamics (CFD)

I. INTRODUCTION

Bubble flow in liquid metal occurs in industrial processes such as metal stirring, purification, continuous casting, etc. These processes can potentially be controlled and stabilized via applied magnetic field (MF) [1-4]. However, bubble flow exhibits complex collective dynamics, which make it difficult to predict, especially with applied MF. Some aspects of magnetohydrodynamic (MHD) bubble flow are still not fully understood, preventing accurate modelling with effective Euler-Euler and Lagrangian models. Experimental and numerical data from explicit simulations, such as volume of fluid, are required to understand how MF orientation/intensity and gas flow rate affect system dynamics. To this end, downscaled systems with model liquid metals and gases, such as gallium and argon, are used, wherein bubbles are introduced via submerged tubes such that bubble chain flow forms [1-4]. It is known that bubble trajectories are mostly controlled by wake flow dynamics and are influenced by bubble shape oscillations, which also determines bubble chain flow characteristics [1-4]. Bubble chain flow is a simplified representation of industrially relevant processes, but despite the simplicity exhibits complex quasi periodic patterns and entails a wide range of time scales. This is especially true for higher flow rates when frequent collisions between bubbles ensue. Liquid metal opaqueness to the visible light makes it very challenging to obtain experimental data regarding bubble shapes and trajectories with sufficient precision. Recently, however, there have been significant advances in both neutron [2-4] and X-ray [1] radiography for bubble flow in liquid

metal. Despite this, there are currently no systematic studies available where model systems are imaged for different MF orientations for a broad range of MF magnitudes and gas flow rates, particularly in the case of thicker liquid metal layers. The aim of this publication is to address this issue and present the results of the latest dynamic neutron imaging experiments conducted at the Paul Scherrer Institute (PSI). In addition, we perform numerical simulations mirroring the experimental conditions to verify the results of imaging. We use the data obtained both *in situ* and *in silico* for an in-depth analysis of bubble flow characteristics over the parameter space of our model system.

II. EXPERIMENTS & SIMULATIONS

A modified version of the model gallium/argon system described in [3,4] was designed for the new experiments. As before, we imaged a rectangular 150 mm x 90 mm x 30 mm glass vessel (boron-pure, Figure 1) filled with liquid gallium up to the 130-mm mark.

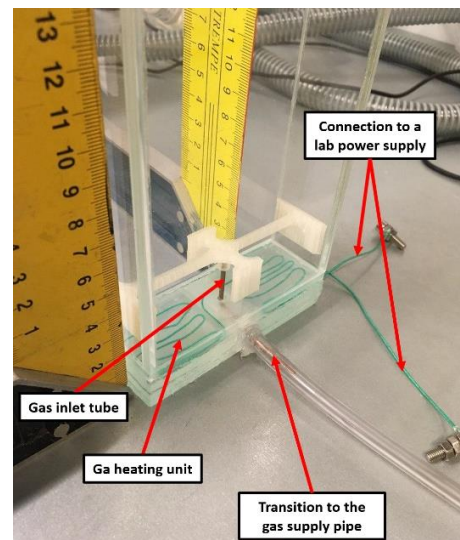


Figure 1. The glass vessel used in the experiments.

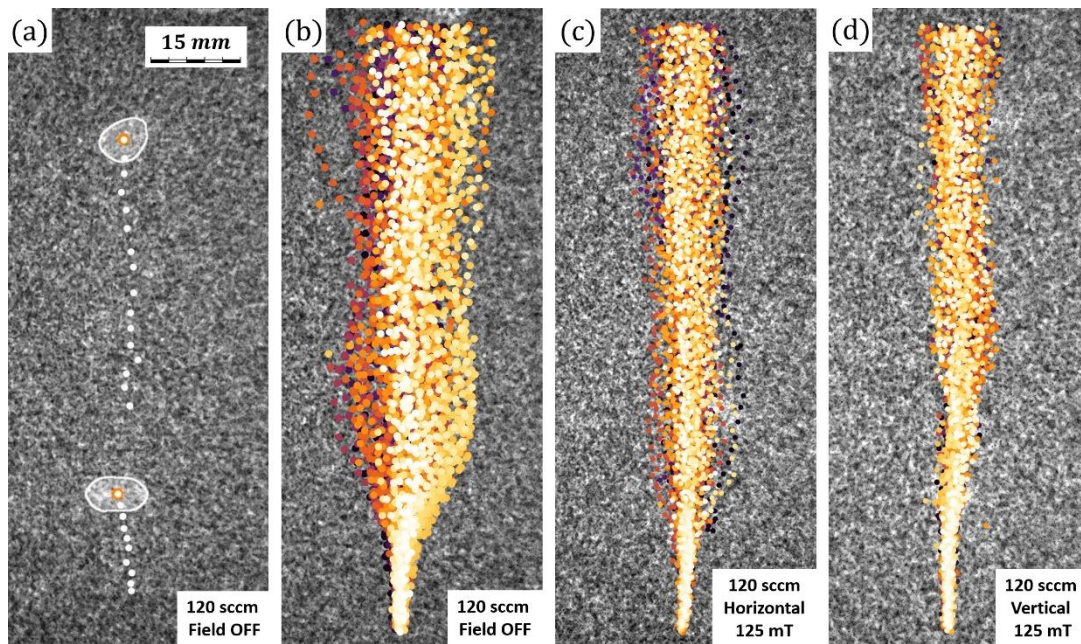


Figure 2. (a) An example of detected bubbles: white contours are shapes, orange dots are current positions and white dots are preceding detections; (b-d) detected bubble positions over 3000 frames (30 seconds), color coded black to white in order of appearance, with (b) no applied MF, (c) ~ 125 mT horizontal MF and (d) ~ 125 mT vertical MF for 120 sccm gas flow rate.

A resistive heating unit at the vessel bottom kept the gallium above its melting point throughout experiments (constant 4.13 W). A vertical copper gas inlet tube (1 mm diameter) was inserted 20 mm into the vessel through the bottom glass plate. The gas flow rate was adjusted via a digital mass flow controller. Neutron imaging was performed at the thermal neutron beamline NEUTRA (SINQ, PSI, 20 mm aperture, $10^7 n cm^{-2} s^{-1} mA^{-1}$ flux) for gas flow rates in the 0-1200 sccm (standard cubic centimetres per minute) range without MF, as well as for {75, 125, 200, 265} mT horizontal MF and {75, 125} mT vertical MF in the bubble flow region. Neutron flux was parallel to the 30-mm dimension of the vessel. A square field of view (FOV, 123.125 mm) above the inlet was imaged at 100 frames per second (FPS). Static MF was generated by tailored permanent magnet/iron yoke systems assembled at the Institute of Physics in Salaspils. Individual bubble trajectories, envelopes of all trajectories, and velocity, aspect ratio, tilt angle and other parameter correlations were obtained. An example of detected bubble positions within the FOV is shown in Figure 2. Image processing was performed using an improved version of the pipeline described in [3,4] which now includes multi-stage global filtering for bubble detection and features multiscale recursive interrogation filtering (among other methods) for improved bubble shape estimates and segmentation for images with many bubbles within the FOV and/or unusually low signal-to-noise ratio (SNR). In addition, reference experiments were performed at the cold neutron beamline ICON (SINQ, PSI, 20 mm aperture, $\sim 1.3 \times$ NEUTRA flux) to

ACKNOWLEDGMENTS

This work is funded by the ERDF project "Development of numerical modelling approaches to study complex multiphysical interactions in electromagnetic liquid metal technologies" (No. 1.1.1.1/18/A/108) and supported by the Paul Scherrer Institut (PSI).

validate the developed image processing methodology. A brass reference body (stationary and moving) with a spherical cavity (5-mm radius) was imaged to reproduce imaging conditions like those for argon bubbles in liquid gallium. It was demonstrated that the image processing code performs well and is therefore adequate for the analysis of images with a priori unknown bubble shapes. Reference neutron imaging with 40- and 80 mm apertures ($4 \times$ and $\sim 11 \times 20$ -mm flux, respectively) was performed to obtain reference images and see how the image processing code performs for different SNR. Finally, greater flux was leveraged for FPS up to 600, which should aid the in-depth analysis of bubble shape variations via image-based strain rate measurements. Numerical simulations were performed with MF configurations and flow rates matching the cases in our imaging experiments. The numerical model used in [3,4] was modified: the previously utilized volume of fluid phase interface compression method was replaced by the *isoAdvector* algorithm, which is more precise and numerically stable, while only slightly more computationally expensive.

III. OUTLOOK

The ultimate goal of this study is to present a "roadmap" describing what flow characteristics to expect for a given combination of MF orientation, magnitude, and flow rate. One can then analyze how different metrics and correlations vary over the parameter space and understand how magnetic control can be applied in industrial systems with bubble flow in liquid metal.

REFERENCES

- [1] O. Keplinger, N. Shevchenko, and S. Eckert, IOP Conf. Ser.: Mater. Sci. Eng. 228, 012009 (2017).
- [2] E. Baake, T. Fehling, D. Musaeva, and T. Steinberg, IOP Conf. Ser.: Mater. Sci. and Eng. 228, 012026 (2017).
- [3] M. Birjukovs, V. Dzelme, A. Jakovics, K. Thomsen, and P. Trtik, Int. J. Appl. Electrom. 63, 209116 (2020).
- [4] M. Birjukovs, V. Dzelme, A. Jakovics, K. Thomsen, and P. Trtik, Phys. Rev. Fluids 5, 061601 (2020).

A inductive joining technology for production of hybrid material composites

Patrick Rochala

*Institute for Machine Tools and
Production Processes (IWP)*
Chemnitz University of Technology
Chemnitz, Germany
patrick.rochala@mb.tu-chemnitz.de

Alexander Fröhlich

*Institute for Machine Tools and
Production Processes (IWP)*
Chemnitz University of Technology
Chemnitz, Germany
alexander.froehlich@mb.tu-
chemnitz.de

Martin Kroll

*Institute for Machine Tools and
Production Processes (IWP)*
Chemnitz University of Technology
Chemnitz, Germany
martin.kroll@mb.tu-chemnitz.de

Verena Kräusel

*Institute for Machine Tools and
Production Processes (IWP)*
Chemnitz University of Technology
Chemnitz, Germany
verena.kraeusel@mb.tu-chemnitz.de

Abstract— In this paper, the new process of "inductive contact joining" (ICJ) for the production of hybrid material composites is introduced and the results of investigations using glass and carbon fiber reinforced polyamide matrix composites are presented. Finite element simulations as well as joining experiments were conducted.

Keywords— Induction joining, composite materials, simulation

I. INTRODUCTION

The importance of lightweight constructions in aerospace, automotive production and shipbuilding will increase significantly in the coming years due to rising energy and fuel prices [1], [2]. As a result, the number of lightweight constructions, particularly fiber-reinforced plastic components, in the aforementioned product areas will also increase enormously. In order to reach wide sales markets in the future, it is necessary to reduce the currently high costs for lightweight materials. Flexible, efficient and cost-effective joining techniques for producing hybrid material composites with sufficiently high strength will be also required. The possibility of integrating new joining technologies into existing process chains, the level of new investments, the costs for the joining elements as well as the joining times are decisive factors for a wide industrial application. The joining method should also be applicable in case of restricted, e.g. one-sided, access to the joint. The manufacturing of lap joints between thermoplastic fiber reinforced composites and metals can be realized by mechanical, thermal, chemical and hybrid joining processes [3]. The novel thermal joining process with inductive heating presented here meets the aforementioned requirements and thus offers the potential for an efficient industrial application.

II. TECHNICAL BACKGROUND

In thermal joining processes, the heat generation in the joining zone can be realized by taking advantage of different physical principles such as radiation (e.g. laser, infrared radiation), convection (e.g. gas phase convection, liquid phase convection), friction (e.g. ultrasonic) and electromagnetism (e.g. induction heating) [3]. Therefore, the choice of energy

input depends mainly on the material properties of the components to be joined and their geometry.

Due to the fast heating rates that are achievable and the very low energy losses, an energy efficient way of introducing thermal energy into electrically conductive components is induction heating [4], [5]. Another advantage is the direct heat generation in the electrically conductive components [5], [6]. Furthermore, by adapting the process parameters, the location of heat generation can be limited.

III. INDUCTIVE CONTACT JOINING (ICJ)

The technology of ICJ, which was originally developed for the joining of fiber-reinforced plastics and metals, uses induction heating to generate heat locally limited at the joining zone [7]. The process sequence is as follows. The components to be joined are positioned in overlap condition. The inductor that is geometrically adjusted to the overlap joint and the geometry of the parts to be joined is placed on the plastic component above the joining zone and the joining force F is applied. When the joining process is started, the alternating electromagnetic field immediately heats the electrically conductive metallic joining partner by resistance heating of induced eddy currents. Due to the heat conduction between the joining partners, the thermoplastic matrix of the fiber reinforced plastic melts in the area of the joining zone and spreads over the metal part. During subsequent solidification, the solidifying polymer matrix and the roughness profile of the metallic component are mechanically interlocked. In addition, adhesive bonding between plastic and metal part is established, i.e. the polymer melt acts as an adhesive. As the copper-coil is water-cooled, in direct contact with the joining partners and positioned close to the joining surface, it constitutes an effective heat sink. The resulting heat flow towards the induction coil causes a rapid temperature reduction in the joint, limits the heating to the joining area and reduces the thermal load of the parts. After the thermoplastic melt has solidified, the inductor can be removed. Compared to conventional processes with spatial and temporal separation of the process steps heating, pressing and cooling, the ICJ process is characterized by the combination of all three steps in one hybrid process. Figure 1 depicts a schematic representation of the ICJ process.

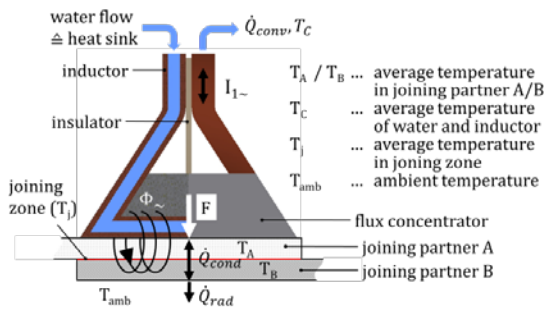


Fig. 1: Schematic principle of the inductive contact joining process [7].

Due to the electrical conductivity of carbon fibers, they can also be inductively heated. As a result, it is possible to join carbon fiber reinforced composites with each other or with other thermoplastic polymer matrix composites. Through the inductive heating of the carbon fibers, the heat thus generated is transferred to the polymer matrix of both components so that they can melt. The plastic melts in the joining zone are mixed and during the cooling step, a firm bond as well as a force-locked joint is established. In this paper, the joining of two fiber-reinforced plastic components, of which at least one component contains carbon fibers, will be investigated. Figure 2 shows the experimental setup for the inductive contact joining of a carbon fiber reinforced sheet (bottom) with a glass fiber reinforced sheet (top).

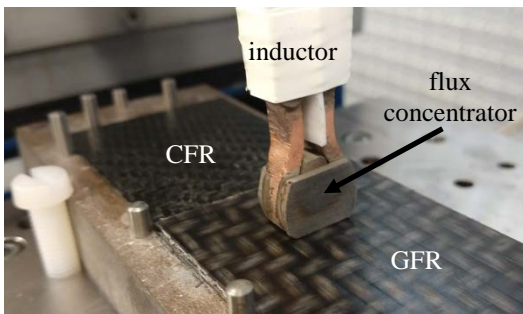


Fig. 2: Experimental setup for the inductive contact joining of a carbon fiber reinforced sheet (CFR, bottom) with a glass fiber reinforced sheet (GFR, top).

IV. EXPERIMENTS

In a first step the process of ICJ was simulated with the software COMSOL Multiphysics 5.4 by using the AC/DC module. The main target of the work on the simulation model was the development of a valid analogous material model that represents the thermal behavior of polyamide matrix composites with carbon fiber or glass fiber fabrics under direct and indirect inductive heating. It was analyzed which frequencies of the magnetic field were necessary to heat the carbon fibers with a very large aspect ratio so that sufficiently high temperatures were reached to melt the matrix. The analyses were performed as a function of temperature and time, using material data from the COMSOL software database. On the basis of geometry and material of the inductor ($m_{Cu} = 99.9$ wt.%), a specific electromagnetic field is generated which penetrates the parts to be joined. The formation of this magnetic field can be determined by simulation. The heat generated by induction in the electrically conductive component is determined on the basis of permeability, relative dielectric constant and geometry of the components as a function of magnetic flux density and field strength. The induction coil temperature was assumed to be

constant at $T_C = 20$ °C as in reality it is water-cooled and does not act as an additional heat source by means of conductive heating during the joining process. In a further step, the inductor geometry was virtually modified in order to adapt the geometry of the electromagnetic field to the geometry of the joining partners and to achieve a homogeneous heat development in the joining zone.

The simulative investigations were supplemented by joining tests methods according to DIN EN ISO 14273. For this purpose, glass fiber reinforced polyamide matrix plastic material was chosen as the lower joining partner and carbon fiber reinforced polyamide matrix plastic material as the upper joining partner. The dimensions of both sheets were $V = 100 \times 50 \times 1$ [mm³] each. The overlap area was selected to be $A = 35.0 \times 50.0$ [mm²]. A joining force of $F = 4450.0$ N was applied to the inductor. The joining test was then started. A heating time of $t = 2.0$ s and a generator output of $P = 3.5$ kW was applied. These process parameters were determined during prior tests and allowed for melting the polyamide matrix without decomposing it and giving the melt enough time to spread over the metal sheet's surface.

V. RESULTS

The manufactured joints were tested in lap shear tests using a Hegewald & Peschke universal testing machine Inspekt 150. Additional microscopic analyses of the fracture surfaces of the tested samples allowed for an analysis of the bonding mechanisms as well as the failure mechanisms. After measuring the maximum tensile force and the effective joined area, a maximum lap shear strength of $\tau \approx 34$ MPa could be determined.

VI. CONCLUSION

The investigations show that joints between heterogeneous materials can be realized without additional joining elements or filler material, with heating as well as holding times of only a few seconds, whereby only one-sided accessibility to the joint is required. The thermal load on the parts is minimized and the surfaces as well as the structure of the metallic joining partners are only slightly affected. This makes the new hybrid technology of ICJ both efficient and highly flexible. In addition, this new joining process can be used for a wide range of applications.

- [1] An analysis of European plastics production, demand and waste data, Plastics-The facts 2019, PlasticsEurope, p. 14, 2019.
- [2] L. Ickert, D. Thomas, L. Eckstein, T. Tröster, Beitrag zum Fortschritt im Automobilleichtbau durch belastungsgerechte Gestaltung und innovative Lösungen für lokale Verstärkungen von Fahrzeugstrukturen in Mischbauweise, FAT-Schriftenreihe, 2012.
- [3] F. Podlesak, Entwicklung und Verifizierung eines vorlochfreien mechanischen Fügeverfahrens zum Verbinden von Leichtmetallen und Faser- Kunststoff-Verbunden, Dissertation, TU Chemnitz, 2016.
- [4] T. Bayerl, M. Duhovic, P. Mitschang, D. Bhattacharyya, The heating of polymer composites by electromagnetic induction - A review, Compos. Part A Appl. Sci. Manuf., vol. 57, pp. 27-40, 2014.
- [5] Z. Huang, S. Sugiyama, J. Yanagimoto, Adhesive-embossing hybrid joining process to fiber-reinforced thermosetting plastic and metallic thin sheets, Procedia Eng., vol. 81, pp. 2123-2128, 2014.
- [6] K. Mizukami, Y. Mizutani, A. Todoroki, Y. Suzuki, Detection of delamination in thermoplastic CFRP welded zones using induction heating assisted eddy current testing, NDT E Int., vol. 74, pp. 106-111, 2015.
- [7] Kräusel, A. Fröhlich, M. Kroll, P. Rochala, J. Kimme, R. Wertheim, A highly efficient hybrid inductive joining technology for metals and composites, CIRP Annals, vol. 67, issue 1, pp. 5-8, 2018

Efficiency-Oriented Comparison of Modulation Strategies of a Multi-Output ZVS Resonant Inverter for Domestic Induction Heating

Pablo Guillen, Héctor Sarnago, Óscar Lucía, and José Miguel Burdío.
 Department of Electronic Engineering and Communications, I3A
 Universidad de Zaragoza
 Zaragoza, Spain
 pguillenm@unizar.es

Abstract— Recent developments in domestic induction heating, such as the increase of the cooktop surface flexibility, lead to the design of new multi-output topologies. Those topologies enable the use of several modulation strategies that have to be considered in order to ensure high efficiency while achieving a satisfactory user experience. This paper presents a power losses model of a multiple-output ZVS resonant inverter in order to evaluate the different modulation strategies. This comparison is not only performed from the overall efficiency point of view, but also, considering the discrete losses of each of the power devices. The simulation results have been validated by means of an experimental 3600-W prototype with three induction heating coils of 2000-W rated power.

Keywords—Induction heating, Induction cooktops, Power losses

I. INTRODUCTION

Current design trends on induction heating cooktops evolve towards more flexible surfaces that allow the usage of any pot, with any shape, placed anywhere over the appliance [1]. This relies on the design of cost-effective multi-output power converters and the development of versatile modulation strategies in order to power the multi-coil structures. One of the main constraints of these new designs is the power losses in the semiconductor devices, which are greatly influenced by the component selection and their modulation strategy. These power losses not only affect the overall efficiency of the appliance but also have to be taken into account in the thermal management of the commercial cooktop.

In this paper, a power losses model for the different power devices of a multi-output ZVS resonant inverter is proposed. The proposed power losses model is used to evaluate different modulation strategies and it allows to compare the overall efficiency of the topology and the different sharing of the power losses among the power devices.

II. TOPOLOGY DESCRIPTION AND MODULATIONS

The selected topology is a unidimensional variant of the multi-output ZVS resonant inverter proposed in [2] (Fig. 1). The proposed converter topology enables independent control of the loads. The configurable modulation parameters to set each IH load output power can be seen in Fig. 2.

The output power of the active loads is controlled by the modulation parameters of the high side transistor gate signal, $v_{G,SH}$, i.e. the switching frequency, f_{sw} , and duty cycle, D . Additionally, an enhanced power controllability is achieved by adjusting individually the low-side transistors gate signals, $v_{G,SLi}$. By varying the activation delay, α_i , and pulse width, φ_i , non-complementary transistor activation is generated, as

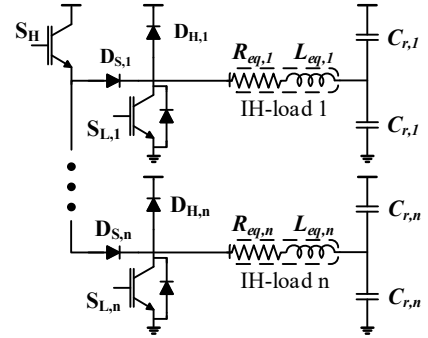


Fig. 1. Unidimensional multi-output ZVS resonant inverter.

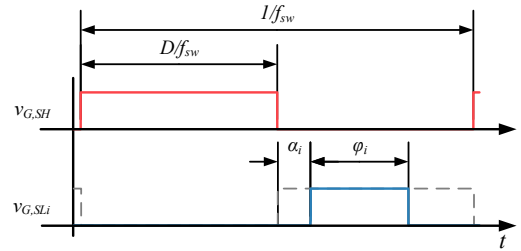


Fig. 2. General scheme of transistor gating signals and main modulation control parameters.

presented in [3]. As a consequence, it is possible to set the desired output power by varying a single parameter, but the parameter selection has implications in the inverter efficiency and power losses share among the different devices.

Therefore, a simulation model of the presented topology has been built in order to obtain the necessary magnitudes to calculate the losses of the different devices.

III. POWER LOSSES MODEL

The power loss contribution of each of the power devices is calculated from the parameters provided by the manufacturers in the data sheets [4].

IGBT losses, P_{IGBT} , are calculated as the sum of conduction losses, $P_{IGBT,on}$, and switching losses, $P_{IGBT,sw}$.

$$P_{IGBT} = P_{IGBT,on} + P_{IGBT,sw} \quad (1)$$

Conduction losses are the consequence of the non-zero on-state voltage drop. It can be approximated by

$$P_{IGBT,on} = V_{CE,on} I_{C,AVG} + R_{DS,on} I_{C,RMS}^2, \quad (2)$$

being $I_{C,AVG}$ and $I_{C,RMS}$ the IGBT collector currents obtained by simulation and dependent on the modulation parameters

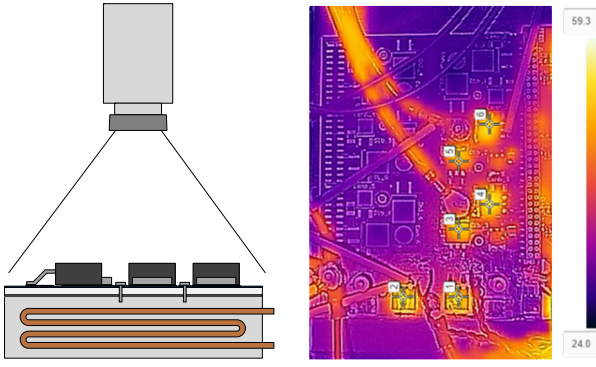


Fig. 3. Test setup schematic and thermal image of the prototype while delivering 3600 W evenly shared between 2 IH loads. Label 1 and 2 are the high-side IGBT, $S_{H,1}$ and $S_{H,2}$, 3 and 4 the series diode, $D_{S,1}$ and $D_{S,2}$, and the low-side IGBT, $S_{L,1}$ and $S_{L,2}$, of the cell 1, and 5 and 6 the series diode, $D_{S,3}$ and $D_{S,4}$, and the low-side IGBT, $S_{L,3}$ and $S_{L,4}$, of the cell 2.

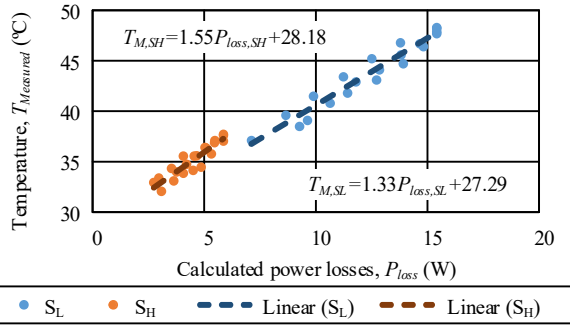


Fig. 4. Linear dependences between the estimated power losses and the measured temperature.

selected, and $V_{CE,on}$ and $R_{DS,on}$ the collector-emitter voltage drop and the channel resistance respectively, obtained from the datasheet curves.

Switching losses are calculated based on the datasheet curves

$$P_{IGBT,sw} = \left(E_{on}(I_{C,on}) + E_{off}(I_{C,off}) \right) f_{sw}, \quad (3)$$

where E_{on} and E_{off} the turn-on and turn-off energy losses provided by the manufacturer as a function of $I_{C,on}$ and $I_{C,off}$, which are the collector current in the turn-on and turn-off transition respectively, dependent on the modulation strategy.

IV. EXPERIMENTAL VERIFICATION

The experimental verification of the power losses model is done by measuring the temperature of the devices [5]. Based on the thermal-resistance approximation, and assuming constant heatsink temperature, $T_{Heatsink}$, the measured temperature can be approximated as

$$T_{Measured} = P_{loss} R_{eq} + T_{Heatsink} \quad (4)$$

In order to verify the power losses model, an experimental setup is built. The power topology prototype to use in the experimental setup is based on the presented topology and comprises, integrated in a IMS board, two parallel IGBT as the high side transistor, S_H (IGB50N65S5), and 3 low side cells composed by a low side transistor, $S_{L,i}$ (IKB40N65ES5), a series diode, $D_{S,i}$ (DSEI36-06AS), and an antiparallel diode, $D_{H,i}$ (VS-15EWX06FN-M3). This prototype is mounted over a cold plate that works as the heatsink temperature reference.

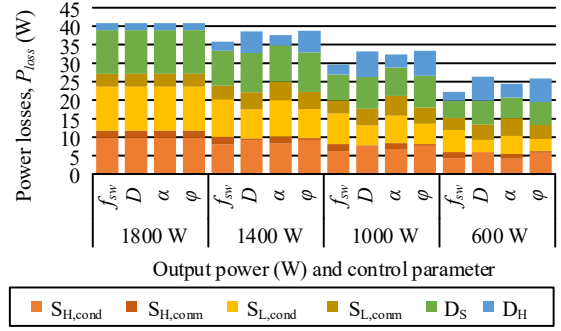


Fig. 5. Comparison of the total losses and the power losses sharing among devices for different power levels and different modulation parameter modification. $S_{H,cond}$ and $S_{H,comm}$ are the sum of the losses of both transistors.

A schematic of the test setup and a capture of the thermal performance can be seen in Fig. 3.

The verification of the power losses model is done by modulating the prototype with a single active load and single parameter variation. The correlation between the calculated power losses and the measured temperature can be seen in Fig. 4. The differences in reference temperature, which is 28 °C, may be due to the no consideration of the different devices temperature influence on the power losses.

V. CONCLUSIONS

In this paper, a power losses model of a multi-output resonant inverter has been proposed and validated through thermography. This model allows efficiency comparison of the different modulation strategies depending on the control parameters (Fig. 5). Square waveform with f_{sw} variation is the most efficient modulation strategy while α_i parameter allows independent power control with lower power losses. Additionally, the individualized power device losses calculation improves the device and packaging selection.

ACKNOWLEDGEMENT

This work was supported in part by the Spanish MICINN and AEI under Project PID2019-103939RB-I00, co-funded by EU through FEDER program, by the DGAFSE, by the MECD under the FPU grant FPU17/01442, and by the BSH Home Appliances Group.

VI. REFERENCES

- [1] O. Lucía, J. Acero, C. Carretero and J. M. Burdío, Induction heating appliances: Towards more flexible cooking surfaces, *IEEE Industrial Electronics Magazine* 7 (2013), 35-47. DOI 10.1109/MIE.2013.2247795.
- [2] H. Sarnago, P. Guillén, J. M. Burdío and O. Lucía, Multiple-Output ZVS Resonant Inverter Architecture for Flexible Induction Heating Appliances, *IEEE Access* 7 (2019), 157046-157056. DOI 10.1109/ACCESS.2019.2950346.
- [3] P. Guillén, H. Sarnago, O. Lucía and J. M. Burdío, Asymmetrical Non-Complementary Modulation Strategies for Independent Power Control in Multi-Output Resonant Inverters, *IEEE Journal of Emerging and Selected Topics in Power Electronics* (2020), 1-1. DOI 10.1109/JESTPE.2020.2965253.
- [4] D. Gravoc and M. Purschel, IGBT power losses calculation using the data-sheet parameters, *Infineon Technologies* (2009), DOI 10.1109/TPEL.2010.2040634.

Optimal programmed control of mass induction heating with guaranteed quality

Yuliya Pleshivtseva
Samara State Technical University
Samara, Russia
yulia_pl@mail.ru

Alexander Nikanorov
Leibniz Universität Hannover
Hannover, Germany
nikanorov@etp.uni-hannover.de

Bernard Nacke
Leibniz Universität Hannover
Hannover, Germany
nacke@etp.uni-hannover.de

Anton Popov
Samara State Technical University
Samara, Russia
antonsam93@mail.ru

Marco Baldan
Leibniz Universität Hannover
Hannover, Germany
baldan@etp.uni-hannover.de

Abstract— The paper is devoted to the implementation of the optimal programmed control in induction system for steel cylindrical billets heating before hot forming with guaranteed quality. For that purpose the time-optimal control problem with additional restriction on the maximum temperature is formulated for induction heating process and solved using alternance method of parametric optimization. The verified numerical 2D model developed in Altair FLUX® software is integrated in optimization procedure. The obtained optimal control algorithms are approved by experimental results obtained on laboratory setup at ETP (Leibniz Universität Hannover).

Keywords—induction heating, optimal programmed control, numerical simulation, FLUX, alternance method, restriction, guaranteed quality.

I. INTRODUCTION

Nowadays the traditional and innovative technologies of the metal heating play the vital role in different industrial processes. In the last decades, induction heating installations are wide-spread because of their undeniable advantages, e.g. intensive local heating of the workpiece, effective use in industry, repeatability of the process, high reliability and small operating expenses. Industrial processes of induction through heating of metal billets up to desired temperatures within the whole volume are widely used for heat treatment of the metals before subsequent technological operations such as plastic deformation in forging, pressing and rolling.

The interest in optimization of induction through heating processes is tightly connected with constantly increasing requirements to effectiveness of production processes with guaranteed quality of the end product.

The main goal of the researches is the development, implementation and investigation of the optimal programmed control in induction system that assures the heating of steel cylindrical billets with prescribed accuracy for a minimum time without overheating during the process. For that purpose the time-optimal control problem with additional restriction on the maximum temperature is formulated and solved using alternance method of parametric optimization.

II. TIME-OPTIMAL CONTROL PROBLEM WITH RESTRICTION ON THE MAXIMUM TEMPERATURE OF THE BILLET

The time-optimal control problem for static induction heating of cylindrical billets with additional restriction on the maximum temperature within the billet' volume can be mathematically formulated as follows. It is necessary to

obtain such time-dependent optimal control $u_{opt}(t)$ by voltage of power supply limited by the constraint $0 \leq u_{opt}(t) \leq u_{max}$, which provides transfer of the controlled object, described by the Maxwell-Fourier system of equations (1)-(2), from the initial condition (3) to desired final state (4) for a minimum time when additional constrain on the maximum temperature (5) is satisfied [1].

$$\text{curl}\bar{H} = \sigma(T)\bar{E} + \frac{\partial\bar{D}}{\partial t}; \text{curl}\bar{E} = -\frac{\partial\bar{B}}{\partial t}; \text{div}\bar{B} = 0; \text{div}\bar{E} = 0; \quad (1)$$

$$c(T)\gamma(T)\frac{\partial T(r,l,t)}{\partial t} = \frac{1}{r}\frac{\partial}{\partial r}\left(\lambda(T)r\frac{\partial T(r,l,t)}{\partial r}\right) + \frac{\partial}{\partial l}\left(\lambda(T)r\frac{\partial T(r,l,t)}{\partial l}\right) + \frac{1}{\sigma(T)}\left(\frac{\partial H(r,l,t)}{\partial r}\right)^2, \quad (2)$$

$$T(r,l,t) = T(r,l,0) = T_0(r,l), r \in [0; R]; l \in [0; L]; \quad (3)$$

$$\max_{\substack{r \in [0; R]; \\ l \in [0; L]}} |T(r,l,t^0) - T^*| \leq \varepsilon_0, \quad (4)$$

$$T_{\max}(t) = \max_{\substack{r \in [0; R] \\ l \in [0; L]}} T(r,l,t) \leq T_{adm}. \quad (5)$$

Here \bar{H} - vector of magnetic field strength, $\sigma(T)$ - electrical conductivity, T - temperature, \bar{E} - vector of electrical field strength, \bar{D} - vector of electric flux density, t - time, \bar{B} - vector of magnetic flux density, $\gamma(T)$, $c(T)$, $\lambda(T)$ - specific heat, density and thermal conductivity of heated metal respectively, $r \in [0; R]$ and $l \in [0; L]$ - radial and longitudinal coordinates respectively, R - radius of the billet, L - length of the billet, ε_0 - maximal admissible deviation of temperature from the desired value T^* , T_{adm} - maximal admissible temperature value.

The solution of the time-optimal control problem without the restriction on the maximum temperature of the billet has the relay shape [1-2]:

$$u_{opt}(t) = \frac{u_{max}}{2} \left[1 + (-1)^{j+1} \right], \sum_{i=1}^{j-1} \Delta_i < t < \sum_{i=1}^j \Delta_i, j = \overline{1, N}, \quad (6)$$

where Δ_i is the duration of the i-th interval of the control algorithm.

It is shown in [1,3] that the additional restriction on the maximum temperature of the workpiece leads to changing the algorithm (6) to the following shape:

$$u_{opt}(t) = \begin{cases} u_{max}, t \in (0, t_1); \\ u^T(t), t \in [t_1; \Delta_1^0); \\ \frac{u_{max}}{2} [1 + (-1)^{j+1}], \Delta_{j-1}^0 \leq t < \Delta_j^0, j = \overline{2, N} \end{cases} \quad (7)$$

The unknown parameters of the time-optimal control algorithm (7) can be found by solving the system of equations written according alternance method of optimal control theory for systems with distributed parameters. The solution of the system represents the solution of the initial formulated optimal control problem.

III. NUMERICAL SIMULATION OF INDUCTION HEATING PROCESS

The considered induction heating system consists of five-turn inductor and steel cylindrical billet of 100 mm diameter. Temperature is controlled by five thermocouples installed along one cross-section located at the distance of 25 mm from the top of the billet (coordinate 70 via y axis).

The heating system was simulated in finite-element software Altair FLUX® [4]. The developed model was verified by comparing the results of the simulation with results of experiments carried out on the real induction heating installation at ETP (Leibniz Universität Hannover) (Fig.1).

IV. OPTIMAL CONTROL PROBLEM SOLUTION AND EXPERIMENTAL RESULTS

The optimal control problem described in section II was formulated for the cross-section of the billet where the thermocouples were installed. Maximal admissible temperature was set on the value of 530°C.

The optimal control algorithm, obtained by coupling of MATLAB® and FLUX® software [5] can be written as:

$$u_{opt}(t) = \begin{cases} 237V, t \in (0, 63.5); \\ 3320e^{-0.0634t} + 233.4e^{-0.0065t}, t \in [63.5, 183); \\ 0, t \in [183, 219.9]. \end{cases} \quad (8)$$

Time-temperature history for optimal control process obtained using FLUX model is shown in fig. 2. The obtained optimal control algorithm was implemented on experimental laboratory setup and approved using temperature measurements by thermocouples during heating process with defined optimal parameters.

CONCLUSIONS

Time-temperature history obtained by measurements using installed thermocouple during time-optimal control

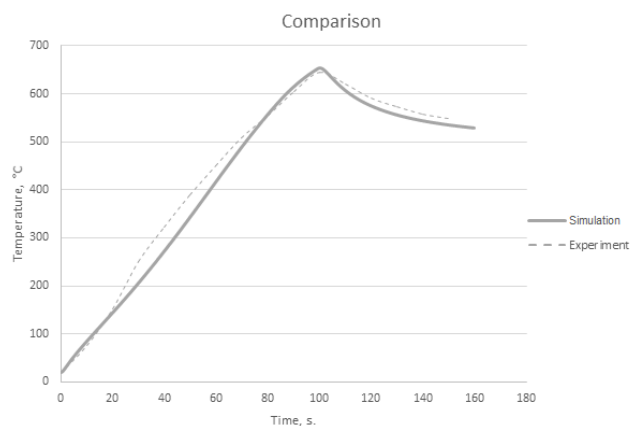


Fig. 1. Verification of the model by test heating during 155 seconds: solid line – FLUX simulation; dotted line – experimental results.

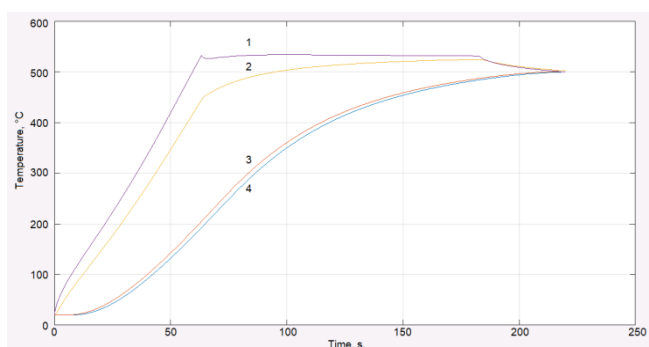


Fig. 2. Results of FLUX simulation - time-temperature history for points of thermocouples installation with coordinates starting from the center of the billet: 1-44 mm, 2-23.34 mm, 3-11 mm, 4-0 mm.

algorithm has confirmed the results of optimal control problem solution. Further analysis and comparison of the FLUX simulation with experimental results lead to the conclusion about quite a good coincidence. The received results also demonstrate that the maximal temperature within the billet volume does not exceed the prescribed admissible level during the whole optimal heating process.

ACKNOWLEDGMENTS

The work is partly supported by Russian Foundation for Basic Researches (project №19-08-00232)».

REFERENCES

- [1] E. Rapoport, Yu. Pleshivtseva. Optimal Control of Induction Heating Processes, CRC Press/Taylor & Francis Group, New York, USA.
- [2] Yu. Pleshivtseva, A. Popov, A. Diakonov Two-dimensional problem of optimal with respect to typical quality criteria control of through induction heating processes [Dvumernaya zadacha optimalnogo po tipovim kriteriyam kachestva upravleniya protsessom skvoznogo induktsionnogo nagreva]. Vestnik of Samara State Technical University. Technical Sciences Series, 2014. №2(42). pp. 148-163.
- [3] A. Popov, A. Diakonov Time-optimal control of batch induction heating process with respect to maximum temperature restriction [Optimalnoe po bistrodeystviyu upravleniye protsessom periodicheskogo induktsionnogo nagreva s uchetom ogranicheniya na maksimalnuyu temperaturu]. Vestnik of Samara State Technical University. Technical Sciences Series, 2015. №3(47). pp. 56-68.
- [4] Altair FLUX. URL: <http://hyperview.eu/product/Flux> (accessed 10.01.2020)
- [5] Yu. Pleshivtseva, G. Rogachev, A. Popov "MATLAB-FLUX Coupling for numerical modeling in education". SHS Web of Conferences 29,02033 (2016).

PFC Rectifier for High Power Quality and High Efficiency Domestic Induction Heating Appliances

Mario Pérez-Tarragona, Héctor Sarnago, Óscar Lucía, and José M. Burdío

Department of Electronic Engineering and Communications, I3A. University of Zaragoza. Zaragoza, Spain.
E-mail: maperta@unizar.es

Abstract—Domestic induction heating technology is present in most of buildings due to the advantages of induction cooktops such as fast heating, efficiency, safety, and cleanness. However, the latest trends in this technology have brought new challenges due to the control restrictions to fulfill EMC standards, and due to the required high power, efficiency, and power density, while keeping a cost-effective implementation. This paper proposes the use of a front-end PFC rectifier in order to address these challenges and get a high power quality and high efficiency solution. A review the state of the art of PFC rectifier is presented, and the main advantages of its application to domestic IH appliances are described.

Keywords—induction heating, home appliances, power factor correction, PFC rectifier, multi-phase.

I. INTRODUCTION

Most of electronic devices connected to the electric distribution of buildings are composed of non-linear loads. These may produce main voltage distortion due to the harmonic content of the current and low power factor, leading to low power quality and low efficiency. In order to avoid these drawbacks, Power Factor Correction (PFC) techniques are widely used.

Induction Heating (IH) is a heating technology that uses electromagnetic fields to increase the temperature of conductive materials. The first developments were applied to industrial metal melting in the early 1900s, and this technology was quickly developed during WWII to reach accurate and fast processes of metal hardening. Later, it was extended to automotive and aircraft industries. Currently, it is used in a wide variety of applications, such as manufacturing processes, medical treatments, and domestic applications, among others.

Since the late 80's, domestic applications were able to take the advantage of this technology due to the advances in power semiconductors, especially with the introduction of the insulated-gate bipolar transistor (IGBT). This improved technology enabled developing compact, reliable and cost-effective solutions. The main domestic application of IH are the IH cookers, that get not only an improved heating times and efficiency compared with classical cookers, but also more safety and cleanness due to the lower surface temperatures [1].

The elements of a typical domestic IH system (Fig. 1) can be classified in three main groups according to its functionality: the inductor-load system, the power electronics, and the control electronics. Each block has to be optimally and coordinately designed to get a good performance, efficiency, and cost-effective final product. Besides, flexible surfaces improve further this experience because of the bigger coils with several concentric windings or fully active surfaces, enabling the use of any pan or pot, regardless the selected size, shape, or position.



Fig. 1. Typical induction cooktop with flexible surfaces.

The remainder of this paper is organized as follows. Section II presents the main challenges of domestic IH appliances and the main drawbacks of current technology. In Section III, PFC rectifiers are introduced as a solution to improve the performance of cookers, and the state of the art for passive and active rectifier systems is presented. In Section IV, the advantages of using a PFC rectifier applied to domestic IH are discussed. Finally, Section V summarizes the main conclusions of this paper.

II. CURRENT CHALLENGES OF DOMESTIC IH TECHNOLOGY

Currently, IH cooktops are usually composed of two isolated electronic boards powered from two mains phases in certain regions, where the maximum phase current in domestic installations is usually limited to 16 A. However, there are different installation limitations in other regions where only a single-phase mains connection exists, but limited to 25 A, or areas where three-phase mains connections can be used. Moreover, the design specifications of flexible surfaces are more restrictive because of the control constraints, higher output power, higher efficiency, the required power density to fit the electronic system into a built-in implementation, EMC restrictions, power coupling issues between mains phases, and, last but not least, the cost.

In this context, using a front-end power stage that allows separating the mains from the IH inverters has been recently identified as a key research because it will allow partially overcoming these limitations, obtaining a good Electro-Magnetic Compatibility (EMC) performance, efficiency and avoiding the control restrictions over downstream inverters. Furthermore, developing a front-end stage that allows merging different mains phases in a common bus voltage will avoid the use of several isolated electronic boards as it is now, leading to a significant cost reduction among other additional advantages to domestic IH [2].

III. STATE OF THE ART OF PFC RECTIFIERS

In an electric power system, a load with a low power factor draws more current than a load with a high power factor

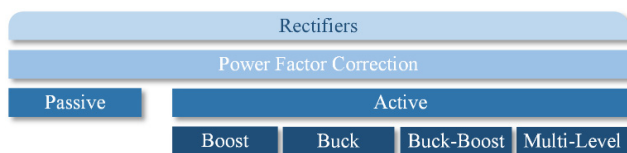


Fig. 2. Classification of the PFC rectifiers.

for the same amount of useful power transferred. The higher currents increase the energy lost in the distribution system and require larger wires and other equipment. Because of the costs of larger equipment and wasted energy, electrical utilities will usually charge a higher cost to industrial or commercial customers where there is a low power factor.

PFC technique reduces the harmonic content with the consequent increases of the power factor of a load, improving efficiency for the distribution system to which it is attached. Linear loads with low power factor, such as induction motors, can be corrected with a passive network of capacitors or inductor. Non-linear loads, such as rectifiers of domestic IH, distort the current drawn from the system. In such cases, active or passive power factor correction may be used to counteract the distortion and raise the power factor (Fig. 2). On the one hand, passive methods include the use of tuned LC filters and avoid the control elements, what represents a robust solution. On the other hand, active methods come as a more efficient solution by using controlled solid-state switches in association with passive elements such as resistors, inductors, and capacitors [3, 4].

A. Passive PFC rectifiers

In the simplest case, conventional rectification systems along with inductances and capacitors for filtering may be used in order to get low complexity power factor correctors. The main advantage is the high robustness because control, sensors, or auxiliary supplies are not necessary. However, larger magnetic components are usually required for filtering, resulting in increased size, weight, and volume converters. Besides, the passive filter may not respond adequately if the load power factor comes to vary. Moreover, the output voltage is not regulated and depends directly on the mains voltage level.

B. Active PFC rectifiers

Active PFC rectifies are able to reach Total Harmonic Distortion of the current (THD_i) smaller than 3% and a higher power density at the cost of a more complex control [5]. In fact, the closed-loop operation of the static power converter dedicated to PFC assures satisfactory performance with high input PF and regulated dc output voltage over a wide operating range. However, the drawback of this rectification method is the increased complexity and reduce robustness in comparison with passive PFC rectification systems.

IV. ACTIVE PFC RECTIFIER APPLIED TO DOMESTIC IH

A multi-phase boost active PFC rectifier provides significant advantages to domestic IH. Firstly, higher power can be delivered to the pots, e.g. typically 3.6 kW systems can be easily rescaled to 11 kW, decreasing significantly the heating times in bigger pots. EMC issues are isolated from the IH design, decreasing the filter size and avoiding the use of complex jitter strategies when non-linear loads are powered.

The control hardware can be also simplified, i.e. a single control unit is able to control both the PFC stage and the multi-phase outputs, removing isolated measurements and auxiliary power supplies for each phase.

Secondly, the IH system control is improved because of the controllable bus voltage, allowing an easier and more accurate power control in several IH load scenarios, enabling also the operation closer to the resonant frequencies, improving the IH inverter efficiency. Furthermore, power coupling issues between different mains phases when multiple inductors are activated in multi-coil IH systems are avoided because a single inductor can be powered from several mains phases.

Finally, the higher the bus voltage is, the lower the required current through the switching devices and coils, decreasing the conduction losses. The inherent higher and low-ripple voltage of the proposed systems enables also a better usage of the switching devices, leading to potential cost reductions in the inverter stage. All these benefits motivate and justify the application of a multi-phase PFC stage to domestic IH in order to achieve a good tradeoff between efficiency, power quality, and cost, improving the energy management of buildings.

V. CONCLUSIONS

This work has proposed the use of PFC rectifiers to improve the performance of current domestic IH appliances, keeping a cost-effective implementation. A review of the state of the art of PFC rectifiers using passive and active methods has been presented in order to find the most effective solution for this application. Finally, the main advantages of a multi-phase boost active rectifier system have been highlighted, such as high power, good EMC performance, and high efficiency. The final version will be completed with an exhaustive comparative of the different state-of-the-art alternatives that improve the current implementation, and the experimental results of the selected alternative will be presented.

ACKNOWLEDGMENT

This work has been partially funded by the Spanish MICINN under the Project MICINN PID2019-103939RB-I00, by the DGA-FSE, and by the BSH Home Appliances Group.

REFERENCES

- [1] O. Lucía, P. Maussion, E. Dede, and J. M. Burdío, "Induction heating technology and its applications: Past developments, current technology, and future challenges," *IEEE Transactions on Industrial Electronics*, vol. 61, no. 5, pp. 2509-2520, May 2014.
- [2] M. Pérez-Tarragona, H. Sarnago, O. Lucía, and J. M. Burdío, "Design and Experimental Analysis of PFC Rectifiers for Domestic Induction Heating Applications," *IEEE Transactions on Power Electronics*, vol. 33, no. 8, pp. 6582-6594, 2018.
- [3] J. W. Kolar and T. Friedli, "The Essence of Three-Phase PFC Rectifier Systems - Part I," *IEEE Transactions on Power Electronics*, vol. 28, no. 1, pp. 176-198, 2013.
- [4] T. Friedli, M. Hartmann, and J. W. Kolar, "The Essence of Three-Phase PFC Rectifier Systems - Part II," *IEEE Transactions on Power Electronics*, vol. 29, no. 2, pp. 543-560, 2014.
- [5] J. Biela, D. Hassler, J. Miniböck, and J. W. Kolar, "Optimal design of a 5kW/dm³ / 98.3% efficient TCM resonant transition single-phase PFC rectifier," in *The 2010 International Power Electronics Conference - ECCE ASIA* -, 2010, pp. 1709-1716.

Electro-thermo-mechanical simulation of the longitudinal HFI-welding process of carbon steel tubes

Martin Kroll

*Institute for Machine Tools and
Production Processes (IWP)
Chemnitz University of Technology
Chemnitz, Germany
martin.kroll@mb.tu-chemnitz.de*

Wladimir Ebel

*Institute of Electrotechnology
Leibniz University Hannover
Hanover, Germany
ebel@etp.uni-hannover.de*

Peter Birnbaum

*Institute for Machine Tools and
Production Processes (IWP)
Chemnitz University of Technology
Chemnitz, Germany
peter.birnbaum@mb.tu-chemnitz.de*

Jonas Gruner

*Institute for Machine Tools and
Production Processes (IWP)
Chemnitz University of Technology
Chemnitz, Germany
jonas.gruner@mb.tu-chemnitz.de*

Verena Kräusel

*Institute for Machine Tools and
Production Processes (IWP)
Chemnitz University of Technology
Chemnitz, Germany
verena.kraeusel@mb.tu-chemnitz.de*

Abstract—This paper addresses the experimental simulation of the longitudinal HFI-welding process of carbon steel tubes. Therefore, the experimental setup facilitates two plain sheets of the tube material. These sheets were moved towards each other while they were conductively heated by a high frequency electrical current. The heated sheets are pressed together to form a pressure weld. Therefore, the approach does not require a tubular specimen or the whole process line to perform experimental investigations of the tube welding process. The approach allows the representation of the current distribution across the tube edges, the subsequent heating and temperature distribution as well as the mechanical and most geometrical conditions of a corresponding tube welding process. Experiments with a HFI-tube welding rig provided reference data from the tube welding process. The temperature distributions during the welding process, the microstructure in the weld cross section as well as the resulting hardness distribution were intercompared between the tube welding process and the experimental simulation to verify the simulation approach.

Keywords—high-frequency induction-welding (HFI), electrical resistance welding (ERW), longitudinal welding, tube manufacturing, pipe manufacturing

I. INTRODUCTION

The tube or pipe production is one of the essential steel processing routes. Thereby, the welded pipe production represents the most common form of production. The highest output quantity of welded tubes is produced by inductive high-frequency welding (HFI-welding). This welding process is part of a coil material processing chain comprising uncoiling, coil joining, edge milling, coil forming, longitudinal welding, weld trimming, annealing, sizing and cutting. Therefore, experimental investigations with process parameter variations and different steels are complex and expensive. As a result, prior investigations focused mainly on the characteristics of the weld or the tube with different materials [1], [2] or on the heat treatment strategies [3]–[5] under constant welding conditions. The lack of systematic experimental studies on the influence of welding conditions in the HFI process also lead to missing recommendations for ideal process conditions and heat treatment strategies for HFI welded tubes.

II. SIMULATION APPROACH

The experimental setup (Fig. 1) facilitates two plain sheets of the tube material, which represent the joining partners, from which one is mechanically fixed on a driven sledge. The other sheet is attached to a static mounting. Both sheets were electrically contacted with each other via a electric bridge on one side and with the energy source at the other side so that a current I can flow through both specimens in opposite direction. During the process, the sledge moves both sheets towards each other with a speed v . From a defined position, the specimens were conductively heated by high frequency electrical current, provided by the aforementioned energy source. The heated sheets are then pressed together to form a pressure weld.

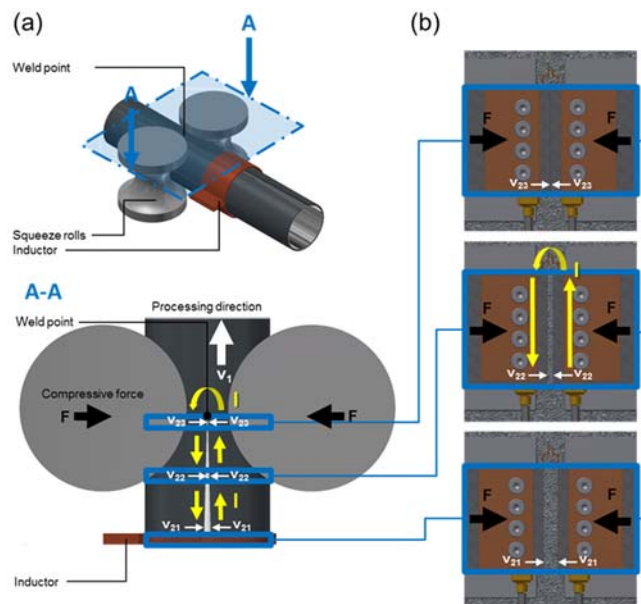


Fig. 1. Schematic illustration and working principle tube welding setup (a) and ETM-simulator (b).

The ETM-simulation directly reproduces critical tube welding parameters such as material (composition and microstructure), wall thickness, welding frequency, direction and distribution of the welding current and the dimensional compression of both specimens. Welding speed and entry angle

can be converted into the speed of the sledge whereas the type, position and efficiency of the coil as well as current and voltage were transferred indirectly and have to be obtained experimentally or analytically.

III. EXPERIMENTAL SETUP AND PROCEDURE

The experimental investigations were carried out with S355 J2+N carbon steel from a single sheet. For the longitudinal welding, the sheets of 300 mm length were cut and formed to a tubular specimen. Subsequently, sacrificial steel tubes of the same cross-sectional dimensions were attached by TIG butt-welding. The specimens for the ETM-simulation were obtained by water-jet cutting and machining.

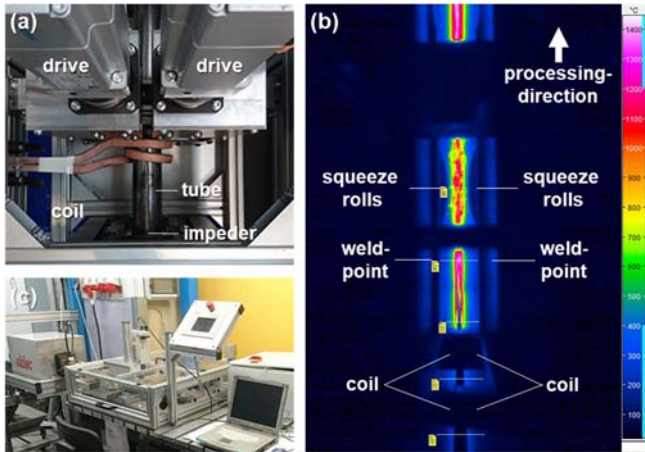


Fig. 2. Experimental tube welding setup (a), thermal camera recording to tube welding process (b) and ETM-simulator (c)

The tube welding test was performed with an experimental tube welding rig (Fig. 2) at a processing speed of 16 m/min, an entry angle of 2.8°, and a frequency of 192.5 kHz. ETM-simulations were carried out at a frequency of 216.1 kHz with an experimental ETM-simulator. An EMAG Eldec SDF®225 generator served as the energy source for both welding processes. The surface temperature in both welding processes was measured using an InfraTec VarioCAM® inspect hr 680 thermal camera at the point of the first contact of the tube or sheet edges. The obtained welds were investigated by a Carl Zeiss Axio Vert.A1 MAT optical microscope and an EMCO-TEST MIC 010 to obtain the microstructure and hardness.

IV. RESULTS

Pressure welding processes produce characteristic welds, comprising weld bead, weld junction, coarse and fine grained zones as well as thermomechanically affected zone. This applies also for both investigated welding processes.

TABLE I. COMPARISON OF RESULTING MICROSTRUCTURE IN DEFINED DISTANCE FROM CONTACT SURFACE

0.15 mm (Coarse grained zone)		1.5 mm (Fine grained zone)	
S0201 (Tube)	PS0201-C1 (ETM)	S0201 (Tube)	PS0201-C1 (ETM)

An experimental simulation should be able to produce a comparable microstructure and distribution of the latter. Table 1 provides an exemplary comparison of microstructures of tube and ETM-simulation welds.

The temperature distribution across the specimens and the resulting hardness through the sheet (Fig. 3) show a high conformity between tube and ETM-simulation. In both welding processes, deviations of the measured temperature occur within a distance of 1 mm from the joining surface at temperatures above 1000 °C due to the formation of scale. The hardness of the tube-specimen outside the HAZ is higher due to work hardening caused by the forming process. Within the HAZ the hardness profiles shows the same characteristic increase due to high cooling rates after welding. The drop of hardness in the weld junction is caused by carbon depletion and a higher porosity due to oxidation during the heating in the process.

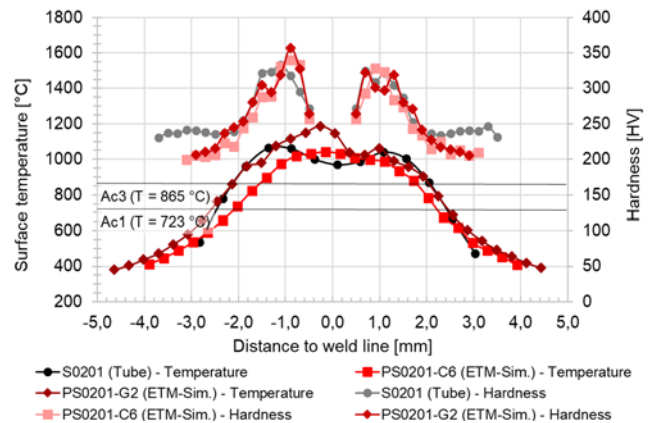


Fig. 3. Distribution of surface temperature and hardness in the sheet center perpendicular to the weld seam for tube weld and two ETM-simulations

V. CONCLUSION

The ability of the ETM-simulation to represent the tube welding process, in terms of geometric and mechanical conditions, temperature distribution and compression of the joining partners as well as the resulting microstructure and hardness, has been demonstrated. Therefore, the ETM-simulation constitutes a suitable experimental approach and setup that allows systematic investigations of the factors influencing the HFI tube welding process without tubular specimen.

REFERENCES

- [1] Ö. E. Güngör, P. Yan, P. Thibaux, M. Liebeherr, H. K. D. H. Bhadeshia, and D. Quidort, "Investigations into the microstructure - Toughness relation in high frequency induction welded pipes," in *Proceedings of the 8th International Pipeline Conference IPC2010*, 2010, pp. 1–9.
- [2] K. Banerjee, "Hydrogen-Induced Cold Cracking in High-Frequency Induction Welded Steel Tubes," *Metall. Mater. Trans. A Phys. Metall. Mater. Sci.*, vol. 47, no. 4, pp. 1677–1685, 2016.
- [3] P. Yan, Ö. E. Güngör, P. Thibaux, M. Liebeherr, and H. K. D. H. K. D. H. Bhadeshia, "Tackling the toughness of steel pipes produced by high frequency induction welding and heat-treatment," *Mater. Sci. Eng. A*, vol. 528, no. 29–30, pp. 8492–8499, Nov. 2011.
- [4] M. Kroll, P. Birnbaum, J. Zeisig, V. Krausel, and M. F.-X. Wagner, "Manufacturing of 42SiCr-Pipes for Quenching and Partitioning by Longitudinal HFI-Welding," *Metals (Basel)*, vol. 9, no. 6, p. 716, 2019.
- [5] A. Kavousi Sisi and S. E. Mirsalehi, "Effect of PWHT Larson–Miller Parameter on Mechanical Properties and Microstructure of Line Pipe Microalloyed Steel Joints," *Metall. Mater. Trans. A Phys. Metall. Mater. Sci.*, vol. 50, no. 9, pp. 4141–4147, 2019.

Development of high-performance air heater based on an inductively heated packed bed

Sergej Belik
 Thermal Process Technology
 German Aerospace Center – DLR e.V.
 Stuttgart, Germany
 sergej.belik@dlr.de

Abstract — Electrical Energy Storage supports the expanding integration of intermittent renewable energy sources. However, capital costs of existing storage concepts are still too high for an economical operation. Therefore, the implementation of additional Power-to-Heat (PtH) unit into a Compressed Air Energy Storage (CAES) is proposed to increase system's energy density and thus reduce capital costs. This paper discusses an experimental study with associated simulations based on a modeling approach for a novel PtH concept comprising an inductively heated packed bed. The objective is to gain a greater understanding for the power transmission from the inductor via packed bed to the adjacent airflow and to quantify the process efficiency. First, an experimental laboratory setup has been realized. Second, experiments with various flow rates and induced power densities have been carried out. Afterwards, an appropriate electro-thermal model for the PtH concept has been applied to investigate the power transmission to the packed bed. At the end, this modeling approach is compared to the experimental results, which confirm high efficiencies for the proposed PtH concept.

Keywords—Induction heating, Power-to-Heat, aerated packed bed, air heater

I. INTRODUCTION

Utility-scale Electrical Energy Storage (EES) supports the expanding integration of intermittent renewable energy sources allowing a reliable and flexible supply of low-carbon or even zero-carbon electricity. Emerging EES technologies introduced in Fig. 1 (left) are considered adiabatic due to the implementation of thermal energy storage (TES) following the adiabatic compression in a Carnot heat pump cycle. On the one hand, such adiabatic EES concepts are highly efficient due to the temporarily stored heat inside the TES. On the other hand, the capital costs of these concepts are still too high for an economical operation in future electricity transmission systems.

To decrease the capitals costs we propose to increase the energy density of the EES through an additional integration of electrically generated high temperature heat. Fig. 1 (right) shows exemplarily this integration in a heat pump cycle of a Compressed Air Energy Storage (CAES) system. Such a process hybridization through the integration of Power-to-Heat (PtH) decreases the round-trip efficiency on the one hand, but, opens up the potential for improvements in flexibility as well as cost efficiency on the other hand. To this end, we are developing a high-performance PtH unit based on an inductively heated packed bed of spheres to heat up the working fluid (air) to temperatures of up to 700 °C.

Induction heating of a packed spheres bed allows high power densities and a uniform heating procedure. Moreover, the high number of spheres leads to a large surface area enhancing the convective heat transfer to the airflow.

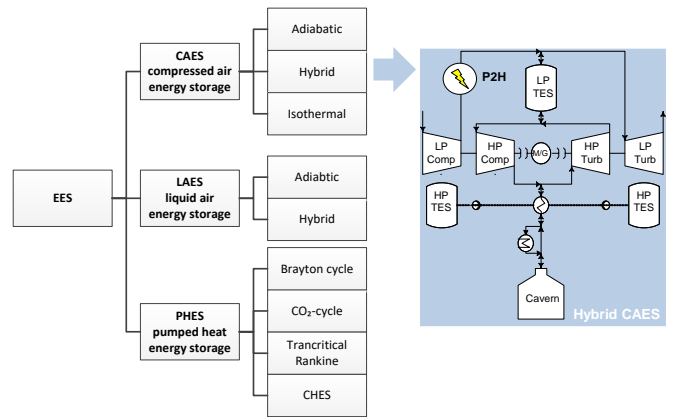


Fig. 1. System level: Electric Energy storage technologies (left) and hybrid concept of CAES (right)

These conceptual advantages have together with the specific advantages of induction heating the great potential for a promising application in the power generation sector.

II. CONCEPTION

A. System configuration

The technical system from Fig. 2 comprises a pressure vessel and an inductively heated and aerated spheres bed placed inside a ceramic tube. Dry air flows from the top of the pressure vessel through a flow straightener inside the inductively heated porous zone where convective heat is transferred to the air. This laboratory setup enables with its installed power of 40 kW outlet temperatures up to 800 °C with associated flow rates up to 350 Nm³/h. The solenoid used for the experimental as well as for the numerical investigation has the diameter of 0.140 m, the length of 0.40 m and comprises 10 windings.



Fig. 2. Component level: CAD-model (left) and experimental setup (right) of the air heater unit based on induction heating of packed bed

B. Conceptual arrangement

Previous conceptual investigations of induction heating concepts for air heating purposes have shown large potential for the PtH concept of inductively heated packed bed. Fig. 3 shows experimental results of the air outlet temperature for various concepts with an electric input of 5.0 kW and a flow rate of 25 Nm³/h. Highest temperature and thus exergetic values are obtained for the packed bed.

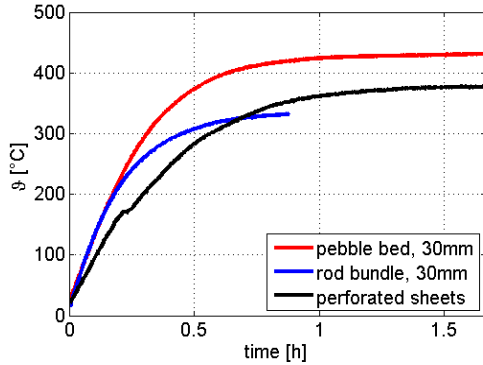


Fig. 3. Experimental results for air outlet temperature of various PtH concepts operated with $f=24$ kHz, $P_{\text{Gen}}=5$ kW and $V=25$ Nm³/h

Therefore, this concept combined with induction heating has been chosen for the development of the air heater. Its conceptual arrangement is schematically illustrated in Fig. 4. To meet the requirements for high efficiency and power density during the heating process in a CAES heat pump cycle, the ferritic stainless steel X10CrAlSi7 has been chosen for further experimental investigation.

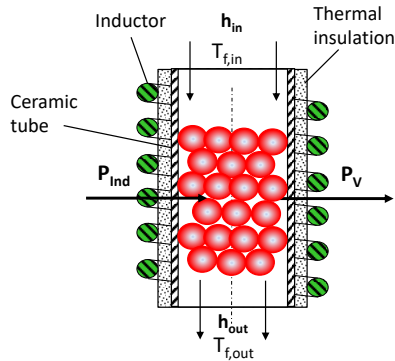


Fig. 4. Conceptual arrangement of the inductively heated packed bed

III. EXPERIMENTAL AND NUMERICAL INVESTIGATION

The objective of the experimental study is to analyze the efficiency of the proposed PtH concept. This investigation is accompanied with a simulation study based on the modelling approach derived from Duquenne et al. [1]. This approach presupposes an equal heat generation inside a pile of well-ordered spheres to the cylindrical rod with identical heat capacity and mass. This analogy has been proven on the basis of results from a 2d FEM simulation using a simplified sphere arrangement from Fig. 5. Thus, this analogy allows calculating the induced power with an analytical approach for cylindrical bodies described by Baker et al. [2]. This power is implemented in a thermodynamic 1d-model given by Belik [3] to calculate the temperature fields for Fig. 6.

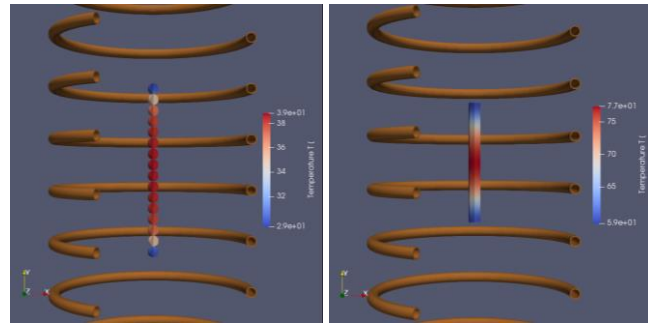


Fig. 5. Results for sphere arrangement and mass equivalent cylindrical rod at $I_{\text{coil}}=250$ A and $f=25$ kHz using CENOS simulation software

Experimental and numerical results from Fig. 6 clarify the energy-efficient use for air heating purposes, since process efficiencies greater than 80% has been achieved for flow rates up to 100 Nm³/h. Here, the use of smallest particle diameters results in high thermal efficiencies due to the large heat transfer area. The comparison between simulation and experiment in Fig. 6 shows moderate deviations to the experimental results. Reasons for these deviations are in particular the neglected thermal radiation losses from the packed bed to the cooled inductor windings and the insufficient Nusselt correlation for Reynold numbers < 2000 [3]. Nevertheless, the used modelling approach is suitable for further investigations of the efficiency and power density in large-scale CAES application.

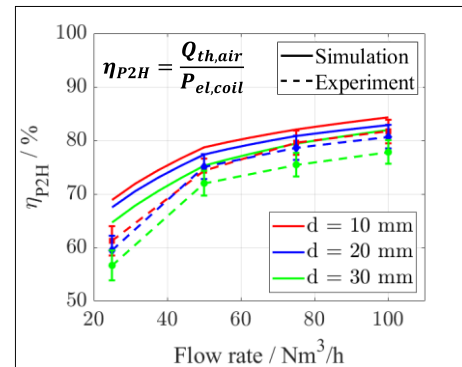


Fig. 6. Validation of the 1d electro-thermal model [3] at $f=25$ kHz and $I_{\text{coil}}=250$ A: Results for PtH efficiency of the laboratory 10 kW-setup

IV. CONCLUSIONS

The present contribution focusses on an experimental study with associated simulations based on a modelling approach for a novel PtH concept comprising an inductively heated and aerated packed bed. The electro-thermal model is validated on the basis of an experimental study since acceptable deviations occur due to neglected thermal radiation losses. In conclusion, a greater process understanding has been established and a process efficiency > 80% has been demonstrated for this novel PtH concept.

REFERENCES

- [1] Duquenne, Phillipe, Alain Deltour, and Germain Lacoste, "Application of inductive heating to granular media: Modelling of electrical phenomena" The Canadian Journal of Chemical Engineering, vol. 72.6, pp. 975-980, December 1994.
- [2] Baker, R.M.: "Design and calculation of induction heating coils". AIEE Trans, vol. 57, 1957, No.4, pp.31-40.
- [3] Belik, Sergej. "Numerical modelling of an induction heating process for packed rods with adjacent airflow." UIE Congress 2017: 405-410.

FE Simulation of Hot Single Point Incremental Forming Assisted by Induction Heating

Amar Al-Obaidi

*Institute for Machine Tools and
Production Processes (IWP)
Chemnitz University of Technology
Chemnitz, Germany
amar.al-obaidi@mb.tu-chemnitz.de*

Verena Kräusel

*Institute for Machine Tools and
Production Processes (IWP)
Chemnitz University of Technology
Chemnitz, Germany
verena.kraeusel@mb.tu-chemnitz.de*

Martin Kroll

*Institute for Machine Tools and
Production Processes (IWP)
Chemnitz University of Technology
Chemnitz, Germany
martin.kroll@mb.tu-chemnitz.de*

Abstract— Single Point Incremental Forming (SPIF) of high-strength is challenging. It requires high forming-forces, also the materials exhibit relatively low formability and distinctive springback behavior. Consequently the forming process is limited and the geometrical accuracy is decreased. Therefore hot SPIF was introduced. In the present study, with induction assisted locally heated single point incremental forming (IASPIF) a variant of this approach is investigated. This process was accomplished by forming on the upper side of the sheet using the forming tool while the heat was generated by a circular heating disc moving on the lower side of the sheet. The heat was transferred from the heating disc to the sheet during forming. The sheet was heated locally by this method, in which the heating disc was following the forming tool, by applying the same path for both of them.

Keywords— Induction heating, Single point incremental forming, High strength steel, FE modeling

I. EXPERIMENTAL PROCEDURE

The investigated component was a square pyramid with wall angle of 62° formed from 1.2 mm thick DP1000 steel. The stated sheet metal was selected because it represents a modern high strength steel dual phase steel with a wide range of applications. The modeled sheet was divided into three layers in thickness direction and investigated. Moreover, in the sheet model and a strip of meshes was selected to record the mechanical and thermal behavior of the sheet metal after forming.

II. THE OBJECTIVE OF THE RESEARCH

The Abaqus CAE program was used to perform finite element simulations of this SPIF process. The simulation process of the IASPIF was carried out to investigate the following effects:

- Effect of heating temperature on forming forces in the IASPIF process
- Calculation of the equivalent effective plastic stresses and strains
- Position and value of the maximum stress and strain that appear during forming
- Thinning behavior during forming in the formed wall part by maximum allowable plastic strain in the thickness direction and comparison with experimental results

III. FE SIMULATION

Two methods were applied for the numerical simulation of HSPIF: a Plastic behavior model and a fully coupled model.

The plastic properties, represented by the flow curves, of the DP1000 steel sheet metal were calculated from the tensile properties obtained by tensile tests performed at different temperatures ranging from room temperature to 700°C . Therefore, the Swift law was utilized by considering the hardening exponent. The resulting flow curves were used in the metal's mechanical plastic properties within the Abaqus program model.

The Abaqus program has the ability to analyze the induction heating by coupled simulation between the heat transfer and the electromagnetic process. The simulation of induction heating requires the surfaces of the components inductor, air and the workpiece to be continuously fixed together during simulation. Moreover, the meshing elements must be combined with each other for the three aforementioned components. The problem in simulating the IASPIF process with the Abaqus program is the continuous movement of the tool along a spiral path, resulting in high strains. At the same time, the inductor is moved simultaneously with the tool under the sheet with the same path. In the Abaqus program, it is not possible to simulate the movable tool and inductor simultaneously due to the fact that the four modeled basic parts (air, tool, sheet and inductor) must statistically be combined together during analysis. Therefore, alternative methods were utilized to heat up the sheet during IASPIF instead simulating the induction process. The process was substituted by heating the formed sheet with a heating disk in the lower side of the sheet. Furthermore, the heat generated in the sheet was caused by the effect of heat transfer from the heating disk.

SPIF simulation is well known for the huge time required to analyze the deformation process, so many researchers have preferred to simulate only a pie model, e. g. a 45° pie or 40° pie, in the circular formed parts. In the present work, anisotropy of the material is not considered in the analyzed model and the isotropic von Mises yield criterion was assumed. The fully coupled model is simplified by applying a coupled dynamic and temperature displacement of explicit step analysis. A 75×75 mm quarter of the 150×150 mm sheet was taken in the simulation to decrease the number of nodes and the simulation time. In addition, the symmetry boundary condition was considered for simulating this quarter portion taken from the whole model. The mesh

elements applied in the sheet were three-dimensional solid elements of brick-shaped 8-node C3D8T thermally coupled bricks with trilinear displacement. These mesh elements are well known for their capability to simulate the heat transfer with displacement due to the high calculation accuracy. In other words, the brick element type was used because of the capability to simulate the through-thickness deformation that occurred in the SPIF method. Furthermore, the brick element is capable of deforming uniformly during the SPIF process, and SPIF is well known for the high plastic strain values. The tool and heating disc were considered as rigid non-deformable elements. From the initial analyses, the fully coupled method was selected and used as the basic simulation process in the research.

IV. CONCLUSIONS

Hot SPIF FEM method was performed to simulate the behavior of DP1000 sheet metal. Therefore, the hot SPIF was carried out by heating the sheet during forming with a

circular disc that moved simultaneously with the forming tool. The main simulation results can be concluded as follows:

- a. The difference between FE simulation and experiment in the Fz values during forming at room temperature was 4%.
- b. The highest stresses were found in the Z-axis and were also located a compressive stress type.
- c. The PEEQ value increased by increasing the depth of the formed part. At the same time, the PEEQ and plastic strain component were increased by increasing the heating temperature during forming.
- d. Thinning of the formed wall angle occurred in both the experiment and simulation process due to the stretching stress.
- e. Reverse bending appeared during simulation, whereas during the experiment the reverse bending was very small.

Microwave Heating of Water in a Rectangular Waveguide: Validating EOF-Library Against COMSOL Multiphysics and Existing Data

Mihails Birjukovs
Institute of Numerical Modelling
University of Latvia
Riga, Latvia
mihails.birjukovs@lu.lv

Peter Raback
CSC - IT Center for Science
Espoo, Finland
peter.raback@csc.fi

Juris Vencels
EOF Consulting LLC
Riga, Latvia
vencels@eof-consulting.com

Juhani Kataja
Department of Micro- and
Nanosciences
Aalto University
Helsinki, Finland
juhani.m.kataja@aalto.fi

Abstract — EOF-Library, our open-source efficient coupler for Elmer FEM and OpenFOAM, is successfully validated against COMSOL Multiphysics, a commercial simulation package. We inform about discrepancies between our results and data from a series of research papers in the field. Simulations wherein microwaves are supplied to a water domain through a rectangular waveguide are used as benchmarks. The cases are conjugate problems involving fluid property dependence on temperature, microwave propagation and absorption, Marangoni effect and buoyancy-driven flow. We also report surface flow instabilities arising during prolonged microwave heating.

Keywords — microwave heating, convection, EOF-Library, Elmer, OpenFOAM, COMSOL Multiphysics.

I. INTRODUCTION

Microwave (MW) heating of liquids is used in food industry (cooking, pasteurization, extraction) and chemical industry (microwave-assisted organic synthesis) [1,2]. Other prospective applications are currently in the research phase, such as oil/bitumen recovery from the ground [3]. In almost all cases MWs are used to accelerate heating, because they penetrate materials causing volumetric heating. Other common benefits of MW heating include safety and efficiency. Modelling MW heating of liquids involves solving Maxwell equations for electromagnetics (EM), Navier-Stokes equations for hydrodynamics (HD), combined with the heat transfer equation. Proprietary software package COMSOL Multiphysics is among those with out-of-the-box functionality for solving coupled EM and HD problems. On the open-source software side, we use EOF-Library [4]. The reason we seek open-source alternatives is that COMSOL is well suited for EM, but sometimes has convergence issues in HD problems, where it is also generally more difficult to configure for both necessary precision and acceptable solution time. For advection dominated transient fluid flows, especially highly turbulent ones, the finite volume method (FVM) has a reputation of being more robust and is used more frequently than FEM. Therefore, the common tool of choice is OpenFOAM (FVM). EOF-Library couples Elmer (FEM) and OpenFOAM simulation packages [5,6]. It enables accurate internal field interpolation and communication between the two frameworks. The coupling is based on the message passing interface (MPI) resulting in low latency, high data bandwidth and parallel scalability [4]. While EOF is a

relatively new solution, it was already validated for magnetohydrodynamics (MHD) and plasma physics [7,8]. There are early developments for convective cooling of electrical devices with potential applications in electrical motors, flow sensors and transformers. To benchmark EOF, we choose a problem involving the heating an open (topside) water reservoir placed inside a vertically oriented rectangular waveguide with MWs (2.45 GHz, TE₁₀ mode) are introduced at the inlet port at the top of the waveguide. Ratanadecho et al. measured temperature and compared readings with 2D simulations [9]. Water and NaCl-water solution were studied, considering the dependence of relative permittivity on temperature. This problem was studied experimentally and numerically for different liquids, MW heating power and system geometry [10–13]. Laminar flow regime was assumed, and Marangoni effect was accounted for. The physical picture is as follows. The incident wave reaches the free surface of water, where much of its energy is reflected and exits the computational domain through the inlet port. The transmitted wave penetrates and heats water, inducing buoyancy-driven flow. Waveguide walls are assumed fully reflective and the water reservoir is fully transparent (0.75 mm thick polypropylene walls). The EM problem is solved for air and water domains, while the heat and mass transfer problem are solved for water only. The reservoir is considered a thermal insulator, so heat is lost through the free water surface only. OpenFOAM is not equipped with 2D solvers, so a 3D geometry with a structured mesh in the x-z plane and 1 element extrusion in the y direction was defined, which is equivalent to a 2D problem if one enforces symmetry conditions on extrusion faces.

II. RESULTS

We replicated the case described in [11,12] – the Boussinesq approximation was used and Marangoni effect at the free surface of water was considered. Default MW power is 300 W (we also use 500 W to verify the results from [13]) and initial water temperature is 28 °C. Water properties are taken from [11]. For benchmarks, the first 60 seconds of the heating process were simulated. We found that EOF and COMSOL solutions are in very good agreement throughout the series of benchmark tests, as seen in Figures 1 and 2. However, both experiments and simulations by [9–13] were in stark contrast with our own findings – an example of this is shown in Figure 2b, where it is evident that experiments and

simulations do not agree for [11,12]. In fact, we found that thermal camera images from [11] are contradictory and agree more with our current simulations than results in [11,12]. Weirdly enough, in Figure 2 one can see that the 500W case by Klinbun et al. indicates less generated heat than the 300W case. The agreement between EOF and COMSOL and the discrepancies between ours and reported results persisted when we chose 0 °C initial temperature, transitioned to the full buoyancy model, set all properties as temperature dependent and even set container walls as thermally conductive [14].

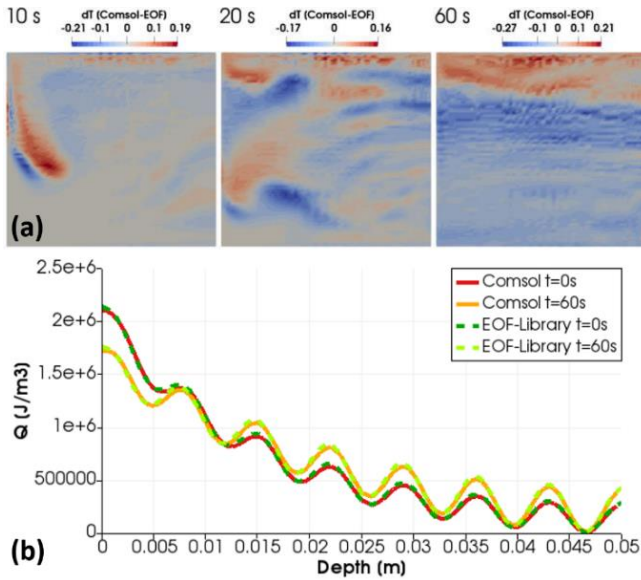


Figure 1. The difference between EOF-Library and COMSOL at different time stamps: (a) temperature field and (b) total dissipated power on container vertical axis at the beginning/end of the simulation.

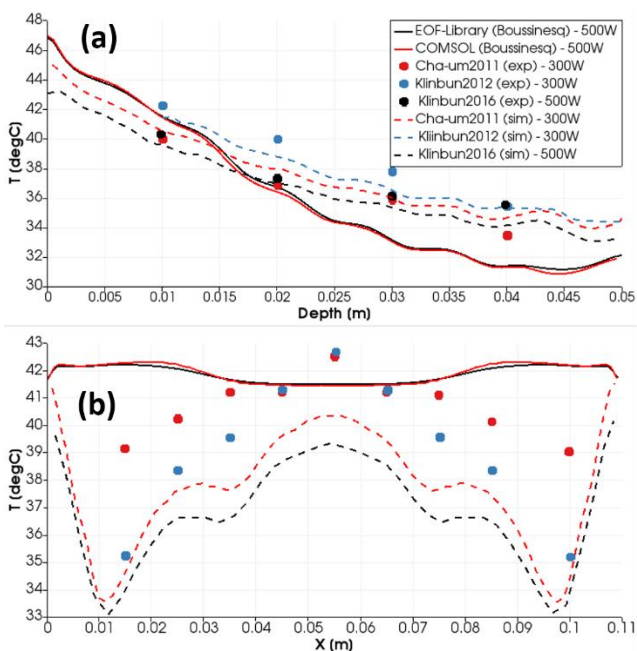


Figure 2. Temperature distribution along (a) the vertical axis and (b) the horizontal axis at 1 cm depth after 60 seconds of heating.

We suspect the issues might be due to errors in implementation or case setup in [9-13] – this is because the source cases are also rather inconsistently documented.

Interestingly, extending the simulation duration to beyond 150 seconds reveals unexpected behavior – depending on the prescribed heat transfer coefficient for the free surface, surface velocity irregularities set in which then develop into pulse-like perturbations that propagate across the surface from the center of the reservoir surface. This results in sporadic velocity oscillations (Figure 3a) and symmetry breaking (Figure 3b). We are currently determining the nature of these instabilities, which, to our knowledge, have not been reported for MW heating problems of this type.

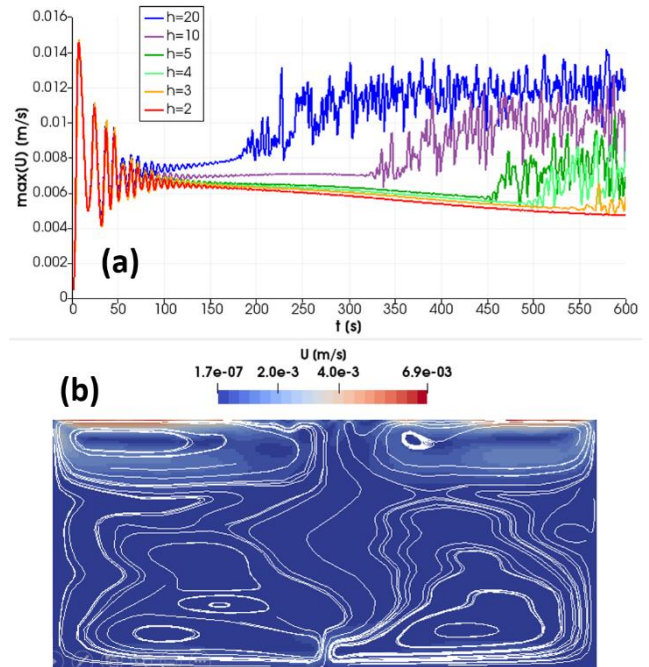


Figure 3. (a) Maximum velocity magnitude over time for different heat transfer coefficients (designated as h) and (b) velocity magnitude and streamlines for $h = 5$ W/(m²·K) at 600 seconds of flow time.

REFERENCES

- [1] F.-G.C. Ekezie, D.-W. Sun, Z. Han and J.-H. Cheng, Trends Food Sci. Technol. 67 (2017)
- [2] J.D. Moseley and C.O. Kappe, Green Chem. 13 (4) (2011)
- [3] A. Bera and T. Babadagli, Appl. Energy 151 (2015)
- [4] J. Vencels, P. Raback and V. Geza, SoftwareX 9 (2019)
- [5] Ruokolainen, M. Malinen, P. Raback, T. Zwinger, A. Pursula and M. Byckling, Elmer solver manual, CSC-IT Center for Science.
- [6] H.G. Weller, G. Tabor, H. Jasak and C. Fureby, Comput. Phys. 12 (6) (1998)
- [7] J. Vencels, A. Jakovics and V. Geza, Magnetohydrodynamics 53 (4) (2017)
- [8] M. Kubecka, A. Obrusnik, P. Zikan, M. Jilek Jr, J. Vencels and Z. Bonaventura, Preprint submitted to Surface and Coatings Technology
- [9] P. Rattanadecho, K. Aoki and M. Akahori, Appl. Math. Model. 26 (3) (2002)
- [10] W. Cha-um, P. Rattanadecho and W. Pakdee, Exp. Therm. Fluid Sci. 33 (3) (2009)
- [11] W. Cha-um, P. Rattanadecho and W. Pakdee, Food Bioprocess Technol. 4 (4) (2011)
- [12] W. Klinbun and P. Rattanadecho, Appl. Math. Model. 36 (2) (2012)
- [13] W. Klinbun and P. Rattanadecho, Int. Commun. Heat Mass Transf. 70 (2016)
- [14] Juris Vencels, Mihails Birjukovs, Juhani Kataja and Peter Raback, Case Stud. Therm. Eng. 15 (2019)

Load capacity of cables insulated materials of high thermal conductivity

Nikolay Khrenkov
 OKB «Gamma» LLC
 Special Systems and Technologies group of companies
 Russia, Mytischy, Moscow region
 hrenkov@sst.ru

Abstract – The influence of thermal conductivity of electrical insulation materials on the load capacity of power and installation cables is investigated.

Keywords: cables, thermal conductivity, load capacity

I. INTRODUCTION

Polyvinyl chloride compound (PVC) is widely used in power and installation cables for insulation and sheaths. The load capacity of PVC insulated cables is determined by the heat resistance and thermal conductivity of the material. In regulatory documents for cables of this type, the load capacity is determined for the following conditions: the temperature of the conductive cores should not exceed + 65°C and the ambient temperature is +25°C. One of the main drawbacks of the PVC plastic compound is that material contains chlorine; in addition, it has a fairly low coefficient of thermal conductivity.

Halogen-free compounds are developed and used to replace PVC. One of these compounds – BIC 15, which has good electrical properties and high thermal conductivity, was developed in the SST group of companies and is used in the manufacture of installation cables.

The results of studies of insulation resistance (R_{ins}) and thermal conductivity (λ) of two types of halogen-free compounds in comparison with similar properties of PVC are given below (table 1).

TABLE 1 PROPERTIES OF THE MATERIALS

Material	Manufacturer	R_{ins}	λ
		Ohm·m	W/m·K
PVC compound IT 105 P-A-16c	Prominvest, Ukraine	$1.2 \cdot 10^{14}$	0.19
Compound BIC 15	OKB «Gamma», Russia	$2.8 \cdot 10^{15}$	0.90
Compound Fragom PR/555K1	Crosspolimeri spa, Italy	$2.5 \cdot 10^{14}$	0.72

The appearance of a three-core cable of the One Key Electro brand, manufactured by the OKB «Gamma» - the part of the SST group, for which the calculations presented below were made is shown in Fig. 1.

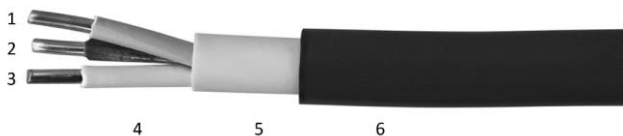


Fig. 1. Three-core One Key Electro power cable, $3 \times 6 \text{ mm}^2$
 1, 2, 3-conductive cores; 4-insulation; 5-filling; 6-sheath.

Calculation of heat flows and temperatures in cables, when current is flowing through them, for various environmental conditions, is performed using a set of

programs for modeling physical fields using the finite element method ELCUT v. 6.3 [1].

II. HEAT TRANSFER FROM CABLES TO THE AIR

The results of modeling thermal fields in cables of the same design, with cores of $3 \times 6 \text{ mm}^2$, but with different insulation materials are shown below. The current flows in two cores (the first and third), and the second core is used for grounding. The outdoor temperature in all cases is the same +25°C. The coefficients of heat transfer to still air were calculated as the sum of the convective and radiation components, based on the temperature difference between the cable surface and the surrounding air.

Table 2 shows the results of calculations for the case of the same heat release in the cores at a current of 50 A, normalized in the Rules on design of power electric installations - PUE (table 1.3.6). This calculation confirmed that at the current set in the PUE for PVC insulation, the cores do not heat above 65°C. When the insulation and cable sheaths are made of materials with high thermal conductivity, the thermal resistance of the polymer layers is significantly less. As a result, at approximately the same surface temperature, the cores are heated significantly less, not least because of the fact, that the resistance of copper increases to a lesser extent.

Less heating of cables with insulation and sheath made of halogen-free compounds, at the same currents as in PVC cables, indicates their greater thermal safety.

TABLE 2 HEAT TRANSFER TO THE AIR AT A CURRENT OF 50 AMPERES

Material	P	T _{cor}	T _{she}	α sum	ΔT	R sum
	W/m	°C	°C	W/m ² ·K	°C	m·K/W
PVC	8.5x2	64.7	52.1	15.4	12.6	0.741
BIC 15	8.0x2	52.5	50.1	15.2	2.35	0.147
Fragom	8.05x2	54.7	51.5	15.3	3.20	0.199

The symbols in table 2: P - the flow of heat released in the cable cores at the current of 50 A; T_{cor} - the heating temperature of the conductive cores; T_{she} - the surface temperature of the cable sheath; α sum - the total coefficient of heat transfer from the cable surface; ΔT - the temperature difference in the cable insulation layers; R sum - the thermal resistance of the cable insulation layers.

Low thermal resistance of insulation layers made of polymers with high thermal conductivity allows increasing the current load on the cables. Also, taking into account the condition that the cores should not be heated above 65°C, we calculated the level of permissible current loads and thermal characteristics, which are presented in the table 3.

The permissible current load in cables insulated with halogen-free compounds increased by 22-24% in relation to cables with PVC insulation and sheaths, but at the same time,

due to increased heat generation in the cores and lower thermal resistance of the insulation layers, the surface temperature of these cables increased by 17%. Symbols in the table 3 the same as in table 2.

TABLE 3 HEAT TRANSFER TO THE AIR AT MAXIMUM CURRENT

Material	I	P	T cor	T she	α sum	ΔT
	A	W/m	$^{\circ}C$	$^{\circ}C$	W/m ² ·K	$^{\circ}C$
PVC	50	8.5 x 2	64.7	52.1	15.4	12.6
BIC 15	62.2	12.5 x 2	64.5	60.8	16.2	3.7
Fragom	61.0	12.0 x 2	64.4	60.0	16.0	4.4

III. HEAT TRANSFER FROM THE CABLE LAID IN THE WALL

The models, when the cable is laid horizontally within a vertical wall with thermal conductivity of the wall material 0.7 W/m·K are considered. The distance from the cable to the surface of the wall is 5 mm. Wall thickness is 100 mm. The temperature on both sides of the wall +25°C. The results of the calculations are presented in table 4. In this calculation, the same level of heat generation in the cores was set as before, when determining the maximum load capacity of the cables (table 3).

TABLE 4 HEAT TRANSFER FROM THE CABLE IN THE WALL

Material	T cor	T _{1m}	T _{1ave}	T _{2ave}	α_1	α_2	ΔT
	$^{\circ}C$	$^{\circ}C$	$^{\circ}C$	$^{\circ}C$	W/m ² ·K	W/m ² ·K	$^{\circ}C$
PVC	51.7	36.5	28.7	27.0	10.34	9.6	23.0
BIC 15	48.0	41.5	30.2	27.7	10.8	9.95	17.8
Fragom	48.05	41.0	29.9	27.6	10.7	9.9	18.2

The symbols in table 4: T_{1m} - maximum temperature of the front wall (where the cable); T_{1ave} - the average temperature of the front wall; T_{2ave} - the average temperature of the back wall; α_1 - the coefficient of heat transfer from the front wall; α_2 - the coefficient of heat transfer from the back wall; ΔT - temperature difference between the core and the average temperature of the front wall.

Due to the fact that the heat flow in all three cases has the ability to dissipate through a larger surface than in the case of a single cable in the air, the degree of heating of the cores is reduced by 25% for cables with PVC insulation, and by 35% for cables with insulation from halogen-free compounds. At the same time, the wall itself is heated more strongly near the cable with insulation from halogen-free compounds.

The coefficient of heat transfer from the front and back walls was calculated as the sum of convective and radiation mechanisms of heat transfer from the vertical wall. The difference between the average wall temperature and the air temperature (25 °C) was taken as the temperature difference.

IV. HEAT TRANSFER FROM THE CABLE LAID ON THE WALL

In the case of horizontal cable routing in a thin-walled stainless steel tube along a vertical wall, the heat transfer conditions change. The air inside the tube prevents heat dissipation and thus the maximum permissible current levels in the cables are reduced in relation to the limit levels defined earlier (table 3). The results of calculations for this cable installation option are presented in table 5. For PVC-insulated cables, the maximum permissible current has been reduced by 10 %, and for cables with halogen-free compounds by 13%.

TABLE 5 HEAT TRANSFER FROM THE CABLE IN THE TUBE

Material	I	P	T cor	Tt	αt	ΔT
	A	W/m	$^{\circ}C$	$^{\circ}C$	W/m ² ·K	$^{\circ}C$
PVC	45	6.9 x 2	64.8	34.7	12.8	30.1
BIC 15	53	9.5 x 2	65.2	37.6	13.5	27.6
Fragom	52	9.1 x 2	64.8	37.4	13.5	27.4

The symbols in table 5: T_t - temperature of the surface of the tube; αt - the coefficient of heat transfer from the surface of the tube; ΔT - temperature difference between the core and the average temperature of the surface of the tube.

V. CONCLUSION

The use of halogen-free compounds with high thermal conductivity for insulation and sheaths of power and installation cables, instead of PVC compounds, improves the conditions of heat transfer from conductive cores and allows you to increase the load capacity of cables by 15-20 %. depending on the specific operating conditions of the cables.

REFERENCES

- [1] Programs for modeling physical fields ELCUT v. 6.3

Induction Tempering of Surface Hardened Components

Bernard Nacke
 Institute of Electrotechnology
 Leibniz University Hannover
 Hannover, Germany
 nacke@etp.uni-hannover.de

Marco Baldan
 Institute for Industrial Mathematics
 Fraunhofer-Gesellschaft
 Kaiserslautern, Germany
 marco.baldan@itwm.fraunhofer.de

Abstract—Induction hardening is an energy-efficient and highly reproducible heat treatment process for surface hardening. Due to process-related thermal gradients between the surface and core areas of induction hardened components, the process is accompanied by residual stresses that promote crack formation. This problem is countered by tempering in the first tempering stage for a period of one to two hours after the hardening process. This is conventionally carried out in furnaces, which in the process chain involves additional transport and energy costs and prevents the production process from becoming more flexible. A resource-saving and environmentally friendly alternative is inductive tempering, which lasts a few seconds and enables integration into a running production line. The paper presents the results of a research project to develop a numerical model for the design of an induction tempering process, taking into account the previous induction hardening.

Keywords—induction tempering, induction surface hardening, numerical simulation, FEM

I. INTRODUCTION

As part of the German AIF funding program, an innovative approach for modeling induction tempering in the process of inductive surface hardening was studied. The goal was twofold. On the one hand, the development of a comprehensive multi-physical numerical model of induction tempering that takes into account the previous induction hardening. On the other, the usage of the model for the field analysis in few inverse design test cases. The novelty of the paper mainly lies in the model of induction tempering since most of papers available in literature are limited to electromagnetic-thermal coupled analyses [1]-[2]. Our work not only considers hardening before tempering, but also it deals with three physics (electromagnetic, thermal, microstructural) in which all material properties (electromagnetic too [3]) are temperature and microstructure dependent.

II. NUMERICAL MODEL

During the heating stages, in the integrated modeling of induction hardening and tempering processes, coupled electromagnetic-thermal and microstructural analyses have been considered. (Fig. 1). On the other hand, the quenching stages (occurring after both processes) are simulated in an analogous way, excluded the electromagnetic solution, here not necessary.

The electromagnetic analysis is described by the Maxwell equations evaluated in frequency domain. The magnetic permeability results to be not only temperature and field strength, but also microstructure dependent [3]. The electrical resistivity is temperature and microstructure dependent as well. Hysteretic losses are neglected because they play a very

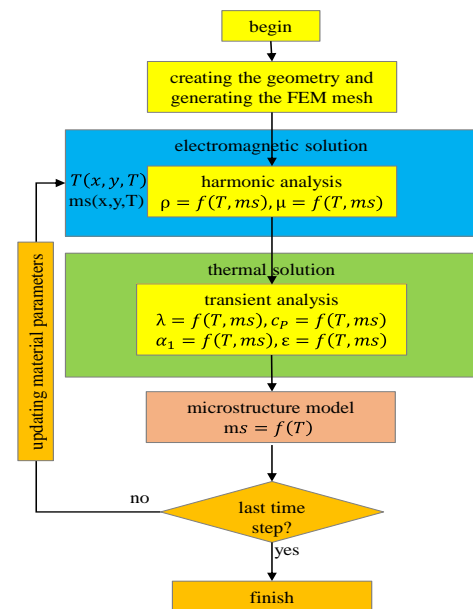
minor role compared to Joule's ones [4]. The thermal analysis relies on the heat conduction equation that includes convective and radiation effects. The source term depends not only on the induced power but also on the latent heat exchanged during phase-phase microstructural transformations. Finally, the microstructural analysis involves both heating and quenching stages in case of hardening. Therefore, it is able to predict the distribution of austenite and martensite. In case of tempering, the model evaluates the map of carbides and, mostly important, the final hardness. This is obtained as a rule of mixture from the different microstructures. In particular, the hardness of tempered martensite is calculated as a linear dependency from the Hollomon-Jaffe tempering parameter (TP):

$$TP = \frac{T + 273.15}{1000} \left(C + \log \frac{t}{3600} \right)$$

Where T , t , C are temperature, time and a material constant, respectively. It is straightforward to recognize that, compared to the conventional treatment, induction tempering, due to the short heating time, requires higher temperatures to get an equivalent hardness reduction. However, the temperature increase is much more limited in comparison to the time diminution.

Simulations were carried out with the commercial software package ANSYS® making extensive use of user-written subroutines to guarantee enough flexibility in the modelling step. The work-piece is always supposed to be made of AISI 4140 (German grade 42CrMo4).

Fig. 1. Electromagnetic-thermally coupled model with feedback of the temperature and microstructure dependent electro-magnetic and thermo-physical material data

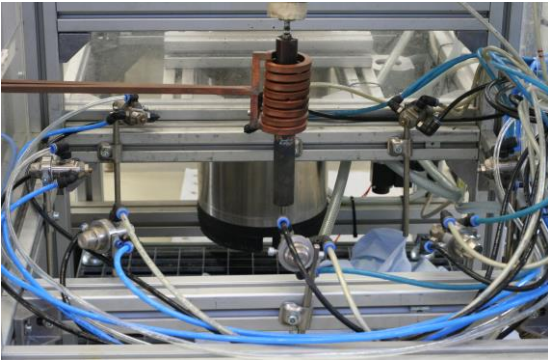


III. PROJECT RESULTS

A. Verification of the numerical model with a test configuration

A test-setup has been built in our laboratory in order to validate the numerical model (Fig. 2). The choice of a cylindrical work-piece comes from the will to minimize the sources of inaccuracy. The heating processes, in both hardening and tempering, are performed with the same inductor. Moreover, as in most industrial applications, in order to facilitate the integration in the production line, tempering and hardening employ an equal frequency. With a desired hardening depth of 2 mm, the choice falls on 12 kHz [5]. In the hardening process, in order to guarantee the transformation of austenite in martensite, heating must be followed by the quenching. In our test-setup pressurized water is used as quenching medium. Validation includes comparison of simulated and measured temperatures.

Fig. 2. Test-setup at ETP. The 8-windings coil is surrounded by 8 nozzles that are responsible for the cooling



B. Verification of hardening and tempering models of the industrial process

Preliminary experiments in industry have been performed. The work-piece under analysis has a “L-shape” and the inductor consists of a single turn surrounded by flux concentrating material (Fig. 3). Such piece geometries are broadly diffused in automotive and aerospace components. During the heating processes, the surface temperature is measured with a pyrometer through a hole in the coil. The heating time in the hardening process has been chosen equal to 0.5 s.

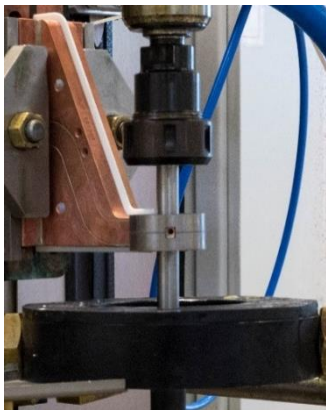
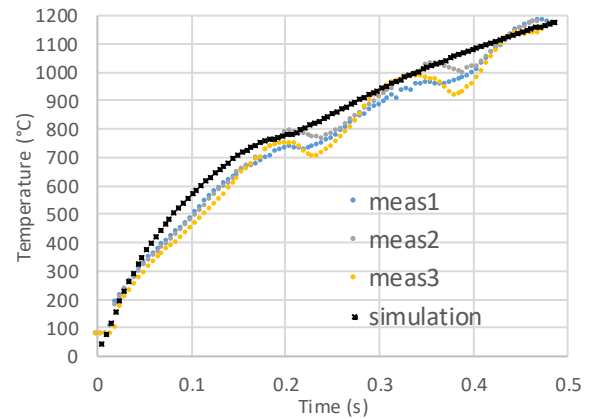


Fig. 3. Experimental setup in industry. The power supply provides a constant power of 100 kW while the frequency is 12 kHz. A good agreement has been reached between measured and simulated temperature (Fig. 4).

Since the whole tempering process occurs under the Curie temperature and the used frequency remains 12 kHz, in order to avoid overheating, it is mandatory to modulate the power in time. In this case, three 8 kW power pulses are followed by as many soaking intervals. The total time is just below 20 s. Similar to hardening, also in tempering the simulated temperature meets excellently the experimental results. Final hardness distributions show good agreement too.

Fig. 4. Hardening: comparison between simulated (black) and measured temperatures (meas1, meas2, meas3)



C. Inverse design of an industrial induction hardening and tempering configuration

Once the numerical model has been validated, it has been used for the inverse design of the overall heat treatment. Ideally, given the wished final hardness distribution, our numerical tool is capable to predict the inductor geometry and the heating regimes (power, time and frequency in both hardening and tempering). Few inverse design test cases relative to induction tempering have been performed. Design variables concerned the heating profiles, while the objectives relate to a uniform hardness distribution around a desired value and/or a short time process. If in the preliminary experiments, the maximum deviation from 58 HRC varied between 3.3 and 5.5 HRC, thanks to the inverse design this value dropped to 2.1 HRC. A further reduction was achieved exploiting the residual heat during quenching after hardening.

SUMMARY

A multi-physical numerical tool has been developed for the simulation of induction hardening and tempering in order to get a better understating of the overall process and exploit the advantages of the induction technology: time and energy saving among all. Results of the inverse problems look encouraging in the hope of making this technology attractive.

ACKNOWLEDGMENT

The research project was supported by the Federal Ministry of Economic Affairs and Energy through the German Federation of Industrial Research Associations (AiF) as part of the programme for promoting industrial cooperative research (IGF) on the basis of the German Bundestag.

REFERENCES

- [1] Zabet A., Mohamadi A., Azghandi S.H.; Simulation of induction tempering process of carbon steel using finite element method; *Materials and Design*, 36 (2012), pp. 415-420
- [2] Vieweg A., Raninger P., Prevedel P., Ressel G., Ecker W., Marsoner S., Ebner R., Experimentelle und num. Untersuchung des induktiven Anlassens eines Vergütungsstahles, *J.He. Treatm. Mat.* 72 (4), (2017)
- [3] Baldan M., Stolte M., Nacke B., Nürnberger F., Improving the Accuracy of FE Simulations of Induction Tempering Toward a Microstructure-Dep. *Electrom. Model, IEEE T. Mag.*, 56 (10), (2020)
- [4] Rudnev V., Loveless D., Cook D., Black M., *Handbook of induction heating*. (2003), Marcel Dekker Inc.
- [5] Baldan M., Nikanorov A., Nacke B.; Hierarchical optimization approaches in designing surface hardening induction systems; *IOP Conf. Series Materials Science and Engineering* 424:012067, (2018)

Density of the System $\text{Al}_2\text{O}_3\text{-ZrO}_2$ in a Liquid Phase

Jan Hrbek
Nuclear Fuel Cycle Department
Research Centre Řež
Husinec-Řež, Czech Republic
jan.hrbek@cvrez.cz

Bence Mészáros
Nuclear Fuel Cycle Department
Research Centre Řež
Husinec-Řež, Czech Republic
bence.meszaros@cvrez.cz

Mykhaylo Paukov
Nuclear Fuel Cycle Department
Research Centre Řež
Husinec-Řež, Czech Republic
mykhaylo.paukov@cvrez.cz

Martin Kudláč
Nuclear Fuel Cycle Department
Research Centre Řež
Husinec-Řež, Czech Republic
martin.kudlac@cvrez.cz

Abstract— Physical properties of materials should be studied in order to describe their behavior for design of new devices or modeling of physical processes. However, it is difficult to determine them for materials at high-temperatures. In this study, a method suitable for determination of density in a liquid phase at high temperature is proposed and tested on $\text{Al}_2\text{O}_3\text{-ZrO}_2$ system. The material was melted in an induction furnace with a cold crucible. The measurement was based on evaluation of the volume of the melt at different temperatures. The density of material was calculated from the mass and volume of the melt. The densities of material in the solid-state and skull-layer were measured using pycnometer. A temperature dependence of density was established, and the results were compared with literature. The difference between existing data and experimental one was about 10%. Thus, proposed methodology provides reliable density values in extreme conditions. And further it will be used as a fundamental support to increase the amount of experimental data in material properties databases.

Keywords—density, induction melting, cold crucible, Al_2O_3 , ZrO_2

I. INTRODUCTION

The material properties are important in many branches of science and engineering. Nowadays, special methods for the determination of physical properties of materials based on calculation exist [1]. However, it is necessary to realize that material parameters should be determined experimentally, or at least to verify the data obtained using computational methods. Our research aims to develop and verify the method which can be used for the determination of the density of oxides and their mixtures in a liquid phase at high temperature and establishment of its temperature dependence. Several researches studies focused on this issue are available [2] but many materials and mixtures are not described in sufficient range of temperatures or at all. Several mixtures were chosen for verification of the suggested method. The experiment for verification of the method was performed in the wider temperature range than the one in the comparative data. After verification of the method, it will be used for the density determination of materials with unknown dependence of density on temperature.

The density of a material is defined by its mass per unit volume. Thus, the suggested technique has to allow the measurement of the volume of the material and its weight. Investigation of density has been performed in both solid-state at room temperature and liquid phase.

Density measurements were performed in the range of temperatures from 2100 °C to 2400 °C. The lower level of the temperature range was chosen with respect to the liquidus

temperature of the mixture [3]. Our aim was to measure the density in liquid phase. Therefore, the melt temperature had to be above the liquidus temperature. The brand-new equipment was developed for the density measurement. It was decided to use lower parameters for the first experiment in this system configuration, thus, 2400 °C was chosen as the upper level of the range.

II. EXPERIMENT AND METHODS

The experiment was designed to measure the density of the mixture 50 % Al_2O_3 and 50 % ZrO_2 in the liquid phase. In order to obtain the liquid phase of the oxide mixture, the induction skull melting (ISM) was used. The principle of ISM consists in melting by a time-varying electromagnetic field in a water-cooled crucible, in a so-called cold crucible. A thin protective layer between the cold crucible and the melt, called skull, is created. It prevents contamination of the melt and reduces thermal stress of the crucible. The density was measured with a temperature step of 100 °C, and its value was calculated from the measurement of the melt volume and its weight. Two quenched samples were taken for X-ray powder diffraction (XRD) to define the exact composition of the melt. The melt was assumed to be homogeneous due to intensive stirring. The temperature of the melt surface was measured using chromatic pyrometer.

The volume was calculated from the height of the melt, which was measured by a special stainless-steel sample. For each measured temperature, 3 samples were taken to calculate the average height of the melt. The sample was immersed into the melt for a short period of time (2 s) and it was colored due to the oxidation processes taking place on the surface. The diameter of the melt was measured by two-step measurements after cooling the ingot. The first step was the measurement of the ingot volume. Then, after the ingot was cut into halves the thickness of the skull layer and diameter of the melted part in different vertical positions were determined. The measurement was made using self-developed software with calibrated scale developed for this measurement. The same measurement was performed using an optical microscope and the results were compared to detect potential errors. However, it was shown that the results are in very good agreement.

The weight of the ingot was further measured. Then, the samples of the skull layer and ingot were taken and their densities in the solid phase were measured. The measurements were done by pycnometry in water [4]. Five measurements for each of 3 samples of the skull layer and 3 samples of the material in the solid-state were carried out, and the average values were used for the calculations. The mass of the skull

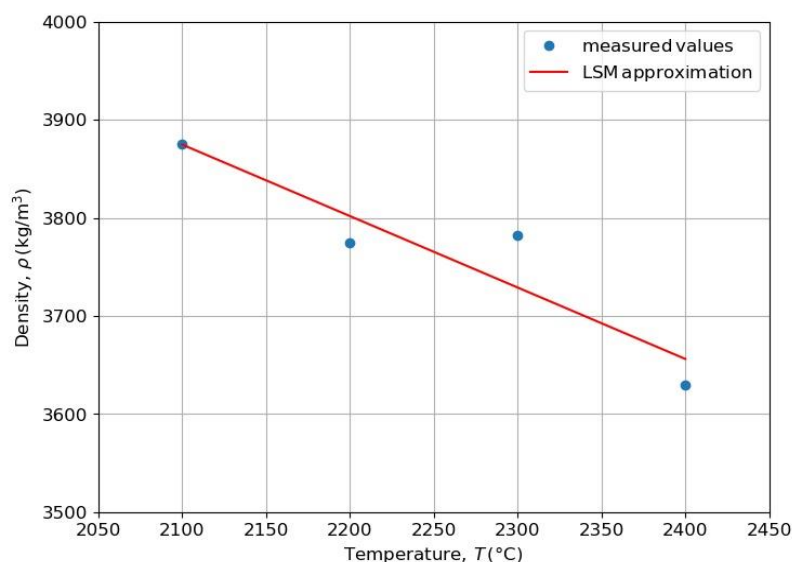


Fig. 1. Temperature dependence of density of 50% Al₂O₃ + 50% ZrO₂

was calculated using the density of the skull and its volume. It was subtracted from the mass of ingot to obtain the mass of the melt.

From the known mass and volume of the melt the density in the liquid phase for each measured temperature was calculated.

The material was melted using an electric current with a frequency of 1.7 MHz in a 4-turns inductor with an inner diameter of 110 mm. The inner diameter of the used cold crucible was 57 mm and the height of the melt was 35 mm. The power transferred into the melt was 8 kW at 2100 °C and 15 kW at 2400 °C.

III. RESULTS

The weights, volumes and calculated values of densities are listed in Table I. The values of the density were approximated using the least-squares method (LSM). The density (kg/m³) dependence on temperature (°C) of 50% Al₂O₃ + 50% ZrO₂ was approximated by a linear function:

$$\rho = -0.729 \cdot T + 5405.28 \quad (1)$$

The measured results are shown in Fig. 1 together with the dependence of density on temperature according to the linear regression.

IV. DISCUSSION AND CONCLUSION

The result for the temperature of 2100 °C was compared with published value [5]. It was not possible to compare more data because the published research was focused on the densities in the area of the lower temperatures. Our experiment was carried out at 2100 °C to verify the measurement function. For further experiments, a temperature closer to the liquidus temperature will be considered.

The density is equal to 3523.0 kg/m³ according to [5], the value obtained by our experiment is 3875.17 kg/m³. The difference 352.17 kg/m³ is about 10%. Thus, this result is in a good accordance with [5]. In principle, the density should decrease with increasing temperature, so the slope of (1) and the slope presented in [5] were compared.

TABLE I. WEIGHT, VOLUME AND DENSITY OF MELT DEPENDING ON THE TEMPERATURE

T (°C)	m (g)	V (cm ³)	ρ (kg/m ³)
2100	264.97	68.38	3875.17
2200	264.97	70.20	3774.61
2300	264.97	70.06	3782.16
2400	264.97	73.00	3629.71

The difference between them is caused by different temperature ranges. The measurements published in [5] were carried out also in the area of the solidus and liquidus temperatures. In this area, the dependence of density should be less steep than in the liquid phase and this assumption is fulfilled. The density comparison at the same temperature has a higher value for verification of the method. From this point of view, the methodology appears to be reliable. Currently, an experiment to validate and refine the data obtained from the presented one is being prepared.

ACKNOWLEDGMENT

The presented work has been realized within Institutional Support by Ministry of Industry and Trade.

REFERENCES

- [1] W. K. Kim, J. H. Shim, M. Kaviyani, "Thermophysical properties of liquid UO₂, ZrO₂ and corium by molecular dynamics and predictive models", *Journal of Nuclear Materials*, Vol. 491, pp. 126-137, 2017.
- [2] D. Grishchenko, P. Piluso, "Recent progress in the gas-film levitation as a method for thermophysical properties measurements: application to ZrO₂-Al₂O₃ system", *High Temperatures-High Pressures*, vol. 40, No. 2, pp. 127-149, 2011.
- [3] D.A. Jerebtsov, G.G. Mikhailov, S.V. Sverdina, "Phase diagram of the system: Al₂O₃-ZrO₂", *Ceramics International*, vol. 26, pp.821-823, 2000
- [4] S. Davidson, M. Perkin, "An investigation of density determination methods for porous materials, small samples and particulates", *Measurement*, vol. 46, no. 5, pp.1766-1770, 2012.
- [5] D. V. Grishchenko, "Complex of methods of research of properties of melts of ZrO₂-Al₂O₃ system", PhD dissertation, St. Petersburg State Technological Institute, St. Petersburg, Russia, 2008. (in Russian)

ELECTRICAL EFFICIENCY OF INDUCTION CONTOUR HARDENING SYSTEMS

Jerzy Barglik
Silesian University of Technology
Katowice, Poland
jerzy.barglik@polsl.pl
ORCID: 0000-0002-1994-3266

Adrian Smagór
Silesian University of Technology
Katowice, Poland
adrian.smagor@polsl.pl
ORCID: 0000-0001-7667-6697

Albert Smalcerz
Silesian University of Technology
Katowice, Poland
albert.smalcerz@polsl.pl
ORCID: 0000-0003-0957-1291

Abstract— The paper deals with the mathematical modeling of induction contour hardening of gear wheels. Uniformity criteria of obtained contour profile are discussed. In order to determine the electrical efficiency of the process its first stage: induction heating is considered. Numerical modelling of coupled non-linear electromagnetic and temperature fields are described. In order to evaluate accuracy of the proposed approach exemplary computations of the full process are provided. Results are compared with measurements and satisfactory accordance is achieved.

Keywords— induction heating, contour hardening, coupled problems, critical temperatures

I. INDUCTION CONTOUR HARDENING (ICH)

The ICH process makes possible to obtain a thin hardened zone along the working surface of treated elements. The process is effective: short in time and energy-saving in opposite to a long-term, energy consuming, classical surface heat treatment like for instance carbonizing and consequent hardening [1]. In many advanced industrial applications the crucial quality condition is connected not only with thickness but also with the uniformity of the hardened contour zone. Its thickness is described by the Surface Depth Hardening (SDH) [2] defined as the distance perpendicular to any surface point to a such inside point where the hardness decreases to the 80 % of the maximal value. Uniform shape of profile is especially important in a case of gear wheels used in automobile and aerospace industries. For the ICH process of gear wheels with modulus $m > 6$ mm satisfactory results could be achieved by means of the Tooth-by-Tooth Induction Hardening (TTIH) method [3]. For smaller gear wheels mostly the Dual Frequency Induction Hardening (DFIH) method is applied [4], but anyway it is not easy to obtain the uniform thickness of the hardened contour zone [5]. Uniformity of the contour profile could be represented by the coefficient K (see Fig.1):

$$K = \frac{h + h_1 - h_2}{h} \quad (1)$$

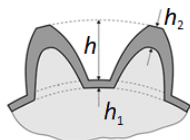


Fig.1 Definition of uniformity coefficient K . h – height of the tooth, h_1 – SDH coefficient on the axis of the root, h_2 – SDH coefficient on the axis of the top

The paper concentrates on mathematical modelling of induction heating as the first stage of the ICH process, which makes possible to determine electrical efficiency of the

The paper was prepared within the NCBiR project PBS2/A5/41/2014.

process and also to analyse which parameters of the system influenced on it. As the example the Consecutive Dual Frequency Induction Hardening (CDFIH) for small gear wheels is considered.

II. MATHEMATICAL MODELLING

The ISH process consists of two consecutive stages: rapid induction heating and intensive cooling. A break between these two stages (austenitization) is very short and it could be neglected. In order to calculate the electrical efficiency of the ICH process we should concentrate on the induction heating stage only. The electrical efficiency η_e is defined

$$\eta_e = \frac{1}{P_t} \cdot \int_V p_v \cdot dV \quad (2)$$

where: P_t – total active power delivered to the system from the generator calculated by means of Poynting theorem [6], p_v – volumetric density representing the sum of MF and HF power released in the element.

The block scheme of the applied algorithm is presented in Fig. 2

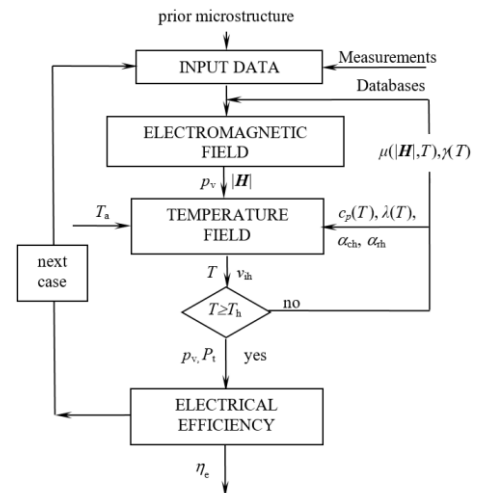


Fig.2 Block scheme of the heating stage of the ICH process

Input data are completed based upon measurements or taken from proper databases. A kind of prior microstructure influencing on critical temperature is taken into account as well [7]. Computations are provided by means of the Flux 3D software for coupled electromagnetic and temperature fields [8]. Based upon electromagnetic computations volumetric density of active power p_v , absolute value of the magnetic field intensity and velocity of induction heating v_{ih} . Non-linear dependence of electric conductivity γ on temperature is

noticed. The magnetic permeability changes rapidly because of magnetic transformation at the Curie point A_{c2} . It is determined by measurements and considered as dependent on the absolute value of the magnetic field intensity and on the temperature [9]. Other material properties (specific heat c_p , thermal conductivity λ) as well as convection heat transfer α_{ch} and radiation heat transfer α_{rh} are considered as temperature dependent. It is assumed that temperature of convection and radiation environments are the same

$$T_{ac} \approx T_{ar} = T_a \quad (3)$$

Multiple reflection phenomena are neglected [10]. Computations of induction heating terminate when the average temperature exceeds the hardening temperature T_h

$$T_h \geq A_{c3}(v_{ih}) = A_{c3m} + \Delta T \quad (4)$$

where: A_{c3} – upper critical temperature guaranteed termination of austenite transformation, A_{c3m} – modified value of the upper critical temperature dependent on heating rate, ΔT – increase of temperature, $\Delta T = 15 - 30$ K.

In case of a special quality kind of steel having as a prior microstructure the tempered martensite (like for instance steel AISI 4340 or other similar) the temperature increase $\Delta T = 100$ K in order to exceed the critical temperature $A_{cm}(v_{ih})$ guaranteed the uniform austenite microstructure. Exemplary dependences of the critical temperatures for investigated steel on heating rate are determined from the Time-Temperature-Austenitization (TTA) diagram taken from specialized measurements. Final step of computations is determination of the electric efficiency and its comparison with classical hardening methods.

III. ILLUSTRATIVE EXAMPLE

Exemplary computations are provided for small gear wheels with modulus $m = 2$ mm and number of teeth $n = 16$, made of steel AISI4340 by the Consecutive Dual Frequency Induction Hardening (CDFIH). Configuration of the inductors-sprayer system is shown in Fig. 3



Fig.3 Configuration of the inductors-sprayer system during CDFIH process [11]

Dimensions and parameters of the analysed CDFIH system are listed in details in [11]. Modified upper critical temperature A_{c3m} for real induction heating conditions with the heating rate of 230 K/s is equal to 840°C. It means that the hardening temperature reaches value of about 940°C. In order to evaluate the accuracy of the proposed modelling it is necessary to compare distribution of calculated and measured hardness. It means that we calculate the full process of

induction hardening. For the cooling stage also the Flux 3D software for temperature field coupled with the modified QT steel software supported by several own numerical procedures for calculation of hardness and microstructure fields are applied.

Comparison of obtained results are collected in Table 1

TABLE 1 COMPUTED (HVc) AND MEASURED (HVm) HARDNESS DISTRIBUTION

Distance, mm	0	0.25	0.5	0.75	1	1.5	2
HVc	690	686	682	676	660	590	490
HVm	684	680	672	666	650	571	480

Quite reasonable accordance between calculations and measurements are achieved.

CONCLUSIONS

The paper deals with the mathematical modelling of induction contour hardening of gear wheels. In order to optimize the process two main evaluation criteria should be taken into account. The first of them is the criterion of uniformity of the hardened profile. But in this paper a special emphasis is put on the second criterion: the electrical efficiency of the process in comparison with classical hardening systems. In order to determine the electrical efficiency of the process: induction heating stage is considered. Numerical modelling of coupled non-linear electromagnetic and temperature fields is provided and described. In order to evaluate accuracy of the proposed approach exemplary computations are provided. Computed hardness is compared with measurements and satisfactory accordance is achieved.

REFERENCES

- [1] X. Wang, B. Li, "A carburizing-quenching Jominy curve hardness model," *Materials Letters*, vol 265, pp. 1-4, April 2020.
- [2] V. Rudnev, G. Totten, *Induction Heating and Heat Treatment*, ASM International, 4C 2014.
- [3] R. D. Yadav, A. K. Singh, "A novel magnetorheological gear profile finishing with high shape accuracy", *International Journal of Machine Tools and Manufacture*, vol. 139, pp. 75-90, April 2019.
- [4] J. Barglik, "Mathematical modelling of induction surface hardening", *COMPEL- The international journal for computation and mathematics in electrical and electronic engineering*, vol. 35, no. 4, pp. 1403 – 1417, 2016.
- [5] J. Barglik, K. Ducki, D. Kukla, J. Mizera, G. Mrówka-Nowotnik, J. Sieniawski and A. Smalcerz, "Comparison of single and consecutive dual frequency induction surface hardening of gear wheels", *IOP Conference Series: Materials Science and Engineering*, 2018
- [6] J. Barglik, *Induction Heating in Technological Processes. Issues of the Silesian University of Technology*. Gliwice 2015.
- [7] T. Shinozaki, Y. Tomota, T. Fukino and T. Suzuki, "Microstructure evolution during reverse transformation of austenite from tempered martensite in low alloy steel", *ISIJ International*, vol. 57, no. 3, pp. 740 -743, 2017.
- [8] www.altair.com/flux/ February5/2020
- [9] J. Barglik and A. Smalcerz, "Influence of the magnetic permeability on modelling of induction surface hardening", *COMPEL-The international journal for computation and mathematics in electrical and electronic engineering*, vol. 36, Issue 2, pp. 555-564, 2017.
- [10] J. Barglik, M. Czerwiński, M. Hering, M. Wesolowski, "Radiation in modelling of induction heating systems," *IOS Press Amsterdam, Berlin, Oxford, Tokyo, Washington DC*, pp. 202-211, 2008.
- [11] Barglik, A. Smalcerz, A. Smagór and G. Kopeć, "Experimental Stand for Investigation of Induction Hardening of Steel Elements", *Metalurgija*, vol. 57, no. 4, pp. 341-344, 2018

Welding of Carbon Fibers Composite by Induction Heating

WASSELYNCK Guillaume
IREENA

University of Nantes
Saint-Nazaire, France
guillaume.wasselynck@univ-nantes.fr

BUI Huu-Kien
IREENA

University of Nantes
Saint-Nazaire, France
huu-kien.bui@univ-nantes.fr

PIERQUIN Antoine
IREENA

University of Nantes
Saint-Nazaire, France
antoine.pierquin@univ-nantes.fr

TRICHET Didier
IREENA

University of Nantes
Saint-Nazaire, France
didier.trichet@univ-nantes.fr

BERTHIAU Gérard
IREENA

University of Nantes
Saint-Nazaire, France
gerard.berthiau@univ-nantes.fr

KANE Banda
IREENA

University of Nantes
Saint-Nazaire, France
banda.kane@univ-nantes.fr

FOULADGAR Javad
IREENA

University of Nantes
Saint-Nazaire, France
javad.fouladgar@univ-nantes.fr

BA Abdoulaye
IREENA

University of Nantes
Saint-Nazaire, France
abdoulaye.ba@univ-nantes.fr

Abstract—This paper presents works done by IREENA laboratory on induction heating of composite material. These works are based on characterisation of electrical properties and modelling of process.

Keywords—Carbon Fibre Reinforced Polymer Composite, Characterisation, Modelling, Welding, Induction Heating

I. INTRODUCTION

Before composite material, the shape of a piece was designed according the mechanical strength of the material and mechanical solicitation. Composite material allows to design the material according the wanted shape and mechanical constraint. Composite material is pileup of several layers, in each layer carbon fibres are in the same direction and hold together by thermoplastic matrix. The relative orientation of each layers is defined according mechanical constraints. This configuration leads to a lighter weight for the same mechanical performance.

However, composite production is only 1% of metal production. To grow up this production, it is necessary to find new technological approach to improve the duration, the energetic consumption and the cost of assembly. For 20 years, IREENA laboratory works on solutions using induction heating. Indeed, it is possible to heat by induction composite material to weld composite or apply on composite thermal-induction NDT process.

It is very challenging to determine the induced current path due to the complex nature of composite material. IREENA laboratory works on two ways to develop a tool that assists to process optimization. First way, methods of identification and characterisation of electrical properties of composite and for the second way, a software of multi-physics modelling which takes into account the physical phenomena, and equipments.

II. UNDERSTANDING OF INDUCED CURRENT PATH

Identification of electrical properties of composite begins with experimental trials and micrographic observations.

A. Induction heating with U shaped inductor

The first experimentation done was to heat by induction two kind of composite material with a U-shaped inductor. The first kind of composite, called UD, is a composite with all layer in the same direction. The second one, called QI, the layers follow the sequence [0, 45, 90, 135, 135, 90,45,0]_{2s}. Three trials was done with a frequency of 237 kHz and a current of 106A. First, UD plate was heated with fibres along the inductor-axis, an elevation of temperature of 12°C was observed. Second test, the UD plate was oriented in perpendicular direction, no elevation of temperature was detected. Third one, the QI plate was heated with an elevation of several hundred degrees in few seconds.

The first and second tests show the anisotropic behaviour of composite plates. The third one shows the strong impact of the layers' orientation on circulation of current.

B. Micrographic observation

From micrographic observation [1], it is observed that fibres are random position in the layer, fibres are not straight but wavy which allow electrical contact between fibres in one layer and in interface between layers.

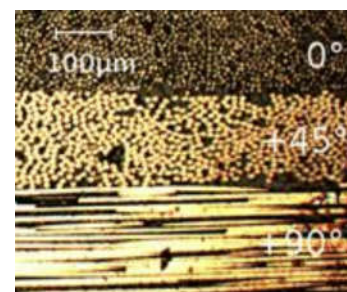


Fig. 1. Micrographic observation

C. Voltammetric trial

The last set of trial is voltammetric to determine the tensor of conductivity of one layer. It is not possible to work one a

single layer due to problem of electrical contact. It is why, UD composite as used. Due to the random distribution of fibres, several samples was tested. Results are shown in Table 1.

The high anisotropic behaviour of composite is confirmed with the conductivity along fibres' orientation σ_{\parallel} and in transverse direction. However, the conductivity in transverse σ_{\perp} and thickness σ_t is not equal. Even if, analyse of microscopic shows uniform distribution of fibres in both directions. The measurement of conductivity along thickness for QI composite reveals specific phenomena in interface between layers and the effect of layers' orientation in global behaviour of composite.

	Conductivity (S.m ⁻¹)			
	UD σ_{\parallel}	UD σ_{\perp}	UD σ_t	QI σ_t
Measures	35062±872	7.29±0.52	1.46±0.21	2.56±0.42
Model	34724±0.37	7.27±0.06	1.28±0.08	3.07±0.26

TABLE I. CONDUCTIVITIES TENSOR

D. Homogenisation procedure

Diameters of fibres are closed to 7 μ m, thickness of one layer is nearly 160-180 μ m and a composite piece can reach several meters. This scale factor leads the necessity of a homogenisation procedure to be able to simulate the magnetic and thermal behaviour of composite. To homogenise, the material is divided in Representative Elementary Volume REV. Voltammetric trial are performed on REV to estimate the conductivity along the three directions. Due to the random distribution of fibres, a statistical analysis is done to assure the results. In our procedure, a virtual material is generated to obtain REV of one layer or with interface between two layers[2], as shown Fig. 2. A comparison between our simulated results and experimental ones is shown Table 1. The good concordance between them show our capacity to simulate the good behaviour of current path in composite. Use generation virtual material allow to study impact of each parameters. More details of homogenisation procedure are given in paper [2].

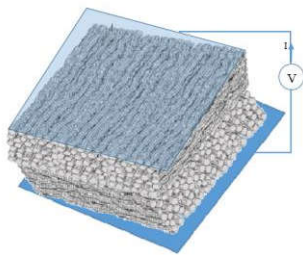


Fig. 2. Voltammetric trial on virtual material.

Inductance and capacitive effects are negligible compared to electrical contact for frequencies lower than 1GHz [1].

III. MULTI-PHYSICS MODELING

After identify the tensor of conductivity of one layer and the interface phenomena between layers, modelling of induction heating of composite can be done using Finite Elements [3]. Solving electromagnetic EM problem allow to calculate EM power density which is the source term for thermal simulation. The modelling constraints are: 1. Anisotropic and layers' orientation which lead 3D model. 2.

dependency of electrical conductivity at temperature which lead a coupling between electromagnetic and thermal phenomena. 3. Thin layer which lead use of hexahedron or degenerated element to avoid mesh deformation sensitivity [4]. 4. Reaction between load and inductor which lead to use surface impedance on inductor parts [5-6]. Moreover, surface's impedances allow to reduce time consumption. 5. Movement of inductor leads to use regular mesh to avoid interpolation. 6. To finish, to apply an optimization procedure, time consumption has to be reduced. Details to consider interface phenomena in model are given in paper [2].

IV. APPLICATIONS

Induction heating of composite can be used for welding airplane structure or NDT process. The welding of composite is briefly presented in this paper. To build the structure of airplane with composite, constructor affix omega reinforcement on large plate. To weld the two part, temperature in interface has to be reached 400°C during few seconds. Fig. 2 show the demonstrator of dynamic welding of composite. In recent development, chemicophysical model is added to magneto-thermal model to estimate the level of crystallisation of composite.

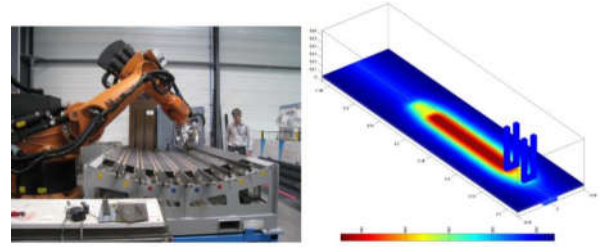


Fig. 3. Dynamic welding of composite

V. CONCLUSION

In this paper, an overview of IREENA's work on induction heating of carbon composite was done. The studies on identification and modelling allow to develop a tool of optimization of heating process. The future work will focus on application of model order reduction to improve time consumption and join works on welding and NDT to be able to ensure quality of the joint at the end of welding.

REFERENCES

- [1] G. Wasselynck, D. Trichet, J. Fouladagar, "Determination of electrical conductivity tensor of CFRP using a 3D percolation model", IEEE Transactions on Magnetics, 49(5) : 1825-1828, may 2013.
- [2] B. Kane, A. Pierquin, G. Wasselynck and D. Trichet, "Coupled Numerical and Experimental Identification of Geometrical Parameters for Predicting the Electrical Conductivity of CFRP Layers", IEEE Transactions on Magnetics 56 (2), January 2020
- [3] O. Biró, "Edge element formulations of eddy current problems," Computer Methods in Applied Mechanics and Engineering, vol. 169, no. 3-4, pp. 391-405)
- [4] H.K. Bui, G. Wasselynck, D. Trichet, G. Berthiau, "Degenerated hexahedral Whitney elements for electromagnetic fields computation in multi-layer anisotropic thin regions", IEEE Transactions on Magnetics, 52(3), march 2016
- [5] H.K. Bui, A. Ba, G. Berthiau, D. Trichet, "Fast 3D simulation of various applications of induction heating", IOP Conference Series: Materials Science and Engineering, vol. 424, no. 1, 2018..
- [6] A. Desmoort, Z. De Grève, P. Dular, C. Geuzaine and O. Deblecker, "Surface Impedance Boundary Condition With Circuit Coupling for the 3-D Finite-Element Modeling of Wireless Power Transfer," IEEE Transactions on Magnetics, vol. 53, 2017.

Tailored Heating Of Billets For Hot Forming Using An Induction Heating Approach

Martin Ennen
Institute of Electrotechnology
Leibniz University Hanover
 Hanover, Germany
 ennen@etp.uni-hannover.de

Egbert Baake
Institute of Electrotechnology
Leibniz University Hanover
 Hanover, Germany
 baake@etp.uni-hannover.de

Igor Niedzwiecki
Institute of Electrotechnology
Leibniz University Hanover
 Hanover, Germany
 niedzwiecki.igor@googlemail.com

Abstract— This paper deals with an induction heating approach in order to realize a tailored heating of round billets for hot forming processes. In particular, this work examines the limits in which tailor-made temperature profiles can be achieved in the billet. In this way, a flow stress distribution based on the temperature field in the material can be set in a targeted manner, which is decisive for forming processes. The peculiarity of the tailored heating approach is that, in contrast to partial heating, where only partial areas are heated, the entire component is heated to the target.

Keywords—induction heating, tailored temperature profiles, optimization, numerical simulation

I. INTRODUCTION

The massive forming can be divided into various forming processes. A classification of the methods can be made among other things according to the process temperature. Thus, a forming process in a temperature range up to 500 °C referred to “cold massive forming”, above as a “warm forging” and finally in a temperature range between 1000 °C and 1300 °C as “hot massive forming” [1]. The latter is characterized by a low power and energy requirement during forming. Due to the high temperature of the workpiece, the flow stress is significantly reduced in the material and thus yields to a high formability. Usually, forging is used with a homogeneous temperature distribution in the billet. Inhomogeneities in the temperature distribution and the resulting different flow stresses usually lead to a lower or defective component quality (e.g. wrinkles). The main type of heating used in die forging parts is induction heating. However, small and medium-sized enterprises in particular also use conduction heating or heating by direct flame impingement with natural gas. Within a preliminary study, a first investigation of the influence of an inhomogeneous temperature distribution on deformation processes “flattening” and “upsetting” was investigated using FEM simulations. Therefore, cylindrical and rectangular blank sections were considered. In the FEM software FORGE3, a temperature profile was assigned to the billets and after a short compensation time the respective forming process was carried out (see Fig. 1).

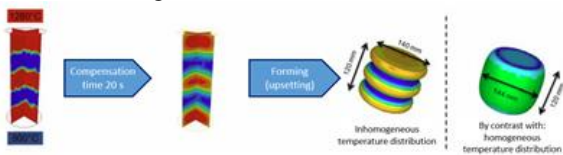


Fig. 1. Result of the preliminary study using inhomogeneous temperature distributions for forming (upsetting).

From this fact, the idea for the research project can be deduced: The targeted use of an inhomogeneous temperature distribution enables the possibility to produce suitable and

complex preforms without special forming aggregates (e.g. cross wedge rolling) or to achieve a better forming behaviour in the billet due to the tailored flow stress. In this paper it will be shown how to design an induction coil using a numerical optimization method. The numerical optimized induction coil can be used to generate different hot zones in the workpiece respectively with through heating of each zone. Measurements on the real inductor and the comparison between simulation data and measured data, conclude this paper.

II. TEMPERATURE PROFILE TO BE ACHIEVED

As described in the previous chapter, there was a preliminary study investigating the forming behaviour of a cylindrical workpiece with different hot zones. In addition, within the research of [2], an inductor was designed that allows zone-wise heating with a through heated core in each zone.

In order to facilitate the comparability of the achieved temperature profiles, an axial target temperature profile is given, which has been deduced from the results of the above-mentioned research work. Fig. 2 shows the idealized target temperature distribution together with the geometrical dimensions. The tolerance range of the respective zone is highlighted and is 1250 °C ± 30 K for a “hot zone” and 950 °C ± 30 K for a “cold zone”.

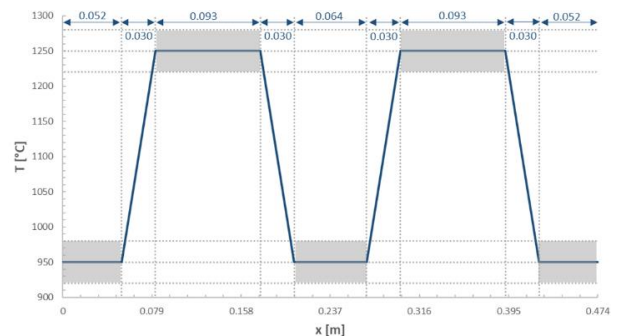


Fig. 2. Temperature profile with dimensions deduced from the investigation of [2] showing three coldzones and two hotzones.

Within the scope of the investigations, common geometries of forging billets (round and squared with different diameters) and different steels (1.4301 – stainless steel, 1.7225 – 42CrMo4 steel and 1.0503 – C45 steel) are examined.

III. FEM-SIMULATION AND OPTIMIZATION

For the investigation and design of the induction coil, suitable numerical FEM models and solution algorithms for

the electromagnetic-thermal problem are developed using ANSYS® 19.0. In order to keep the calculation time as efficient as possible, symmetries of the geometry are used. The arrangement of the round billet can thus be reduced to a rotationally symmetrical 2D model. Fig. 3. below shows a quarter of the real arrangement after a symmetrical expansion (180 ° rotation around z-axis).

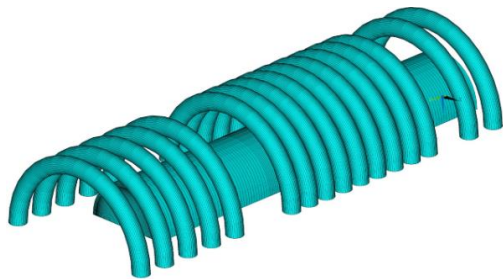


Fig. 3. FEM model of the round billet showing the quarter of the whole arrangement.

The arrangement for the rectangular billet is implemented as a 3D model and reduced to one eighth of the full model using suitable electromagnetic and thermal boundary conditions. Fig. 4. shows a quarter of the real arrangement after symmetrical expansion (Reflection about xy-plane).

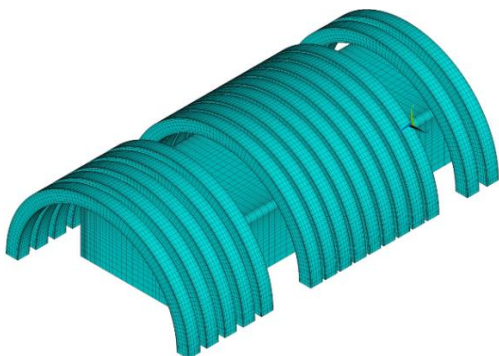


Fig. 4. FEM model of the squared billet showing the quarter of the whole arrangement.

The inductor in both models is represented by a series of individual short-circuit rings. A separate current flow can be fed to each turn. By specifying the same current in each turn, this corresponds to a stranded coil or a single inductor. Furthermore, all of the workpiece's temperature dependent electromagnetic and thermal material properties which are relevant for the heating process are taken into account. Especially the field strength-dependent magnetic permeability is also taken into account for the ferromagnetic 1.0503 - C45 steel due to its significant influence on the heating behaviour.

To set the three dimensional temperature profile according to Fig. 2 for the respective geometries, the number of turns in each zone and their spacing from one another can be varied with the aim to achieve the sharpest possible separation or the highest possible temperature gradient between the respective through heated zones. Due to the complex problem in the generation of the temperature profile with regard to the dependence on geometric and electrical parameters and also the heating time, the simulation models are designed so that an interface to an optimization algorithm is given. This ensures an efficient way to get the best possible result as

quickly as possible. The exact operation mode of the optimization algorithm is described in [3].

IV. PRELIMINARY RESULTS FROM SIMULATION AND MEASUREMENT

An inductor geometry was designed and constructed for tailored heating of round billets with a diameter of 50 mm. Heating experiments have been carried out using the manufactured inductor prototype based on the simulation results. On the one hand, the inductor current and its frequency and on the other hand the surface temperature (using a thermographic camera) and five core temperatures (using a thermocouple) in different zones were measured. The measured electrical values were transferred to the simulation model and the temperature distribution was numerically calculated. Figure 5 below shows the comparison between measured temperature values and the simulated temperature distribution.

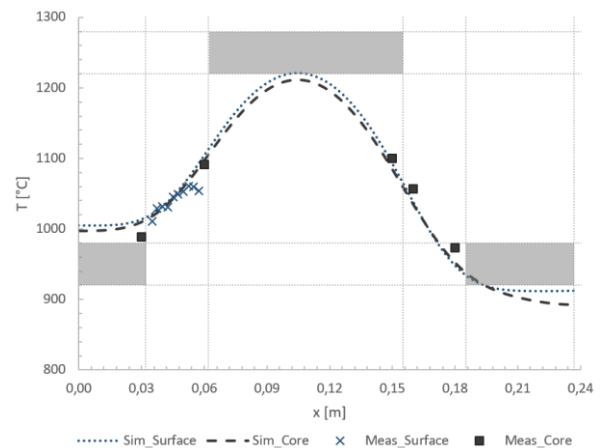


Fig. 5. Comparison between the simulated temperature profile of the round billet and the measured data.

The measured values show a very good coincidence with the simulated temperature profile. The model for ferromagnetic steels has thus been successfully validated.

In addition to the detailed description of the simulations and the validation measurements, the conference paper also describes the ongoing parameter studies with regard to the maximum adjustable temperature gradients for both applications.

ACKNOWLEDGMENT

The IGF-project 19511 N "Tailored Heating" of the AiF was supported by German Federation of Industrial Research Associations (AiF) in the frame of the Industrial Collective Research program (IGF) from Federal Ministry for Economic Affairs and Energy.

REFERENCES

- [1] F. Severin, Was ist Massivumformung.08/2014. S.1.
- [2] M. Baldan, T. Steinberg, E. Baake, "Optimal design of inductor addressed to a tailored heating forging process", International Journal Microstructure and Material Properties, Vol. 13, Nos. 1/2, 2018
- [3] M. Schulze and E. Baake, "Tailored heating of forging billets using induction and conduction heating approaches", COMPEL - The international journal for computation and mathematics in electrical and electronic engineering, Vol. ahead-of-print No. ahead-of-print

Influence of Double-Frequency Lorentz Force Component in modelling Electromagnetic Stirring of Molten Metals

Mattia Guglielmi
Institute of Electrotechnology
Leibniz University Hannover
Hannover, Germany
guglielmi@etp.uni-hannover.de

Marco Baldan
Institute of Electrotechnology
Leibniz University Hannover
Hannover, Germany
baldan@etp.uni-hannover.de

Egbert Baake
Institute of Electrotechnology
Leibniz University Hannover
Hannover, Germany
baake@etp.uni-hannover.de

Martin Schulze
Institute of Electrotechnology
Leibniz University Hannover
Hannover, Germany
schulze@etp.uni-hannover.de

Abstract—Electromagnetic stirring (EMS) is nowadays widely applied in continuous casting of metals, in order to increase the quality of the solidified cast. Therefore, an accurate investigation of the stirring effect represents a matter of great interest. Numerical simulations normally calculate only the average Lorentz force distribution inside the molten metal, which plays the major role in the final velocity field generation. Double-frequency component of the force is then neglected, and the real Lorentz force is approximated. In this paper, the stirring effect under the influence of the real Lorentz force distribution is investigated: both average and double-frequency components are calculated, and the resulting flow field inside the melt is analysed. Numerical simulations are experimentally validated with the use of GaInSn melt and UDV probe.

Keywords—electromagnetic stirring, Lorentz force, GaInSn melt, coupled simulation

I. INTRODUCTION

Electromagnetic stirring (EMS) plays nowadays a fundamental role in the continuous casting of metals, since it allows to strongly increase the mechanical properties of the final cast. Increasing interest on the stirring process over the last decades made electromagnetic stirring an attractive matter of study, due to its widely spread applications in the industry of continuous casting. Travelling magnetic field (TMF) represents in some cases an attractive solution to achieve intense stirring within the molten metal [1]: multiphase power supply induces a distribution of the Lorentz forces whose peak shifts over the time according to the phase sequence itself; a unique toroidal vortex is therefore generated inside the melt. The dimension of the vortex corresponds to the global length of the inductor. Direct measurements on the stirring effects, though, still remains a strong limit in the investigation of the process; therefore, numerical simulations represent powerful tools to achieve a global overview of the process, both from the electromagnetic point of view, and the hydrodynamic one. Furthermore, they allow to easily investigate any variation in the stirring setup: geometry of the setup and its electrical parameters (e.g. working frequency and magnitude of the current supplied to the inductor) play a fundamental role in the mixing of metal, in terms of velocity magnitude and flow field distribution. In order to investigate the electromagnetic stirring effect, coupled electromagnetic (EM) and hydrodynamic (HD) simulations are realized: Lorentz force distribution, generated by the inductor within the melt, is the

input for a subsequent calculation of the melt velocity field. Normally, only the average component of the Lorentz force is calculated, since it has the main influence on the distribution of the flow field. Double-frequency component of the force is commonly neglected, since it plays a minor role in the stirring effect at the main frequency: mechanical inertia of the melt is too high to follow the variation of the Lorentz force double-frequency component. The aim of this paper consists in investigating the effect of the double-frequency Lorentz force on the stirring process, for a range of frequencies lower than the main one ($f < 50$ Hz). Two numerical simulations of the stirring effect are carried out on the same setup: the former simulates the electromagnetic stirring effect under the influence of the averaged Lorentz force only; the latter calculates the real distribution of the Lorentz force (sum of the average and double-frequency components) to simulate the stirring effect. Flow field within the molten metal is qualitatively and quantitatively compared in the two cases. Numerical simulations are finally validated through experimental activities: instantaneous velocity of the flow is measured along the crucible axis. The investigated setup consists on a laboratory-scale, cylindrical vessel, containing Galinstan and velocity of the flow is practically measured thanks to a UDV probe, fixed on the same axis direction.

II. EXPERIMENTAL SETUP AND SIMULATION STRATEGY

A. Experimental setup

The experimental setup consists of a cylindrical vessel containing GaInSn, an eutectic alloy, already molten at the ambient temperature. Thanks to its properties (Tab. 1), GaInSn melt has been widely applied in the experimental investigation of electromagnetic stirring [2]: its low-melting point allows direct measurement of the flow field generated inside of it. The vessel, made of plexiglass, is 240 mm long and has a radius of 31 mm. The vessel is surrounded by a cylindrical, 6-turns copper inductor, with a radius of 61 mm. Three-phase power is supplied to the inductor and each phase consists therefore of two turns: phase sequence starts from the bottom, with phase A, and goes to the top, with a final phase C. Current supplied to each phase of the inductor has the same magnitude of $I_{\text{rms}} = 200$ A, and it is shifted by 120 electrical

Ga 68%, In 20 %, Sn 12 %		
Parameter	Notation	Value
Density, kg/m ³	ρ	6440
Dynamic viscosity, Pa·s	μ	0.0024
Thermal conductivity, W/(m·K)	λ	16.5
Melting temperature, °C	T	- 19
Electric conductivity, S/m	σ	$3.46 \cdot 10^6$

Tab. 1 Properities of GaInSn melt at ambient temperature (20 °C)

degrees between subsequent phases. Working frequency represent the only electrical parameter of the investigation: frequency values of $f = [2, 5, 10, 15, 25, 50]$ Hz are selected to investigate the stirring effect within the molten metal. In the experimental activity, velocity of the flow is measured along the axis of the melt volume with the help of a Ultrasound Doppler Velocity meter (UDV). This probe allows to achieve velocity distribution along the crucible axis with a sampling time of 300 ms, to be compared with the instantaneous velocity calculated in the related numerical simulation.

B. Simulation Strategy

The numerical FEM model is based on coupled EM and HD simulation: electromagnetic results are carried out with ANSYS Mechanical APDL, while the hydrodynamic simulation is performed with ANSYS Fluent. A 2D-axisymmetric model is realized, and two different approaches are chosen to carry the simulations out: the former EM solution is harmonic and calculates only the average Lorentz force distribution within the melt; double-frequency component of the force is therefore neglected. The latter performs a time-dependent EM solution, and real force distribution is calculated with a step of 12 electrical degrees. Both EM simulations are subsequently coupled with a time-dependent HD simulation. In this last case, k- ϵ model is applied, since the flow is supposed to be fully turbulent. Free surface of melt is fixed, since magnitude of the force density is low enough to produce no significant variation in the surface shape. Flow field distribution over time is plotted in the two cases, and velocity magnitude along the axis is calculated. Maximum velocity of the flow is finally analysed within the entire melt volume. Total HD simulation time is 25 s, since it represents a correct compromise between computational cost of the simulation and steady-state FD regime of the flow.

C. Lorentz force calculation in the two simulation cases

Lorentz force that emerges from inside the melt upon the application of an alternated magnetic field is expressed as

$$\vec{f}_{em} = \vec{j} \times \vec{B}, \quad (1)$$

where $\vec{j} \left(\frac{A}{m^2}\right)$ is the current density, and $\vec{B} (T)$ the magnetic induction field.

This force can be split in two components: an average component, constant over time, and a time-dependent force, oscillating with a frequency equal to the double of the main Velocity field within the molten metal, generated by the TMF: on the left, velocity isovalues within the melt in m/s;

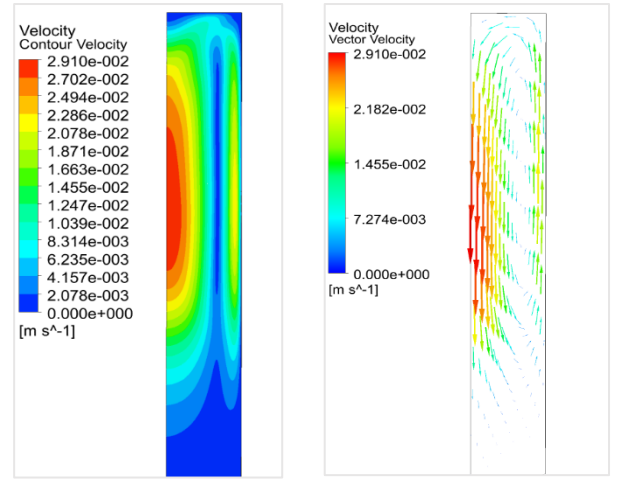


Fig. 1. Velocity field distribution within the molten metal, at the working frequency of $f = 15$ Hz. On the left, velocity isovalues in m/s; on the right, vector velocity field in m/s. Travelling Magnetic Field generates a unique toroidal vortex inside the melt.

on the right, the related vector field in m/s. Working frequency is $f = 15$ Hz.

In the hypothesis of harmonic regime, current density and magnetic induction field can be written in the following way:

$$\vec{J}(t) = \sqrt{2} \cdot J \cdot \sin(\omega t + \gamma), \quad (2)$$

$$\vec{B}(t) = \sqrt{2} \cdot B \cdot \sin(\omega t + \beta), \quad (3)$$

with J, B – RMS values of the current density and magnetic induction field, γ, β – initial phase of the current density and the magnetic induction field respectively.

In this way, average component of the force can be explicated as

$$\vec{f}_{em, avg} = 0.5 \cdot J \cdot B \cdot \cos(\gamma - \beta), \quad (4)$$

while double-frequency oscillating component

$$\vec{f}_{em, 2\omega} = 0.5 \cdot J \cdot B \cdot \cos(2\omega t + \gamma + \beta). \quad (5)$$

III. PRELIMINARY RESULTS

Preliminary analysis in the two simulation cases evidences the same qualitative distribution of the velocity field: a unique, toroidal vortex is generated in both cases (see Fig. 1), for all of the frequency values in the considered frequency range. Maximum velocity of the flow, though, is expected to be higher when double frequency component of the force is implemented; difference between the two simulations is expected to be more evident for lower frequency values.

REFERENCES

- [1] D. Musaeva, E. Baake, A. Köppen and P. Vontobel, “Application of Neutron Radiography for In-Situ Visualization of Gallium Solidification in Travelling Magnetic Field” *Magnetohydrodynamics*, vol. 53 (2017), No. 3, pp. 583–593.
- [2] D. Musaeva, V. Ilyin, V. Geza, E. Baake, “Experimental investigation of low-frequency pulsed Lorentz force influence on the motion of Galinstan melt” *St. Petersburg Polytechnical University Journal: Physics and Mathematics*, 000 (2016), pp. 1–8

Liquid metal flow generating by unsymmetric traveling magnetic field

Igor Sokolov¹, Evgeniy Shvydkiy¹, Gennadiy Losev², Ilya Kolesnichenko² and Vasiliy Frizen¹

¹Ural Federal University, Department of Electric Engineering and Electrotechnology Systems, Yekaterinburg 62002, Russian Federation

²Institute of Continuous Media Mechanics of the Ural Branch of Russian Academy of Science, Perm, Russian Federation
i.v.sokolov@urfu.ru

Abstract—The object of present work is a investigation of inductor currents parameters influence on a liquid metal flow. The investigation was carried out using the finite element method. Verification was performed using experimental data.

The aim of this work is to obtain the flow dependence on the asymmetry coefficient of the three-phase currents, which will predict the flows of liquid metal in the cell at a significant asymmetry of the windings or current source.

Index Terms—Finite element analysis, Electromagnetic forces, Magneto hydrodynamics, Gallium alloys.

I. INTRODUCTION

Electromagnetic stirring is widely applied technique in modern industry, successfully used in casting of ferrous and non-ferrous alloys [1], because it can help to enhance heat and mass transfer in liquid metals. That phenomenon promotes grain refinement, avoiding segregation and consequently increases mechanical properties of casting production.

The source of the magnetic field for this type of application is a travelling magnetic field inductor. However, this type of electromagnetic device is often cause asymmetry of supply currents as shown in work [2]. This asymmetry can result in nonuniform Lorentz forces a more complex flow pattern. This phenomenon is insufficiently investigated, in this article it is suggested to study more closely and to consider at the influence of phase shift and current magnitude on the flow pattern. So we want to investigate hypothesis that asymmetrical inductor currents cause ununiform forces in the melt, resulting in more unstable flows that can improve heat transfer.

Thus, the goal of research is to investigate a wide range of asymmetry coefficients and determine the character of instability.

II. EXPERIMENTAL SETUP

The investigated installation is shown at Figure 1. The source of TMF is a linear induction machine consists of 6 coils that are supplied by a controllable 3-phase source Pacific Smart Source 360 ASX-UPC3. The magnetic flux is going through the magnetic core and penetrates into the GaSnZn alloy. The frequency of the supply current is 50 Hz. Induced current density occurs into metal under the influence of TMF.

The work of Institute of Continuous Media Mechanics team is supported by the RFBR grant 17-48-590539_r_a and the work of Ural Federal University team is supported by the RFBR grant 19-38-90236

The product of this current and magnetic flux is the Lorentz forces. That forces impacts on a GaSnZn volume and lead to move a liquid part of metal. The description of setup in more detail is given in [3].

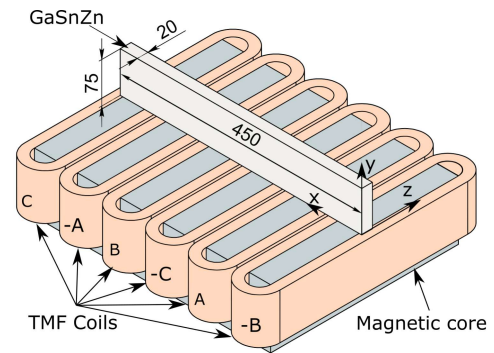


Fig. 1. Experimental setup.

III. METHODS

3D numerical calculations were carried out by the finite element method using the Comsol Multiphysics software.

Under the assumption of low magnetic Reynolds number ($Re_m = 0.065$), induction-free approximation was used, therefore, it is possible to divide the calculation into two parts, taking into account the rigid body approximation, electromagnetic and hydrodynamic, the forces from the first stage are transferred into second:

At the first stage for electromagnetic calculations we used the Maxwell equations, which were formulated in terms of the magnetic vector potential. The calculations of the magnetic field, induced current and Lorentz force distribution were made with the use of the Magnetic Fields interface.

Analysis of magnetic saturation showed that the magnetic core saturates at 25 A and more [4]. Therefore, the magnetic permeability was specified by a constant $\mu = 150$. The coil was a homogenized multi-turn coil, whose winding consisted of 170 turns of copper wire. To validate numerical results the magnetic flux density was measured by Hall effect sensor above the linear induction motor surface. The electromagnetic force acting on a liquid metal was calculated as $\mathbf{f}_{EM} = \mathbf{J} \times \mathbf{B}$, where \mathbf{B} is the magnetic flux density and \mathbf{J} is the induced current density.

Supply currents are described using the method of symmetrical components, taking into account the following assumptions:

$$\begin{cases} \mathbf{I}_a = \mathbf{I}_{a1} + \mathbf{I}_{a2} + \mathbf{I}_{a0} \\ \mathbf{I}_b = \alpha^2 \mathbf{I}_{a1} + \alpha \mathbf{I}_{a2} + \mathbf{I}_{a0} \\ \mathbf{I}_c = \alpha \mathbf{I}_{a1} + \alpha^2 \mathbf{I}_{a2} + \mathbf{I}_{a0} \end{cases} \quad (1)$$

$$\mathbf{I}_a = \mathbf{I}_{a0} + \mathbf{I}_{a1} + \mathbf{I}_{a2} = const, \frac{\mathbf{I}_{a2}}{\mathbf{I}_{a1}} = var, \frac{\mathbf{I}_{a0}}{\mathbf{I}_{a1}} = var \quad (2)$$

where \mathbf{I}_a , \mathbf{I}_b , \mathbf{I}_c is the phase currents respectively, \mathbf{I}_{a0} is the zero sequence current, \mathbf{I}_{a1} is the positive sequence current, \mathbf{I}_{a2} is the negative sequence current and α is the phasor rotation operator equal $e^{\frac{2}{3}\pi i}$

At the second stage the calculation of hydrodynamics was carried out by Navier-Stokes equations, using k- ϵ turbulence model, walls are considered as no-slip condition, top surface was set as slip. The low melting point Ga based alloy was used as a working fluid, its temperature-dependent properties within the range of 323 to 823 K [5] are listed in the Table I.

TABLE I
PHYSICAL PROPERTIES LIQUID GAsNZn

Property	Value	Unit
Conductivity	$3560000-4130 \cdot T+2.82 \cdot T^2$	$S \cdot m^{-1}$
Density	$6332-0.610 \cdot T$	kg/m^3
Surface tension	$0.71648-0.074 \cdot 10^{-3} \cdot T$	N^{-1}
Dynamic viscosity	$0.000376 \cdot \exp(3824.3/(8.314 \cdot T))$	$Pa \cdot s$

IV. RESULTS

Figures 2-3 show the results obtained for the symmetric case (a) and for the case $I_{a2}/I_{a1} = 0.5$ (b). As can be seen, asymmetric distribution of currents in a windings lead to distortion of the magnetic field, which causes flow fluctuations. Further consideration of the conditions of instability occurrence can help to control the flows.

As a result the dependence of current asymmetry parameter on intensity of flow and pattern is obtained.

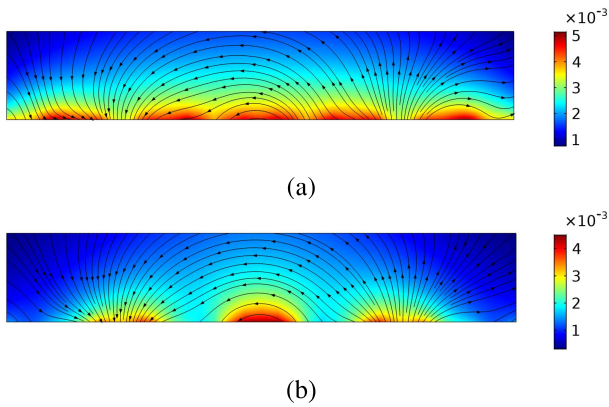


Fig. 2. Distribution of magnetic flux density (T) at symmetrical power supply (a) and $I_{a2}/I_{a1} = 0.5$ (b)

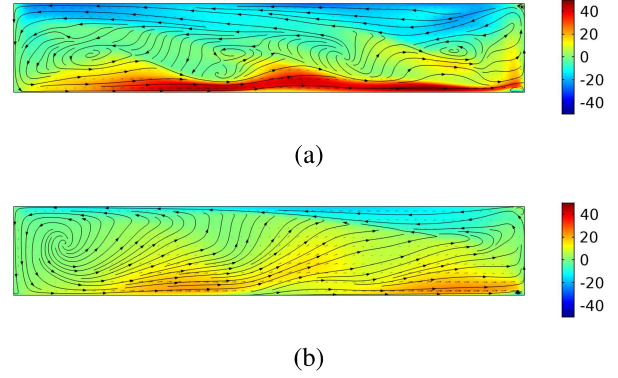


Fig. 3. Instantaneous velocity (mm/s) at symmetrical power supply (a) and $I_{a2}/I_{a1} = 0.5$ (b)

REFERENCES

- [1] C. Liu, "Refined Model Development and Performance Assessment of a Linear Induction-Type Electromagnetic Stirrer," *IEEE Trans. Magn.*, vol. 46, no. 10, pp. 3724-3730, Oct.2010.
- [2] I. Sokolov, E. Shvydkiy, G. Losev, K. Bolotin, and S. Bychkov, "The influence of traveling magnetic field inductor asymmetric power supply on the liquid metal flow," *IOP Conf. Ser. Mater. Sci. Eng.*, vol. 581, p. 012002, Jul. 2019.
- [3] G. Losev and I. Kolesnichenko "Solidification front shape control through modulating the traveling magnetic field," *Journal of Crystal Growth.*, vol. 528, pp. 125249, 2019.
- [4] E. Shvydkiy and I. Kolesnichenko "3D numerical simulation of the linear induction motor, considering magnetic saturation," *Proc. of 2018 IEEE Conf. of Russian Young Researchers in Electrical and Electronic Engineering (EIConRus)*, DOI: 10.1109/EIConRus.2018.8317206, 2018.
- [5] A. Dobosz, Y. Plevachuk, V. Sklyarchuk, B. Sokoliuk, and T. Gancarz, "Thermophysical properties of the liquid Ga-Sn-Zn eutectic alloy," *Fluid Phase Equilib.*, vol. 465, pp. 1-9, Jun. 2018.

Melt Electrovortex Flow in DC EAF Model with Two Bottom Electrodes in Axial Magnetic Field

Sergejs Pavlovs
Institute of Numerical Modelling
University of Latvia
Riga, Latvia
sergejs.pavlovs@lu.lv

Andris Jakovics
Institute of Numerical Modelling
University of Latvia
Riga, Latvia
andris.jakovics@lu.lv

Alexander Chudnovsky
JSC LATVO
Riga, Latvia
eivf19@gmail.com

Abstract—Paper presents computation results for molten steel flow in truncated cone bath in Electrical Arc Furnaces (EAF) of industrial scale. EVF is driven with direct electrical current (DC), supplied over arc spot at melt mirror and two bottom non-submerged electrodes. Several cases of time-averaged flow patterns, computed with large eddy simulation (LES) model of turbulence, are discussed: i) electrovortex flow (EVF); ii) melt rotation in external magnetic field; iii) influence of geomagnetic field on EVF.

Keywords—DC EAF, EVF, melt rotation, external magnetic field, geomagnetic field, LES study.

I. INTRODUCTION

The numerical research, concerned with LES-study of melt flow patterns in metallurgical MHD devices with combined power supply by inductor and over electrodes [1], is enhanced for computations taking into account external uniform magnetic field. The aim is the estimation of influence of external magnetic field on EVF in industrial scale DC EAF.

The computation approach is verified by comparison with measurements of magnetic field [2] and EVF velocity and flow patterns [2–4] in experimental setups with two cooper electrodes, fully submerged into cylindrical or rectangle bath with *GalSn* or mercury melts.

II. COMPUTATIONAL MODEL

A schematic of DC EAF computational model is shown in Fig. 1. Melt vessel geometry and melt parameters are provided in Table I. Electrodes geometry and parameters of conductive power supply are given in Table II. Industrial scale DC EAF equipment is chosen as the prototype for numerical model. Note, that similar model (bottom electrodes are not shifted from vertical symmetry plane) is considered in [5].

III. PECULIARITIES OF NUMERICAL COMPUTATIONS

Stationary magnetic field for multi-electrode models supplied with DC as well as *Lorentz* force in liquid metal (considering external magnetic field) was computed in *ANSYS Maxwell*.

Transient hydrodynamic (HD) field in the liquid metal was computed with *ANSYS FLUENT* using LES turbulence modelling. *Reynolds* number estimates with geometric and liquid metal parameters given in Table I and computed velocity values (Fig. 2 and 3) give $Re \sim 4.8 \cdot 10^5$.

Computational mesh for the HD field has $\sim 3M$ elements with inflation at wall near bottom unsubmerged electrodes.

This work was funded by European Regional Development Fund under contract “Development of numerical modelling approaches to study complex multiphysical interactions in electromagnetic liquid metal technologies” (No. 1.1.1.1/18/A/108)

TABLE I. GEOMETRIC PARAMETERS OF THE MELT VESSEL AND MELT PROPERTIES

Melt bath (truncated cone)	
Top (melt mirror) radius	$r_{melt}^{top} = 0.9 \text{ m}$
Bottom radius	$r_{melt}^{bottom} = 0.5 \text{ m}$
Height	$H_{melt} = 0.335 \text{ m}$
Molten steel	
Electrical conductivity	$\sigma_{melt} = 1.1 \cdot 10^6 \text{ S/m}$
Density	$\rho_{melt} = 6.9 \cdot 10^3 \text{ kg/m}^3$
Dynamic viscosity (laminar)	$\eta_{melt} = 6 \cdot 10^{-3} \text{ kg/(m} \cdot \text{s)}$
Cinematic viscosity (laminar)	$\nu_{melt} = 8.7 \cdot 10^{-7} \text{ m}^2/\text{s}$

TABLE II. GEOMETRIC PARAMETERS OF ELECTRODES AND SUPPLIED DIRECT CURRENT

Top electrode	
Radius of arc spot at the melt mirror	$r_{el}^{top} = 0.14 \text{ m}$
Bottom electrodes	
Radius	$r_{el}^{bottom} = 0.0575 \text{ m}$
Distance between the axes of electrodes	$l_{el-el}^{bottom} = 0.6 \text{ m}$
Offset of the electrodes axes from symmetry plane	$l_{shift}^{bottom} = 0.1 \text{ m}$
Direct current (DC)	
Top electrode	$I_{el}^{top} = 40 \text{ kA}$
Bottom electrodes	$I_{el}^{bottom} = 20 \text{ kA}$

IV. LORENTZ FORCE FOR EVF IN EXTERNAL MAGNETIC FIELD

EVF in the melt is driven by *Lorentz* force \mathbf{f}^{self} , which is the result of interaction between electrical current \mathbf{j} and self-magnetic field \mathbf{B}^{self} :

$$\mathbf{f}^{self} = \mathbf{j} \times \mathbf{B}^{self} \quad (1)$$

Electrical current \mathbf{j} in melt interacts also with external uniform magnetic field. For chosen external magnetic field \mathbf{B}^{ext} the contribution \mathbf{f}^{ext} to *Lorentz* force is:

$$\mathbf{f}^{ext} = \mathbf{j} \times \mathbf{B}^{ext} \quad (2)$$

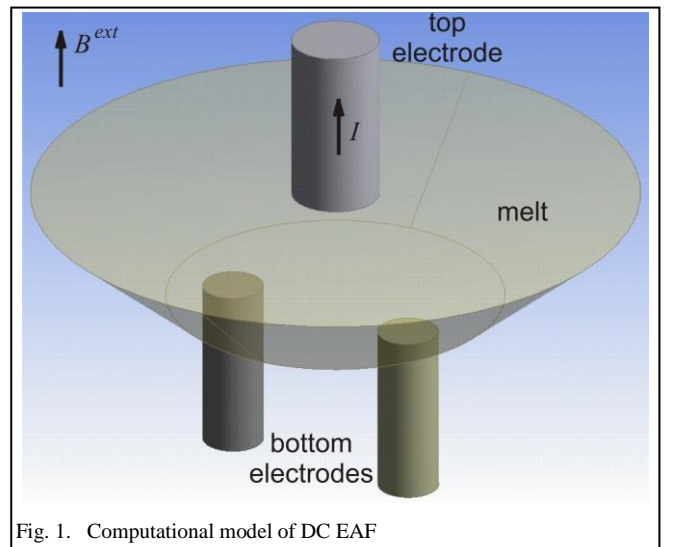


Fig. 1. Computational model of DC EAF

Total *Lorentz* force is:

$$\mathbf{f}^{total} = \mathbf{f}^{self} + \mathbf{f}^{ext} \quad (3)$$

Contribution of terms in formula (3) can be estimated by comparison of two non-dimensional numbers:

$$S = \frac{\mu_0 (i_{el}^{top})^2 H_{melt}^3}{2\pi^2 (r_{el}^{top})^3 \rho v^2}; N = \frac{i_{el}^{top} \cdot B^{ext} H_{melt}^3}{\pi (r_{el}^{top})^2 \rho v^2} \quad (4)$$

where S is parameter of EVF and N is parameter of influence of external magnetic field.

V. COMPUTATIONAL RESULTS

Computational results for the melt flow driven by various distribution of the *Lorentz* force are presented in Fig. 2 and 3, and Table III.

TABLE III. MAGNETIC FIELD, ELECTRICAL CURRENT AND *LORENTZ* FORCE IN THE MELT

Highest computed values in the melt	
Current density magnitude – $\max \mathbf{j} $	$1.07 \cdot 10^6 \text{ A/m}^2$
Self-magnetic field magnitude – $\max \mathbf{B}^{self} $	0.0581 T
External magnetic field \mathbf{B}^{ext}	
External magnetic field magnitude	$B^{ext} = 0.0575 \text{ T}$
Geomagnetic field (coordinates – Riga, Latvia)	$B^{Earth} = 0.00005 \text{ T}$
<i>Lorentz</i> force magnitude – current interaction with:	
self-magnetic field – $\max \mathbf{f}^{self} $	$7.35 \cdot 10^4 \text{ N/m}^3$
external magnetic field – $\max \mathbf{f}^{ext} $	$5.45 \cdot 10^4 \text{ N/m}^3$
geomagnetic field – $\max \mathbf{f}^{Earth} $	$5.47 \cdot 10 \text{ N/m}^3$
Total <i>Lorentz</i> force – $\max \mathbf{f}^{total} $	$8.92 \cdot 10^4 \text{ N/m}^3$

A. Structure of EVF

Maximum value of the *Lorentz* force (Table III), determined in (1), is reached in immediate proximity to the top electrode where the force distribution is almost axis-symmetrical (Fig. 3a). The velocity field is almost axis-symmetrical not only in the melt mirror zone, but also in bottom zone (Fig. 2a) despite of *Lorentz* force symmetry about each of the two bottom electrodes. Streamlines indicates dominating toroidal vortex (Fig. 3a) with jet direction from the top electrode to the bottom zone. There are also two small vortices in peripheral zone near side wall that are similar to the patterns discussed in [5, Fig. 9a] and [6, Fig. 12].

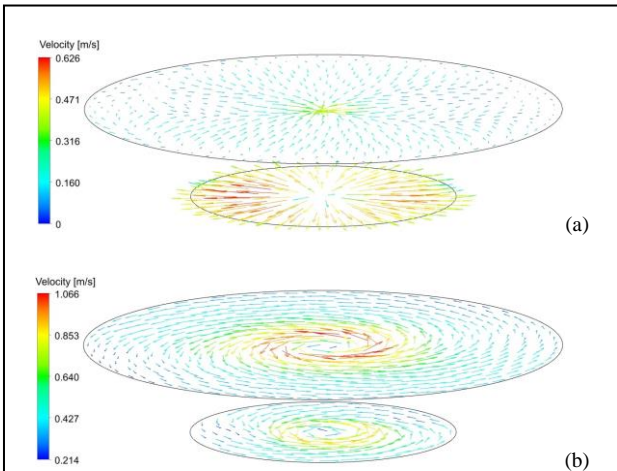


Fig. 2. Time-averaged velocity (LES, flow time 20 s) field in the horizontal cross-sections near the top ($z = 0.334 \text{ m}$) and near the bottom ($z = 0.001 \text{ m}$) surface of the melt:

a) EVF for $B^{ext} = 0$ – parameter $S \sim 2.68 \cdot 10^{11}$;
b) EVF+rotation about vertical axis for $B^{ext} = 0.0575 \text{ T}$ – parameter $N \sim 2.69 \cdot 10^{11}$

B. Melt rotation in external magnetic field

If magnetic field \mathbf{B}^{ext} is of the same order with the self-magnetic field \mathbf{B}^{self} (Table III) and $S \sim N \sim 2.7 \cdot 10^{11}$ (4), the *Lorentz* force (2) has a strong azimuthal component (Fig. 3b) that drives rotation in the melt mirror zone about the top electrode axis (Fig. 2b). The rotation is counter clock-wise in the case of external axial magnetic field with upward direction (Fig. 1).

C. Influence of geomagnetic field

The maximum value of contribution to *Lorentz* force due to interaction of electrical current with geomagnetic field $\mathbf{f}^{Earth} = \mathbf{j} \times \mathbf{B}^{Earth}$ is three orders of magnitude smaller than the result (1) of electrical current interaction with the self-magnetic field – $\max|\mathbf{f}^{Earth}| \ll \max|\mathbf{f}^{self}|$ (Table III). Similarly parameter N is three orders smaller – $N \sim 2.4 \cdot 10^8$ (compare with value in previous section B). Thus the geomagnetic field does not affect EVF in the considered DC EAF of industrial scale.

Note, that in the case when *Lorentz* force \mathbf{f}^{self} (1) is artificially “switched off” the rotation is clock-wise because geomagnetic field has downward direction.

REFERENCES

- [1] S. Pavlovs, A. Jakovics, E. Baake, and B. Nacke, “Melt flow patterns in metallurgical MHD devices with combined inductive and conductive power supply,” *Magneto hydrodynamics*, vol. 50, pp. 303–316, 2014.
- [2] A. Chudnovsky, Yu. Ivochkin, A. Jakovics, I. Teplyakov, S. Pavlov and D. Vinogradov, “Investigations of electrovortex flows with multi electrodes power supply,” *Magneto hydrodynamics*, vol. 56, pp. 487–498, 2020.
- [3] S. Pavlovs and A. Jakovics, “Comparison of experimental and numerical velocity for electrovortex flow in multi-electrode furnace”, *International Symposium on Heating by Electromagnetic Sources*, Padua, Italy, pp. 143–148, May, 2019.
- [4] S. B. Dement’ev, A. I. Chaikovskii and A. Yu. Chudnovskii, “Generation of electrovortex flows in liquid-metal baths with a multielectrode current input,” *Magneto hydrodynamics*, vol. 24, pp. 76–80, 1988.
- [5] S.A. Smirnov, V.V. Kalaev, S.M. Hekhamin, M.M. Krutyanskii, S.N. Kolgatin, and I.S. Nekhamin, “Mathematical simulation of electromagnetic stirring of liquid steel in a DC arc furnace,” *High Temperature*, vol. 48, pp. 68–76, 2010.
- [6] A. Chudnovsky, “Physical modelling of 3D melts mixing for electrometallurgical aggregates,” *Magneto hydrodynamics*, vol. 53, pp. 747–758, 2017.

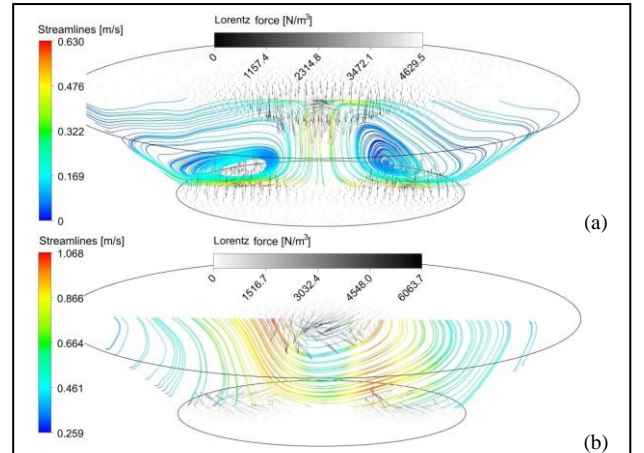


Fig. 3. Lorentz force density in the horizontal cross-sections near the top ($z = 0.334 \text{ m}$) and near the bottom ($z = 0.001 \text{ m}$) surface of the melt as well as time-averaged (LES, flow time 20 s) streamlines in the plane crossing the centers of the top and the two bottom electrodes:

a) EVF for $B^{ext} = 0$ – parameter $S \sim 2.68 \cdot 10^{11}$;
b) EVF+rotation about the vertical axis for $B^{ext} = 0.0575 \text{ T}$ – parameter $N \sim 2.69 \cdot 10^{11}$

Thermal behaviour of synthetic countertop used as cooker surface over induction hobs

Fabrizio Dughiero

Department of Industrial Engineering
Università degli Studi di Padova
Padova 35122, Italy
fabrizio.dughiero@unipd.it

Michele Forzan

Department of Industrial Engineering
Università degli Studi di Padova
Padova 35122, Italy
michele.forzan@unipd.it

Matteo Lazzarin

Department of Industrial Engineering
Università degli Studi di Padova
Padova 35122, Italy
matteo.lazzarin.4@phd.unipd.it

Abstract—In recent years, domestic induction hobs have become very popular due to their excellent performance, easy cleaning process, safety and high efficiency [1]. Currently, most induction hobs are placed inside a hole dug into the kitchen countertop. This approach, which is mandatory for traditional gas cooktops, can easily be avoided by installing the induction hob under the countertop. In fact, induction heating appliances transfer power to the pot via electromagnetic coupling and the heating of the magnetic steel bottom is achieved through the circulation of eddy currents. This way, the surface of the cooker is heated only by the pot and usually reaches relatively low temperatures. A key factor in the design of this type of solution is the choice of material for the countertop, which should have good mechanical and thermal properties in order to endure the typical temperatures reached in the cooking process. Many different materials have been taken into account, such as marble, quartz and granite [2].

In this paper, a popular material used for synthetic countertops, Corian[®] manufactured by DuPont, is proposed as a possible solution for the use of the induction cooker under the kitchen counter.

Keywords— induction hob, kitchen countertop, cooktop, induction heating, countertop material, Corian[®] solid surface

I. INTRODUCTION

Corian[®] is a brand of solid surface material developed by DuPont and is mainly composed of polymethyl methacrylate (34-45%) and aluminum trihydroxide (55-66%) [3]. Some experimental tests were conducted to characterize the behaviour of this material under the typical thermal stresses produced while cooking. The experimental set-up used for the tests comprises: a portable induction hob with a rated power of 2 kW, a pot with a top diameter of 22 cm and a bottom diameter of 18 cm and a 12 mm thick slab of white Corian[®]. A data acquisition system, composed of a digital data logger and a personal computer, recorded at regular time intervals the temperatures measured by a series of thermocouples installed in different positions along the solid surface and the pot.

II. TEST WITH BOILING WATER

Five thermocouples were installed on the upper surface of the Corian[®] slab at different distances from the pot and one additional thermocouple was fixed to its bottom. The pot was filled with 4 litres of water and placed directly onto the solid surface slab. The pot was heated up until it reached 100 °C and the water was left boiling for a total of 90 minutes before switching off the induction hob. Temperatures were measured and stored once per minute.

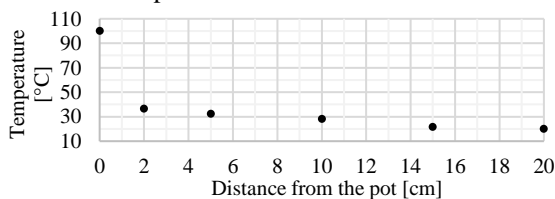


Fig. 1. Temperature of the solid surface as a function of the distance from the pot after 90 minutes of boiling.

Fig. 1 shows the temperature on the solid surface rapidly decreasing below 40 °C within the first 2 cm. Therefore, users can safely place their hands on the surface around the pot without any risk of burns.

No visible damage was found at the end of the test.

III. THERMAL SHOCK

As it emerged from simple preliminary tests, Corian[®] has a tendency to deform and yellow slightly around 160 °C. Hence, this temperature was chosen as reference for the subsequent tests.

In order to check if the solid surface could resist sudden temperature variations, the temperature of the pot was raised to 160 °C and maintained for about 41 minutes by manually controlling the power level of the induction hob. Then, the first pot was quickly switched with another pot of the same dimensions containing ice at -10 °C. Temperatures were measured and stored once per second by the data acquisition system. Fig. 2 shows a scheme of the measurement points where the thermocouples were installed, both over and below the surface of the Corian[®] slab.

As can be seen in Fig. 3, after the swap the temperature measured by the probe T/C 2 placed on the pot boundary dropped about 70 °C in 15 seconds, then dropped below 40 °C within the first minute. The material showed no cracks and the slab retained its integrity. However, permanent yellowish marks were left in correspondance to the pot bottom due to the high temperature. In addition, some bulges and asperities appeared in the area, as shown in Fig. 4.

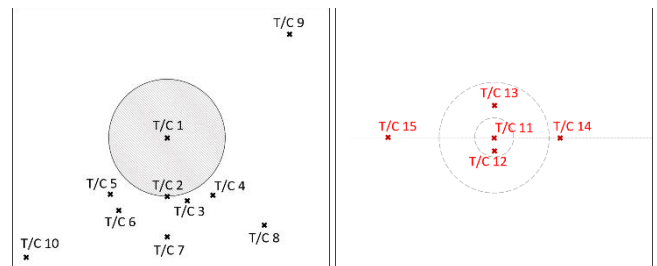


Fig. 2. Positions of the thermocouples over the surface (left) and below the surface (right).

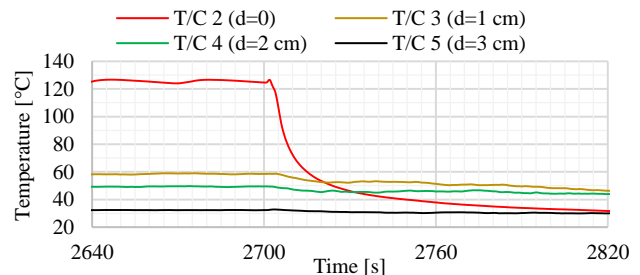


Fig. 3. Temperatures as a function of time in four measurement points over the solid surface during the temperature jump phase.

TABLE I. TEMPERATURES ON PROBE T/C 2

Time [s]	2702	2717	2732	2762
Temperature [°C]	126.540	56.959	45.336	37.444



Fig. 4. Picture of the damages left to the surface after the test (the photo has been treated to enhance the effect, otherwise inappreciable).

IV. TEST WITH A SILICONE MAT UNDER THE POT

In view of the previous results, a silicone mat with a thickness of 3 mm was interposed between the Corian[®] slab and the pot to try to prevent damages to the surface. Six thermocouples were installed inside the pot at different radial distances from the center. Six thermocouples were placed under the mat at the same radial distances. Note that, in this experiment, the positions of the thermocouples are different from those reported in Fig. 2. Table II shows the distance of each probe from the center of the pot. The test consisted of five steps. At each step, the temperature of the pot was raised to a predetermined value and maintained for a given time period. Among the thermocouples placed on the pot bottom, the one with the highest temperature reading (B5) was considered for the manual control of the temperature. This leads to much lower temperatures at the center of the pot, compared to the previous test. Table III shows the temperature values and the duration of each step. A real-time plot can be seen in Fig. 5.

TABLE II. DISTANCE OF THE PROBES FROM THE CENTER OF THE POT

N.	Bottom	B1	B2	B3	B4	B5	B6
	Mat	M7	M8	M9	M10	M11	M12
	Distance [cm]	0	2	4	6	8	9

TABLE III. TEMPERATURES AND DURATIONS OF THE STEPS

Step number	1	2	3	4	5
Temperature [°C]	160	170	180	190	200
Duration [min]	30	30	30	15	15

During the first three steps, the temperature under the silicone mat did not exceed 160 °C throughout the whole area, as can be seen in Fig. 7. When the highest temperature on the pot base exceeded 180 °C, the 160 °C threshold was surpassed below the mat.

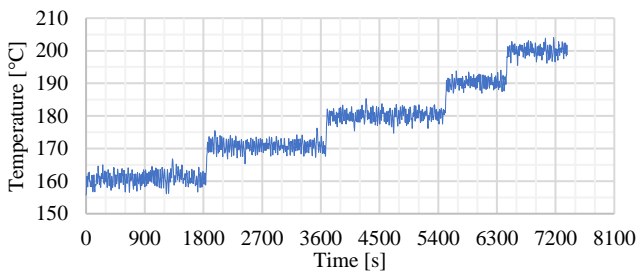


Fig. 5. Temperature on B5 as a function of time.



Fig. 6. Experimental set-up.

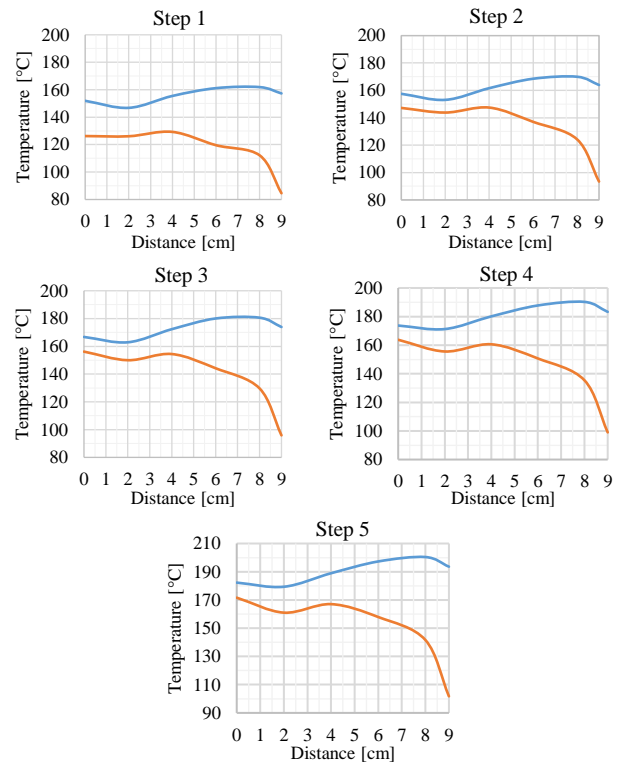


Fig. 7. Temperature as a function of the distance from the center of the pot under the silicone mat (orange line) and on the pot bottom (blue line).

V. CONCLUSION

In all the tests, the slab of Corian[®] showed good overall mechanical performances. In fact, no visible cracks were found on the cooktop after experimenting intense thermal stress. However, a problem of local deformation and yellowing emerged at around 160 °C. Thus, for high temperature preparations (i.e. frying), cooking with an insulation mat under the pot is highly recommended. A 3 mm thick silicone mat was used to correlate the temperature of the pot with the temperature on the solid surface. In order to keep the temperature on the Corian[®] slab below 160 °C, the pot should not exceed temperatures greater than 180 °C. For some recipes, like deep-fried foods, the temperatures involved can range between 175 °C and 190 °C. Hence, some kind of control is required. For example, some sensors located inside the mat could prevent the induction hob from feeding the pot when the mat is not in place or the temperature reaches dangerous values. Alternatively, one could adopt some easier solutions like a more performing insulation material, a thicker silicone mat or a raised pot equipped with supporting feet. However, none of these solutions eliminates the risk associated to user errors. If the mat is not placed or a conventional pot is used, the surface could be damaged. In addition, increasing the mat thickness lowers the power transferred to the pot and, thus, the efficiency of the system.

REFERENCES

- [1] J. Acero, J. M. Burdio, L. A. Barragan, D. Navarro, R. Alonso, J. R. Garcia, F. Monverde, P. Hernandez, S. Llorente, I. Garde, "The domestic induction heating appliance: An overview of recent research", *Twenty-Third Annual IEEE Applied Power Electronics Conference and Exposition*, Austin, Texas, 2008, pp. 651-657.
- [2] <http://offmat.marmoarredo.com/en/catalogue/tuler>
- [3] https://www.corian.com/IMG/pdf/k-30025-corian-solid-surface-material-composition-bulletin_sec.pdf

Optimal Synthesis of Dual Frequency Transverse Flux Induction Heating of Metal Strips

S. Lupi, M. Forzan

Dept. Industrial Engineering
Padova University

Padova, Italy

{sergio.lupi, michele.forzan}@unipd.it

P. Di Barba, M.E. Mognaschi

Dept. Electrical, Computer and
Biomedical Engineering

Pavia University

Pavia, Italy

{paolo.dibarba,
eve.mognaschi}@unipv.it

E. Sieni

Dept. Theoretical and Applied Sciences
Insubria University

Varese, Italy

elisabetta.sieni@uninsubria.it

Abstract—The paper focuses on synthesizing the supply frequencies of the two coils of a transverse flux induction heater with the aim of achieving a uniform distribution of temperature in non-ferrous metal strips of different widths.

Keywords—transverse flux induction heating, multi-objective optimization.

I. INTRODUCTION

The well-known process of transverse flux induction heating of non-magnetic metal strips has been proposed and studied since the middle of the last century for the advantages of using relatively low frequencies and the possibility of obtaining high electrical efficiencies. The acceptance of the process in industry has been very slow due to the complexity of designing and optimizing the inductors in order to avoid excessive localized heating which in particular can produce uneven heating of the strip edges. In fact, the optimal design of the inductor requires the control of the effects of many geometric and physical variables of the system, the frequency and the intensity of the supply current. For this reason, the major developments of the process for its application in industry occurred in the last twenty years with the availability of powerful numerical calculation means, application of mathematical optimization methods and invention and patenting of new inductor geometries. [1÷3]

Nowadays, these developments have led to the construction of industrial plants of considerable power, so that in new casting and rolling mill lines a total power up to 50 MW of transverse flux heaters is installed. [4] However, due to the complexity of the system geometry, the dependence of the characteristics of materials on temperature and, for the magnetic cores, on the intensity of the magnetic field, and the large number of variables that have influence on the results, even today a complete numerical optimization of the heater is not practicable. In recent years, some authors have examined the possibility of applying the so-called "Zone Control Heating" to the transverse flux induction heating, using inductors coils supplied at different frequencies. [5]

As known, the shape and value of the overheating or under-heating phenomena that occur at the strip edges depend, beside other factors, on the distance of the coils from the strip edges and the coil supply current and frequency. [6] This research aims to explore the possibility of obtaining a more uniform heating of nonmagnetic stainless steel strips of various widths by a transverse flux heater with two separate coils. As shown in Fig. 1, the over-heating or under-heating of the strip edges depend on the width of the inductor, that can be inner or outer with respect to the strip edges, on the distance between the strip edge and the coil edge and on the coil supply current and frequency.

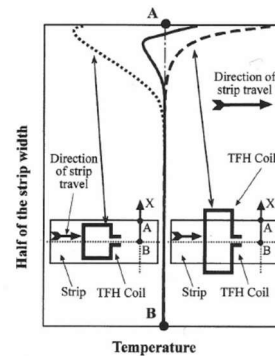


Fig. 1. Typical TFH coils: the coil on the left produces lower temperature on the strip edge (dotted line) while the one on the right produces higher temperature on the strip edge (dashed line). The combination of the effects may lead to a more uniform temperature distribution (continuous line) [3]

II. MODEL DESCRIPTION

The considered system is composed of

- an inductor with two couples of top and bottom coils one protruding (or 'big') and one "internal" (or 'small') to the tape edges, as schematized in figure 2; the dimensions of "internal" coil: 600x600mm, copper: 50x3 mm; distance from strip edge: 50 mm; dimensions of protruding coils: 900x600 mm, copper: 50x3 mm; distance from strip edge: 50 mm.
- the strips to be heated, moving in the gap between top and bottom coils at constant speed; strip: non-magnetic steel: 1 mm thickness, 700-750-800 mm width; gap: 60 mm
- top and bottom magnetic yokes used for concentration of magnetic field in the internal volume of the inductor; relative permeability: 50, no losses.

Transverse flux heaters produce a spatial distribution of the induced power that can be calculated by resorting to 3D models. In this research, the electromagnetic problem is solved by means of a standard vector potential formulation, where the metal sheet is described as a surface region [7]. A sequence of repeated 3D finite-element analyses, by varying frequency and current values, has been performed, this has made it possible to set up a database the subsequent optimization procedure was based on.

III. INVERSE PROBLEM

The goal of the inverse problem is to maximize the flatness of the profile of the total induced energy along the cross-section of the strip at the exit of the inductor system. The design variables are two independent supply frequencies and two inductor current intensities. The inverse problem identifies frequency and current values minimizing the following triplet of objectives, each of which contribute to

make the energy profile along the cross-section of the strip as flat as possible:

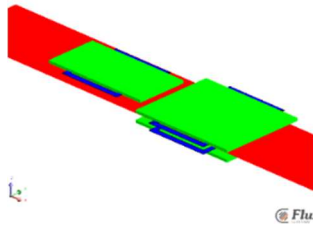


Fig. 2. Schematic of inductor (blue), strip (red) and magnetic yokes (green) system

$$f_1 = \frac{\max(E_{t,w}) - \min(E_{t,w})}{\max(E_{t,w})} \quad (1)$$

$$f_2 = \min \left(\sum_{i=1}^N \frac{|E_{t,i}(w) - E_{t,mean}(w)|}{\Delta E(w)} \right) \quad (2)$$

$$f_3 = \frac{\max(E_{s,w}) - \min(E_{s,w})}{\max(E_{s,w})} + \frac{\max(E_{b,w}) - \min(E_{b,w})}{\max(E_{b,w})} \quad (3)$$

where: $E_{t,w}$ is the total energy induced on the strip of 'w' width that is computed as the sum of the energy produced by the protruding inductor, $E_{b,w}$, and the internal inductor, E_{sw} . $E_{t,i}(w)$, with $i=1,..,N$, is a set of $N=10$ energy values, sampled along the width of the strip; $E_{t,mean}(w)$ is the average of the N $E_{t,i}(w)$ values, $\Delta E(w)$ is the admitted variation (1%) around the average value $E_{t,mean}(w)$ equal to 5 MJ.

The inverse problem exploits the aforementioned database of energies, evaluated with a current amplitude of 1000 A_{rms} at different frequencies from 50 Hz to 1500 Hz with a step of 50 Hz, supplying one inductor at time. The optimization is performed by the Genetic Algorithm, MNSGA, as presented in [6]. The design variables are the frequency and current in each inductor. Due to the linearity of the model, the energy values in the database can be scaled, modifying the supplied currents with quadratic law, in order to reach the total energy required by the process.

IV. RESULTS

The two inductors system was designed in order to heat 750 mm width strips. This preliminary analysis aims to investigate the possibility of heating strips of different widths (700 and 800 mm) within the same inductors fed at different frequencies. In Fig. 3, the improvement obtained for the 750 mm strips, where the small inductor is fed at 250 Hz and the big one at 50 Hz, is presented with the energy distributions that can be obtained by feeding both the inductors at the same frequency, of 250 Hz, 50 Hz and 150 Hz, respectively.

The figure shows that results are poorly sensitive to frequency variation when the strip is the one for which the inductor system has been designed, i.e. 750 mm. In Fig.4, the improved distributions calculated with the design variables related to the Pareto fronts for the three types of strips are presented. The distributions of induced energy are along half of the width of the strip (from the center to the edge) because of the system symmetry. In Fig. 5, the improvement obtained for the 800 mm strips, feeding the small inductor at 1050 Hz and the big one at 250 Hz, is presented together with the energy distributions that can be obtained by feeding both the inductors at the same frequency, 1050 Hz, 250 Hz and 650 Hz. For this case, the use of two appropriate optimal frequencies shows a more uniform distribution of the total induced energy

and that this solution is non-dominated with respect to the tentative initial solution with respect to all three objectives

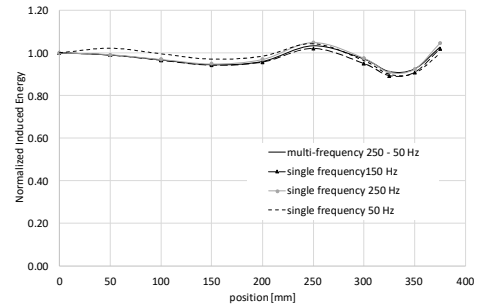


Fig. 3. 750 mm width strip. Improved distribution with dual frequency and the best distributions obtained with a single frequency.

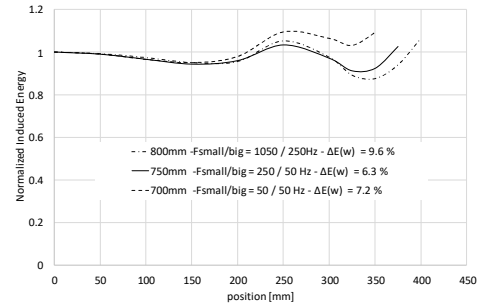


Fig. 4. Improved distribution of the induced energy at the exit of the inductors. (0 mm - Strip axis; 450 mm - Strip edge).

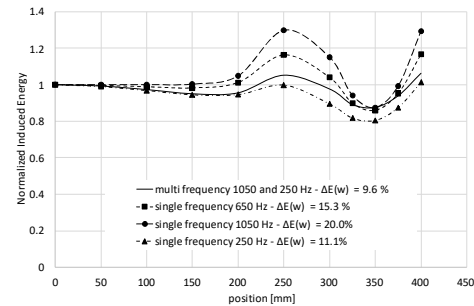


Fig. 5. 800 mm width strip. Improved distribution with dual frequency and the best distributions obtained with a single frequency.

REFERENCES

- [1] F.Dughiero, S.Lupi, A.Mühlbauer, A. Nikanorov, "TFH - Transverse flux induction heating of non-ferrous and precious metal strip - Results of a EU research project", COMPEL, (2003), 22, n.1, pp.134-148
- [2] Y.Neau, et Al., "High power (3 MW) transverse flux inductor for heating of wide range size strips", Lion (France), Proc. of EPM 2003, 4th Int. Conf. on EM Processing of Materials, 2003, pp. 570-575
- [3] H.Schulbe, A.Nikanorov, B.Nacke, "Flexible transverse flux heaters of metal strips", Padua (Italy), Proc. of HES-04, Int. Symposium on Heating by Electromagnetic Sources, June 22-25 2004, pp. 293-300
- [4] S.Lupi, M.Forzan, A.Aliferov, "Induction and direct resistance heating", Switzerland: Springer International Publishing, 2015.
- [5] A.Spagnolo, M.Forzan, S.Lupi, O.Pateau and B.Paya, "Space control optimization of multi-coil transverse flux induction heating of metal strips", Padua (Italy), Proc. of HES-10 Int. Conf. on Heating by Electromagnetic Sources, May 18-21, 2010, pp.455-463
- [6] P. Di Barba, F. Dughiero, M. Forzan, and E. Sieni, "Migration-corrected NSGA-II for improving multiobjective design optimization in electromagnetics," *International Journal of Applied Electromagnetics and Mechanics*, vol. 51, no. 2, pp. 161-172, 2016.
- [7] Guérin C., Tanneau G., Meunier G., Ngngueu T., "A shell element for computing eddy currents in 3D. Application to transformers", IEEE Trans. Mag., vol. 31, no. 3, May 1995, pp. 1360-1363.
- [8] Battistetti, M., Di Barba, P., Dughiero, F., Farina, M., Lupi, S., Savini, A., "Optimal design of an inductor for transverse flux heating using a combined evolutionary - simplex method", COMPEL, 2001.

The destruction model of cylindrical billet's hard shell during heating and melting by internal sources

Maxim Khatsayuk
Department of Electrotechnology
and Electrotechnics
Siberian Federal University
Krasnoyarsk, Russia
maxhac@ya.ru

Viktor Demidovich
Russian Technologies of Induction
Heating Ltd.
Saint-Petersburg, Russia
vbdemidovich@mail.ru

Viktor Timofeev
Department of Electrotechnology
and Electrotechnics
Siberian Federal University
Krasnoyarsk, Russia
viktortim0807@mail.ru

Abstract — This article deals with the findings of researches and development of the theory for non-crucible induction melting of non-magnetic billets with due account of the MHD effect.

Keywords — induction melting, magnetohydrodynamics, numerical simulation, mathematical modeling, MHD

I. INTRODUCTION

This article deals with the findings of researches and development of the theory for non-crucible induction melting of non-magnetic billets with due account of the MHD effect. The prior experimental researches [1] of technology have provided basis for the assumption of significant impact of the

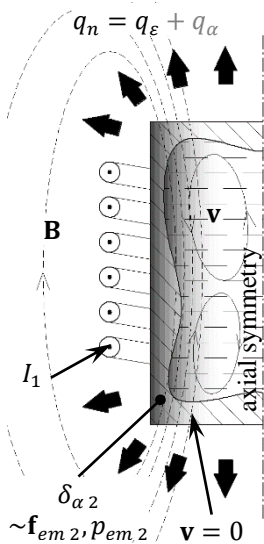


Fig. 1 – Non-crucible induction melting

natural MHD flows during the liquefaction and the necessity of their accounting at theory researches to the fullest extent possible. The computational process model has been developed therefore based on the created conjunction algorithm, such model inclusive of the related electromagnetic, thermal and hydrodynamic processes with due account of the turbulence as well as solidification and melting processes [2]. Convective q_α and radiation q_ϵ heat losses have been accounted for at nonlinear boundary conditions. Pre-evaluation of the process by similarity parameters has shown that the problem can be solved in non-inductive approximation, though the full-developed turbulence and free convection in the liquid phase should be expected. Fig. 1 provides the sketchy description of the process. The detailed description has been provided in earlier papers [3-5]. The essence of this technology lies in the fact that the liquid phase can be formed in the inner layers in case of the classical system of induction heating of the billets with a certain set of parameters and conditions.

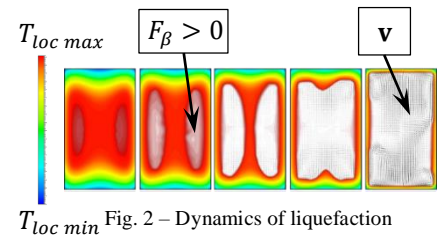
II. NUMERICAL MODELING

A. Magnetohydrodynamics processes

The unsteady 3D numerical computation of the process (Fig. 2) has been performed based on the elaborated model and the available initial data corresponding to the executed

This research was carried out with financial support from Russian Foundation for Basic Research and Government of the Krasnoyarsk Territory as part of the Science Project No18-48-242013 on Research of the Influence of Spatial and Time-and-Frequency Distribution of Electromagnetic Forces in Melt on MHD process behavior in molten metal.

experiments, such process consisting of three parts: preheating, melting and solidification. The computations have proved that MHD processes significantly affect the liquefaction pattern, such effect being, in the first place, evident as the liquid phase temperature field alignment which will inevitably change the thermal transfer conditions as well as the shape and volume of the liquid phase (Fig. 3). It was revealed that even slight circulation of melt will not allow its overheating in



excess of the temperature T_{LIQ} without the surface being melt-through. This fact turns round the view of the process behavior and creates its own peculiarities. The process chart has been modified accordingly and the respective peculiarities and their accounting principles have been considered.

B. Mechanical problem

Also, one the technological peculiarities revealed besides the linear thermal expansion when preheating the billet is that phase transitions go along with the step change of the density and, respectively, the volume approximately by ρ_{SOL}/ρ_{LIQ} times. In this technology the produced liquid volume is confined in the solid tight shell of some thickness. The phase transition in the liquid volume is possible only when that shell is respectively expanded otherwise pressure starts increasing pro rata the heating until the shell is expanded or destroyed. This is evidently related, in the first place, to the shell thickness and requires the corresponding analysis to search for the stable modes. Problem of the stress-strain behavior (SSB) has been numerically solved to study the shell deformation. Therefore, the geometry of shell produced following the thermal hydrodynamic calculations has been approximately transposed to the numerical SSB solver ANSYS Mechanical – Static Structural. The problem reduces to calculation of the deformation vector u and equivalent stresses σ . Therewith the pressure problem is search solved until the required increase through deformation of the volume presented by the inner surface of the solid shell. As can be seen from the calculation results in Fig. 4, the most critical region is the angular belt on the billet inner surface. Also, regions of maximum stress and deformations are found at the centerline point on the face and in the center of a cylindrical billet. Thus, the billet destruction shall be expected with the face being broken away because of the tensile strength being exceeded. The predicted melt-through and destruction of the solid shell is one of the prerequisites of the technology as liquid phase shall be extracted for casting immediately after its liquefaction. Several solutions of the same kind are suggested in the Section. Fig. 5 provides one exemplary calculation of the

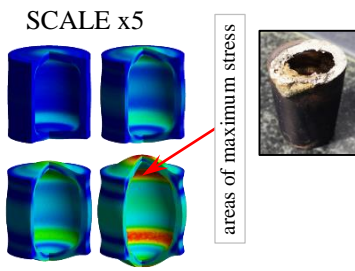


Fig. 4 – Scaled pattern of the billet deformation

deliberate bottom melt-through with the ingot being asymmetrically positioned.

III. ANALYTICAL MODELS

Any specific recommendations on selection of parameters of different billets are intricate if made only on

the basis of computational simulation as this technology is multi-discipline and accommodates electromagnetic, thermodynamic, hydrodynamic and mechanic processes in the solid body. Behavior of processes is accordingly governed by the set of parameters related therewith which cannot be considered individually. The comprehensive analytical solution of the problem through the existing theories and

procedures has been found therefore on the grounds of some assumptions which allowed significant simplifying of the problem and reduction of the most parameters to their generalized non-dimensional similarities. Therewith the thermoelectric part is considered jointly with the analytical solution of the problem concerning deformation of the shell surfaces. Expressions to calculate dynamics of the radial temperature distribution with

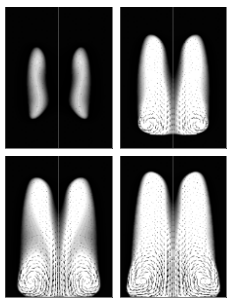


Fig. 5 – Asymmetrical bottom melt-through

application of S-functions known from the induction heating theory are presented. Nevertheless, the steady-state operating conditions with $\eta_r \rightarrow 0$ are of more concern for the technology. This allows significant simplification of the analytical expressions which are recorded with the set surface temperature of T_r (Fig. 6).

Problem of the deformation of the cylindrical shell being formed and the respective mechanical stresses therein has been analytically solved to select the permissible wall thickness (safety margin k_{st}).

Thus, the second prerequisite of the process is keeping the integrity of the billet outer solid layer $\sigma_{MAX} < \sigma_u$ (or $k_{st} > 1$). Analysis of the received expressions shows that there are two process stability points (Fig. 7). The billet outer layer is destroyed and the liquid phase is bleeding-over in the range of $\beta_{w1} - \beta_{w2}$. Thus, keeping the hardness of the shell with the relative thickness of β_w depends on the shape H' , ductility σ' , relative deformation ν and the required expansion of the billet V' . Increase of the billet height leads to offset of the point β_{w1} and reduction of the respective working range of the wall thickness. Therewith, the possible range of parameters is expanded for more ductile materials with the minimum expansion at the phase transition and the processes become accordingly more stable when implementing this technology. The material deformation behavior (Poisson ratio) has almost no effect on the range typical for the maximum capacity. The range $\beta_{w2} - 1$ is of little interest as the required wall thickness is thick enough which complicates the liquid phase extraction and decreases the capacity.

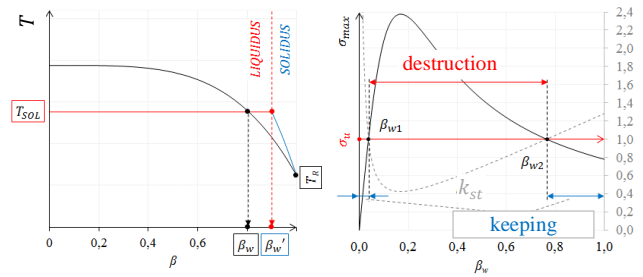


Fig. 6 – Determination of the shell thickness

Fig. 7 – Analysis of the shell destruction

CONCLUSION

It has been established by the simulation of MHD-processes at non-crucible induction melting of non-magnetic billets that melt circulation prevents overheating of the inner layers in excess of the liquidus temperature without the surface being melt-through. The correction has been performed accordingly and the resultant peculiarities and technology restraints have been stated. It has also been established that the solid shell being formed is subject to deformation and mechanical stresses because of the required volume expansion of the liquid phase. Three critical areas have been theoretically found, therewith the maximum stress area is the angular belt on the inner surface.

Recommendation-based analytical expressions representative of thermoelectrical and mechanical processes have been set for selection of parameters of non-crucible induction melting. The procedure comes down to selection of sequential minimum wall thickness by the required volume of liquid phase of the original billet material, frequency and minimum power from the presented expressions and dependencies. It has been revealed that the system has two steady spots as regards the relative shell thickness which correspond to the ranges of maximum and minimum capacity. The thickness selected between these two spots will result in the billet destruction thus allowing the expected liquid phase extraction.

REFERENCES

- [1] V.B. Demidovich, P.A. Maslikov, "The role of MHD for producing a liquid phase in a titanium ingot during non-crucible melting in air," Induction heating, vol. 2, 2013, pp. 33–36. (Роль МГД явлений для получения жидкой фазы в титановом слитке при безтигельной плавке на воздухе).
- [2] V.B. Demidovich, M.Yu. Khatsayuk, V.N. Timofeev, A.A. Maksimov, I.I. Rastvorova, "Numerical simulation of non-crucible melting of titanium alloy in the alternating electromagnetic field," Magneto hydrodynamics, Vol. 4, 2015, pp. 785–794.
- [3] V.B. Demidovich, M.Yu. Khatsayuk, V.N. Timofeev, A.A. Maksimov, "Numerical modeling of crucibleless melting of titanium alloy in the electromagnetic field," Metallurgy Engineering, Vol. 3, 2017, pp. 2–5. (Численное моделирование безтигельного плавления титанового сплава в переменном электромагнитном поле).
- [4] V.B. Demidovich, I.I. Rastvorova, M.Yu. Khatsayuk, V.N. Timofeev, A.A. Maksimov, "Non-crucible induction melting of titanium," Technology of light metals, Vol. 2, 2015, pp. 82–88. (Индукционная безтигельная плавка титана).
- [5] V.B. Demidovich, M.Yu. Khatsayuk, V.N. Timofeev, A.A. Maksimov, I.I. Rastvorova, "Numerical simulation of MHD processes in the technology of non-crucible induction melting of titanium alloys," 8th International Conference on Electromagnetic Processing of Materials EPM-2015, Cannes, 2015, 4 p.

Research of multicentric ring coils in comparison to classic ring coils

Schubotz Stefan
EFD Induction GmbH
Freiburg im Breisgau, Germany
stefan.schubotz@efd-induction.com

Abstract—The topic is about ring coils with eccentric orientated semi-windings for heating of parts with different diameters. These are compared to classic ring coils that only have one inner diameter and one center. Especially the efficiency is considered and compared between both types of coils.

Keywords — induction heating, multicentric ring coil, simulation

I. INTRODUCTION

If a workpiece has different diameters or is built asymmetrically, it can still be heated with only one classic ring coil that has one inner diameter. This applies also if several workpieces with different diameters shall be heated. The result from that is a low efficiency for the workpiece areas where the

coupling gap (distance between the inner diameter of the coil and the outer diameter of the workpiece) is large. Usually, the coupling gap shall be held to a minimum [1].

Another approach is to use different coils for each zone to be heated. Then, the coils are dimensioned individually for the areas to be warmed so one can achieve a small coupling gap. On the other hand, this makes further coils necessary and it leads to additional work in changing between the coils. In some cases, also another heating station might be required.

A good compromise solution seems to be coils that have two eccentric orientated semi-windings making it possible to have partly a small coupling gap for both zones to be heated by induction (see. Fig. 1). In practise, these types of coils are often referred as “snowman”- or “keyhole”-coils due to its shape. Since there are also coils possible, that do have more than two half windings, these types of coils will be defined in this elaboration as multicentric ring coils. An example of a multicentric ring coil for at least three different workpieces / workpiece zones is shown in Fig. 2.

Thus, there are several approaches about how to proceed when workpiece zones with different diameters have to be heated

II. MOTIVATION

The aim of this study is a research of these types of coils. Especially, the efficiency is interesting and helps to find out if it is better to apply such a coil or if it is more feasible to use coils with different diameters. Besides that, also other aspects like rotation speed and inductance are considered. In this way, one can gain a clear view about the behaviour of multicentric ring coils and may find out how and when they shall preferably be applied.

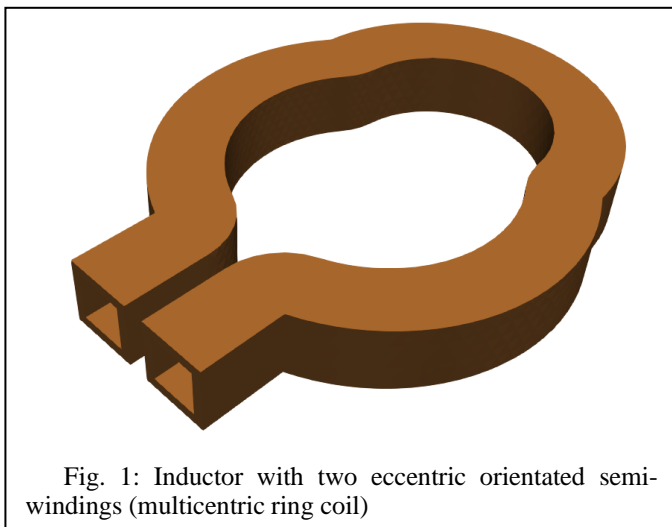


Fig. 1: Inductor with two eccentric orientated semi-windings (multicentric ring coil)

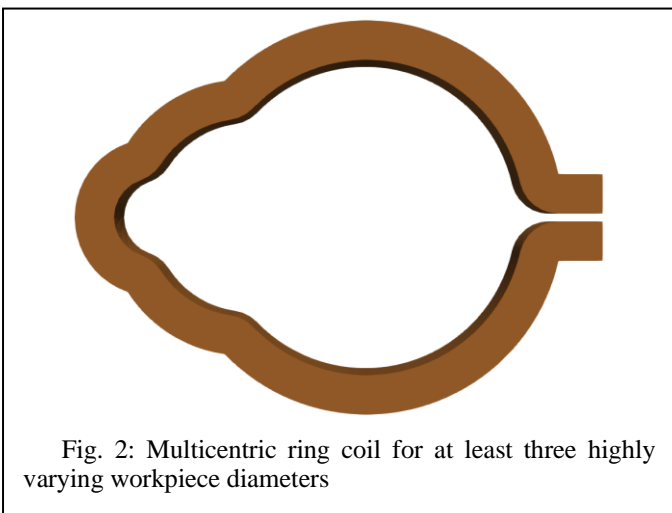


Fig. 2: Multicentric ring coil for at least three highly varying workpiece diameters

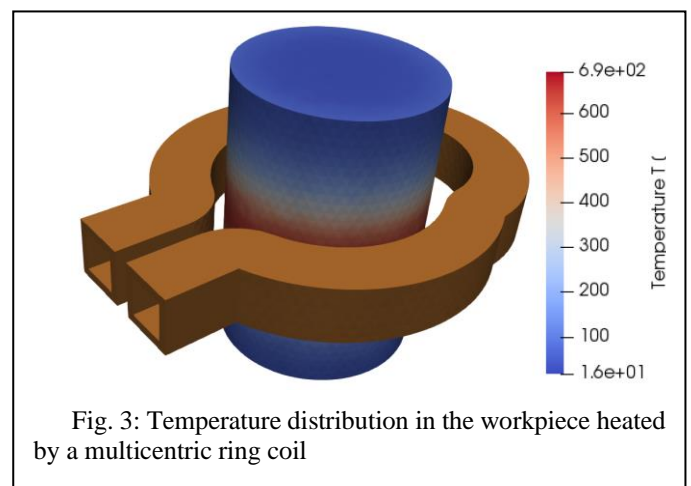


Fig. 3: Temperature distribution in the workpiece heated by a multicentric ring coil

III. APPROACH

Coils with different diameters are considered in this elaboration. Here, the efficiency of the version with two eccentric orientated semi-windings and classic ring coils are compared. For this, simulations have been done with multicentric ring coils for different workpieces (ϕ : 30 and 50 mm). For this research, simulations have been done with the software CENOS that does the calculations with finite element method [2]. An exemplary modelling result of the temperature field in the workpiece is shown in Fig 3. All simulations in this examination have been done in 3D. For many simulations, only the electromagnetic field has been regarded and calculated because the heat sources do already reveal the efficiency of the coil-workpiece constellation.

IV. RESULTS

The results in Fig. 4. show that a multicentric ring-coil achieves a bigger efficiency at the small workpiece but a reduced efficiency at the big workpiece. Therefore, it needs to be checked where the high-power demand is expected or if two individual coils can be used. However, especially if the two diameters to be heated belong to the same workpiece, using of separated coils is often not possible. For example, at camshafts, there are asymmetrically formed cams and rotational symmetric formed bearings. There, one process approach is to heat the rotating cam with the big ring of the multicentric ring coil and the bearing with the small ring. One small single ring coil for heating the bearing cannot be used here because the cams would mechanically block the coil.

Another important result concerns the rotation speed. In general, multicentric ring coils require a higher rotation speed

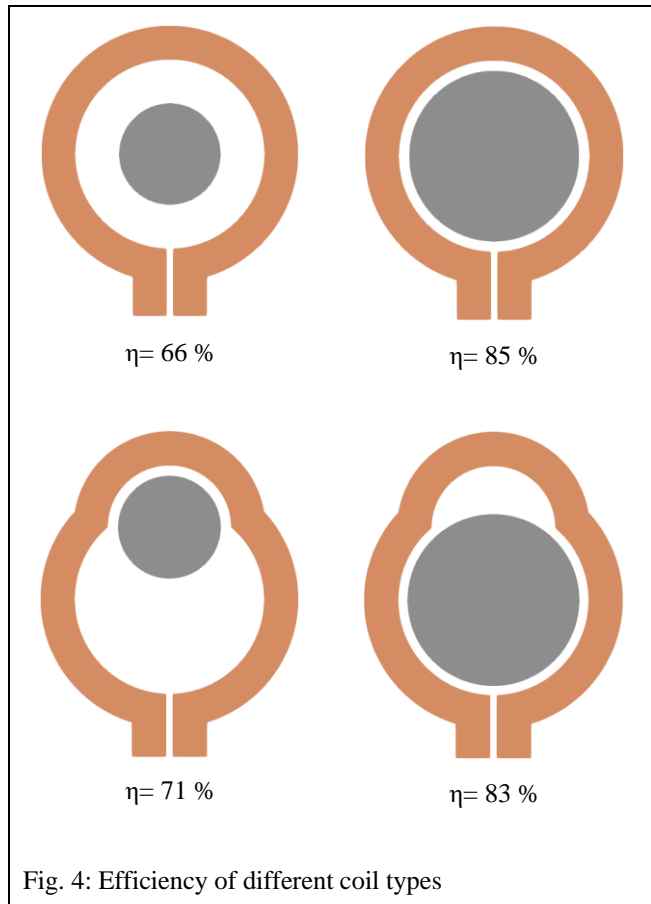


Fig. 4: Efficiency of different coil types

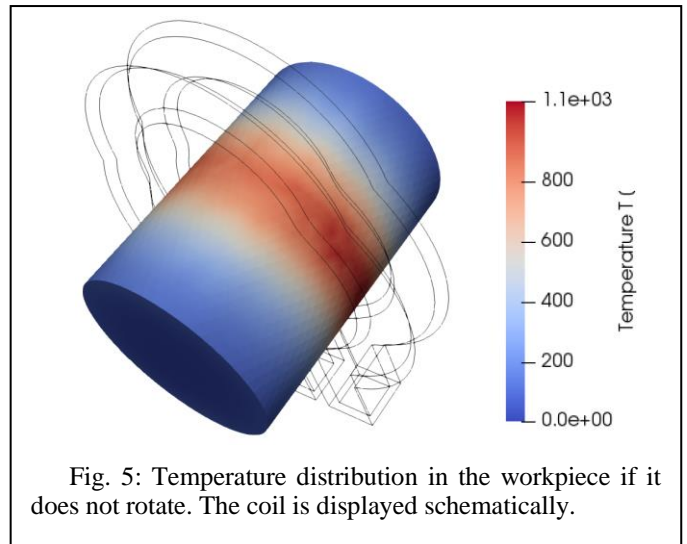


Fig. 5: Temperature distribution in the workpiece if it does not rotate. The coil is displayed schematically.

in comparison to typical ring coils where the workpiece is centred in the coil. The common rotation speeds that usual systems can provide are in most cases sufficient. Fig 5 shows the temperature distribution of the workpiece surface if it does not rotate. There, the unequal temperature distribution in tangential direction can be observed. This verifies that multicentric coils cannot be used at non-rotating workpieces.

The inductance of the coil is also increasing when compared to a standard ring coil. Therefore, it needs to be ensured that the converter is dimensioned right for the electric load. On the other hand, the change of inductance when different workpieces / workpiece zones are heated is smaller in comparison if coils with different inner diameters are used. This makes it in general easier to match the converter to the load when using a multicentric ring coil. Especially in cases where the output circuit (matching transformer, capacitors) behind the converter does not provide a possibility to be adjusted, the use of a multicentric ring coil can create advantages.

V. CONCLUSION

The simulation results reveal that coils with two eccentric semi-windings are quite efficient.

At present, still many applications with rotationally symmetrical workpieces of different diameters are heated with a big set of different coils. This creates a lot more cost and time to change the coils. Therefore, processes should be checked carefully, if a multicentric ring coil might not be the better alternative. In might be better to use such a coil than just to build one standard ring coil with a big diameter that shall also heat up the smaller workpieces / workpiece zones.

Finally, in processes where energy efficiency plays a superior role, it is still better to use different coils for the according workpieces. Therefore, it is a question of the process and the priorities which principle shall be applied.

- [1] Rudnev, V. ; Loveless, D. ; Cook, R. ; Black, M.: Handbook of Induction Heating.. 1. Edition. New York, Basel : Marcel Dekker, Inc., 2003
- [2] Website: CENOS - <https://www.cenos-platform.com/> - Access: 27.02.2020

Investigation of the induction heating spherical bodies dispersed in the continuous load inductor stove

Aleksandr Antipin
Ural Federal University
620000 Yekaterinburg
Russia
e-mail: a.s_antipin@mail.ru

Vasily Frizen
Ural Federal University
620000 Yekaterinburg
Russia
e-mail: vfrizen@yandex.ru

Abstract—The article presents a drying unit in which it is possible to provide an unlimited amount of energy to a process medium containing metal balls-heaters, which can be implemented using induction heating. The dependences of the electrical parameters of the steel load in a general view are considered taking into account the mutual influence. A model for calculating the maximum effective power of a dispersed steel charge with a dielectric component has been developed

Keywords—bulk load, energy parameters, high temperature furnaces, induction heating, iron shot

I. INTRODUCTION

In the processes of production of powder materials, often the original is obtained in the form of a suspension, and moisture removal is required to prepare the product for further processing. During the process of removing excess moisture, both gas furnaces and resistance furnaces with a ventilated chamber can be used [1-4].

In this case, the heating of the material goes from the surface into the interior of the medium, and in order to ensure sufficient process performance, it is necessary to provide a large surface area of the material onto which the radiation of the heaters falls, or which is washed by convective flows from heat sources. In such installations with a developed surface of the medium to be treated, in the presence of a powerful ventilation system of the heating chamber, a significant part of the material is carried out through the ventilation, and therefore the drying installation requires the installation of complex multi-stage filters to catch the product removed from the heating chamber. Such a system requires frequent and costly maintenance. In addition, the product removed from the heating chamber is often under-processed, since chemically bound moisture does not have time to be removed from it, and in some cases such a product needs to be processed again.

Suspension drying systems have been developed that use indirect heating of the processed material using preheated steel balls [5-8]. Since the transfer of heat from the balls to the heated medium occurs in direct contact with the processed material, the volume of the heating chamber can be reduced. Product loss through the ventilation system is also reduced. However, in such a system, the energy transferred to the material during the drying process is limited by the energy accumulated by the steel balls during preheating.

A drying unit, in which it is possible to provide an unlimited amount of energy to a process medium containing metal balls-heaters, can be implemented using induction heating [9]. To ensure maximum performance of such an

installation, it is required to determine the number and size of ball heaters loaded into the installation.

II. EASE OF USE

One of the possible designs of an induction drying plant that transfers energy to the processed material through metal balls-heaters is shown in fig. 1. The heating chamber is a ceramic crucible - 1, located in the opening of the inductor – solenoid - 2. The processed material is loaded into the crucible with steel balls previously mixed into it - 3, a heat insulator, kaolin wool - 4.

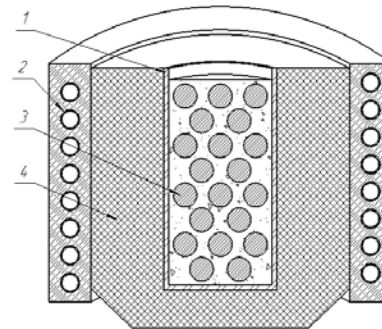


Fig. 1. The design of the induction dryer

When determining the maximum efficiency of the system, the following assumptions were made: the efficiency of the heating system will be the higher, the greater the total surface of the ball-heaters; energy costs for the drying process will increase with increasing mass of balls loaded with the processed material; efficiency increases with increasing electrical efficiency of the inductor with the load.

The assumptions made do not change their significance for all operating modes of the drying installation. For simplicity of analysis, it is more convenient to consider the removal of chemically unbound moisture contained in the treated suspension as the basic mode. In this mode, the temperature in the chamber stabilizes at 100 ° C under normal pressure.

Each of the assumptions can be expressed mathematically in the form of corresponding coefficients, the product of which will give the desired expression of the objective function.

The first coefficient shows the ratio of power supplied to the load and heat loss from the crucible walls.

The second coefficient shows the ratio of the energy accumulated by the balls and transferred to the charge.

The third coefficient is determined by the ratio of the heat dissipation power in the balls-heaters and losses in the inductor.

The electrical parameters of the inductor-loading system are calculated according to the "classical" method using a T-shaped equivalent circuit [10-11]. When calculating the reduction coefficient C , both the active and reactive resistance of the load are taken into account, as well as the scattering in the gap, inside and outside the inductor. In this case, the coefficient is calculated for the actual arrangement of the balls in the load, and when determining the scattering inductance inside the inductor's opening, we consider that the calculated arrangement of the balls along the axis of the inductor is close to each other in order to take into account the magnetic resistance of the sections of the magnetic circuit between the layers during loose laying (Table 1).

TABLE I. THE PARAMETERS OF THE BALL IN THE LOAD ARRAY WITH A UNIFORM ARRANGEMENT

b/d	$H_{\text{ноб}}$	P	r	x	K_r	K_x
	A·m	W	mOhm	mOhm		
5	14600	-	0,0108	0,0167	1,00	1,00
1,01	23965	0,00942	0,072	0,0120	0,66	0,72
1,06	17952	0,00787	0,091	0,0145	0,84	0,87
1,11	13246	0,00705	0,0120	0,0186	1,10	1,12
1,15	11411	0,00670	0,0137	0,0211	1,26	1,26
1,18	10964	0,00656	0,0142	0,0217	1,311	1,30
1,19	10871	0,00653	0,0143	0,0219	1,321	1,310
1,20	10850	0,00648	0,0143	0,0218	1,312	1,308
1,21	10898	0,00647	0,0142	0,0217	1,314	1,301
1,30	11741	0,00631	0,0132	0,0199	1,22	1,20
1,40	12491	0,00663	0,0124	0,0187	1,15	1,12
2	13922	0,00633	0,0113	0,0169	1,04	1,01

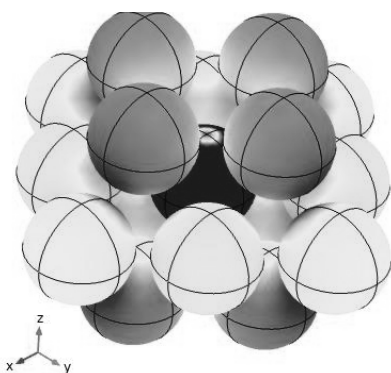


Fig. 2. Arrangement of spheres in an array with a field strength gradient over a surface

The electrical parameters of a single ball are determined using the expressions [12]. The objective function, which is a product of the three above-described coefficients, must have an extremum when changing the number and diameter of the loaded balls, since the first and third coefficients will monotonously decrease with decreasing mass of the ball-heaters, and the second when the same changes will grow (fig. 3).

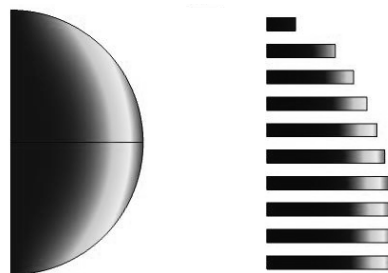


Fig. 3. Decomposition of a sphere into disks with a level of heat transfer on a body surface

The maximum number of balls in a layer, as well as the maximum number of layers during tight packing to calculate bulk density (fig. 2), can be determined using the methodology [13].

REFERENCES

- [1] Patent RF № 2057404 ot 22.12.93 na IZOBRETENIE "Sushil'naya ustanovka". Avtory: Nefedov V.N., Karpenko Yu.V., Korneev S.V., Valeev G.G. // Opubl. 27.03.96. Byul. № 9.
- [2] Patent RF № 2258877 ot 26.12.2003 na IZOBRETENIE "Sposob sushki dispersionnykh materialov". Avtory: Ledenev V.P., Polyakov V.A., Kononenko V.V., Kovalevskii A.P., Chorbachidi P.G., Rysin A.P. // Opubl. 20.08.2005. Byul. № 23.
- [3] Patent RF № 2592150 ot 20.04.2015 na IZOBRETENIE "Sposob sushki vlazhnogo polimernogo poroshka i prigodnoe dlya etogo oborudovanie". Avtory: Ben'e M., Kammerkhofer P. // Opubl. 20.07.2016. Byul. № 20.
- [4] Kiselev E.V., Kut'in V.B., Matyukhin V.I. Elektricheskie pechi soprotilivleniya: Ucheb. posobie. - Ekaterinburg: UGTU-UIPI, 2010. - 79 s.
- [5] Patent RF № 2571065 ot 17.10.2014 na IZOBRETENIE "Sposob sushki pylyashchikh melkozernistykh materialov i ustanovka dlya ego osushchestvleniya (Varianty)". Avtory: Zainullin L.A., Karelin V.G., Epishin A.Yu., Artov D. A., Zainullin R.L., Chen' Kai // Opubl. 20.15.2015. Byul. № 15.
- [6] Patent RF № 2618585 ot 21.10.2015 na IZOBRETENIE "Sposob vysokotemperaturnoi obrabotki melkodispersnykh sypuchikh materialov i ustanovka dlya ego osushchestvleniya". Avtory: Zainullin L.A., Karelin V.G., Spirin N.A., Epishin A.Yu., Artov D. A., Zainullin R.L. // Opubl. 04.05.2017. Byul. № 13.
- [7] Patent RF № 2618585 ot 26.07.2010 na poleznuyu model' "Sushil'no-izmel'chitel'naya ustanovka". Avtory: Bol'shukhin A.Yu. // Opubl. 27.12.2010. Byul. № 36.
- [8] Zaitsev E. D. Induktsionnaya termicheskaya obrabotka sypuchikh dielektricheskikh materialov / E. D. Zaitsev, A. I. Slosman, V. V. Kharchenko // Izvestiya Tomskogo politekhnicheskogo instituta [Izvestiya TPI]. 1973. - T. 235. - S. 18-22.
- [9] Belik, Sergej (2019) Kalorimetrische Untersuchung der induktiven Erwärmung von Kugelarrordnungen für elektrothermische Speicheranwendungen. In: Tagungsband Workshop Elektroprozessstechnik, 2019, e79-e87. Workshop Elektroprozessstechnik, 12.-13. Sept. 2019, Ilmenau, Deutschland.
- [10] Slukhotskii A. E., Nemkov V. S., Pavlov N. A., Bamuner A. V. Ustanovki induktsionnogo nagreva: Uchebnoe posobie dlya vuzov. Pod red A.E. Slukhotskogo. - L. : Energoizdat. Leningr. otd-nie, 1981. - 328 s.
- [11] Fomin N. I., Zatulovskii L. M. Elektricheskie pechi i ustanovki induktsionnogo nagreva. - M. : Metallurgiya, 1979. - 247 s.
- [12] Babat G. I. Induktsionnyi nagrev metallov i ego promyshlennoe primenenie. - L. : Energiya, 1965. - 552 s.
- [13] Eckard Specht. Packomania. 2018. URL: <http://www.packomania.com/>.

Induction heat treatment of large rolls with two independent power sources

Yuri Perevalov

Department of Electrotechnology, Faculty of Electrical Engineering
and Automation
St.Petersburg Electrotechnical University (LETI)
St.Petersburg, Russian
yyperevalov@yandex.ru

Victor Demidovich

Russian Technologies of Induction Heating (RTIH) Ltd.
St.Petersburg, Russian
vbdemidovich@mail.ru

Abstract—The two-inductor heat treatment system for rolls of rolling mills is highly flexible and can improve the quality of heat treatment while solving energy-efficiency and productivity problems. A digital model of induction heat treatment of rolls with the computation of electromagnetic, temperature and stress fields is developed taking into account the characteristics of power supplies and control systems for heat treatment modes. Particular attention is paid to the reliability of frequency converters in the presence of magnetic coupling between inductors. Recommendations on frequency selection and inverter settings are given. A universal method of digital design and control of thermal conditions in induction heat treatment systems is considered.

Keywords— *Coupled Electromagnetic and Temperature Fields, Electromagnetic processing of metals, Induction heating, Multiphysics Problems, two-inductor heat treatment system, frequency converters*

I. INTRODUCTION

In the metallurgical industry the induction heating devices have a power level up to several hundreds of kilowatts or megawatts. The frequency range of used power sources is from tens of Hz to MHz.

Thermal processing of pipes and rolls is an important stage in manufacturing of high quality steel products like lengthy pipes and rolls with big diameters for rolling mills. Solidification and annealing are main types of heat treatment of pipes and rolls. Modern heat treatment requires strict implementation of temperature evaluation during heating, controlled cooling and, probably, repeated heating.

The developed numerical models of technological thermal processing include two-dimensional modeling of electromagnetic and thermal fields in the system. Thermal tension during processes of heating and cooling the pipes and rolls is simulated. These information is essential for defining the structure, hardness, size of a grain and other characteristics of the pipes' and rolls' metal.

The developed two-dimensional model was extremely effective not only for the induction heat treatment systems design of pipes and rolls, but also for a digital control of these complexes. However, it is necessary to use the temperature

feedback under the presence of perturbations. The original way of controlling the temperature at the heater' exit is proposed by the control of the temperature at the special point in the "active zone".

The use of modular structure of induction heaters has a significant advantages in induction heating technology, since it allows optimizing the operation modes of equipment in relation to: energy consumption; scale formation; ability to maintain a constant exit temperature.

The advanced digital control allows to effectively process the possible disturbances, such as: changes of speed, diameter and initial temperature of the workpiece, and, therefore, to minimize the amount of defects during heating.

II. PROBLEM

Figure 1 shows the temperature distribution along the roll during quenching in 2 different modes. Each mode should provide the exit temperature of 1000 °C after the second inductor on the surface [1]. Two modes of hardening of the roll are presented in fig.1. 1 (indicated by 1) – is the hardening mode of the rolling mill's roll from two power supplies (each power source operates on its inductance coil) power of the first is 570 kW, power of the second power source is 200 kW. The operating frequency of both power supplies is 100Hz [2]. Tempering mode 2 (indicated by 2) – is the hardening mode from one power source, inductor connected in series, power 820 kW, frequency 65 Hz. The inductive speed in each case is 0.1 cm/s. 3 shows temperature at a depth of 100 mm for two quenching modes.

Inductors must be placed in a short distance from each other to ensure the required temperature distribution. In the 2 mode, the surface temperature has a strong unevenness. Just a small area reaches the required temperature, which requires a decrease in the speed of the inductor to maintain the necessary time for the recrystallization of the metal. Extension of the holding time can lead to overheating of the local zones of the part.

The mode 2 is much more complex, and the derived surface has a much lower quality, in comparison with the mode 1.

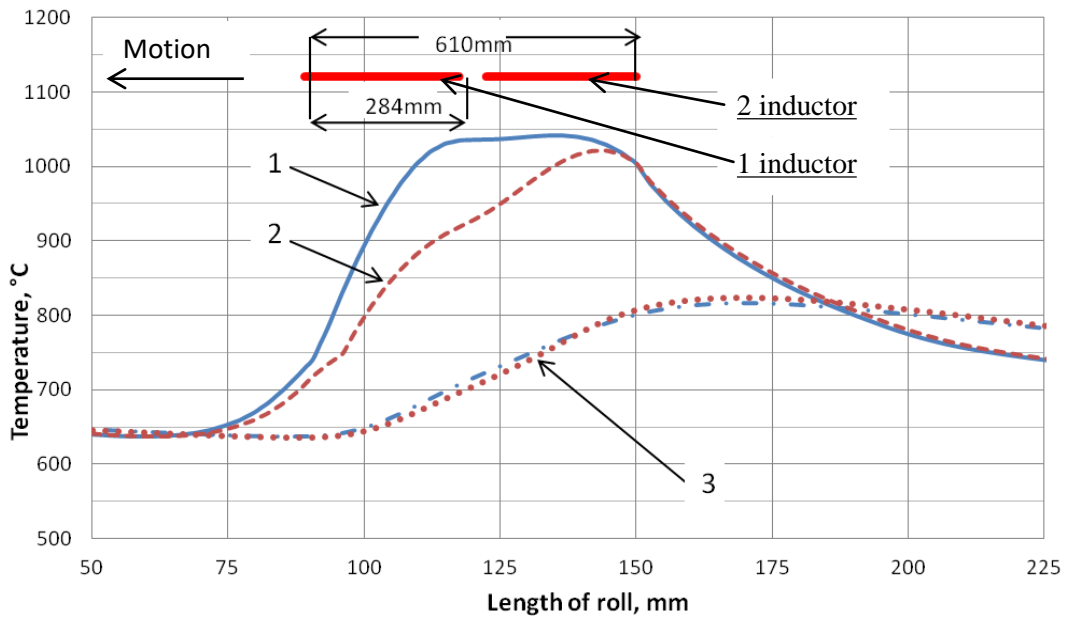


Figure 1. Hardening of the rolling mill roll

The 1 mode allows to achieve uniformity of the temperature almost under the entire surface of the 2nd inductor, avoiding the appearance of local maxima of the temperature distribution.

Thus, the use of the mode 2 allows obtaining a surface with improved characteristics, reducing the probability of defects, while increasing the productivity, in comparison with the mode 1.

Since the inductor is located at close range, there is instability in the operation of power sources due to the presence of magnetic coupling between the inductors.

Fig. 2 shows the hodograph of the induced reaction on the adjacent contour in conventional units of frequency, where f_1 , f_2 are the resonant frequencies of the magnetically coupled circuits, the frequency f_1 is the resonant frequency of the load circuit, and f_2 is the magnetically coupled circuit.

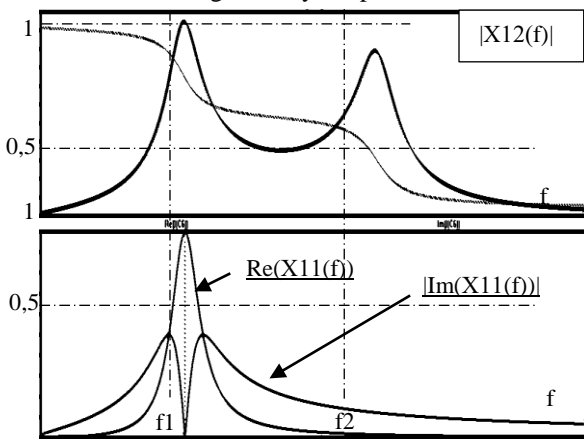


Figure 2. Dependence of the modulus of the induced reaction on the frequency and the dependence of the active and reactive components of the frequency

It can be seen that $X12(f)$ has two local maximas: at the resonance frequency of the intrinsic circuit and at a frequency close to the resonance frequency of the neighboring contour. Also there are the modules of the imaginary and real parts of the response of the loading circuit in the graph. Thus, it can be seen that with a deviation from the frequency of the resonance, the amplitude of the induced interference sharply decreases, and the active component of the reaction also decreases, but the reactive component increases (within certain limits).

From the foregoing, we can determine the conclusion that the constructed model allows you to accurately determine the area of stable operation of inductors and power supplies for hardening rolls of rolling mills

CONCLUSIONS

New technologies for induction heat treatment of large diameter rolls of rolling mills with a barrel diameter of up to 65" are developed. It was found that the digital model of the induction system must necessarily include the calculation of electromagnetic and thermal fields, the calculation of stress and strain fields, as well as the calculation of power source parameters. This digital model can be used to create an intelligent control system for the installation of induction heat treatment of large-sized rolls of rolling mills.

REFERENCES

- [1] A. Muehlbauer: History of Induction Heating and Melting. (2008), Vulkan Verlag.
- [2] V. Demidovich , V. Andrushkevich , Yu. Perevalov, Induction heat treatment of large diameter pipes and coils // 9th International Symposium on Electromagnetic Processing of Materials (EPM2018): IOP Conf. Series, 2018. - p.1-4. doi:10.1088/1757-899X/424/1/012064

Technology development for manual laser cladding of high-alloy tool steels with simultaneous inductive preheating for crack prevention

Jonas Kimme
Institute for Machine Tools and
Production Processes (IWP)
Chemnitz University of Technology
Chemnitz, Germany
jonas.kimme@mb.tu-chemnitz.de

Josephine Zeisig
Leibniz-IFW Dresden
Institute for Complex Materials
Dresden, Germany
j.zeisig@ifw-dresden.de

Alexander Fröhlich
Institute for Machine Tools and
Production Processes (IWP)
Chemnitz University of Technology
Chemnitz, Germany
alexander.froehlich@mb.tu-chemnitz.de

Verena Kräusel
Institute for Machine Tools and
Production Processes (IWP)
Chemnitz University of Technology
Chemnitz, Germany
verena.kraeusel@mb.tu-chemnitz.de

Abstract—The paper presents the development and successful application of simultaneous inductive preheating during manual laser cladding for repair purposes of weld-critical materials. The design and optimization of a suitable inductor as well as the analysis of the welding process was carried out by means of FE-simulation in order to generate material deposition without imperfections. Based on suitable parameter variation studies, crack and pore-free deposition layers could be produced with the tailor-made process, which shows a high potential for the repair of high-performance tools.

Index Terms—repair welding, laser cladding, tool steels, powder metallurgy, inductive preheating

I. INTRODUCTION

Laser deposition welding occupies a key position in modern toolmaking [1]. The increasing processing of high-strength alloys and composite materials in areas such as the automotive industry or mechanical engineering leads to reduced tool life. In order to extend the service life and develop high-performance tool components, deposition and repair welding represents a cost and resource-saving alternative to the continuous purchase of new tools [2]. The process of repair welding is performed by first removing the damaged or worn material by grinding and then polishing the part to obtain a bright and clean surface. Afterwards, an operator uses a welding process to manually apply additional material in form of a filler wire. Fig. 1b shows the principle of laser cladding. Finally, the original shape of the tool is restored by cutting processing or spark erosion. By using a suitable welding process and a suitable filler material, hard and wear-resistant edge layers with sufficient toughness can be produced so that both worn areas and chipped edges can be rebuilt. However, the repair of tools made of selected special tool steels poses a great challenge, as these are considered to have limited weldability.

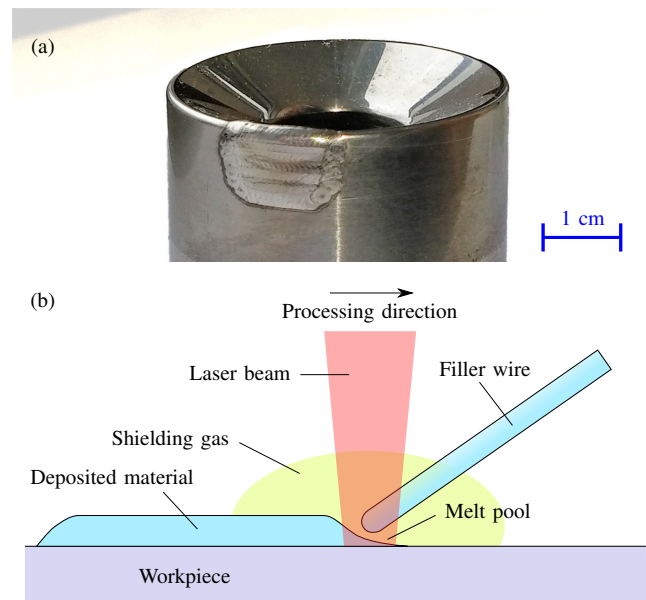


Fig. 1. Laser repaired tool before machining (a) and principle of manual laser deposition welding (b).

II. TECHNICAL BACKGROUND

During the welding process of high-alloy tool steels e.g. produced by powder metallurgy, there is a high susceptibility to cracking due to the special alloy compositions. High residual stresses result from the high temperature gradients during cooling or from phase transformations, which can ultimately lead to failure of the weld seam and to tearing out all of the applied material.

One way to counteract this behaviour of the material is to preheat the substrate to temperatures above 200 °C [3], [4]. This measure extends the cooling time of both the weld metal

as well as the heat-affected zone (HAZ) and reduces the risk of cold cracks. The aim of the presented work is to achieve this by means of a suitable simultaneous inductive preheating of the base material.

III. PREPARATION AND EXPERIMENTS

In the first step, a suitable inductor geometry was determined using the FEA software COMSOL Multiphysics 5.4. For one thing, the inductor must preheat respectively postheat the area of the weld seam. Furthermore, the inductor must not hamper the operator in his work, so that good accessibility to the welding point is guaranteed during the process. The developed C-shaped inductor that was used is shown in Fig. 2a.

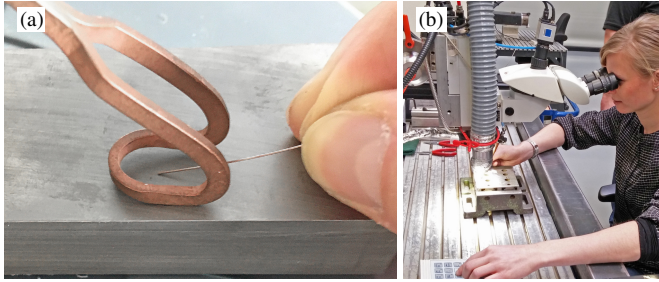


Fig. 2. Inductor for preheating (a) and experimental setup for manual laser cladding (b).

The welding tests were carried out on an experimental setup for manual laser cladding (Fig. 2b). This includes a Nd:YAG laser, which was operated in pulse mode (rectangular) with a power of 2800 W, a pulse frequency of 8.9 Hz and a pulse duration of 8 ms. That equals a pulse energy of 22.4 J and an average power of about 200 W. The welding speed was 340 mm/min. For preheating an induction generator MFG 10 from EMAG Eldec with an output of 10 kW was chosen. A conventional high-performance wire QuFe60 (1.3348, quada V+F) with a diameter of 0.4 mm was used as filler material. The high chrome tool steel Elmax (Uddeholm) hardened to 62 HRC served as the base material. The shielding gas was argon.

By means of preheating tests without laser welding, a Micro-Epsilon thermoMETER CTLaser pyrometer was used to determine the maximum preheating temperature that can be achieved when moving at welding speed at the focal point of the laser on the substrate surface. These tests showed that a stable preheating temperature of 210 °C was reached about 6 s after switching on the induction generator.

IV. RESULTS

During the welding tests without preheating, the applied material tore out of the substrate already after the first layer (Fig. 3a). As a result, multilayer cladding welds were not possible. With the addition of the inductor, the material had significantly better weldability. By means of preheating, cladding welds with ten layers exhibiting no cracks could be achieved (Fig. 3b), which is already sufficient for common repair welds. In addition, larger areas could be welded without failure compared to no preheating (see Fig. 3a and b). In the comparison regarding the achieved hardness of the layers no considerable deviations could be detected. This means

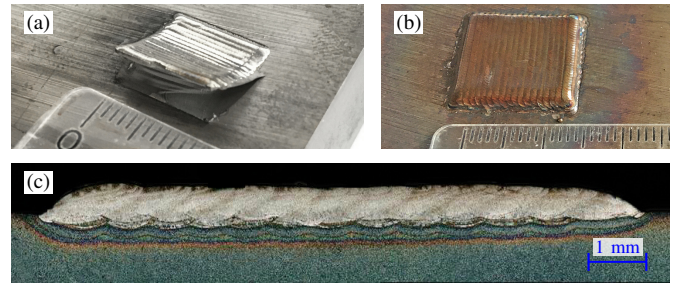


Fig. 3. Torn out single-layer cladding without preheating (a), preheated ten-layer cladding without cracks (b) and microsection of a three-layer cladding.

that consistently high hardnesses can be achieved despite preheating. Microsections show cladded layers without cracks or pores and a good bond to the base material (Fig. 3c).

This behaviour is due to the significantly reduced cooling rates of the weld metal and the HAZ. The findings generated from the tests validate the results of a simulation model created with the FEA software simufact.welding 8.0. A weld bead consisting of 26 single spots was analyzed once without and once with the preheating used in the tests showing a strongly reduced cooling rate when preheating (Fig. 4).

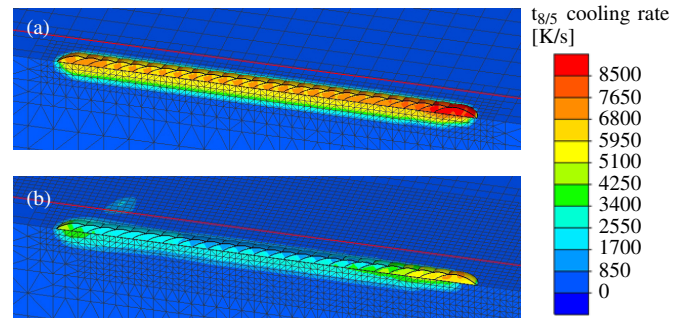


Fig. 4. Sectional view of the weld seam and FE calculated $t_{8/5}$ cooling rate without (a) and with preheating (b).

V. CONCLUSION

The results of the investigations show that by means of inductive preheating crack-free cladding of high-alloy tool steels, which tend to crack strongly during welding, is possible. As a result, tools repaired by the used procedure can be expected to have a longer service life before they fail again. Simultaneous heating with the developed C-shaped inductor eliminates the need for upstream complete heating of large workpieces, reduces the process time and energy consumption.

REFERENCES

- [1] Jhavar, S., Paul, C. P., Jain, N. K. (2013). "Causes of failure and repairing options for dies and molds: A review," *Engineering Failure Analysis*, 34, 519–535, September 2013.
- [2] Toyserkani, E., Khajepour, A., Corbin S. (2004). "Laser Cladding," CRC Press, July 2004.
- [3] Šturm, R., Štefanikova, M., Steiner Petrovič, D. (2015). "Influence of pre-heating on the surface modification of powder-metallurgy processed cold-work tool steel during laser surface melting," *Applied Surface Science*, Volume 325, 203–210, January 2015.
- [4] W. T. Preciado, C. E. N. Bohorquez (2006). "Repair welding of polymer injection molds manufactured in AISI P20 and VP50IM steels," *Journal of Materials Processing Technology*, 179, 244–250, October 2006.

Model experiments using slag during CdO recovery

E. Blumbergs^{1*}, J. Freibergs¹, E. Platacis¹, M. Maiorov¹, V. Serga²

¹ Institute of Physics University of Latvia, Miera str. 32, Salaspils, LV-2169, Latvia.

² Institute of Inorganic Chemistry, Riga Technical University, P. Valdena, 3/7, 1048 Riga, Latvia

* eblumb@edu.lu.lv

Abstract— A new method of production of cadmium from shredded cadmium-containing batteries using electroslag remelting was proposed, investigated theoretically and experimentally.

The reduction of cadmium from cadmium oxide with carbon occurs in electroslag remelting equipment in a liquid slag bath. The resulting molten cadmium is collected in a crucible under a layer of molten flux. The intensity of the reduction process is affected by the liquid flux movement. This movement is caused by thermal convection and also by the electrical current interacting with the magnetic field. The work explores the possibility of intensifying the process using the external magnetic field. Magnetic fields are induced by different configurations of permanent magnet systems located outside the bath.

Keywords— Metallurgical applications, Numerical and experimental methods.

I. INTRODUCTION

The development of the technology for recycling and repossession of the exhausted small batteries and storage batteries is a vital problem worldwide, nevertheless, the process keeps going on and new methods of solving the problem appear. The project proposes a new method for recycling cadmium-containing storage batteries and small batteries. The method implies electroslag remelting of preliminary grinded cadmium-containing storage batteries and small batteries.

II. PRESENTATION OF THE PROBLEM

The collecting and recycling of the exhausted batteries and accumulators is very urgent nowadays. The repossession of these wastes is one of the most challenging problems of the secondary raw materials recycling. In fact, almost all batteries contain toxic substances in the form of various metals and chemical compounds, which, when the battery bodies are destroyed, contaminate the surroundings. Lead, nickel, cadmium, mercury, silver oxide, cobalt and lithium are used in the production of the batteries. Nickel-cadmium batteries used in cell phones are the most significant potential sources of cadmium; of large danger are also mercury and lithium batteries as mercury and lithium contaminants to the environment.

The battery recycling is a process aimed to reduce and operate the materials from which the batteries are made of. During this process, the metals are extracted from the batteries, which are then recycled to new products. The goal of this process is the preservation of electricity and raw materials. Recycling of such products contributes to the preservation of the environment for healthy life of human beings.

The project proposes a method for recycling cadmium-containing storage batteries and small batteries. The method implies electroslag remelting of preliminary

grinded cadmium-containing storage batteries and small batteries. The cadmium contained in the storage batteries is powder-like cadmium/cadmium oxide. The reduction of cadmium by carbon from cadmium oxide during electroslag remelting ensures a maximum extraction of cadmium from secondary waste.

The reduced cadmium and the cadmium contained in the metal scrap in the crucible are liquid under the layer of melted flux which prevents the evaporation of cadmium and cadmium oxide. The temperature regime of electroslag remelting will ensure the melting of cadmium and the reduction of cadmium oxide by carbon, without bringing cadmium and cadmium oxide to boiling during the reduction. The cadmium from the crucible will be cast into molds from under the flux layer which is molten on the surface in the crucible, which ensures ecological safety of the technological process.

When investigating the electroslag remelting of the cadmium-containing scrap, it is planned to select a composition of the fluxes acting in the process, with the following criteria: the density in molten state should be lower than the density of cadmium oxide and cadmium, the flux melting point should be lower than the melting point of cadmium oxide and cadmium. The flux components must not interact with cadmium oxide and cadmium. A study of the chemical composition of flux and metallic cadmium and their morphology is planned at all stages of electroslag remelting.

We are also investigating the influence of temperature regimes² of electroslag remelting on the quality and quantity of the final product (cadmium).

An advantage of this technology is that when applied it can easily replace the traditional grinding systems with compact and high-performance units. Moreover, the new method is characterized by the low power consumption and is perfect for grinding solid materials, but in this case, the full period of recycling of waste batteries remains incomplete.

The method used in the project for the recycling of cadmium-containing storage batteries and small batteries is devoid of the drawbacks of previous projects and ensures the recycling completeness. The preliminary grinding of the cadmium-containing storage batteries and small batteries prior to electroslag remelting will contribute to the maximal reduction of cadmium by carbon from cadmium oxide:



The reduction reaction occurs at a temperature exceeding 500 °C.

Electroslag remelting will be performed by a graphite electrode.

Some characteristics of cadmium are important for choosing material of liquid slag in the remelting bath:

Melting temperature of Cd: 321.1°C.

Boiling temperature of Cd: 766.8°C.
Density of Cd at the melting temperature: 7.996 g/cm³.

For such big temperature diapason of liquid Cd it was easy to choose the slag with melting and boiling temperatures lower than those of cadmium and density smaller than that of Cd. These characteristics corresponding for ZnCl₂:

Melting temperature of ZnCl₂: 290°C.
Boiling temperature of ZnCl₂: 756°C.
Density of ZnCl₂ at the melting temperature: 2.54 g/cm³.

The boiling temperature of ZnCl₂ is 10.8°C lower than that of Cd. This is very important from the ecological point of view. When the temperature in the remelting process of cadmium containing waste is raised above the working temperature 600°C and reaches the vaporization temperature of ZnCl₂ (756°C), first starts evaporate covering flocs ZnCl₂, and only after covering flocs is fully vaporized and temperature raised by 10.8°C, starts the evaporation of Cd. So, the ecologically safe conversion and extraction of Cd from cadmium containing waste is performed.

III. CONCLUSIONS

The experimental device for electroslag remelting has been developed and produced (Fig. 1).

In a series of experiments a possibility to obtain cadmium from scrap of batteries containing cadmium was shown. The scrap was poured with liquid zinc chloride and brought their temperature to the temperature of cadmium reduction from cadmium oxide. The carbon was added to crap and carbon electrodes were used in the electroslag installation.

In first experiments, the difference was not observed between cases with and without the external magnetic field applied.

In the course of investigations, model experiments on the reduction of Cd by carbon C from cadmium oxide CdO under a ZnCl₂ flux layer were carried out.

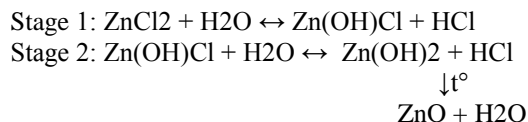
The experimental conditions were the following:

1. the reduction of Cd under the flux was performed in a muffle furnace at 500 0C during one hour;
2. the amount of CdO was 128 g;
3. the amount of carbon C was 24 g (powder-like fraction);
4. cadmium oxide CdO and carbon C were being stirred for 5 minutes in a closed 2-litre plastic container;
5. after stirring, the mixture of CdO and C was poured into a metallic mold made of stainless steel;
6. in the mold, 0.5 kg of zinc chloride ZnCl₂ was put over the surface of the CdO and C mixture;
7. the mold was placed into the muffle furnace heated up to 123 °C and was kept heating at the heating rate 12.5 °C/min.

Upon the reduction in the muffle furnace and analysis and visual observation of the samples using the optical microscope, the following conclusions have been drawn.

The hygroscopicity of zinc chloride ZnCl₂ was of significant impact on the obtained results. The mold heating

in the presence of moisture in the zinc chloride leads to its partial hydrolysis in two stages.



When heating zinc chloride ZnCl₂, in the flux there are Zn(OH)Cl, Zn(OH)₂, and ZnO.

When exposed to cold and humid air, a reaction takes place:

$2\text{Zn(OH)Cl} + 3\text{ZnO} + 4\text{H}_2\text{O} \rightarrow \text{Zn}_5(\text{OH})_8\text{Cl}_2 \cdot \text{H}_2\text{O}$
is simoncolleite which was found in the samples as the main crystalline phase after leaching by H₂O.

Therefore, with reference to the results of the XRD analysis, it is not possible to definitely conclude on the form of Cd (either Cd or CdO) in the analyzed sample.

Preparation of powder samples for investigation.

The obtained after the reduction reaction samples were milled in the agate mortar, washed in distilled water for 15 min and rinsed by distilled water twice to remove ZnCl₂. The obtained black powder contains unreacted CdO, reduced Cd, insoluble in water Zn₅(OH)₈Cl₂·H₂O, prepared for light microscopy. The investigated black powder was placed on a white surface covered with a sticky layer. By pressing it to the surface, the material under investigation is maximally covered. The excess powder is removed. Using another surface with a sticky layer, non-sticky particles of the powder material are removed. This procedure is repeated several times. In this way, a sample with a monolayer of the material under study and with the cleared outer surface of the metal particles is prepared for optical microscopy. By choosing the polarized light lighting mode, glowing is achieved (reflection of metallic spherical particles; the spherical reflective particles most likely are metallic Cd).

Acknowledgments. The work was supported by project no. Z-LZP16-ZR-N-815.

REFERENCES

- [1] R. Kachaev, C. Suleimanov, O. Shabanov. Structure and electrical conductivity of melted zinc chloride in balanced and strongly non-balanced state. Sci. J. Melts, 2011, no. 6, pp. 40-47 (in Russian).
- [2] M. Babaev, S. Gadzhiev, A. Iskakova et al. Behaviour of melted ZnCl₂ in pulsed electric fields of high intensity. Electrochemistry, 2009, vol. 45, no. 2, pp. 245-249 (in Russian).
- [3] S. Gadzhiev, A. Iskakova, R. Kachaev et al. Win effect in melted magnesium chloride. Electrochemistry, 2011, vol. 47, no. 2, pp. 235-239 (in Russian).

Chip-level bonding for microelectronic components by induction sintering of micro structured Ag particles

Patrick Rochala
Institute for Machine Tools and
Production Processes (IWP)
Chemnitz University of Technology
Chemnitz, Germany
patrick.rochala@mb.tu-chemnitz.de

Christian Hofmann
Department System Packaging
Fraunhofer Institute for Electronic
Nano Systems (ENAS)
Chemnitz, Germany
christian.hofmann@enas.fraunhofer.de

Martin Kroll
Institute for Machine Tools and
Production Processes (IWP)
Chemnitz University of Technology
Chemnitz, Germany
martin.kroll@mb.tu-chemnitz.de

Maik Wiemer
Department System Packaging
Fraunhofer Institute for Electronic
Nano Systems (ENAS)
Chemnitz, Germany
maik.wiemer@enas.fraunhofer.de

Verena Kräusel
Institute for Machine Tools and
Production Processes (IWP)
Chemnitz University of Technology
Chemnitz, Germany
verena.kraeusel@mb.tu-chemnitz.de

Abstract— A new induction based sintering process for chip level bonding of power electronics components is presented in which silver particles containing pastes are used as bonding material. Using finite element methods, the bonding process was analyzed and optimized so that efficient sintering of the particles could be achieved in subsequent heating and bonding tests. Therefore, the process has great potential for application in the industrial production of electronic components.

Keywords— Induction bonding, chip-level packaging, FE simulation

I. INTRODUCTION

Power electronics can be regarded as a solution for a multitude of technical challenges of the 21st century. For example, power electronic modules are primarily integrated into electric drives, power supply systems, converters for photovoltaic and wind energy plants, rail vehicles as well as hybrid and electric vehicles. Typical power electronic components are diodes, IGBTs (Insulated Gate Bipolar Transistor), MOSFETs (Metal-Oxide-Semiconductor Field-Effect Transistor), bipolar transistors or power LEDs. Figure 1 shows the schematic structure of a power electronics module.

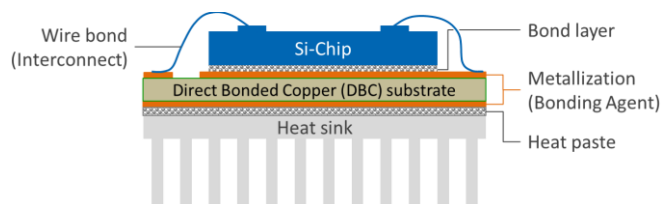


Figure 1: Schematic structure of a power electronics module in semiconductor technology.

In order to meet the rapidly increasing requirements in the electronics industry, the integration of complex and highly efficient power modules into electronic assemblies is essential. This is accompanied by the need to improve heat dissipation through thermal conductivity, temperature resistance, electrical conductivity and current carrying capacity [1]. The aforementioned properties are determined by the semiconductor-related packaging and interconnection technology, in particular the connection techniques and materials between

chip and substrate. The resulting pressure to innovate has the effect that most technological improvements in power electronics are currently taking place in the area of chip bonding [2] [3]. The present work contributes to this trend.

II. TECHNICAL BACKGROUND

For the bonding of silicon chips with a ceramic based substrate commonly used in power electronics (Direct Bonded Copper, DBC), several alternative bonding technologies are available in addition to lead-free soldering. Examples are thermocompression bonding, eutectic bonding, adhesive bonding, and as of late silver sintering (e.g. Ag sintering). The induction based Ag sintering technology presented here is a new promising process for realizing cohesive connections between semiconductor components and DBC.

To date, the particle sintering in chip bonding is based on thermal conduction. The heat is produced by an external ceramic hotplate and transferred through the whole bonding setup with process temperatures of up to $T_p = 280\text{ °C}$ [4] at high pressure loads of up to $p = 30\text{ MPa}$ [5]. Consequently, temperature sensitive power modules and bonding connections of heterogeneous materials with different thermal expansion coefficients can only be manufactured to a limited extent, since thermomechanical stresses in the bonding zone lead to the failure of the connections. Thus, the integration density and the choice of filler materials are limited. Time-intensive heating and cooling phases also cause long cycle and process times.

The induction based sintering process with rapid heating presented here allows for selective heating of the bond. In comparison to convective Ag particle sintering, the aim is to bond components onto a DBC substrate without integral heating, at low pressure and within short process times. Compared to other chip bonding processes currently used, the new inductive process offers advantages due to the formation of a highly thermally conductive Ag intermediate layer and high energy efficiency.

III. BONDING BY INDUCTION SINTERING

The process sequence of the newly developed method is as follows: The micro structured silver paste layer is applied

by screen printing to the DBC substrate. The silver sintering paste is then dried at moderate temperatures so the organic components of the paste can evaporate and only polymer chains of higher volatilization temperature remain in the layer. They act as an adhesive and stick the particles together. The electronic component is then placed on the sinter paste and the stack is inserted, positioned and fixed in the jig of a chip bonder. Subsequently, a single turn inductor is positioned around the chip so that the sinter layer can be heated through the inner field. A bond head that acts as a pressure stamp is placed on top of the chip to apply the bonding force. The bonding process is introduced when the electromagnetic field is applied. The electromagnetic field induces eddy currents in the metallic particles. These currents cause resistance heating, especially at the particle boundaries due to the contact resistance. As a result of the temperature increase and the applied pressure, the particles start to sinter and bond to the substrates so a firm bonding between the components is established. Depending on the bonding pressure, bonding time and the applied electromagnetic field, the densification of the sintered layer can be varied. Additionally, diffusion between sintered layer and substrate can be controlled by means of the process parameters and thus the quality of the bonding can be adjusted. Figure 2 shows the schematic experimental setup of the new inductive bonding process.

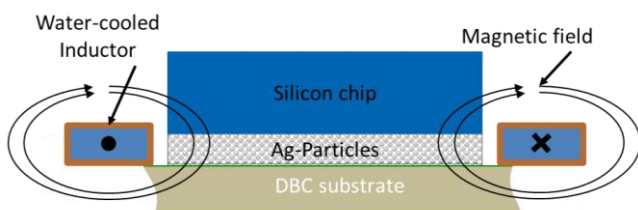


Figure 2: Schematic depiction of the experimental setup of the new inductive bonding process.

IV. EXPERIMENTAL AND SIMULATION INVESTIGATIONS

In a first step, the process of heating both in the sintered layer and in the components was simulated using finite element methods. The software COMSOL Multiphysics and the corresponding AC/DC module were used. The planned experimental setup for bonding was modeled for this purpose. Simplifications on the model, especially with regard to temperature and pressure dependent material properties of the sintered layer, were necessary because the simulation of the sintering and melting behavior of the particles is complex. Furthermore, the thermodynamic behavior of the nano particles are not yet fully understood and depends on a large number of boundary conditions. The aim of the simulations was to map the heat generation and distribution both in the sintered layer and in the components to be bonded, depending on the electromagnetic power input, the bonding time and the inductor geometry. Furthermore, a suitable inductor geometry had been developed to facilitate an effective and homogeneous heating limited to the bonding area.

The simulation analyses were complemented by heating and bonding tests. Therefore, diodes and Si dummies (Figure 3) constituted electronic components and DBC as well as Si substrates bonding partners. The bonding surface of the components was coated by Ag or Au bonding agents. The Si substrate was Au-coated. The silver paste consisted of micro scaled Ag powder (μAg) which was applied by dispensing, aerosol-jet-printing and screen-printing and then dried at temperatures $T_d < 120$ °C. To perform and monitor heating,

sintering and bonding experiments, a setup was developed. The most important features of this installation are the precise positioning of the bonding partners and the induction coil, the controlled introduction of a bonding pressure as well as the possibility to observe the components during the bonding process by means of an infrared transparent pressure stamp using a thermal camera. The test data thus generated could then be used to validate the simulation results.

V. RESULTS

By means of simulation, a suitable inductor geometry for the bonding process could be determined. By multistage fitting of the inductor geometry to the workpiece geometry as well as the adaptation of coil contour to the chip dimensions, the heat generation in the heating process could be effectively limited to the bonding zone. In the heating experiments, the findings from the simulation could be validated to a large extent. In the bonding experiments, it was also possible to bond the DBC substrate firmly to the chip. Figure 3 shows the scanning electron microscope image of an inductively sintered silver layer obtained by focused ion beam (FIB).

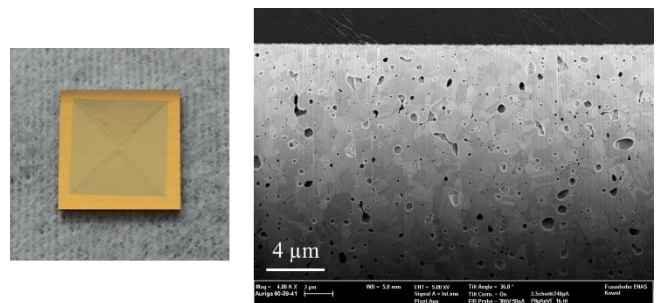


Figure 3: Sinter paste printed on Si-dummy coated with Au bonding agent (left), scanning electron microscope image of an inductively sintered silver layer (right).

VI. CONCLUSION

Within the scope of the investigations it could be shown that induction sintering of micro structured silver particles may be used for bonding processes on chip-level. Using simulation tools, an inductor geometry adapted to the geometry of the components to be bonded was determined for the bonding process and tested in heating and bonding experiments. Due to the very rapid heat generation by means of induction, potentially very short process times for bonding can be realized. As a result, the bonding process has great potential for application in industrial power electronics production.

REFERENCES

- [1] C. Rössle, T. Gottwald, Anforderungen an die Leistungselektronik, Teil 1, all-electronics, 2016.
- [2] C. Le Bret, J. Azémar, P. Gueguen, From Technologies to Market - Power packaging 2015, 2015.
- [3] C. Le Bret, Z. Zong, M. Grao Txapartegi, P. Gueguen, H. Lin, M. Rosina, From Technologies to Market - Status of power electronics industry 2016, 2016.
- [4] C. Mertens, Die Niedertemperatur-Verbindungstechnik der Leistungselektronik, Dissertation, Technische Universität Braunschweig, 2004.
- [5] F. Roscher, Printed metallic nanoparticles as intermediate layers for low temperature wafer level packaging and as alternative towards conventional wire bonding, WaferBond '15 - Conference on Wafer Bonding for Microsystems, 3D- and Wafer Level Integration, 2015.

Advanced Induction Heat Treatment Systems of Pipes

Ivan Vegera

The Physical-Technical Institute
of the National Academy of Sciences of
Belarus
Minsk, Belarus
smt0@tut.by

Victor Demidovich

Russian Technologies of Induction
Heating Ltd.
Saint-Petersburg, Russia
vbdemidovich@mail.ru

Yuri Perevalov

Saint Petersburg
Saint-Petersburg Electrotechnical
University «LETI»
Saint-Petersburg, Russia
yyperevalov@yandex.ru

Abstract — New approach of designing and control of induction heat treatment installations of pipes with utilizing of numerical models is developed. Models include two-dimensional simulation of coupling electromagnetic and temperature fields in cylindrical systems for processing of pipes. Also, thermal and structural tension during heating and cooling of pipes are simulated. These data allow defining structure, hardness, the size of grain and other properties of the pipes. They allow optimizing design and a choice of equipment, a heat treatment mode for achievement of the maximum quality and minimization of energy consumption. The developed models were used not only for the design of induction heat treatment systems of pipes and rolls, but also for a digital control of these complexes.

Keywords - continuous heat treatment line, temperature control system, induction heating, multi-zone heating

I. INTRODUCTION

Induction heating technology is widely used in steel industry. Induction heating installations in the metallurgical industry have a power level that may exceed several hundreds of kilowatts or even tens of megawatts. In spite of the fact that induction hardening has successfully been applied in industry for many years [1], there is a growing demand in industry for a more precise process control. Also, it is necessary to develop new technology of induction heating of pipes with big diameter. Heat treatment of pipes is important stage in manufacturing of high quality steel products like lengthy pipes with big diameters. Hardening and annealing are main types of heat treatment of pipes. Modern heat treatment means strict observance of temperature evaluation during heating, controlled cooling and, probably, repeated heating. Using of computer simulation is a powerful and necessary approach for solving these problems [2].

II. MATHEMATICAL MODELS

From the physical point of view the induction hardening is a very complicated process (Fig. 1). We should include all the significant phenomena to the mathematical description to achieve an acceptable calculation result. Moreover, it is very important to understand that all phenomena are coupled with each other. It is obvious that induction hardening mathematical description should include the electromagnetic, thermal and phase transformations phenomena. But the resulting workpiece properties are strongly depend on stress-strain state (residual stress) due to summation stress effect with the external load. Moreover, stress is an additional

driving force for the phase transformation. That's why it is desirable to describe this phenomenon too.

Effective numerical models of technological process of heat treatment are developed. They include two-dimensional modeling of electromagnetic and temperature fields in system [3]. Also, thermal tension during heating and cooling of pipes and rolls are simulated. These data allow defining structure, hardness, the size of grain and other properties of metal of the pipes and rolls.

The developed two-dimensional models were extremely effective not only at design of induction heat treatment systems of pipes, but also for a digital control these complexes. Using modular structure of induction heaters gives significant advantages in induction heating technology, since it allows optimizing the operation modes of equipment in relation to: energy consumption; scale formation; the ability to maintain a constant exit temperature.

III. INDUCTION HEAT TREATMENT OF PIPES

The heat treatment of pipes is important stage in production of high quality pipes with big diameters. Main types of heat treatment of pipes are annealing, normalization, aging, hardening etc. Dispersive hardening for two-phase (duplex) steel significantly improves properties of pipes.

Advantages of induction furnaces, such as absence of thermal inertia and high energy efficiency, are especially shown in the conditions of flexible change of temperature - time profile of the heat treatment. For pipes of small diameter, the greatest distribution was gained by induction installations of continuous action when the heating - cooling mode by direct placement of a zone of cooling behind the inductor is easily realized. Advanced digital control allows effective processing of possible disturbances, such as: changes in the speed, diameter and initial temperature of the workpiece, and therefore to minimize the amount of rejects during heating.

To fully realize the advantages of modular induction units, an advanced digital control system should include control algorithms for stationary and non-stationary operation modes of the heater that occur during the initial start-up of a heater or when the technological lines stop and restart after a stop, with a change in the productivity of processing lines. Non-stationary modes can be characterized by a strong change in the temperature field of the load and the electrical parameters of the heater, and potentially can lead to a large percentage of rejects.

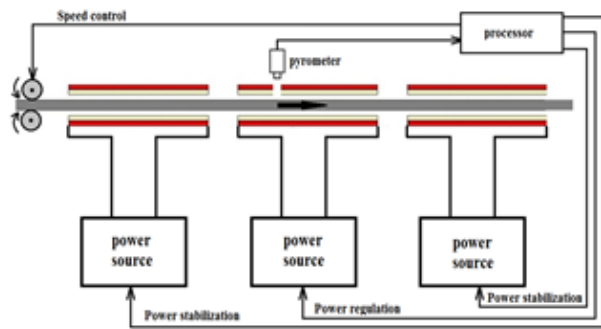


Fig.1. Diagram of the control system of a modular induction heater of the second type with a single control point

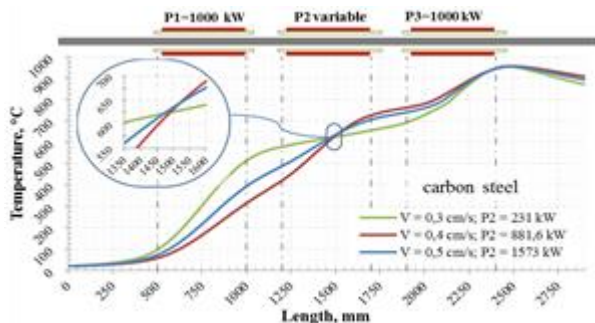


Fig.2 Distribution of the temperature field on the surface of the billet along the length of the modular induction heater using a 2-type ACS with single-point control for different power: 1 -3.5 t / h, 2 - 4.125 t / h, 3 - 4.7 t / h, 4 - 5.5 t / h

Investigation of the regulation of non-stationary operation modes of modular induction heaters was performed to determine the possibilities of reducing the changes in the temperature field of the load at the exit of the induction heater by means of an automatic control system with one temperature control point within the heater when controlling heating during the transient process, i.e. only one induction module (active zone).

The results of numerical modeling of the process of heating cylindrical billets using several modules with independent frequency converters have shown a high efficiency of induction heaters with this configuration. They enable the creation of a highly efficient and reliable control system for an induction heater based on three or more modules. In the installation of the three modules, the heating control of the workpiece occurs only on the second module (the "active zone") along the pyrometer, the sighting point of which is located at a certain point inside the second inductor, while the power in the first and third inductor is maintained at a constant level (Fig.1).

Temperature curves for this type of control (Fig. 2) obtained for different velocity of pipes intersect at one point inside the second induction module and have the same temperature at the exit from the last module of the induction heater. For heated thin bodies with linear properties, the existence of this point was analytically proved [3].

For cylindrical nonlinear bodies, modeling showed that, while maintaining a constant temperature at the point of intersection of temperature curves, by creating a system of automatic power control of the generator with feedback on the temperature fixed by an optical pyrometer at the control point, this method of regulation allows almost completely to remove fluctuations in the temperature at the exit of an

induction heating installation during the temperature transient processes.

However, realization of a necessary mode of heat treatment by space distribution of heating and cooling zones at a constant speed of movement of pipes in many cases is difficult to pipes of big diameter and demands unfairly big power of heating. And in this case, it is preferable to realize a stage induction heating of lengthy pipes that provides flexibility at realization of heat treatment. In this way heat treatment line consists of two separate zones: induction oscillating heating and quenching [4]. After heating to the required temperature, the pipe quickly moves to the cooling zone (Fig. 3).



Fig.3 – Stage hardening (two separate zones: induction oscillating heating and quenching)

Induction heating of pipes of big diameter possesses several features which need to be considered at equipment design.

1. For each diameter and thickness of pipes wall there is an optimum frequency of current with strong expressing of themaximum of electric efficiency. Therefore, a proper frequency choice is important at designing of energy saving induction heating systems.

2. In practice there is wide nomenclature of pipes diameters and thickness of a pipes wall. Procedure of a choice of number of replaceable inductors is developed for a guarantee of heating of any pipe with electric efficiency not lower than 10-15% from the maximum.

3. Special attention is paid to a lining choice at high-temperature heat treatment because of a big surface of thermal radiation. As temperature differences on thickness of a wall of pipes usually don't limit power, the choice of power of inductors is defined not only by productivity, but also achievement of high thermal efficiency.

REFERENCES

- [1] A. Muehlbauer, "History of Induction Heating and Melting", Vulkan Verlag, 2008.
- [2] Rudnev V., Loveless D., Lamonte J., Demidovich V., Powell J. "A balanced approach to induction tube and pipe heating Industrial Heating ",1998, 65(6) 53-57
- [3] Demidovich V.B. "Computer simulation and optimal designing of energy-saving technologies of the induction heating of metals", Thermal Engineering. 2012, vol. 59, № 14, pp. 1023-1034.
- [4] V. Demidovich , V. Andrushkevich , Yu. Perevalov, " Induction heat treatment of large diameter pipes and coils" 9th International Symposium on Electromagnetic Processing of Materials (EPM2018): IOP Conf. Series, 2018. - p.1-4. doi:10.1088/1757-899X/424/1/012064

Refined Model of Induction Heater Taken into Account Static Characteristics of Inverter

Vasily Frizen, Ivan Smolyanov, Salavat Fatkullin, Fedor Tarasov
Department of Electric Engineering and Electrotechnology Systems
Ural Federal University
Ekaterinburg, Russia
vfrizen@yandex.ru, i.a.smolyanov@gmail.com, solon2004@yandex.ru, f.e.tarasov@urfu.ru

Abstract — The paper is concerned with feasibility of the through heating calculation by using thermal circuits at the one-dimensional approximation. A part of paper is dedicated to justification of such approach applicability. The calculation is considered for a particular case of titanium cylindrical plants' treatment. Application of the proposed approach allows for considerable reduction of calculation time during the design process.

Keywords— Equivalent circuit, induction heating, thermal circuit,

I. INTRODUCTION

When solving problems of cylindrical workpieces' induction heating for the purpose of plastic deformation under real industrial conditions, one often faces a case when it is required to heat the workpieces of different lengths and diameters with different thermal and electrical properties in one and the same inductor. The present problem solving includes the ability to predict behavior of thermal and electromagnetic processes in such plants for correct adjustment of control system. The correct adjustment means selection of optimal parameters of temperature regulator for different operation modes providing the required heat quality (temperature distribution uniformity over a heated workpiece section) as well as maximum energy efficiency (high heat rate and minimum electric energy consumption) for each specific workpiece.

This paper is a sequel to the series of papers [1, 2] concerning titanium workpieces' treatment. The problems of the plant design optimization, the possibility of elimination of nonuniform heating over the workpieces' length and radius as well as numerical models' verification by means of experiment were considered in previous papers. The finite elements method was used in the previous papers as a basic method for calculation of titanium workpieces' induction heating. This method requires considerable computational resources and computation time. The new approach to solving the coupled task concerning computation of electromagnetic and thermal field for induction heating of cylindrical workpieces is presented in this paper.

II. DESCRIPTION OF THE HEATER

The heater consists of two copper water-cooled external and internal windings of inductor, which are connected in series. Every winding contains 54 turns. The external winding has a number of taps for efficient control of the workpieces' heating zone (bypassing the magnetic field). The paper considers a connection with all turns of the external winding. A lining is placed between the workpiece and the inductor. The geometry of the induction heating system is shown in Fig. 1. The installation is supplied by

frequency inverter with maximum full power of 300 kVA and rated frequency from 100 till 300 Hz and connected to compensation capacity. The inductor, the workpiece, the compensated battery and the supply source create the oscillation circuit. The full cycle of work of the induction heaters system is described in work [3].

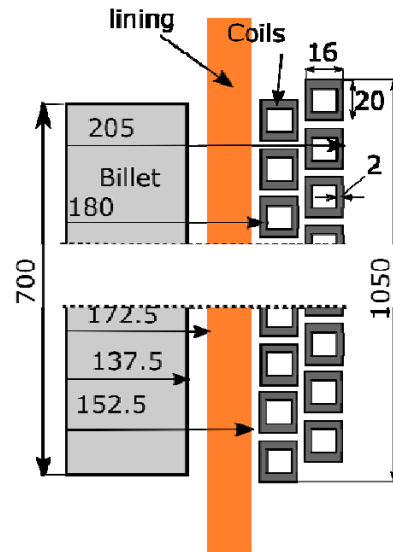


Fig. 1. Geometry of the induction heater

III. DESCRIPTION OF THE PROPOSED APPROACH

When solving electromagnetic field equation one can restrict to determination of integral parameters for the whole workpiece volume by means of equivalent circuit of inductive load due to small temperature difference during heating at the field penetration depth. In this case the source term of differential equation of heat balance (distribution of volumetric heat release in the load) can be calculated later on the basis of obtained solution of the differential equation of electromagnetic field in a one-dimensional statement. The frequency converter involves a certain difficulty during modeling. In this case the output parameters of the frequency converter depend on both the load circuit impedance, which changes during heating, and power control signal arriving at the input from the temperature regulator. Moreover, voltage at the converter output is non-sinusoidal and its harmonic composition depends largely on the operation mode (the set power level). The direct integration of converter model (with determination of instantaneous electrical values during solving) results in considerable increase in the required computational power in case the problem solving by the numerical methods due to a big difference between the time constants in the thermal and electrical problems. Therefore, for a converter model integration the array of stable operation modes across the entire range of the load

impedance variation and across the whole range of power variation was preliminary calculated in order to obtain the numerical model of converter by means of the calculated data interpolation. In this case the converter output current restriction was considered. The control circuit operates in the same time scale as the thermal model and therefore it can be described by means of the ordinary differential equations.

The equations system, the solution of which describes the system state, is as follows:

$$\frac{1}{r} \frac{\partial}{\partial r} \left(\lambda_r r \frac{\partial T}{\partial r} \right) + \frac{\partial}{\partial z} \left(\lambda_z \frac{\partial T}{\partial z} \right) = -q - c\rho \frac{\partial T}{\partial \tau}; \quad (1)$$

$$\frac{\partial}{\partial r} \left(\frac{1}{r m_z} \frac{\partial (rA)}{\partial r} \right) + \frac{\partial}{\partial z} \left(\frac{1}{m_r} \frac{\partial A}{\partial z} \right) - i\omega g A = -j_0 \quad (2)$$

$$j = -i\omega g A; \quad (3)$$

$$q = g^{-1} j^2; \quad (4)$$

$$j_0 = \frac{U}{Z_u \cdot S}; \quad (5)$$

$$U = f(Z_k, P_r); \quad \omega = f(Z_k, P_r); \quad (6)$$

$$P_r = K_p \cdot \Delta T + K_i \cdot \int_0^{\tau} \Delta T dt. \quad (7)$$

With consideration of the assumptions made, the system equation (1) can be presented in a one-dimensional statement and it can be solved by one of the numerical methods (in this case it is convenient to use the finite difference method or equivalent heat balance diagrams' method) (7)

$$\frac{1}{r} \frac{\partial}{\partial r} \left(\lambda_r r \frac{\partial T}{\partial r} \right) = -q - c\rho \frac{\partial T}{\partial \tau}. \quad (7)$$

Equations (2) – (5) can be replaced by a ready-made solution of the current density distribution in a cylinder with radius of m2:

$$J_m(m, T) = \frac{\sqrt{-2 \cdot i}}{\Delta(T)} \cdot H_{me} \cdot \frac{I_1(m)}{I_0(m_2(T))}, \quad (8)$$

IV. RESULTS

The heating process modeling and the regulators parameters optimization was performed both for the bar stock and cylindrical titanium workpieces of different size in inductors of two different diameters. Geometrical dimensions of one of inductors are presented in Table 1.

Table 1 – Geometrical dimensions of induction heater

Workpiece diameter, mm	165..196
Internal diameter of inductor, mm	285
Internal diameter of lining (concrete), mm	216
External diameter of lining (concrete), mm	248
Inductor length, mm	1050

The computation results of the Ti6Al4V alloy bar stock workpiece heating are presented below. The workpiece length is 380 mm, the workpiece diameter is 166 mm and the heating temperature is 850 °C. The obtained heating curves are presented in Fig. 2, the power and frequency curves are presented in Fig. 3

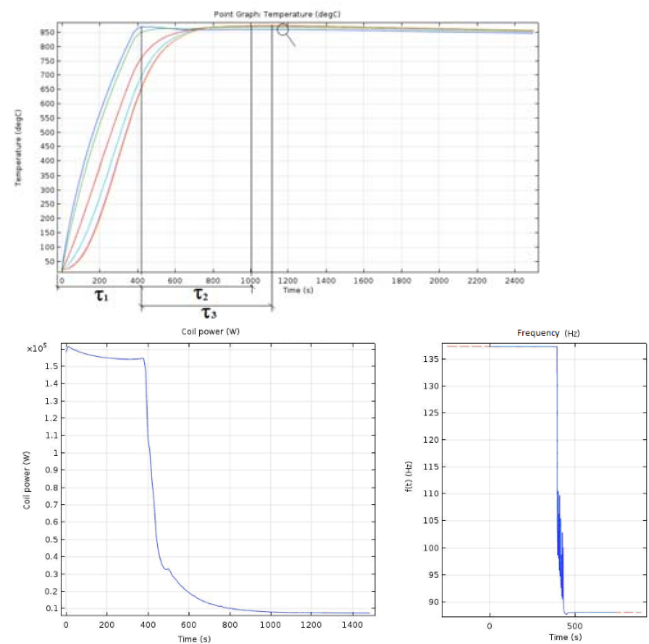


Fig. 3. Time dependence of the inductor power and current frequency

The variation of power consumed by inductor under the regulator control is seen from the obtained diagrams (maximum consumed power is 160.5 kW, maximum consumed power is 6.5 kW). The required heating quality was obtained for the regulator parameters calculated with the help of the model: the workpiece temperature at the end of heating was 850_{+8}^{-2} °C.

V. CONCLUSION

The obtained model of induction heating plant permits to make fast calculations of temperature fields in the cylindrical workpiece to sufficient detail with accuracy reasonable for temperature regulation. The model considers the peculiarities of the inductor electrical parameters variation during heating as well as operation peculiarities of the frequency converter being a part of induction equipment. For the induction unit model implementation one can use any mathematical software package capable for obtaining numerical solutions of differential equations systems.

ACKNOWLEDGMENT (Heading 5)

The work was supported by Act 211 of the Russian Federation Government, contract № 02.A03.21.0006.

REFERENCES

- [1] I. A. Smolyanov, V. Kotlan, I. Do;eze, «Optimal heat induction treatment of titanium alloys» COMPEL (In Press)
- [2] I. Smolyanov F. Sarapulov, S. Sarapulov « Induction Heating Control of Titanium Alloys» Proc. Int. Conf. CSCMP pp. 106-111, 2019.
- [3] Demidovich, V. & Pervalov, Y. 2019, "Advanced automated complex using induction and resistance furnaces for precise heating of the titanium billets", Proceedings - ICOECS 2019: 2019 International Conference on Electrotechnical Complexes and Systems.

Exposure to electromagnetic fields produced by industrial processes

Koen VAN REUSEL
Laborelec
Belgium
koen.vanreusel@engie.com

Abstract— The penetration in industrial practice of electrothermal processes is dependent on compliance with the legislation on the exposure of workers to electromagnetic fields. The purpose of this paper is to provide some typical values of the electromagnetic field around installations of industrial processing. To illustrate the typical values relevant for workers, three case studies with measurement results at industrial sites will be given going from 0 Hz (electrolysis), over kHz (induction heating installation), to MHz (dielectric drying line). A fourth case study with a three-phase cable at power frequency will illustrate how a modelling tool can be helpful to define a safety distance for workers and for the general public respectively.

Keywords—electromagnetic field, exposure limits, safety distance, exposure of workers, exposure of general public

I. INTRODUCTION

On 29th June 2013, Directive 2013/35/EU of the European Parliament and of the Council concerning the minimum health and safety requirements regarding the exposure of workers to the risks arising from physical agents (electromagnetic fields) entered into force [1]. The limits of exposure as listed in the Directive are based on the guidelines established by the International Commission on Non-Ionizing Radiation Protection (ICNIRP) [2]. The Directive makes a distinction between non-thermal effects (frequency between 0 Hz and 10 MHz) and thermal effects (frequency between 100 kHz and 300 GHz) of electromagnetic fields on the human body. The thermal effects are the most straightforward and the safety limits can be based on the maximum absorption of power that can be safely absorbed per unit mass of body tissue generated from exposure to electric and magnetic fields. From this maximum acceptable power, limits for the electric and magnetic field can be derived. For the non-thermal effects, it is the force of the fields that has an effect on the nerve system. As to the general public, the limits of exposure can be found in the European Council Recommendation on the limitation of exposure of the general public to electromagnetic fields (0 Hz to 300 GHz), published on 12th of July 1999 [3].

II. MEASURED VALUES AROUND INDUSTRIAL INSTALLATIONS TO ASSESS THE SAFETY FOR WORKERS

A. Electrolysis

Table I gives for 8 points of measurement the values for the static magnetic field (0 Hz) in mT for an electrolysis installation.

TABLE I - STATIC MAGNETIC FIELD AROUND ELECTROLYSIS INSTALLATION

Point	1	2	3	4	5	6	7	8
[mT]	18	22	25	56	63	73	84	87

The measurements are taken in the electrolysis hall at 1.5 m above the floor. The copper bars are at the ceiling (~ 5 m height). (For the sake of confidentiality, no pictures of the points of measurement can be shown.) At the instance of measurement, the direct current in the electrolysis system was 182 kA.

For the measurement of the static magnetic field (0 Hz), an isotropic Hall effect sensor with detection in the 3 axes is used (Holaday Industries, Model HI-3550). The device detects the peak of the static magnetic field and it is this value that is noted at each measurement point.

For the static magnetic field (0 Hz), there is a strong overshoot of the limit of 3 mT, which entails a risk of interference with active implanted devices such as cardiac pacemakers (risk already present from 500 μ T). These values also entail a significant risk of attraction and projection (risk present already from 3 mT). On the other hand, there is no exceeding of the exposure limit (2T).

B. Induction heating

The limit set out in the Directive (see Annex 2 of the Directive) decreases from 564 μ T to 526 μ T for frequencies between 532 Hz and 570 Hz and from 375 μ T to 300 μ T for the frequencies between 800 Hz and 1000 Hz, see Annex 2 of the just mentioned directive.

An isotropic probe (MASCHEK ESM-100) is used for the measurement.

For an induction heating installation of 240 kW and a frequency range between 800 Hz and 1 kHz, a maximum value of the magnetic field of 93 μ T has been measured at the operator's position at the filling of the crucible. This value is below the limit of 300 μ T. For an induction heating installation of 1250 kW and a frequency range between 530 Hz and 570 Hz, at the point where the electrical busbars enter the operation room (measurement taken at 1.5 m above the floor), a maximum value of the magnetic field of 110 μ T has been measured at 532 Hz. This value is below the limit of 564 μ T. (For the sake of confidentiality, no pictures of the points of measurement can be shown.)

C. Radiofrequency installation

A radiofrequency drying installation at 27,12 MHz is measured at nominal power (for reasons of confidentiality no further details can be given).

The measurements of the electric field are carried out using a Holaday isotropic electric probe, type HI-4422.

Magnetic field measurements are performed using a Schwarzbeck type FSH3D antenna installed on a Rohde and Schwarz type FSH8 spectrum analyzer.

TABLE II – ELECTROMAGNETIC FIELD AROUND HIGH FREQUENCY DRYER

Point of measurement	B (μT)	E (V/m)
1	0,02	2,3
2	0,00	0,3
3	0,01	0,4
4	0,00	0,2
5	0,00	0,3
6	0,00	0,2
7	0,00	2,8
8	0,00	0,7
9	0,00	0,3
10	0,00	0,3
11	0,01	0,8
12	0,00	0,3
13	0,00	0,3
14	0,01	1,0
15	0,00	2,4

The measurements are taken along the installation - in the immediate vicinity - that is to say 30 cm - from the outer casing. (For the sake of confidentiality, no pictures of the points of measurement can be shown.)

In the frequency band between 10 MHz and 400 MHz, the electric field cannot exceed 61 V/m. The magnetic field cannot exceed 0.2 μT . Table II gives the measured values for the magnetic and electric field at 15 different points of measurement around the installation at 30 cm from the casing.

The conclusion here is that at a distance of 30 cm from the outer casing, the limit of 61 V/m for the electric field and 0.2 μT for the magnetic induction is nowhere exceeded.

III. MODELISATION OF A CABLE AT POWER FREQUENCY TO DEFINE A SAFETY DISTANCE FOR WORKERS AND FOR THE GENERAL PUBLIC

New cables (type EXeCVB 1 x 240 RM / 25, 15kV) will be placed on the façade of a factory. The cables are cable ladders in galvanized steel (type HD KL 110). The cables are in trefoil position.

Each conductor traversed by a current emits a magnetic field. Each energized conductor emits an electric field. The magnetic field is evaluated by simulation and the results are compared with the limits prescribed in the standard for workers and in the European Recommendation for the general public. The evaluation of the electric field does not require calculation because the cables are fitted with a screen. It is enough to put at least one of the two ends of this screen to ground to suppress the electric field. The evaluation of the magnetic field requires a calculation by finite elements in 2 dimensions. The modeling is done in COMSOL Multiphysics® Modeling. The result of the modelisation is given in Fig. 1.

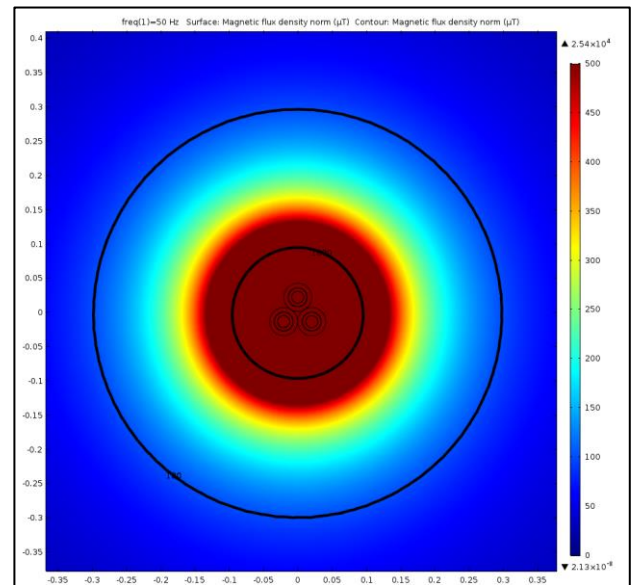


Fig. 1 - The magnetic field [μT] around a cable (distance in [m])

The model does not take into account the galvanized steel ladders. Galvanized steel is a low-magnetic steel, its shielding capacity extends only to high frequency and not to 50 Hz frequency.

The current is 630 A.

The value of the magnetic field decreases with the distance of the cable and the two circles in black give the distance at which the field decreased down to 1000 μT (limit for workers) and 100 μT (limit for the general public). The value of 1000 μT is located 10 cm from the cable; the value of 100 μT is reached at 30 cm from the cable. Consequently, a safety distance of 10 cm for workers, and 30 cm for the general public can be respectively defined.

IV. CONCLUSION

The values for the electromagnetic field around installations of industrial processing can be easily obtained by measurement and/or by numerical modelling. The European Directive 2013 /35/EU and the European Council Recommendation 1999/519/EC provide limits for safety assessments for workers and the general public. The assessment is not only a legal obligation, but it offers also a possibility to define safety distances where necessary.

REFERENCES

- [1] DIRECTIVE 2013/35/EU OF THE EUROPEAN PARLIAMENT AND OF THE COUNCIL of 26 June 2013 on the minimum health and safety requirements regarding the exposure of workers to the risks arising from physical agents (electromagnetic fields).
- [2] <https://www.icnirp.org/>
- [3] COUNCIL RECOMMENDATION of 12 July 1999 on the limitation of exposure of the general public to electromagnetic fields (0 Hz to 300 GHz) (1999/519/EC).
- [4] Cigré Technical Brochure 795 – Extrapolation of measured values of power-frequency magnetic fields in the vicinity of power links (2020), Cigré WG C4.28, www.e-cigre.org.

Jesus Oswaldo Garcia
 Cemef / Mines ParisTech
 Sophia Antipolis, France
 jesus-oswaldo.garcia-carrero @mines-paristech.fr

François Bay
 Cemef/Mines ParisTech and Transvalor
 Sophia Antipolis, France
 francois.bay@mines-paristech.fr

Jose Alves
 Transvalor
 Sophia Antipolis, France
 jose.alves@transvalor.com

Julien Barlier
 Transvalor
 Sophia Antipolis, France
 julien.barlier@transvalor.com

Abstract—This paper focuses on error analysis for modelling induction heating processes

Keywords— finite element modelling, error analysis, mesh refinement

I. INTRODUCTION

The Induction heating process is widely used today in manufacturing processes - for instance, to preheat the material before forming process (forging, stamping, rolling, brazing), or during heat treatment (quenching), surface treatment [1]. This process relies on the use of eddy currents generated inside a workpiece by an AC current running through a coil (Fig.1). The computational modelling tools for designing these processes require dealing with at least electromagnetic/heat transfer couplings.

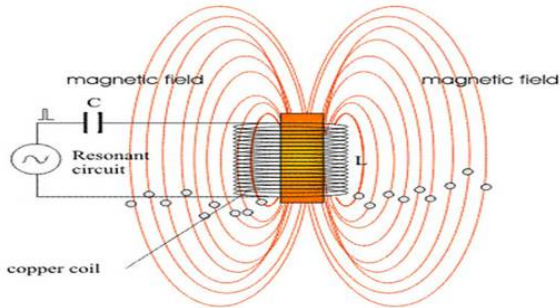


Fig. 1. Induction heating processes

However, one of the problems with the finite element tools used for modelling these processes is to make sure that these tools can be used in a reliable way.

We shall introduce here cases for which we will carry out an error analysis by studying convergence with the mesh size.

These cases will be modelled with the FORGE Induction software [2], which we will describe in the next section.

II. THE COMPUTATIONAL TOOL

A. The mathematical model

The model couples the electromagnetic model with the heat transfer one. The electromagnetic model is classically

based on the quasi-static Maxwell equations (1) completed by the electromagnetic constitutive laws (2).

$$\begin{aligned}\vec{\nabla} \times \vec{E} &= -\partial_t \vec{B} \\ \vec{\nabla} \times \vec{H} &= \vec{j} \\ \vec{\nabla} \cdot \vec{B} &= 0\end{aligned}\quad (1)$$

$$\begin{aligned}\vec{j} &= \sigma \vec{E} \\ \vec{B} &= \mu \vec{H}\end{aligned}\quad (2)$$

The heat transfer model is given by (3)

$$\rho C \frac{\partial T}{\partial t} - \vec{\nabla} \cdot (k \vec{\nabla} T) = \vec{j} \cdot \vec{E}\quad (3)$$

B. The numerical approximation

The electromagnetic equations are then integrated in global A-V potential formulation. Finite element discretisation is then carried out using tetrahedral finite elements; edge finite elements [3] are used for determining the magnetic vector potential field 'A' while classical nodal elements are used for the electric potential 'V'. In order to be more efficient in terms of parallel computations, it has been decided to use a global finite element approach to solve the problem – rather than a mixed finite element/boundary element approach. A global domain is thus defined - embedding the workpiece, the inductors, as well as an air domain wide enough in order to model accurately electromagnetic wave propagation. A weak coupling strategy is used for coupling the electromagnetic and thermal problems; EM computations are carried out only when variations of electromagnetic parameters with temperature exceed a given threshold specified by the user – typically 5%.

III. ERROR ANALYSIS FOR SPECIFIC CASES

A. The a posteriori error estimator

The error estimator implemented in this work is based on a smooth recovery method, which does not require solving problems on patches and involves global problems that can be solved in parallel. The methodology consists on building a smooth magnetic field [4], starting from one that is already known. In order to build the smooth field for determining the numerical solution error, we have implemented the Galerkin or residual minimization method to obtain a stable approach based on a conservation problem. Let \vec{X}_{P_0} be the field obtained from the finite

element analysis and \vec{X}_{P_1} the recovered field. The method consists in solving the global minimization problem

$$\min \|\vec{X}_{P_1} - \vec{X}_{P_0}\|^2 \quad (4)$$

Now, let $\vec{\psi}_d$ be the interpolation function on the edges. The field can then be expressed in a discrete form by

$$\vec{X}_{P_1} = \sum_j x_{P_{1j}} \vec{\psi}_j \quad ; \quad \vec{X}_{P_0} = \sum_i x_{P_{0i}} \vec{\psi}_i \quad (5)$$

Since \vec{X}_{P_1} is the unknown, the minimisation problem is solved by projecting $\vec{X}_{P_1} - \vec{X}_{P_0}$ on the base functions of the edge mesh as follows:

$$\langle \sum_j x_{P_{1j}} \vec{\psi}_j - \sum_i x_{P_{0i}} \vec{\psi}_i, \vec{\psi}_k \rangle = 0 \quad (6)$$

$$\sum_j \langle \vec{\psi}_j, \vec{\psi}_k \rangle x_{P_{1j}} = \sum_i \langle x_{P_{0i}} \vec{\psi}_i, \vec{\psi}_k \rangle \quad (7)$$

Knowing that the term $x_{P_{0i}} \vec{\psi}_i$ is provided by the finite element solution, we have:

$$\sum_j \langle \vec{\psi}_j, \vec{\psi}_k \rangle x_{P_{1j}} = \sum_i \langle \vec{X}_{P_0}, \vec{\psi}_k \rangle \quad (8)$$

The field calculated by system (8) is represented on the edges elements ($\vec{X}_{P_1}^{edges}$). Thus, a transformation must be performed to compare it with the initial field. This technique allows to transform the field from the edges to the integration points ($\vec{X}_{P_1}^{int.p}$), where the initial field is also stored. The transformation is performed by the following expression:

$$\vec{X}_{P_1}^{int.p} = \sum_{i=1}^{edges} \sum_{k=1}^{int.p} (\vec{X}_{P_1}^{edges} \vec{\psi}_i)_k \quad (9)$$

The linear field specified above has a one order higher accuracy compared to the initial field. By comparing the smooth P_1 field to the P_0 solution, we can calculate the error as:

$$e_H = \|\vec{H}_{P_1} - \vec{H}_{P_0}\| \quad (10)$$

B. Case study

We present the well know benchmark problem “TEAM7” (Testing Electromagnetic Analysis Methods) of the International Compumag Society. This problem consists of a thick aluminium plate with a hole, which is placed eccentrically, is set unsymmetrically in a non-uniform magnetic field. The field is produced by the exciting current which varies sinusoidally with time.

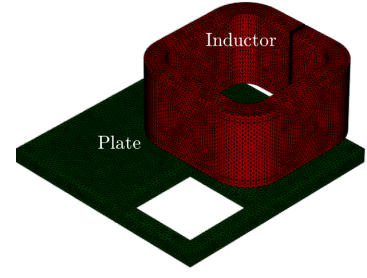


Fig 2: Benchmark problem TEAM 7

The error estimator is verified by performing a convergence analysis on decreasing uniform mesh sizes. The mesh size and the estimator results are show in the Fig 3.

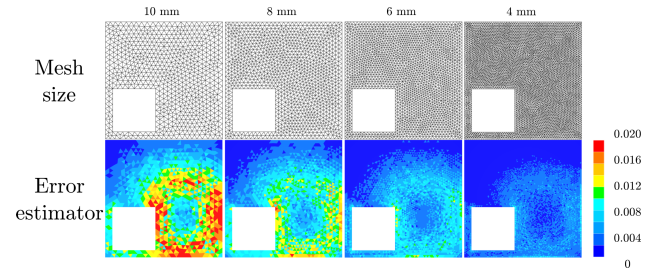


Fig. 3: Magnetic field error.

C. Conclusion

We presented recovery-based *a posteriori* error estimator for the Induction heating process modelling, applied to a fully immersed finite element method approach in conjunction with a full-time integration of the Maxwell equations. This estimator uses the Galerkin method, and has been implemented to build a magnetic field with a higher interpolation order. Finally, results on a Benchmark case test were presented, showing the convergence of the estimator.

REFERENCES

- [1] “Conduction and induction heating (Livre, 1990) [WorldCat.org].” [Online]. Available: <https://www.worldcat.org/title/conduction-and-induction-heating/oclc/20016205>. [Accessed: 19-Oct-2020].
- [2] J. R. Alves Zapata and F. Bay, “Modeling and Analysis of Electromagnetism in Magnetic Forming Processes,” *IEEE Trans. Magn.*, vol. 52, no. 5, May 2016, doi: 10.1109/TMAG.2015.2501758.
- [3] J. C. Nédélec, “A new family of mixed finite elements in \mathbb{R}^3 ,” *Numer. Math.*, vol. 50, no. 1, pp. 57–81, Jan. 1986, doi: 10.1007/BF01389668.
- [4] M. Ainsworth and A. Craig, “A posteriori error estimators in the finite element method,” *Numer. Math.*, vol. 60, no. 1, pp. 429–463, Dec. 1991, doi: 10.1007/BF01385730.

Numerical Approaches to Analyzing of MHD Processes Occuring to Induction Pump

I. Smolyanov, E. Shmakov, D. Braznik
 Department of Electric Engineering and Electrotechnology
 Systems
 Ural Federal University
 Ekaterinburg, Russia
 i.a.smolyanov@gmail.com

Juris Vencels
 EOF Consulting
 Riga, Latvia
vencels@eof-consulting.com

Abstract— The major aim of the work is to show new modern opportunities of numerical simulation of magnetohydrodynamic phenomena using open source codes. The work is considered a question of calculating main induction pumps features taken into account process of continuum dynamics. In order to solve the strong coupled problem of electromagnetic and velocity fields it was used a coupler between Elmer and OpenFOAM programs. The coupler called EOF-library serves to properly transfer calculating data between Elmer and OpenFOAM. Electromagnetic field is described by well-known A-V formulation implemented to finite element program Elmer. And hydrodynamic field is calculated by finite volume method, implemented to OpneFOAM, using modified pimpleFoam solver. The obtained results are compared to date calculated by Comsol Multiphysics software.

Keywords— FVM, FEA, FEM, induction pump, head-capacity curve, instability of flow, EOF, OpenFOAM, Comsol

I. INTRODUCTION

Induction pumps as a special case of magnetohydrodynamic pumps are used in many industries, for example, metallurgy, nuclear energy, military, etc. The major purpose of the pump is to pump out a liquid metal having electrical conductivity from one place to other. The opportunity of contactless action on metal is a main advantage among pumps aimed to pumping metal. The main disadvantages are difficult operating conditions of these pumps (high temperatures) and lack of pumps capable of operating in a certain operating range. The problem of difficult operating conditional, as a result of which the windings of pump inductor burn out, have been solved in work [1], and the drawback associated with lack of pump working under certain pressure and mass flow rate have been solve in work [2]. The solutions are shape optimization and design problems, and in the work MHD processes causing instability of flows are neglected. The flows essentially act on performance capability of the pumps. The issue is especially acute in work related to nuclear energy, as in [3, 4], in which opened type of magnetic circuit of inductor (longitudinal edge effect, see Fig. 1), asymmetry of supply currents, finite duct width (transversal edge effect, see Fig. 2), increased gap between duct and inductor cause instability of flow of pumped liquid.

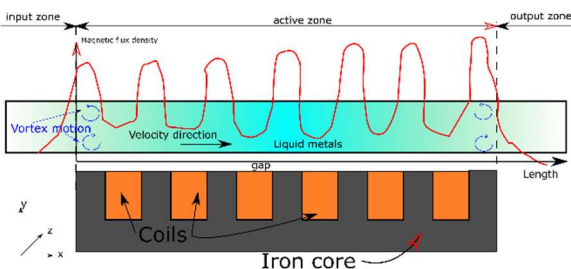


Fig. 1. Longitudinal edge effect

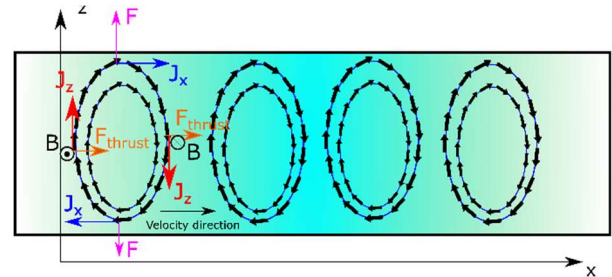


Fig. 2. Transversal edge effect

These effects are often difficult to consider when calculating this type of pump. In [5], a simplified model based on detailed equivalent circuits is used to calculate such installations, and the transverse edge effect is taken into account using the analytical coefficient. The authors of [6, 7, 2] used the commercial ANSYS package in their calculations of MHD pumps, which uses finite volume method to calculate velocity field and magnetic field using finite element method. The main drawback is method of data transfer from FEA model to FVM model and vice versa. This procedure, implemented in these works, significantly increases the calculation time and accuracy. There are a number of works in which MHD completely consider the problem with the help of FEM, for example, in [5]. As is well known, the Navier-Stokes equation is poorly resolved using finite element discretization, which is a drawback of this calculation approach. For this purpose, magnetic problem will be solved using the finite element method implemented to open source Elmer program, and CFD problem will be calculated by the FVM realized to OpenFOAM free software. Data transfer between these problems will be realized by open coupler EOF-library.

The purpose of this work is to combine the unanimous experience of previous work in calculating the related problems of magnetic and field velocity using the example of an induction pump for pumping magnesium. The major advantages of the coupler are several types of data extrapolation and fast and accurate data exchange between the problems. Detailed information of the coupler was published in the article [8].

II. FORMULATION OF THE PROBLEM

Calculation of magnetic field of induction pump [1], was executed using well known A-V formulation (1) by Elmer and Comsol, that was discussed to works [1, 5]. Both programs is based on FEM, but for the last one scalar electric potential is equal $V = 0$.

$$\Delta \mathbf{A} + \mu \sigma \nabla V + j \mu \sigma \omega \mathbf{A} - \mu \sigma [\mathbf{v} \times \text{rot} \mathbf{A}] = \mu \mathbf{j}_{ext}, \quad (1)$$

where \mathbf{A} is the value of magnetic potential vector, σ is the electrical conductivity, μ is depicted the magnetic permeability, \mathbf{j}_{ext} is the current density, \mathbf{v} is the velocity, V is the electric scalar potential.

Velocity field was calculated in OpenFOAM working with finite volumes and in Comsol based on finite elements using the well-known Navier-Stokes equation for incompressible liquids (2-3):

$$\frac{\partial \mathbf{u}}{\partial t} + (\mathbf{u} \cdot \nabla) \mathbf{u} + \nu \Delta \mathbf{u} - \frac{1}{\rho} \nabla p + \mathbf{f} \quad (2)$$

$$\nabla \cdot \mathbf{u} = 0 \quad (3)$$

\mathbf{u} is the velocity vector, ν is the kinematic viscosity, ρ is the mass density, p is the pressure, \mathbf{f} is the vector of electromagnetic force.

Data exchange during the decision process between OpenFOAM and Elmer is carried out using the EOF coupler [8]. Comsol Multiphysics is a commercial program that allows using the user interface to establish an exchange between tasks for calculating magnetic and field velocities.

III. RESULTS

Head-capacity curve for 2D case were obtained using Comsol and EOF (Fig. 3). It is worth noting that in the Comsol transverse edge effect was taken into account using the Bolton coefficient. These differences are caused by flux instabilities in the magnetic field, which must be correctly resolved in order to obtain accurate results. For this purpose, three-dimensional cases with fine and coarse meshes were solved by EOF. In the main part of the work, the main measures to reduce the instability of flows will be discussed. It is also worth noting that the quality of the mesh in some modes significantly affects the quality of the results (Fig. 4 and Fig 5) with an increase in speed, the influence of the quality of the mesh decreases.

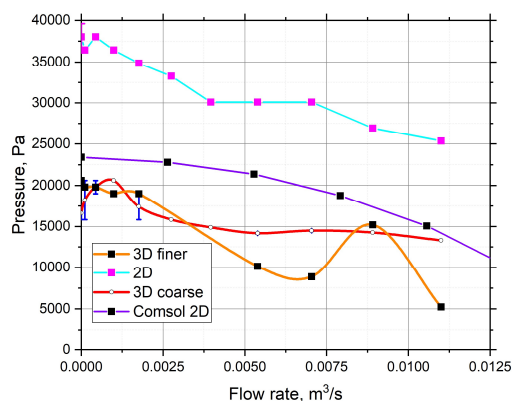


Fig. 3. Head-capacity curve

ACKNOWLEDGMENT

The work was supported by Act 211 Government of the Russia Federation, contract № 02.A03.21.0006.

I would also like to thank Andris Jakovics, who organized the MHD summer school at the University of Latvia. The knowledge gained in these courses helped to conduct these studies.

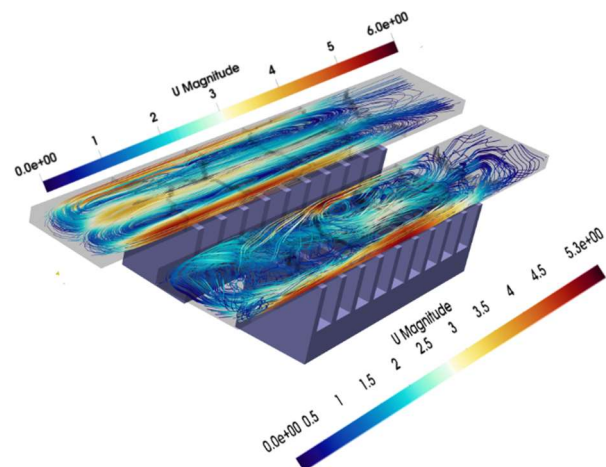


Fig. 4. Velocity profile coarse (up case) and fine (down case) mesh at 0 m/s inlet velocity

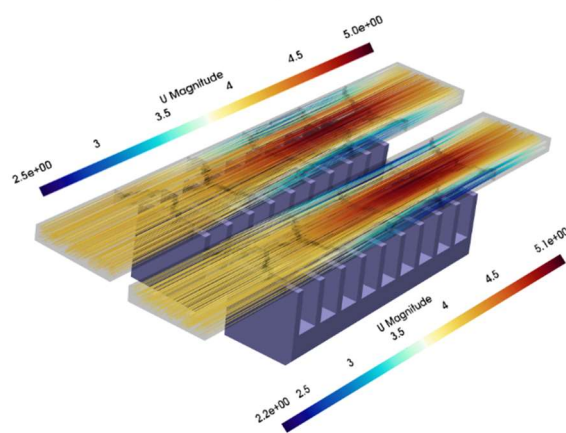


Fig. 5. Velocity profile coarse (up case) and fine (down case) mesh at 81/20 m/s inlet velocity

REFERENCES

- [1] Tarasov, F.E. et. al. InductionMHD-pump with flat coils, Acta Technica CSAV, Vol. 60 No. 1 pp. 71-79, 2015
- [2] V. Geza, B. Nacke, «Numeroca; simulation of core-free design of a large electromagnetic pump with double stator» Magnetohydrodynamics, Vol. 52, No. 3, pp. 417-431, 2016
- [3] Araseki, H., Kirillov, I.R., Preslitsky, G.V., Ogorodnikov, A.P. «Magnetohydrodynamic instability in annular linear induction pump. Part II. Suppression of instability by phase shift» Nuclear Engineering and Design, Vol. 236, No. 9, pp. 965-974, 2006
- [4] Araseki, H., Kirillov, I.R., Preslitsky, G.V., Ogorodnikov, A.P., «Magnetohydrodynamic instability in annular linear induction pump: Part I. Experiment and numerical analysis» Nuclear Engineering and Design, Vol. 227, No. 1, pp. 29-50, 2004
- [5] Sarapulov F., Smolyanov I., Tarasov F., Bolotin K., Shvydkiy E. «Numerical simulation of double side linear induction pump for liquid magnesium», Magnetohydrodynamics, Vol. 53, No. 4, pp. 603-609, 2017
- [6] Timofeev V., Khatsayuk M., Timofeev S. «Analysis of the transverse end effect in the MHD stirrer for molten metals» Magnetohydrodynamics, Vol. 53, No. 3, pp.521-536, 2017
- [7] Khatsayuk, M., Timofeev, V., Demidovich, V. «Numerical simulation and verification of MHD-vortex» COMPEL - The International Journal for Computation and Mathematics in Electrical and Electronic Engineering (in Press).
- [8] Juris Vencels, Peter Raback, Vadims Geza «EOF-Library: Opensource Elmer FEM and OpenFOAM coupler for electromagnetics and fluid dynamics»

Investigation of Heating of Rotating Disks in an Electromagnetic Field Using Strong Permanent Magnets

Alexander Lepeshkin
Institute of Technology
Moscow Aviation Institute – National
Research University
Moscow, Russia
lepeshkin.ar@gmail.com

Alexander Kuvaldin
Institute of Electrical Engineering
National Research University –
Moscow Power Engineering Institute
Moscow, Russia
a.kuvaldin2013@yandex.ru

Stepan Lepeshkin
Institute of Electrical Engineering
National Research University –
Moscow Power Engineering Institute
Moscow, Russia
stepan111@gmail.com

Abstract—A new method for heating of the rotating disks using strong permanent magnets is proposed. The results of studies of the thermal state of a rotating model disk in a magnetic field created by permanent magnets on the spin rig are presented. The developed method can be used for heating small-sized rotating disks and products.

Keywords—heating, rotating disk, permanent magnets, electromagnetic field, spin rig

INTRODUCTION

The various heating methods are used: induction, aerodynamic, gasdynamic, radiation for the implementation of thermal processes in bodies of revolution for conducting accelerated and thermocyclic tests of disks and parts of aircraft gas turbine engines (GTE) and turbines of power plants on specialized spin rig [1-4]. The induction heating makes it possible to ensure high heating rates and to obtain a predetermined non-uniform distribution of temperatures along the radius of the disk, corresponding to operating conditions during tests on spin rigs [1-3]. A conventional induction heating system consists of several flat ring inductors located at different radii of the disk. Its disadvantage is: the impossibility of obtaining additional thermal energy due to rotation, because axisymmetric inductors. The experiments and acceleration tests with induction heating of rotary disks on the spin rig are associated with significant material costs.

Currently, the development and application of energy-saving heating methods is relevant. One of these new heating methods is the heating of parts using strong permanent magnets with improved characteristics. When a part rotates in a magnet field, the electromotive force (EMF) is induced in it and, thus, thermal energy appears (power of internal heat sources under certain conditions depending on the shape of the magnet).

The development of a heating technique - the generation of thermal energy in disks through rotation (production of power from internal heat sources) in a magnetic field created by permanent magnets is an urgent task. In thermocyclic tests, the maximum rotational speed of the disks can be between 20000 and 60000 rpm.

THE RESULTS OF INVESTIGATIONS

The thermal state of disks rotating in a constant magnetic field at the initial stage was studied using magnets from samarium-cobalt alloys, because they have not only significant magnetic induction up to 1 Tesla, but also operate at elevated temperatures up to 250-300 ° C. However, it should be borne in mind that they are fragile.

EMF is induced when the disk rotates in a magnetic field created by a permanent magnet, in accordance with the law

of Faraday's electromagnetic induction. As a result, induced currents occur. At a low speed, the indicated EMF is small. With an increase in the rotational speed, the rate of change (pulsation) of the magnetic flux in the disk increases and the induced emf becomes significant in the range of high rotational speeds. As a result, the power of internal heat sources increases and the intensity of heating of the rotating disk increases.

In this paper, a new method for heating rotating disks (round plates) in a constant magnetic field is considered, taking into account the release of power from internal heat sources at various rotation frequencies [4]. The paper [5] presents a method of heating a rotating pipe using strong magnets.

The thermal state of the model disk (made of stainless steel) rotating in the field of permanent magnets was studied on the spin rig. The disk was prepared with thermocouples at three radii. The disk and mount with magnets mounted in a vacuum chamber are shown in Fig. 1.

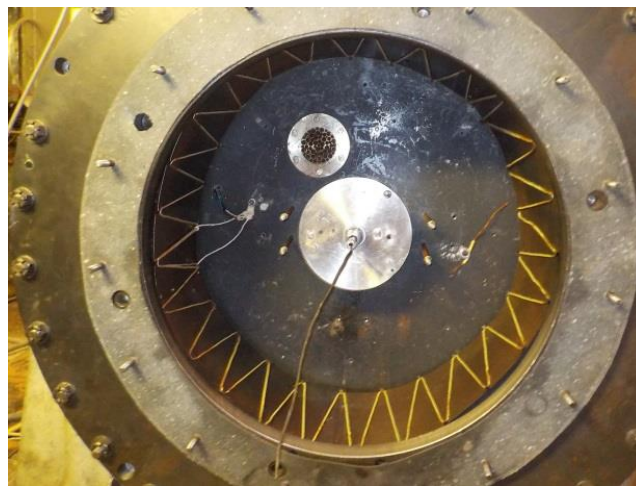


Fig.1. Model disk installed in the vacuum chamber of the spin rig.

A gap of 5 mm is set between the disk and the magnets. Disk temperatures were measured through a mercury current collector using a computer system. In fig. 2 shows the temperature distribution of the disk at different frequencies of rotation of the disk at different radii, depending on the frequency of rotation during the experiment. A maximum temperature was observed at a radius of 100 mm, which was close to the midline of the installed magnets.

In these experiments, the thermal state of the model disk was studied at rotational speeds of up to 15000 rpm. At this speed, the maximum temperature was 440 ° C. From the analysis of the extrapolated dependence 3 (Fig. 2) with a

radius greater than 100 mm, it follows that at the outer radius of the disk the temperature can be 640 °C. At higher speeds, the discs should be expected to heat up to a higher temperature.

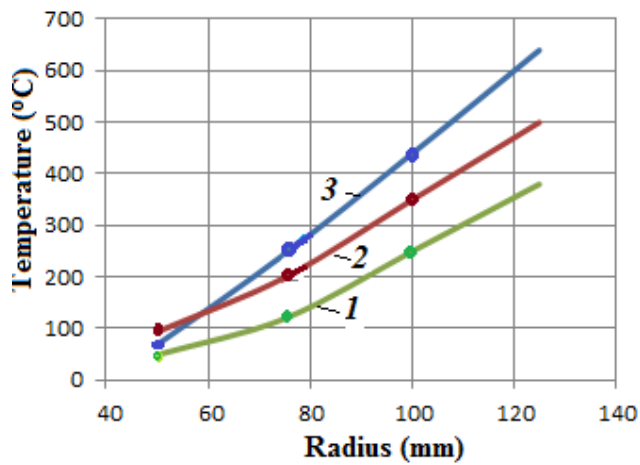


Fig.2. The temperature distribution of the disk at different speeds: 1 - 5000 rpm, 2 - 8000 rpm, 3 - 15000 rpm.

CONCLUSION

A new method (energy-saving) of heating of the rotary disks using permanent magnets is proposed. The results of studies of the thermal state of a model disk rotating in a magnetic field created by permanent magnets on the spin rig are presented. The developed method can be used for heating small-sized rotating disks and products and aluminum and other cylindrical billets.

REFERENCES

- [1] A.B. Kuvaldin and A.R. Lepeshkin, "High-speed modes of induction heating and thermal stress in products," Monograph. M.: Infra-M, 2019, 282 p.
- [2] A.B. Kuvaldin and A.R. Lepeshkin, "High-speed induction heating," Electrotechnical Encyclopedia: in 4 volumes / edited by A.F. Dyakov (ch. ed.), M.: Publishing house MPEI, 2009, vol. 3, p. 175.
- [3] A.B. Kuvaldin, A.R. Lepeshkin and S.A. Lepeshkin, "A test method for disks of turbomachines and bandages of rotors of turbogenerators using induction heating," Electricity, No. 7, 2009, pp. 33–38.
- [4] A.B. Kuvaldin, A.R. Lepeshkin and S.A. Lepeshkin, "A method of producing energy and a device for its implementation," Pat. 2416869, Russian Federation, publ. 04/20/2011, bull. 11.
- [5] P. Karban, F. Mach and I. Dolezel, "Higher-order finite element modelling of rotational induction heating of nonferromagnetic cylindrical billets," International Symposium on Heating by Electromagnetic Sources, Padua, May 18-21, 2010, pp. 515–522.

Calculation Fluid Dynamic of Induction Pump Using Open Source Software

1st Evgeniy Shmakov
Department of Electrical Engineering
and Electrotehnlogy Systems
Ural Federal University
Ekaterinburg, Russia
shmakov.evgeny@urfu.ru

2nd Ivan Smolyanov
Department of Electrical Engineering
and Electrotehnlogy Systems
Ural Federal University
Ekaterinburg, Russia
i.a.smolianov@urfu.ru

3rd Juris Vencels
EOF Consulting
Riga, Latvia
vencels@eof-consulting.com

Abstract—In the paper, when simulation of an induction pump being used two approaches, executing recalculation of electromagnetic problem per a time step and without one. Simulation is carried out by means of open source software packages Elmer and OpenFoam with EOF-library. In the simulation, a three-dimensional model of a laboratory induction pump is used. Ultimately, $p-Q$ characteristics and velocity distributions in the duct is presented, as well as conclusions on the obtained results.

Index Terms—induction pump, EOF, p-Q characteristic, numerical simulation, CFD

I. INTRODUCTION

Modern industry solves a wide range of tasks that arise during technological operations. One of the problems is the non-contact impact on liquid metals, which can occur, for example, in cooling circuits or during operational process at metallurgical enterprises. One solution of this problem is electromagnetic pumps. Non-contact impact can be provided by pumps with rotating permanent magnets [1] as well as induction pumps [2].

In this article the simulation of an induction pump with a three-phase power system is considered. The advantage of such devices is the ability to develop high flow rate compared to other electromagnetic pumps [2].

Today, numerical simulation application is the most promising in this area, since it is possible to take into account most of the effects of such pumps. But the main problem is coupled calculation of the electromagnetic and fluid dynamic problems. Such problem can be solved by means of commercial software packages such as Ansys or Comsol Multiphysics, or by open source softwares, namely, Elmer and OpenFoam with EOF-library [3]. In this work open source softwares are used.

II. POBLEM STATEMENT

A laboratory induction pump is used as an object of study. The main installation parameters of the pump are given in the tab. I.

Liquid aluminum is used as the pumped metal with the following properties: the electrical conductivity equals to $3.85 \cdot 10^6 \frac{Sm}{m}$, the kinematic viscosity equals to $10^{-6} \frac{m^2}{s}$, the density equals to $2380 \frac{kg}{m^3}$.

TABLE I
IDUCTION PUMP SPECIFICATIONS

Parameter	Value
Power supply frequency, Hz	50
Inductor length, m	0.295
Inductor yoke width, m	0.077
Back iron height, m	0.0116
Back iron width, m	0.06
Air gap, m	0.001
Slot width, m	0.02
Slot height, m	0.04
Tooth width, m	0.0115
Number of turns in the slot	136
Number of slots	9
Duct thickness, m	0.0082
Duct width, m	0.077

As mentioned earlier, the calculation is performed by Elmer and OpenFoam. The calculation of the electromagnetic problem is carried out using the finite element method in Elmer, and the calculation of fluid dynamic is performed using the finite volume method in the OpenFoam.

Since velocity in the duct is significant, the magnetic Reynolds number will be more than 1, consequently taking into account the velocity in the duct is required. This article compares two approaches to account for melt velocity:

- 1) For electromagnetic problem, velocity is set uniform throughout the duct and the electromagnetic problem is not recalculated;
- 2) Velocity in the duct is calculated using eq. (4) and electromagnetic problem is recalculated when the velocity changing its value.

III. MATHEMETICAL DESCRIPTION

In this paper, magnetic field is calculated based on the Maxwell's equations in AV-formulation:

$$\Delta \mathbf{A} - \mu \sigma \nabla V - j \mu \sigma \omega \mathbf{A} + \mu \sigma [v \times \text{rot} \mathbf{A}] = -\mu \mathbf{j}_{ext}, \quad (1)$$

where \mathbf{A} is the value of the magnetic vector potential, σ is the electrical conductivity of the material, μ is the magnetic permeability of the material, \mathbf{j}_{ext} is the current density vector, v is the velocity, V is the electric scalar potential.

Induced current density depending on the melt velocity is calculated as follows

$$\sigma(\mathbf{E} + \mathbf{U} \times \mathbf{B}) = \mathbf{j}, \quad (2)$$

where \mathbf{E} is the induced electric field strength, \mathbf{U} is the velocity of fluid, \mathbf{B} is the magnetic flux density.

The force acting on the melt, is calculated by the eq. (3):

$$\mathbf{F}_L = \frac{1}{2} Re(\mathbf{j} \times \bar{\mathbf{B}}), \quad (3)$$

where \mathbf{F}_L is the Lorentz force.

The calculation of fluid dynamic is performed by Navier-Stokes equation for an incompressible fluid:

$$\frac{\partial \mathbf{U}}{\partial t} + (\mathbf{U} \cdot \nabla) \mathbf{U} - \nu \nabla^2 \mathbf{U} = g + \frac{\mathbf{F}_L}{\rho}, \quad (4)$$

where ν is the kinematic viscosity, g is the acceleration of gravity, ρ is the fluid density.

IV. RESULTS

The main aim of this research is to consider various approaches to simulation of induction pump. In the following paragraphs, a comparison of $p-Q$ characteristics and distribution of velocity in the duct is provided.

The calculation is performed at the current density in the slot equals to $2.11 \frac{A}{mm^2}$. Realizable $k-\varepsilon$ model have been chosen as the turbulence model.

A. Comparison of $p-Q$ characteristics

The obtained characteristics are presented in fig. 1.

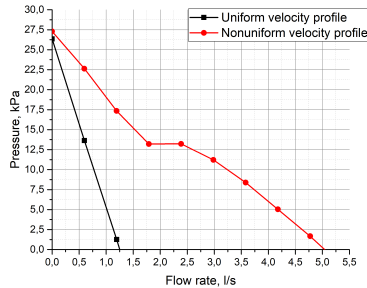


Fig. 1. Comparison of $p-Q$ characteristics

Based on the obtained dependencies, it can be seen that the first approach provides the result, where the maximum flow rate value of the pump will be smaller, since the nonuniform distribution of velocity in the duct is not taken into account. It is also seen that the characteristics have a significant difference.

B. Distribution of velocity in the duct

In the next part of paper, velocity profile in the duct is shown for various above mentioned simulation approaches. In order to conduct the comparison it have been taken zero values of the flow rate for both approaches and $5 \frac{l}{s}$ for hard coupled approach and $1.25 \frac{l}{s}$ for other one.

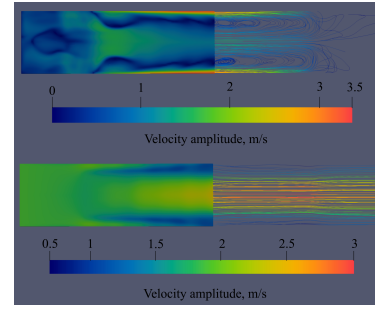


Fig. 2. Distribution of velocity (the first case)

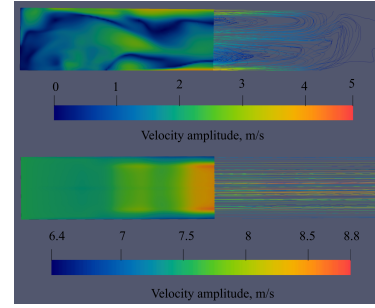


Fig. 3. Distribution of velocity (the second case)

Velocity distribution of the duct for the first and the second cases are presented in fig. 2 and fig. 3.

It can be seen from the figures that the velocity distribution is symmetrical along the duct width in the first case (fig. 2), and the velocity difference between the inlet velocity and the maximum velocity is less than for the second case. Also it should be noted that flow is instable (there are lots of vortices) at initial flow rates, and at higher flow rates it becomes more stable.

V. CONCLUSIONS

Based on the above results, it can be concluded that the results obtained are dramatically different from each other, which indicates that the approach doing calculation of the electromagnetic problem with the assumption of a uniform distribution of velocity in the duct cannot replace the approach executing recalculation of electromagnetic problem when velocity changes its value. The results also show that significant vortices occurs only at low flow rates.

REFERENCES

- [1] V. Dzelme, A. Jakovics, and I. Buceniks, "Numerical modelling of liquid metal electromagnetic pump with rotating permanent magnets," vol. 424, no. 1, 2018.
- [2] V. Geža and B. Nacke, "Numerical simulation of core-free design of a large electromagnetic pump with double stator," *Magnetohydrodynamics*, vol. 52, no. 3, pp. 417–431, 2016.
- [3] J. Vencels, P. Ráback, and V. Geža, "Eof-library: Open-source elmer fem and openfoam coupler for electromagnetics and fluid dynamics," *SoftwareX*, vol. 9, pp. 68–72, 2019.

Applicability of calculation methods of minimum and maximum short circuit currents in grid with voltage up to 1 kV

line 1: Marina Rashevskaya
line 2: *Department of Power Supply of Industrial Enterprises and Electrotechnologies*
line 3: *Moscow Power Engineering Institute*
line 4: Moscow, Russian Federation
line 5: mkr@list.ru

line 1: German Lipinskiy
line 2: *Department of Power Supply of Industrial Enterprises and Electrotechnologies*
line 3: *Moscow Power Engineering Institute*
line 4: Moscow, Russian Federation
line 5: energolux2@mail.ru

line 1: Aleksey Kulikov
line 2: *Department of Power Supply of Industrial Enterprises and Electrotechnologies*
line 3: *Moscow Power Engineering Institute*
line 4: Moscow, Russian Federation
line 5: kulikovali@mpei.ru

Abstract— The values of minimum and maximum short-circuit currents are calculated at the designing of power supply systems for selecting equipment and protection systems. By means of Matlab/Simulink modeling the farthest location of the motor load is defined for which the motor feed to the fault at substation should be considered. The article provides a comparison of different methods for accounting of the arc.

Keywords— *fault current feed, mathematical model, Matlab/Simulink, arc fault, arc resistance.*

I. INTRODUCTION

In the power supply system at a voltage level of 0.4 kV short circuits are calculated in order to select equipment and build circuit protection. Thus, it is required to calculate the value of the maximum and minimum short-circuit current. The calculation process of the highest possible short-circuit current value usually considers both the feed from the motor load and the arc-free direct nature of the short circuit. The minimum current gives an arc short-circuits, which can often occur in confined spaces: busbars shields, at the terminals of the apparatus, input boxes of electric motors, various detachable connections, etc. The settings for the operation of the protection systems are selected by the value of the current of the single-phase arc short circuits in the end of protected line. In this regard, it becomes very important to calculate the values of the arc current.

II. PROBLEM STATEMENT

The calculation of the highest short-circuit current values should account for the contribution from the asynchronous and synchronous motor loads directly connected to the short circuit place at arbitrary time instants including initial and contact opening instants. But in these grids there are a lot of motors. Therefore, the question arises - what power of the motor load and at how long the distance from the busbars should be taken into account when calculating the highest possible direct short circuit current?

When determining the minimum short-circuit current, it is recommended to take into account an increasing in the active resistance of the conductors due to their heating by the short-circuit current (thermal decline of the short-circuit current) by the disconnection time of the circuit. It is introduced temperature coefficient $K_{\theta t}$, depending on the material and temperature of the conductor.

It is recommended to take into account the arc at the short-circuit place by introducing into the design scheme the

active resistance of the arc R_a , which is determined on the base of the probabilistic characteristics of the influence of a stable arc on the short-circuit current. The paper posed the task of determining the arc resistance and short-circuit current in accordance with various existing techniques for the same initial conditions.

III. RESULTS OF NUMERICAL EXPERIMENT AT CALCULATING MAXIMUM SHORT-CIRCUIT CURRENTS

It is believed that the feed current from the motor load may be considered insufficient if less than 1% of the fault current drawn from the grid [1,2].

$$\sum I_{ratIM} \leq 0.01 \cdot I_{SC}^{(3)} \quad (1)$$

Using this equation, the maximum motor load current can be defined that is negligible in short-circuit. Additionally, corresponding surge current of the motor load can be calculated.

$$P_{IM} \leq 0.01 \cdot I_{SC}^{(3)} \cdot \cos \varphi \cdot \eta \cdot U_{rat} \cdot \sqrt{3} \quad (2)$$

The currents of direct short-circuit currents for many typical substations, on the low voltage buses of the transformer are easy to determine, because the resistance of the entire circuit is known. Based on this, there were obtained motor loads, which feed surge current should be taken into account at calculations [3,4]. Also, by means of math modeling in the Matlab / Simulink program, the values of the distance of the motor load from the busbars were obtained, when the influence of this load can be ignored [5,6]. The plots describing the variation of feed currents of the motor loads vs cable length are presented in Fig. 1.

IV. CALCULATION OF SINGLE-PHASE ARC SHORT CIRCUITS

There are many literary sources that determine the methods of calculating short circuit arc currents [1,2]. The electric arc usually can be taken into account at the short-circuits by several methods: introducing the arc active resistance R_a into the design scheme, determined using the formula; using the decreasing coefficient; and using a fixed tabular or plot-determined value of the arc resistance for typical design conditions [1,2,7-10]. However, various literature sources have other recommendations for taking into account the electric arc when calculating the minimum short-circuit current. The results of comparing of the calculation methods of the active arc resistance and the arc single-phase short circuit current are presented in the table 1 [1,2,7-10]. It can be noted that many sources are similar in determining the

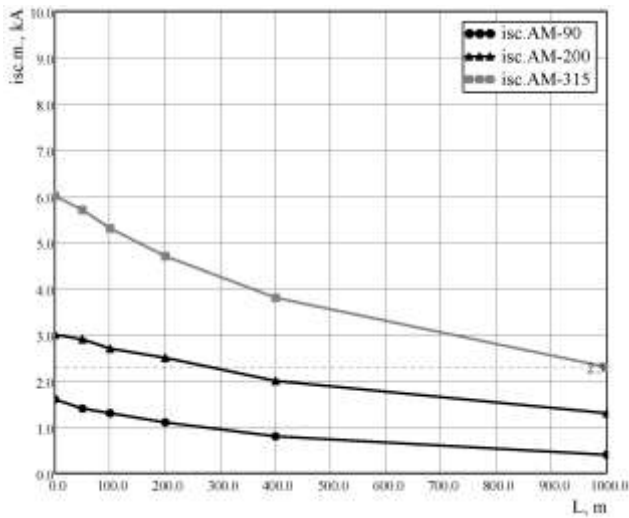


Fig. 1. Variation of feed currents from the motor loads vs cable length for the 1000 kVA 10/0.4 kV transformer.

parameters of the arc, but there are also those that are completely different. Also present are those where experimental data were taken as the base.

TABLE I. COMPARISON OF VARIOUS LITERATURE SOURCES

Source	$R_a, m\Omega$	$I^{(d)}_{as}, kA$
M.A. Shisha	17	5.5
B.N. Neklepaev	29	4.4
I.L. Nebrat	17	5.5
A.B. Belyaev	15	5.7
Y.G. Baribin	20	5.2
V. Terzija, H.-J. Koglin	13	6.0

The values of the arc resistance obtained from various sources for the same conditions differ by more than 2 times, the calculated values of the currents differ by 1.4 times. This suggests that in the calculation, short-circuit currents in the distribution network R_a is relatively large in relation to the total resistance of the short-circuit, and therefore, the reliability of the calculated values of the short-circuit currents will depend on the accuracy of the used value R_a .

V. CONCLUSION

For the correct configuration of the power supply system and the choice of conductors and apparatuses the values of the maximum and minimum possible short-circuit currents are of especially importance. However, to determine the

active resistance of an arc, existing calculation methods often either require knowledge of the full source data, and do not suggest great accuracy, or they recommend using tabular values of the arc resistance, which have a large spread of values. There are very large discrepancies in the matter of calculating of arc resistance. The calculation results according to different methods often differ several times. An arc, like a short circuit, is a random event, the set of parameters of which forms a set of probability parameters. Perhaps, it should be guided by other methods for determining the arc fault, when configuring protections and choosing settings in low-voltage grids. For example, the appearance of harmonics in the network that are characteristic for single-phase faults and for arc faults. There is data that single-phase short-circuits are characterized by a high level of third harmonic of current in the neutral wire. That is also characteristic of stable arc. The development of the arc short circuit gives characteristic even harmonics of the current.

REFERENCES

- [1] Short-circuits in electrical equipment. Calculation methodology in low voltage AC installations, GOST 28249-93, 1993 (in Russian)
- [2] Operational regulations for calculation of short-circuit currents and selection of electrical equipment, RD 153-34.0-20.527-98, 2002 (in Russian).
- [3] R. Vaynshteyn, N. Kolomiyets, K. Lozinsky, "Simulation feed current from induction motors in short circuits," deposited manuscript, VINITI RAS, 2009 (in Russian).
- [4] D. Nurbosynov, Yu. Konovalov, "Method of calculating the surge current of short circuit with the influence of the operating modes of the synchronous motor," Collection of scientific works of the Angarsk state Technical University, vol. 1, no. 1, pp. 217-221, 2016 (in Russian).
- [5] R. Burkart; I. Tsoumas, "In-Depth Analytical Investigation of Induction Motor Short-Circuit Currents," in 2018 XIII International Conference on Electrical Machines (ICEM), Alexandroupoli, Greece, 2018, pp. 2371 – 2377.
- [6] K. L. Koo, "Modeling and cosimulation of AC generator excitation and governor systems using simulink interfaced to PSS/E" IEEE PES Power Systems Conference and Exposition, 2004., New York, NY, 2004, pp. 1095-1100 vol.2.
- [7] Terzija V. V. On the Modeling of Long Arc in Still Air and Arc Resistance Calculation / V. V. Terzija H.-J. Koglin // IEEE Power Engineering Society General Meetin, USA, Denver. – 2004. – pp. 1012-1017.
- [8] I.L. Nebrat, "Short circuit current calculations in grids 0.4 kV: training manual," PIEPK, Saint-Petersburg, Russia, 2001 (in Russian).
- [9] Y.G. Baribin, "Power Engineering Design Reference," Energoatomizdat, Moscow, Russia, 1990 (in Russian).
- [10] A.V. Belyaev, "Selection of equipment, cable protection 0.4 kV", Energoatomizdat, Saint-Petersburg, Russia, 1988 (in Russian).

Investigating the Benefit of Soft Magnetic Composite Inserts on Energy Efficiency in Cold Wall Billet Casters Using Computer Simulation

Tareq Eddir
Engineering
Fluxtrol Inc.
Auburn Hills, MI, USA
teddir@fluxtrol.com

Robert Goldstein
Engineering
Fluxtrol Inc
Auburn Hills, MI, USA
rgoldstein@fluxtrol.com

Robert Haun
Research and Development
Anspanner, LLC
Healdsburg, CA, USA
robhaun@concast.net

Abstract—Cold wall induction (CWI) applications are widely used for melting or processing metals, oxides, glasses, and other reactive or high purity materials. Multiple studies have been made for their optimization, but their energy efficiency is still low compared to other processes. The rise of additive manufacturing (AM) has resulted in renewed interest in the use of CWI applications for powder manufacturing and recycling. The emerging AM techniques require highly consistent powders with a small range of size, shape and chemical composition. Current powder production techniques, such as electrode induction gas atomization (EIGA) and drip melting, tend to have relatively low acceptable yield for AM. Recycling processes which use CWI to convert the out of specification powder back into raw billets for reprocessing are receiving renewed interest.

This paper will look at the use and optimization of soft magnetic composites (SMC) for inserts or other components to increase energy efficiency of cold wall induction billet casters used for powder recycling. Modelling will be used to predict electrical parameters for comparison. Also, some discussion will be had on potential to further improve energy efficiency due to the improved thermal efficiency of the system.

Keywords—cold wall induction, soft magnetic composites, magnetic inserts, computer simulation, energy efficiency, powder metal recycling

I. INTRODUCTION

Cold wall induction (CWI) is a technology used for melting high purity metals, oxides, or reactive metals. Melting occurs within a segmented, water-cooled copper crucible or open bottom mold. These latter devices are used for recycling out of specification powder from other processes into billets. Atomization processes require high purity incoming billets, making CWI technology a viable candidate for powder recycling. However, CWI is a low efficiency technology, making it a costly process.

Previous work has been done on using soft magnetic composite (SMC) inserts which demonstrated the ability to control the magnetic flux to significantly increase electrical efficiency [1]. Subsequent studies on 55 mm OD ingots and 129 kW input power, experimental results showed a 31% increase in casting rate. Additionally, simulation results showed the use of the SMC inserts increase the electrical efficiency from 29.6% to 34.2% [2]. The goal of this study is to model 70 mm diameter billet and determine whether an efficiency increase can be obtained using SMC inserts.

II. COMPUTER SIMULATION STRATEGY

A. Geometry Description

The geometry of the billet caster was chosen based on commonly used dimensions. The cold wall induction mold was designed for a 70 mm diameter billet with a total height of 295 mm. A mold design with 12 segments was used, with 0.51 mm slit width, and segment height of 250 mm. Two SMC inserts were added between each segment near the top and bottom of the coil. The size and location of the inserts was varied for the purposes of this study. The inductor used was a multi-turn coil with rectangular copper tubing. The coil had SMC shunts and an upper and bottom SMC rings attached to it in some of the cases. A schematic of the geometry is shown in Fig. 1.

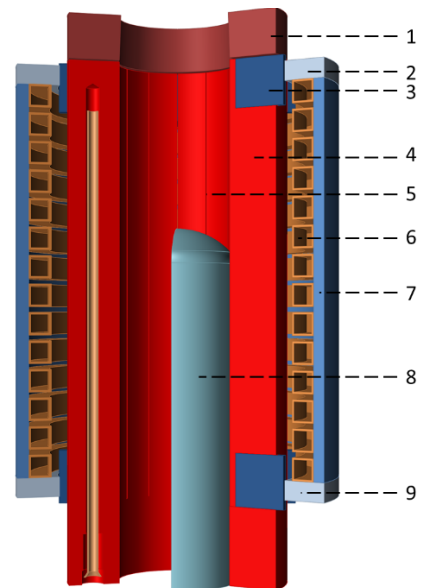


Fig. 1. Schematic of the geometry of the billet caster.

Fig. 1 shows the geometry used. Where 1 is the top copper ring, 2 is the top SMC ring, 3 is the SMC insert, 4 are the water-cooled copper mold segments, 5 is the slit between segments, 6 is the coil copper, 7 is the SMC shunt, 8 is the load, and 9 is the coil's bottom SMC ring.

B. Simulation Description and Strategy

3D electromagnetic simulations were run using Flux 3D software [3]. The simulations used rotational symmetry planes to reduce the simulation size. As a result, 1/24th of the system was modelled. Fluxtrol 100 B(H) curve magnetic properties and loss equations and data were used for the SMC material for the inserts, shunts, and rings [4]. Fig. 2

shows the geometry used in the simulation, where (a) is reduced geometry and (b) is the superimposed geometry.

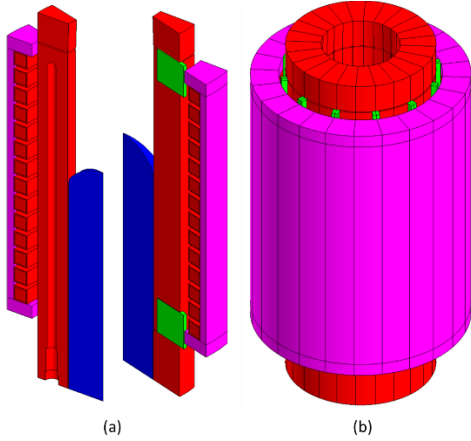


Fig. 2. Geometry example used in the simulation with reduced geometry (a) due to the symmetry and full geometry (b).

The goal of the simulation is to compare the electrical efficiency of the coil head without the use of SMC's and with the SMC's. The efficiency is described by equations (1) and (2).

$$\eta = P_{Load} / P_{Total} \quad (1)$$

$$P_{Total} = P_{Load} + P_{Coil} + P_{Mold} + P_{SMC} \quad (2)$$

Where η is the electrical efficiency, P_{Load} is the power induced in the load through joule heating, and P_{Total} is the total power in the coil head. P_{Total} includes the losses in the coil, load, mold, and SMC's. Other losses, such as coil leads, chamber, and other are not considered in this investigation.

The simulations will also study the changes in electrical parameters as a result of using the different SMC's. Additionally, the distribution of the induced power density is compared between the different models.

C. Simulation Parameters

The simulations will start with an original case, with no SMC's for inserts, shunts or rings. Other cases will include inserts, shunts, and/or top and bottom rings. The inserts' dimensions are 5.4mm thickness x 30mm depth x 30mm height. The coil shunts' dimensions are 85.2 mm ID x 91.55 mm OD x 219 mm height. The coil rings' dimensions are 68 mm ID x 91.55 mm OD x 10.9 mm height.

All simulations use 5 kHz frequency and a constant current source of 1000 A_{rms}. The load used is a titanium bar at a uniform electrical resistivity, ρ , of 1.7 $\mu\Omega\text{m}$. The coil has 14 turns with 12.7 mm square copper tubing and 1.02 mm wall thickness. The coil has an ID is 72.5 mm and height of 219mm.

III. RESULTS

A. Electrical Results

The results for voltage, current, power, and coil head efficiency for the different modelled cases will be tabulated similar to that shown in Table 1.

TABLE I. SIMULATION ELECTRICAL PARAMETER RESULTS

Case	U	P _{Load}	P _{Coil}	P _{Mold}	P _{SMC}	η
Bare	7.9	368	280	612	0	29.2%
In	9.1	634	268	647	4	40.8%
Ri+In	9.8	714	279	733	7.7	41.2%
Ri+Sh	9.4	435	316	771	29	28.0%
Ri+Sh+In	11.1	824	328	872	47	39.8%

Where case Bare case is a coil with no SMC, In indicates the use of inserts, Ri indicates the use of rings, and Sh indicates the use of shunts. The results in the table are for 1/24th of the system.

B. Current Density Results in the load

The addition of SMC's to the coil and caster changes the current density distribution on the load and segments. Figure 3 shows the current density distribution in the load for the different cases.

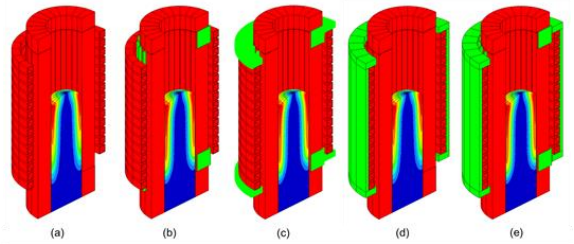


Fig. 3. Current density distribution in the load for the different cases. (a) no SMC, (b) inserts, (c) rings and inserts, (d) rings and shunts, and (e) rings, shunts, and inserts.

IV. SUMMARY

The use of SMC's on power recycling casters was shown to improve coil head efficiency. The use of inserts was shown to improve coil head electrical efficiency of ~10%, while shunts and rings do not provide any substantial benefit to the electrical efficiency. However, the use of magnetic shunts and rings is known to reduce the required current and chamber heating, thus providing potential reductions in overall electrical efficiency and reactive power. Furthermore, the use of inserts may allow for the mold length to be shortened and the design improved for additional improvements, though mold and coil redesigns were not investigated in this work.

REFERENCES

- [1] V. Nemkov, R. Goldstein, K. Kreter, and J. Jackowski, "Modelling and optimization of the cold crucible furnaces for melting metals," HES. Paudua, 2013
- [2] R. Haun *et al.*, "Recent design and operational developments of cold wall induction melting crucible for reactive metals processing," HES. Paudua, 2013
- [3] Flux 3D. (2019.1.1). Altair. [Desktop]. Available: <https://www.altair.com/flux/>
- [4] Fluxtrol 100, Fluxtrol Inc., Mar. 12, 2020. [Online]. Available: <https://fluxtrol.com/fluxtrol-100>

Multiphysical modelling and validation of VIM for Inconel 718 heating and melting

P. García Michelena
*Mechanical and Manufacturing
Department*
Mondragon University
Arrasate-Mondragon, Gipuzkoa, Spain
pgarciam@mondragon.edu

X. Chamorro Sanchez
*Mechanical and Manufacturing
Department*
Mondragon University
Arrasate-Mondragon, Gipuzkoa, Spain
xchamorro@mondragon.edu

E. Ruiz-Reina
*Departamento de Física Aplicada II
Facultad de Ciencias Universidad de
Málaga*
Málaga, Spain
eruizr@uma.es

N. Herrero Dorca
*Mechanical and Manufacturing
Department*
Mondragon University
Arrasate-Mondragon, Gipuzkoa, Spain
nherrero@mondragon.edu

Abstract—In this abstract, the followed methodology for the multiphysical numerical modelling of the heating and melting processes of Inconel 718 superalloy in a laboratory-scale vacuum induction melting furnace is presented. The theoretical results have been compared with experimental transient temperature measurements for solid and liquid states revealing an adequate agreement.

Keywords—induction heating, vacuum induction melting, multiphysics modeling, experimental validation

I. INTRODUCTION

During nickel-based superalloys heating and melting, precise temperature control before mould pouring is essential to assure the correct metallurgical composition of the final component. Vacuum induction melting (VIM) is the most suitable technology due to the protective inert atmosphere conditions and higher electrical efficiency, is widely used in the industry. However, the process has inherent difficulties for measuring high transient temperatures, which are over 1500°C. Therefore, an experimentally validated numerical model is required to study the temperature distribution of the metal and ensure optimum temperature during the process.

II. CHARACTERIZATION

The VIM equipment from MGEP can melt 2 kg of nickel-based superalloys in a ceramic crucible. Considering the industrial standard for a melting cycle, the induced power of a laboratory-scale furnace has been adjusted to fulfil the temperature evolution requirement. Once identifying the Power-Time-Temperature relation, for each power step coil frequencies and currents have been measured. Starting from a bake out of 5kW to melting a phase 16kW the frequencies and currents in the coil ranges between 7-8.5 kHz and 0.5-1.5 kA.

For a precise analysis, it is essential to consider the material non-linearities, Inconel 718 has been characterized thermally and electrically up to 1300°C and properties implemented as temperature-dependent variables with a built-in function in the model. In contrast, for liquid state bibliographic references have been considered [1].

III. NUMERICAL MODEL

Heating and melting process simulation is a complex multiphysics problem, which requires a strong coupling between the magnetic, thermal, and fluid dynamics fields. As

the first approach, the process has been divided into two independent studies one for each state material state. The geometry of study is reduced to a 2D axisymmetric geometry and domains discretized with the FEM method based on the commercial software Comsol Multiphysics®.

A. Solid-State Model

Beginning with a cylindrical charge, the electro-thermal problem has been solved with the induced current as the source term for heating. For a correct calculation of the electromagnetic field, the water-cooled seven turn's coaxial coil and the charge to be melt have been precisely meshed considering the skin effect for the imposed excitation frequencies. Thermal radiation effects have been computed considering the shared views of the surfaces between the crucible and the load. Refrigeration coil water is introduced as a forced thermal convection term.

Preliminary results indicate non-uniform heating, due to the geometry of the crucible and disposition on the coil and load. While the top surface is still around 650 °C the mid-height area reaches liquidus temperature 1360 °C. Fig 1. shows the concordance between the initial incipient melting zone and the removed mesh elements corresponding to the exceeded temperature. This substantial temperature gradient is confirmed by the first melting trials.

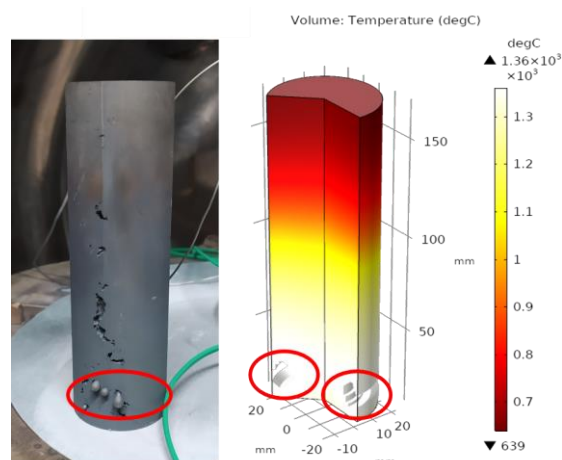


Fig. 1. Temperature distribution and initial melting after 1h of 5 kW.

B. Liquid-State Model

In the second model, the hydrodynamic and free surface problem has been solved separately. Assuming that for a reduced time frame the deformation of the meniscus is insignificant thus the Lorentz force distribution can be considered stationary [2]. With a built-in subroutine, the time-averaged electromagnetic force has been imported to the transient fluid-dynamic model. The multiphase flow has been computed in a fixed grid via the Level-Set method and RANS equations solved with the $k-\omega$ turbulence model. The routine is solved iteratively and when the surface displacement in the previous iteration is small enough the surface transient thermal study is coupled. The accuracy of the solver and routine has been compared with published experimental measurements references [2], [3], and [4]. Fig. 2. Shows the free surface shape for an induced power of 16 kW in the melting phase.

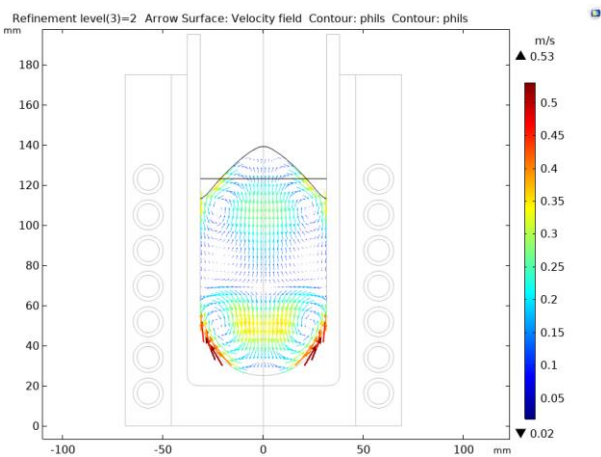


Fig. 2. Velocity field and free surface for a initial height of 95 mm.

IV. EXPERIMENTAL VALIDATION

With the aim to confirm the theoretical results and evaluate the accuracy of the model, an experimental setup has been prepared to obtain data. Four K-type thermocouples, made of Inconel 625, have been attached in the vertical axis of the cylindrical charge and voltage difference measured by the signal conversion unit located inside the furnace. Following the standard heating profile, the first step of 5 kW is applied followed by 11kW, due to the rapid heating; the dynamic response has been studied. Fig 3. reports the comparison between theoretical and experimental for top and bottom thermocouples with a separation of 110 mm. The obtained agreement is acceptable even though the results suggest that the model has lower thermal inertia.

For liquid state, an infrared bichromatic pyrometer pointing to the free surface of the melt is employed which records the maximum temperature of the spot size. Due to the rapid dynamic response melting stage before mould pouring has been computed. First, a 7 minute long heating has been computed with a induced power of 10 kW afterwards it is reduced to 6 kW before pouring and temperature decreased to 1450°C. In the Fig. 4 can be seen the temperature response for both steps and the measurement done by the pyrometer. The correlation is adequate considering the existence of dross particles that hinder the pyrometer capacity.

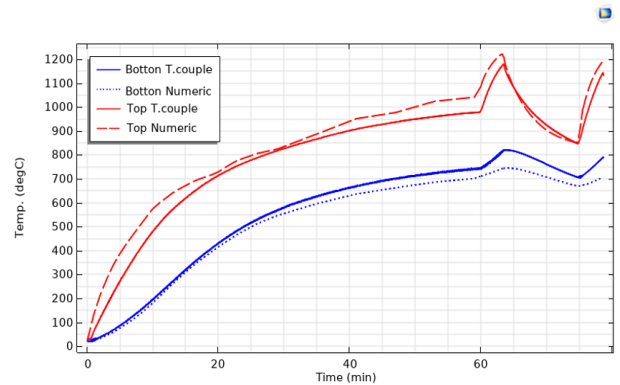


Fig. 3. Comprasion of transient temperature. Blue lines botton probe and red top. Continuous lines thermocouple measurements and discontinuous model result.

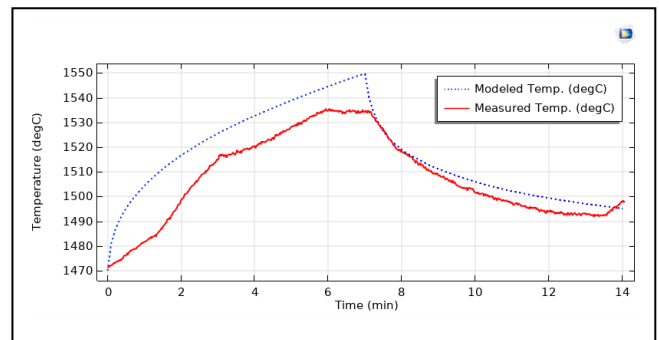


Fig. 4. Temperature transient evolution. Modelede blue dotted and red continous measured.

V. CONCLUSIONS

A multiphysical coupled model that describes the induction heating and melting for Inconel 718 has been proposed. The experimental measurements and validation indicate a satisfactory agreement with numerical results. The global vision provided by the model can be employed as an optimization tool to determine the most efficient melting procedure assuring the correct melt temperature. The research confirms that the temperature gradient between solid-liquid transitions is considerable which could lead to overheating and alloying element dissipation. This temperature difference evidences the necessity to model the phase transition solid-liquid physics.

REFERENCES

- [1] G. Pottlacher, H. Hosaeus, E. Kaschnitz, and A. Seifert, "Thermophysical properties of solid and liquid Inconel 718 Alloy*," *Scand. J. Metall.*, vol. 31, no. 3, pp. 161–168, Jun. 2002.
- [2] S. Spitan, A. Jakovics, E. Baake, and B. Nacke, "Numerical modeling of free surface dynamics of melt in an alternate electromagnetic field: Part I. Implementation and verification of model," *Metall. Mater. Trans. B Process Metall. Mater. Process. Sci.*, vol. 44, no. 3, pp. 593–605, 2013.
- [3] P. Buliński et al., "Numerical and experimental investigation of heat transfer process in electromagnetically driven flow within a vacuum induction furnace," *Appl. Therm. Eng.*, vol. 124, pp. 1003–1013, Sep. 2017.
- [4] X. R. Zhu, R. A. Harding, and J. Campbell, "Calculation of the free surface shape in the electromagnetic processing of liquid metals," *Appl. Math. Model.*, vol. 21, no. 4, pp. 207–214, Apr. 1997.

AC arc electrical load model for new power supply analysis

Andrey Zhurkin

Department of Industrial Enterprises Power Supply Systems and
Electrical Technologies
National Research University Moscow Power Engineering
Institute
Moscow, Russia
ORCID ID: 0000-0001-9291-3613

Michael Pogrebisskiy

Department of Industrial Enterprises Power Supply Systems and
Electrical Technologies
National Research University Moscow Power Engineering
Institute
Moscow, Russia
PogrebisskiyMY@mpei.ru

Sergey Nekhamin

Department of Industrial Enterprises Power Supply Systems and
Electrical Technologies
National Research University Moscow Power Engineering
Institute
Moscow, Russia
NekhaminSM@mpei.ru

Irina Martynova

Department of Industrial Enterprises Power Supply Systems and
Electrical Technologies
National Research University Moscow Power Engineering
Institute
Moscow, Russia
MartynovaIA@mpei.ru

Abstract — This paper describes a model of an AC arc electrical load for analysis of furnace operating in conjunction with high-speed semiconductor converter. The semiconductor converter is part of electric furnace circuit and generates the current that compensates for the inactive power components caused by electric arc load. A dynamic model of the electric arc is developed taking into account random factors. This is necessary to ensure that the converter control system is adjusted to the rapidly changing electrical parameters. This solution allows to reduce the negative load impact on the supply network, as well as increase the useful power and the furnace productivity.

Keywords — nonlinear electrical load, nonparametric current source, power quality

I. INTRODUCTION. A REVIEW

The AC arc steelmaking furnace (electric arc furnace, EAF) is one of the most unfavorable receivers of electrical energy. We are talking about the electromagnetic compatibility problem of the supply network and the consumer [1]. On the other hand, it is necessary to ensure high performance for the process plant in order to be economically and environmentally efficient. Optimization of the electric mode control system of the arc steelmaking furnace solves the problem only partially, since all components of the total power are not compensated.

Currently, solutions to these problems are known. For example, in industry, controlled static converters are used in the low-voltage circuit of a furnace transformer [2]. However, such solutions have limitations due to its high cost, since the power supply is performed at full capacity of the

furnace.

To improve electromagnetic compatibility and ensure high energy performance of an AC arc furnace, it is proposed to consider the concept of a new power source with a static semiconductor converter operating as a nonparametric current source. To analyze the operation of such device, a corresponding model of an arc model has been developed.

II. INSTALLATION POWER OPTIMIZATION METHOD

The single-phase power supply circuit is shown in Fig. 1, where U_2 is the primary voltage of the additional transformer winding, V ; $U_{2,1-2,2}$ is the secondary voltages of the additional transformer windings, V ; U_1 is the primary voltage of the furnace transformer winding, V ; $U_{1,2}$ is the secondary voltage of the furnace transformer winding, V ; U_{arc} is the arc voltage, V ; i_{arc} is the arc current, A ; i_c is the current of the semiconductor converter, A . As can be seen, compensation of inactive components of full power is carried out at low voltage. This solution allows to unload the furnace transformer from inactive power components.

The static converter can consist of three links: three-phase bridge rectifier, DC link, and three-phase chopper. Such solution is possible due to the appearance of particularly powerful semiconductor switches. The converter as a current source allows to compensate arc current harmonics. The reactive power component and the power component from current and voltage asymmetry can be reduced by adjusting the static converter control system.

III. LOAD MODEL AND RESULTS

To analyze the converter operation and configure its control system, a nonlinear arc load model is required. The most significant problem of modeling an AC electric arc is the random nature of arc burning.

The arc model is based on the solution of the nonlinear Cassie differential equation (1) obtained from energy balance equation and has the form

$$\theta_{arc} \frac{dg_{arc}(t)}{dt} = \left(\frac{u_{arc}^2(t)}{E_{arc}^2} - 1 \right) \cdot g_{arc}(t), \quad (1)$$

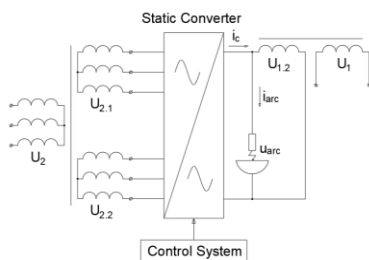


Fig. 1. Equivalent circuit of a power supply with static converter

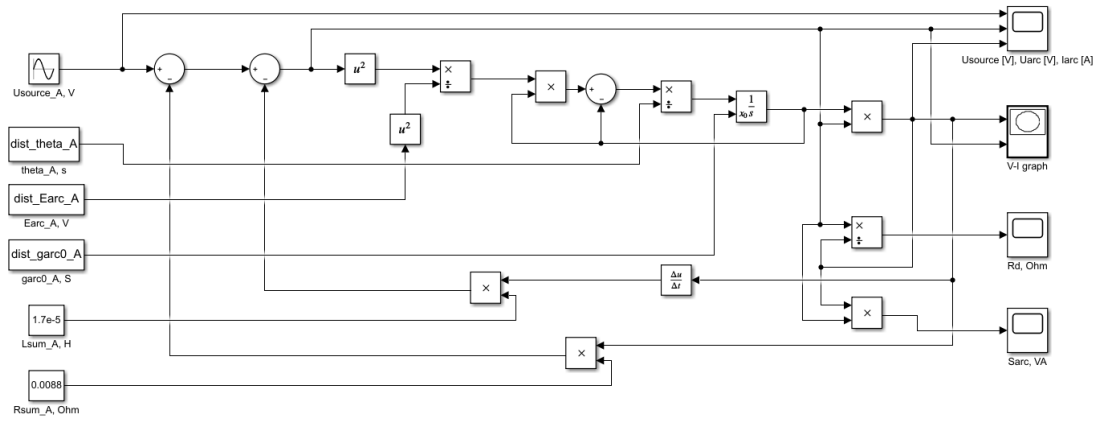


Fig. 2. Simulink scheme for solving the Cassie equation with random signal sources

where Θ_{arc} is the time constant, ms; g_{arc} is the arc conductivity, S; u_{arc} is the arc voltage, V; E_{arc} – counteracting arc EMF, V.

Firstly, this model takes into account the nonlinear V-I characteristic of the electric arc due to the introduction of the coefficient Θ_{arc} . Secondly, the described model simulates random nature of the electric arc burning. To simulate random distortions of the arc time constant, counteracting arc EMF, initial conductivity of the arc column g_0 , sources of random step signals with a normal distribution law of values are used. The calculation scheme for solving the Cassie equation is shown in Fig. 2.

Table I shows the main parameters of the random signals used in phase A. Fig. 3 shows the dynamic V-I characteristic of the electric arc of phase A for the initial melting phase. This is the most unfavorable period of metal melting which corresponds to $\Theta_{arc} = 0.1-0.5$ ms.

TABLE I. PARAMETERS OF THE RANDOM SIGNALS USED

Signal	Expected value, E [X]	Variance, Var [X]
$\Theta_{arc}(t)$, s	$0,5 \cdot 10^{-3}$ s	$2,5 \cdot 10^{-8}$ s ²
$E_{arc}(t)$, V	526,6 V	$3 \cdot 10^2$ V ²
$g_0(t)$, S	86,2 S	$5 \cdot 10^2$ S ²

As can be seen from Table I, the electric mode corresponding to the beginning of melting is considered. The three-phase load is modeled by three independently burning arcs in phases A, B, and C. The arc steelmaking furnace receives power via a 150 200 kVA furnace transformer from

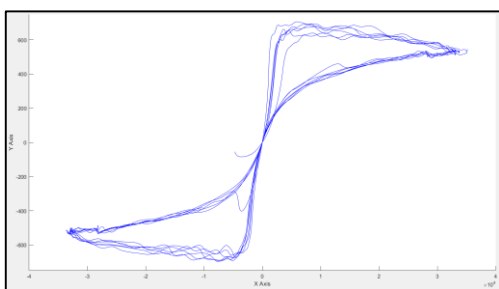


Fig. 3. V-I characteristic of the arc. X axis – I_{arc} , A; Y axis – U_{arc} , V

a 35 kV network with an industrial frequency of 50 Hz [3].

Expression for arc current

$$i_{arc}(t) = \sum_{k=1}^{\infty} I_{km} \cdot \sin(k\omega t + \psi_k) + X_{i_{arc}}(t), \quad (2)$$

where k is the current harmonic ordinal number; I_{km} is the k -th current harmonic amplitude, A; ω is the angular frequency, rad/s; ψ_k is the initial phase of the k -th current harmonic, rad; $X_{i_{arc}}(t)$ is the random component of current signal, A.

The results of frequency analysis of phase current signals are presented in Table II.

TABLE II. FREQUENCY ANALYSIS RESULTS

	Phase A	Phase B	Phase C
$I_{(5)}$, %	9,4	7,9	10,1
$I_{(7)}$, %	3,8	3,7	3,2
THD _i , %	10,7	9,1	10,8

IV. CONCLUSIONS

The described model of the AC arc simulates the arc current and voltage curves, as well as the dynamic V-I characteristics of the industrial EAF-180 with randomly changing parameters. This dynamic model can be used to synthesize and configure the control system of a high-speed semiconductor nonparametric current source that provides compensation for full power inactive components of the electric arc furnace. The purpose of this solution is to increase the useful power and EAF productivity, as well as their electromagnetic compatibility with the supply network.

REFERENCES

- [1] A. Horia, C. Costin, and G. Sorin, "Power quality and electrical arc furnaces," Power Quality, 2014, pp. 77-100.
- [2] G. Postiglione and P. Ladoux, "A new concept of electrical power supply for AC arc furnaces," International Symposium on Power Electronics, Electrical Drives, Automation and Motion, SPEEDAM 2006, pp. 619-624.
- [3] G. P. Kornilov et al., "Feature of the simulation the electric arc furnace as electrotechnical complex," Bulletin of the Magnitogorsk State Technical University, vol. 1, 2013, pp. 76-82.

Numerical simulation of conduction refining of molten aluminum in the casting launder

Mikhail Pervukhin
Siberian federal university
Krasnoyarsk, Russia
pmv_75@mail.ru

Eduard Vinter
Siberian federal university
Krasnoyarsk, Russia
eduard.vinter@gmail.com

Viktor Timofeev
Siberian federal university
Krasnoyarsk, Russia
viktortim0807@mail.ru

In the paper numerical modeling of the process of conduction refining in the casting launder is carried out. The behavior of non-conductive particles in aluminum melt during conduction refining is investigated. Numerical calculation is performed using the MAXWELL and FLUENT software packages. For calculation of non-conductive particle trajectories and distributions the Discrete Phase Model is used. It is shown that electromagnetic forces strongly affect the process of particle migration to the surface. The effective current value for refining the melt in the casting launder is determined.

Keywords — refining, solid inclusions, Euler-Lagrange

I. INTRODUCTION

Currently, the scope of metallurgical products is expanding rapidly. In particular, this applies to aluminum alloys, which today are widely used in aircraft manufacturing, shipbuilding and additive technologies [1]. Moreover, one of the most important stages in the production of aluminum ingots is the refining operation, the purpose of which is to remove unwanted gas and solid impurities from the melt [2].

One of the promising methods for refining aluminum melt is conductive refining by electric current. Significant advantages of this technology include the absence of rotating mechanisms for gas dispersion, the possibility of refining directly in the casting launder, as well as additional heating, which is important during melt transportation.

II. NUMERICAL MODELING

A. Numerical considerations

The problem of conductive refining is a type of the problem of magnetohydrodynamics and currently requires the approach of combining several software packages for numerical simulation [3]. In this work, for the numerical simulation, the combination of the MAXWELL and FLUENT software systems is used.

MAXWELL is a finite element product and is designed to solve the problems of electrostatics in the Coulomb gauge. FLUENT is based on the finite volume method and allows solving heat and mass transfer problems, including multiphase flows. To set the source terms from in FLUENT, file-based transfer and interpolation of the distribution of electromagnetic forces and Joule heat are performed

B. Equations

The electromagnetic field in the computational domain is described by the Laplace equation for the vector magnetic potential [4]. At the boundary of the computational domain, the Dirichlet condition for the normal component of the

vector potential and the Neumann condition for the tangential component [5] are applied.

Heat and mass transfer processes in the melt are described by the equations of motion, continuity and energy for an incompressible fluid [6]. In this paper, we use the SST model to describe turbulence [7]. The Boussinesq-Oberbeck approximation [8] is also used for modeling convective flows.

The motion of the discrete phase is described using the Lagrange equation [9]. The model takes into account buoyancy force, drag force, virtual mass force, lift force and also electromagnetic force. Drag force is calculated using the Chiller-Naumann approximation [10]. Lift force is determined based on the Saffman-Mei model [11]. The electromagnetic force acting on a particle is determined based on the Leenov and Kolin model [12].

III. RESULTS AND DISCUSSION

A. Electromagnetic force distribution

Figure 1 shows the vector distribution of electromagnetic forces in the longitudinal section of the melt. Based on the distribution of electromagnetic forces the melt region can be divided into three zones. First zone is area of the absence of MHD effects. It is the input part of the launder, which also includes a section of the contact of the melt with the electrode. In this zone, the current density is minimal, and, therefore, transit flow expected along the length of the launder in this zone, which is determined by the mass flow rate.

Second zone is area of vortex flows. It is the region located between the zone of the absence of electromagnetic forces and the zone where their distribution has a uniform radial character. Since in this zone the distribution of electromagnetic forces along the length and radius is nonuniformity, the rotor of the field of electromagnetic forces is nonzero. Thus, in this zone, eddy recirculated flows are expected.

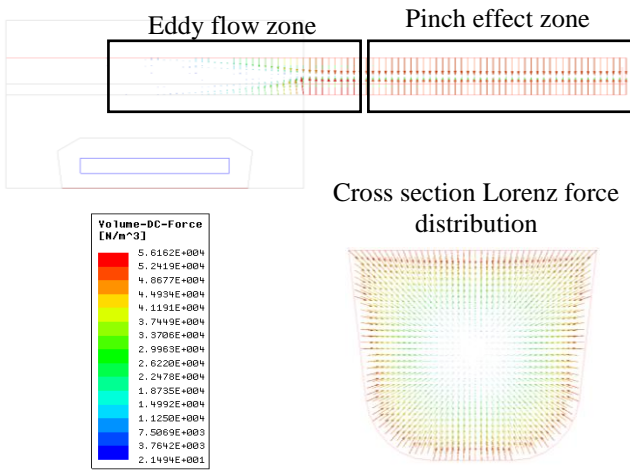


Fig. 1. Lorenz force distribution

The third area is the pinch effect zone. Unlike the second zone, in this area the distribution of electromagnetic forces is uniform in which the radial component of the forces prevails, as shown in Figure 8. However, since the cross-section of the channel has a complex shape, rotational flows are expected in this plane. Also in this zone, the potential part of the electromagnetic force expressed by electromagnetic pressure, compressing the melt in the radial direction.

B. Mass transfer in the melt

Figure 2 shows the vector distribution of the velocity field in the melt at a current of 1000 A. As expected from the distribution of electromagnetic forces, vortex flows are formed in the region of the electrodes. In the cross-section of the melt, a rotational movement of the melt is created, as figure. 3 shows. Figure 3 also shows that the rotational movement changes direction in the middle zone of the launder.

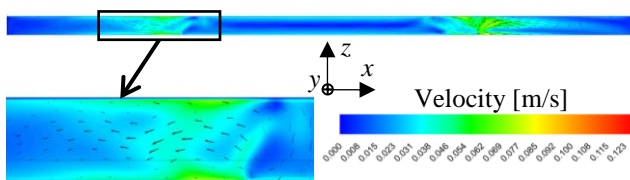


Fig. 2. Velocity field distribution

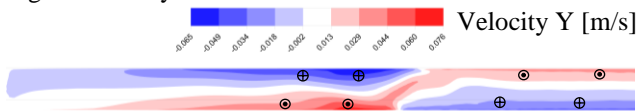


Fig. 3. Y component of velocity field distribution

The magnitude of the melt velocities in the launder has the range of 1-7 cm/s. A further increase of the integral current in the metal leads to more intense flows, especially in the region of the metal surface. More intense currents can lead to oxide film damage and its further stirring into the melt.

C. Transport of particle inclusions

Figure 4 shows the distribution of a cloud of non-conducting particles in the melt. Particles enter the entrance zone under the influence of a low-intensity transit flow. Under the action

of the transit flow, particles migrate through the launder into the region of vortex flows and are involved in the flow.

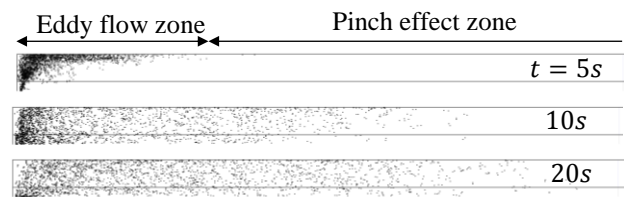


Fig. 4. Particle cloud distribution (particle diameter $20\mu\text{m}$)

Further particles migrate to the area of action of electromagnetic forces and accumulate on the walls of the launder. The electromagnetic force acting on the particles plays the main role in the accumulation of particles on the walls.

IV. CONCLUSION

A numerical simulation of the process of melt conductive refining from non-metallic inclusions is carried out. The pattern of the melt flows in the launder is determined under the influence of electromagnetic forces arising from the flow of electric current. Non-conducting particles distribution in the melt and the zones of particle accumulation under the influence of electromagnetic forces are determined.

REFERENCES

- [1] S. Kenzari, D. Bonina, J.-M. ubois, V. Fournée. Additive manufacturing of lightweight, fully Al-based components using quasicrystals. *Journal of Materials Processing Technology*, vol. 214 (2014) no 12, pp. 3108–3111
- [2] M. Schlesinger. *Aluminum recycling*. CRC press, 2013.
- [3] S. Spitan, A. Jakovics, E. Baake, B. Nacke. Numerical modeling of free surface dynamics of conductive melt in the induction crucible furnace. *Magnetohydrodynamics*, vol. 46 (2010), pp. 317–328.
- [4] Landau, L. D. (Ed.). (2013). *The classical theory of fields (Vol. 2)*. Elsevier.
- [5] Ansys Maxwell 15.0 User's Guide 3D
- [6] Landau, L. D., & Lifshitz, E. M. (1959). *Fluid mechanics*. 1959. Course of theoretical physics.
- [7] Menter F.R. Two-Equation Eddy-Viscosity Turbulence Models for Engineering Applications // *AIAA Journal*. 1994. No. 8. pp. 1598-1605.
- [8] C. Kleinstreuer. *Engineering fluid dynamics: an interdisciplinary systems approach*. Cambridge University Press, 1997.
- [9] J. Young, A. Leeming. A theory of particle deposition in turbulent pipe flow. *Journal of Fluid Mechanics*, vol. 340 (1997), pp. 129-159
- [10] L. Schiller, Z. Naumann. On the fundamental calculation of gravity separation. *Union of German Engineers*, vol. 77 (1933), pp. 318-20 [In German]
- [11] R. Mei. An approximate expression for the shear lift force on a spherical particle at finite Reynolds number. *International Journal of Multiphase Flow*, vol. 1 (1992), pp. 145-147.
- [12] D. Lennov, A. Kolin. Theory of electromagnetophoresis. I. Magnetohydrodynamic forces experienced by spherical and symmetrically oriented cylindrical particles. *Journal of Chemical Physics*, vol. 22 (1954) no 4, pp. 683–689.

Computer simulation of steel microstructure composition for induction hardening of a splined shaft for various cooling rates

MSc. Malvine N. Strakova
Cenos
Riga, Latvia
mns@cenos-platform.com

Dr. Vadims Geža
Cenos
Riga, Latvia
vg@cenos-platform.com

Dr. Mihails Ščepanskis
Cenos
Riga, Latvia
ms@cenos-platform.com

BSc. Alvis Eimuss
Cenos
Riga, Latvia
ae@cenos-platform.com

Abstract— In this study, the microstructure in the hardened zone of a splined shaft after scanning induction heating with two-turn inductors is studied using computational modeling. Different steel microstructures such as bainite and martensite are shown to compare the relative hardness of the workpiece for different cooling rates. It is demonstrated that quick 2D axial-symmetric approximation could give reasonable estimations for gear hardening profile but the wider splines need 3D simulation for a good result. The influence of frequency and power is examined in the hardening profile of the splined shaft. All calculations were done by using CENOS simulation software, which uses a coupled electromagnetic-thermal model to describe the induction heating process. For microstructure calculations, a time-temperature transformation diagram was used.

Keywords—*splined shaft, induction heating, numerical modeling, surface hardening*

I. INTRODUCTION

In the last decades, induction heating has become more and more popular because of the speed and energy efficiency for steel surface hardening and also other thermal treatment applications. The basic principle of induction heating is using an alternating current that creates a time-varying magnetic field which then induces eddy currents on the surface of the workpiece. Eddy currents heat up the workpiece due to the Joule effect. In the case of ferromagnetic material (as it often is in with steels) heating is happening also due to sudden jumps of the magnetic domain walls in the workpiece material called hysteresis losses. The depth in which eddy currents are induced depends on the frequency of the alternating current. Since heated is only the outside of the workpiece, it makes induction heating especially useful for surface hardening.[1]

Even though induction heating is sufficiently more energy effective than other hardening methods, often engineers face an obstacle on how to create the best design induction heating system. Since there are many parameters that have to be adjusted – frequency, heating time, power, current, and others, in more complex cases it is impossible to precisely analyze them. For this reason, in the last decades, numerical

simulation procedure has become a tool for the successful design of complex induction heating and hardening systems. Numerical modeling can replace many expensive, time-consuming, and material wasting physical tests.

Until recently FEM software used to be a quite expensive tool that only enterprise level companies could afford. These tools also required highly qualified engineers with a good understanding of computational simulations to be able to run simulations in time and computationally effective ways. In this study, CENOS software was used to simulate induction hardening of the splined shaft. CENOS uses open-source tools, which have proven to give accurate and fast calculation results, and at the same time offering user friendly design for case building.[2]

In a previous study it has been shown that even though it is tempting to simplify this kind of axisymmetric geometry to 2D geometry, it will not give results accurate enough. Rather a 3D slice should be used as in fig 1. [3]

II. MICROSTRUCTURE CALCULATION

Induction hardening involves workpiece heating up to the austenitization temperature (A_{c3}) continued with rapid cooling (quenching). Different microstructures can be obtained in the steel piece by changing the speed of cooling. In CENOS cooling is done by changing the heat transfer coefficient of the workpiece surface. Knowing the distribution of steel phase microstructure at the end of the surface hardening is very important as it gives an understanding of the final stress in the workpiece.[1]

Martensite is the microstructure with the highest hardness which is normally wanted on the surface of the workpiece. If the cooling is relatively fast, a microstructure called martensite will be achieved, otherwise, other structures – ferrite, pearlite, and bainite starts to form (also called diffusional phases). To calculate austenite transformation to diffusional phases in CENOS software JMAK-type equation was used. [4] Since the finite element method is used, the

JAMAK equation is differentiated and the volumetric fraction of changed microstructure is calculated as:

$$\Delta f(t)_i = \left(k(T)n(T)t^{n(T)-1}e^{-k(T)t^{n(T)}} \right) \Delta t_i \quad (1)$$

Where constants k and n are:

$$n(T) = \frac{\ln \left[\frac{\ln(1-f_s)}{\ln(1-f_e)} \right]}{\ln(t_s/t_e)} \quad (2)$$

$$k(T) = -\frac{\ln(1-f_s)}{t_s^{n(T)}} \quad (3)$$

$f_s(T)$ and $f_e(T)$ are respectively points in Time-Temperature-Transformation diagram which represent the start and the end of transformation (respectively 1% and 99% fraction change) depending on temperature.

When the temperature falls under austenitization temperature (Ac_3), phase change can occur. To define the beginning of phase change Scheil's additivity hypothesis was used.

$$\sum_i \frac{\Delta t}{t_{1\%}} = 1 \quad (4)$$

The total fraction of the changed phase will be the summation of $\Delta f(t)_i$

$$f = \sum_i \Delta f(t)_i \quad (5)$$

III. RESULTS AND DISCUSSION

Engineers are often interested in the hardened profile of the workpiece, but in this study, we want to show, that hardened profiles do not give enough information if the hardening process needs to be fully understood. The temperature field in the workpiece is shown in fig. 2 which shows that reasonable temperature on the surface is achieved to perform surface hardening. In fig. 3a hardened profile,

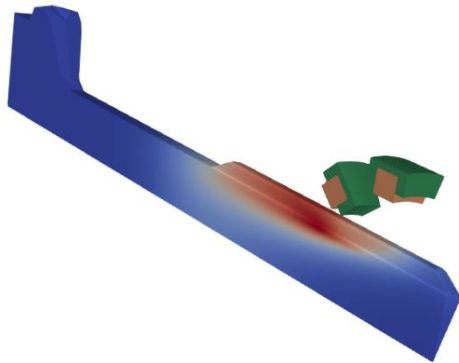


Fig 1: Illustration of the slice of full splined shaft geometry used for simulation.

where temperature above austenitization temperature Ac_3 was reached, is shown. In this case, moderate water flow was used as cooling with heat transfer coefficient from the surface $2000 \text{ W/m}^2\text{K}$. Now, when we look at the final microstructure distribution, we can see that the martensitic structure on the teeth surface is only 80%, but the base of the spline is only 20% martensite and 80% diffusional phases (ferrite, bainite, pearlite). Since the fully martensitic structure is wanted on the surface of the shaft, simulation can be used as a useful tool to pinpoint the flaws in the induction hardening process. In this case, we can see, that faster cooling is needed to achieve martensitic structure at the base of the teeth.

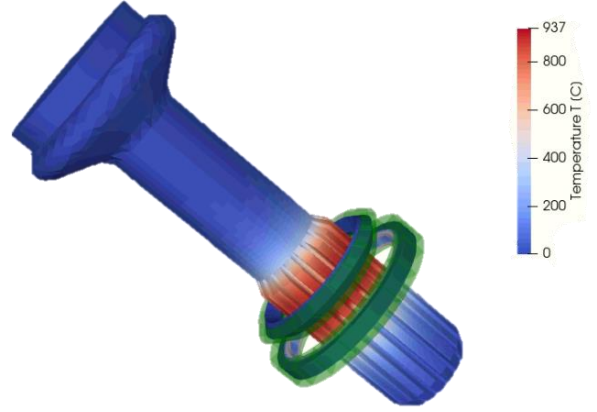


Fig2: Illustration of full geometry with a sector view of inductors and flux

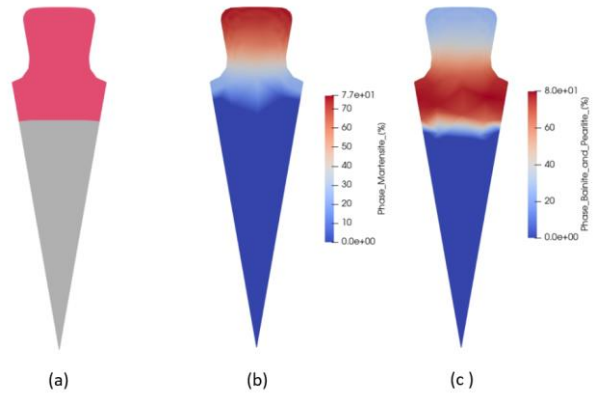


Fig 3: Splined shaft profile of the a) hardened zone b) martensitic structure field c) diffusional phase (ferrite, bainite, pearlite) field

REFERENCES

- [1] ASM Handbook, Volume 4C: Induction Heating and Heat Treatment, ed. By Rudnev, V. & Totten, G. E., ASM International (Materials Park, OH, 2014).
- [2] V. Geža, et al., "Potential of open source simulation tools for induction heating", IOP Conference Series: Materials Science and Engineering, , 424(1), 2018
- [3] V. Geža, et al., "Simulation of scanning induction hardening for splined shaft", 30th ASM Heat Treating Society Conference and Exposition, Heat Treat 2019 - Extended Abstracts, , 1 43-47, 2019.
- [4] J. Yuan and R. D. S. Jr, "FEM Modeling of Induction Hardening Processes in Steel," vol. 12, pp. 589–596, 2003

Energy Efficient Solid-State Microwave Curing of Carbon Fiber Reinforced Composites

1st Suraj Murali
Percyroc AB
Uppsala, Sweden

2nd Christian Bothen
Uppsala University
Uppsala, Sweden

3rd Srivijay Manjunath
Uppsala University
Uppsala, Sweden

4th Ebrahim Bagheri
University of Tehran
Tehran, Iran

5th Mohamed Loukil
RISE
Linköping, Sweden

6th Daniel Pelikan
Percyroc AB
Uppsala, Sweden

7th Kristiaan Pelckmans
Uppsala University
Percyroc AB
Uppsala, Sweden

8th Dragos Dancila
Uppsala University
Percyroc AB
Uppsala, Sweden

corresponding author: Dragos.Dancila@angstrom.uu.se

Abstract—In this paper we present a new set-up for curing carbon fiber composite materials realised around four solid state power amplifiers generating 250 W microwave power in the frequency range 2.4 - 2.5 GHz. This microwave curing set-up improves the homogeneity of the heating pattern by combining different standing waves in a process using an IR camera, as feedback for a machine learning based controller. We show also that the energy used for the curing process is drastically reduced in comparison with curing using conventional methods.

Index Terms—Industrial applications, Microwave, Solid-state, Chemical applications, Scale-up.

I. INTRODUCTION

Carbon fiber reinforced polymers (CFRPs) are high strength, high modulus, low density but relatively priced composite materials. Presently as they are in high demand for the aerospace and automotive industries, fast and energy efficient manufacturing techniques are highly sought after. Conventional curing methods, such as autoclave and oven curing rely on convective heating, where not only the medium surrounding the composite materials has to be heated but also the whole body of the oven is heated. Using microwaves for curing CFRPs has the advantage to heat only the composite materials. This is often attributed to the composites ability to volumetrically absorb electromagnetic energy within the GHz region [1]. The advantage over autoclave and oven curing processes are essentially a decreased curing time and high energy savings [2] [3] [4].

II. PHYSICAL SETUP

We have developed a microwave curing set-up for CFRPs, using a system composed of four solid state microwave power amplifiers, based on the NXP (now Ampleon, Netherlands) quad channel radiofrequency (RF) power generation system. Each channel is composed of a BLAZE 250 power amplifier module, composed of an LDMOS driver, of the type BLF2425M9L(S)30 and a main power amplifier, of the type BLC2425M8L300P. The RF generation and control system board includes four BLP25RFE001 chip-sets. Each channel delivers 250 Watts between 2.4 and 2.5 GHz into a rectangular

multi-mode cavity, with dimensions: 400 mm x 400 mm x 135 mm as shown in Fig. 1. The targeted CFRP composite material with dimensions 150 mm x 250 mm is placed in the center of the cavity, at 30 mm from its bottom, where the E field shows maximal values. Microwave processing is known for its non-uniformity, inevitable presence of hot spots and thus a strong potential non-uniform curing. Therefore, we are using an ensemble of complementary standing waves, as to homogenise the heat distribution. Our implementation is based on a real time IR camera feedback, allowing the selection of the standing waves that complement each other and lead to heat homogenisation. The four generators are set at the same frequency, and the frequency is swept in the interval of frequencies considered while phases are set in increments of 10° phase differences in between ports. Four coaxial to waveguide transitions are used as feeders to the cavity and their orientation is central on each of the sides of the cavity. The coupling to the cavities' modes is assessed and a selection of frequencies resulting in the lowest reflection coefficients is made prior to injecting high power. The solid state generation of microwaves provides unique benefits, as compared to the traditional magnetron generators, as it is only this type of generation that provides the capability to realise the manipulation of the standing waves, i.e. using the differences in phases in between ports and multiple frequencies to excite different standing waves and realise heat homogenisation.

III. EXPERIMENT

CFRPs consist of a binding matrix, often some kind of thermoset polymer such as epoxy, and a reinforcement, such as carbon fibers. When the impregnation occurs before curing, the uncured CFRP sheets are referred to as pre-pregs and can either be unidirectional or woven [5]. In order for the polymer to cure the CFRP needs to be held at the curing temperature (also referred to as dwell temperature) for a certain dwell time. For our experiments, the CFRP samples were made from sheets of HexPly©8552 unidirectional (UD) carbon pre-pregs. These uncured pre-preg materials are placed in a vacuum bag for further processing, as shown in Fig. 2 and

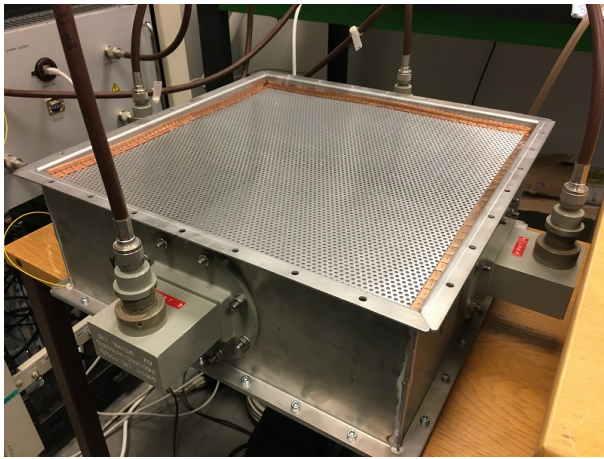


Fig. 1. Experimental setup showing the microwave heating system.

then cured using microwaves at around 180°C.

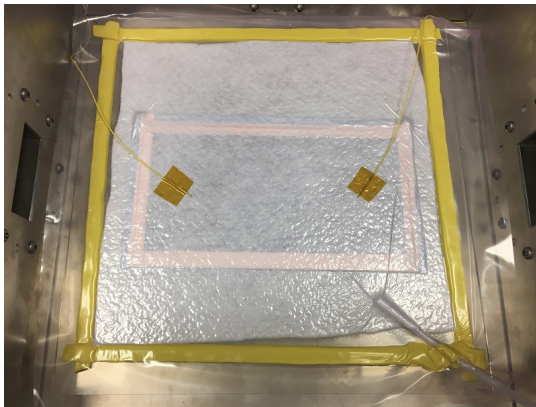


Fig. 2. Vacuum bagging only process

IV. RESULTS

The microwave-cured UD samples were tested using a three-point bending test was performed to investigate the flexural properties of the samples. The test was performed in accordance with the ASTM D790 standard test method [6]. The reference samples of the CFRPs were cured in a Memmert Universal Oven UF450plus industrial oven also using the vacuum bagging technique. The results showed that by using the microwave curing process on unidirectional CFRPs it is possible to reduce the curing time (excluding cooling time) by up to 89% and the energy consumption by up to 90% compared to oven curing. In addition to the increased efficiency, all of the microwaved-cured unidirectional CFRPs showed a higher stiffness than the oven-cured unidirectional CFRP, without showing a considerable reduction in maximum stress. The increased stiffness did however come at an expense of a reduced maximum strain. The results presented in Fig. 3 show that the microwave curing process significantly reduces the

energy consumption compared to the oven curing process. This is specially the case for a heat process in a "sawtooth" profile, as presented in this figure, characterised by an excursion at 180°C followed by a cooling down till 140°C during 5 min and repeated consecutively during the whole duration of the curing time. One of the distinct differences between the microwave and oven curing process is the time needed for the ramp-up phase. It can also be concluded that all microwave-cured samples showed higher Young's modulus than the oven-cured sample. Thus, the microwave curing process was more energy efficient and yielded samples with higher stiffness than the oven curing process.

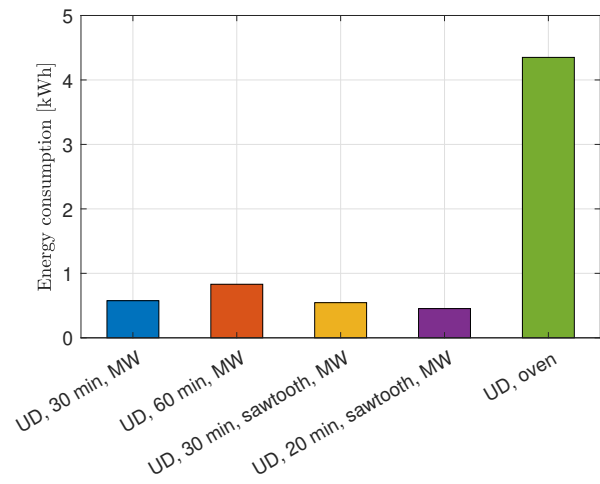


Fig. 3. Estimated energy consumption during microwave and oven curing processes.

V. ACKNOWLEDGMENTS

The authors would like to thank Ampleon Netherlands B.V. for supporting this work. The authors are also thankful to the FREIA laboratory at Uppsala university for assistance and support.

REFERENCES

- [1] B. Nuhiji et al., *Simulation of carbon fibre composites in an industrial microwave*. Proc., vol. 34, pp. 82-92, 12th Int. Conf. on Composite Science and Techn., 2021.
- [2] E. T. Thostenson, T.-W. Chou, *Microwave processing: fundamentals and applications*. Composites Part A: Applied Science and Manufacturing, Volume 30, Issue 9, 1999, Pages 1055-1071, ISSN 1359-835X.
- [3] L. Feher, P. Pozzo, M. Thumm, *Microwave Innovation for Industrial Composite Fabrication - The HEPHAISTOS Technology*. The 30th International Conference on Plasma Science, 2003. IEEE Conference Record - Abstracts., Jeju, South Korea, 2003, pp. 126-.
- [4] L. Cheng, Y. Li, J. Zhou, *Temperature Distribution Optimization during Composites Microwave Curing Using Time-varying Electromagnetic Field*. 2018 IEEE 22nd Int. Conf. on Computer Supported Cooperative Work in Design ((CSCWD)), Nanjing, China, 2018, pp. 202-206,
- [5] P. Morgan, *Carbon Fibers and their Composites* Taylor & Francis, Boca Raton, FL, USA.
- [6] ASTM International. *Standard Test Methods for Flexural Properties of Unreinforced and Reinforced Plastics and Electrical Insulating Materials*. West Conshohocken, PA, USA.

Approaches to Modernize Induction Heater for Purpose of Heat Treatment of Titanium Alloys

I. Smolyanov

Department of Electric Engineering and Electrotechnology
Systems
Ural Federal University
Ekaterinburg, Russia
i.a.smolyanov@gmail.com

V. Kotlan, I. Dolezel

Department of Electrical and Computational Engineering
University of West Bohemia
Plzen, Czech Republic
doleze@fel.cvut.cz

Abstract— Through heating of titanium before plastic deformation is energy and time-consuming process. The main problem carrying out the process is used resistance furnaces which require a lot of time and power. The paper suggests implementing induction heating for purpose of reducing treatment time and power. In order to realize it, the authors are considering several approaches of optimization to find out optimal modes of operation. The proposed ways to optimize heater is shape and topology optimization. The ways are implemented to Comsol Multiphysics and based on obtaining results of finite element analysis. It also discusses what geometric parameters and to what extent affect the technological mode.

Keywords— Optimization techniques, induction heating, uniformity of temperature, numerical analysis, FEM, FEA

I. INTRODUCTION

Titanium is one of the main structural materials used in aircraft construction, military industry, shipbuilding and a number of other industries, requiring high quality materials due to safety requirements. Therefore, each step-in creating titanium products for these areas requires increased attention and the use of the latest technologies. This work is devoted to the heat treatment of titanium billets before plastic deformation.

II. FORMULATION OF THE PROBLEM

A. Finite element formulation of the problem

The process of induction heating can be presented as a doubly coupled electromagnetic-thermal problem. The 2D axis-symmetric problem of magnetic field may be described in terms of magnetic vector potential \underline{A} using complex numbers as shown below

$$\text{curl curl}(\underline{A}) + j \cdot \omega \gamma \mu \underline{A} = \mu \underline{J}_{\text{ext}}, \quad (1)$$

where $\omega = 2\pi f$ denotes the angular frequency γ is the electric conductivity, μ is the magnetic permeability.

The complex current density of coil domains is written as

$$\underline{J}_{\text{ext}} = \sigma \left(j\omega \underline{A} + \frac{U(T)}{l} \right) \quad (3)$$

где, \underline{l} is the vector of the coil length and voltage $U(T)$ is defined as following

$$U = K_p(T_g - T_m) + K_i \int_0^t (T_g - T_m) dt + K_d \frac{dT_m}{dt}. \quad (4)$$

The equation is dependent on the temperature T_m which is measured at a point of workpiece surface in the middle of its length and the given temperature T_g . Control is realized by selecting factors K_p , K_i and K_d . And the temperature is calculated by classic heat transfer equation in the general form

$$\text{div}(\lambda(T)\text{grad}(T)) = \rho C_p(T) \frac{\partial T}{\partial t} - p. \quad (5)$$

Here p is the dissipated Joule power, C_p is the heat capacity, λ is depicted thermal conductivity, ρ is the mass density.

The process of irradiation of heat from surface is taken into account by boundary conditions implemented in Comsol called «Surface-to-surface radiation».

B. Formulation of the problem

The figure 1 is shown geometry of the installation and depicted the main changing parameters.

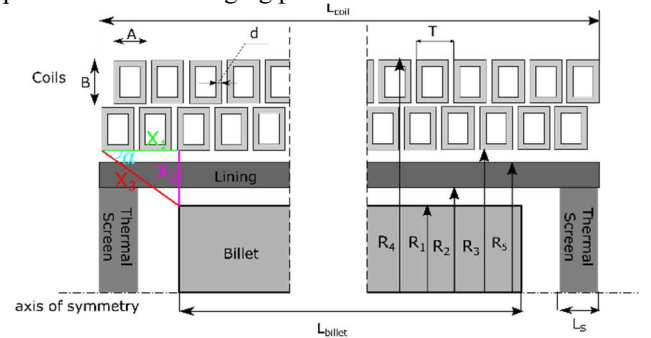


Fig. 1. Main geometry

III. RESULTS

In the classical theory of induction heating, «ideal» cases are considered in which heat losses due to radiative exchange, convective heat transfer, and also nonlinear physical properties of the heating workpiece in space are neglected. This theory also claims that the inductor overhang should be more than 15% of the workpiece length for uniform heating along the workpiece length, and maximum efficiency is achieved by reducing the gap between the inductor and the workpiece. These findings are usually obtained using analytical expressions or empirical experience. But in the process of optimizing the induction heater in [1], it was noted that in some cases, an increase in the gap leads to a decrease in the temperature difference at the end of heating.

Let us consider the two cases of «ideal» and «real». In the ideal case, we neglect any heat loss (radiation, heat transfer), but we take into account the uneven distribution of the magnetic field. In real cases, the exchange of radiation, heat transfer to the environment, the influence of the lining, etc. are taken into account. In order to conduct a correct comparison in all cases, the maximum current is the same, whom is changing dependent on the temperature at a certain point according to a similar law as in equation (4).

Analyzing figure 2, it can be concluded that with an increase in the length of the inductor (a negative overhang indicates that the length of the inductor is less than the length

of the workpiece), both for the real case and for the ideal one, the temperature difference decreases. But for an ideal case, there is a range of minimum difference (extension length 200-250 mm) after which the temperature difference curve begins to increase again. An increase in the gap for both cases leads to an increase in the temperature difference in the volume.

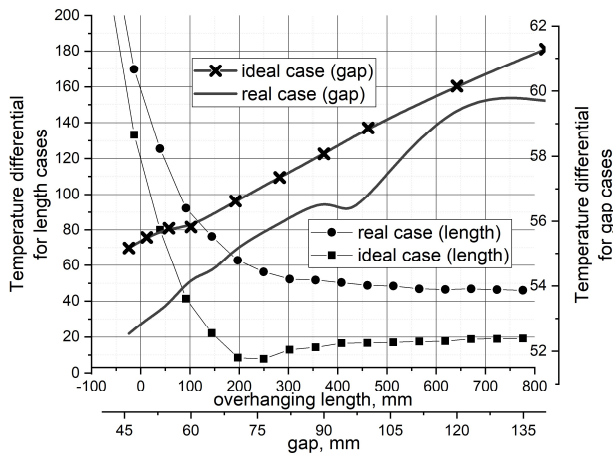


Fig. 2. The temperature difference at the end of heating for a real and idealized case depending on the departure and clearance

It is worth considering several cases with different ratios of the inductor offset and the gap. These results are shown in Fig. 3 for an ideal case and in Fig. 4. for the real case. Analyzing the data of the figures, it can be noted that with an increase in the length of the departure, a moment arises when a further increase in the gap leads to an increase in the uniformity of heating.

One explanation for the fact that there are optimal ratios of length and gap, and as a consequence of the angle between them, is the vortex nature of the magnetic field. In the center of the billet, the magnetic field can be considered almost solid, i.e. only the azimuthal component of the magnetic field prevails, and at the edges of the workpiece, the field has a vortex character and closes to itself through the edges of the workpiece (see Figure 5). The influence of field vortices can be weakened by changing the ratio of the inductor to the gap and the gap, and as a result, align the magnetic field in the workpiece.

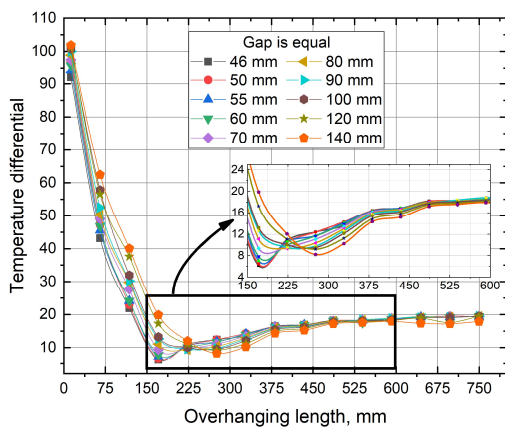


Fig. 3. Temperature difference at the end of heating for an ideal case depending on the inductor

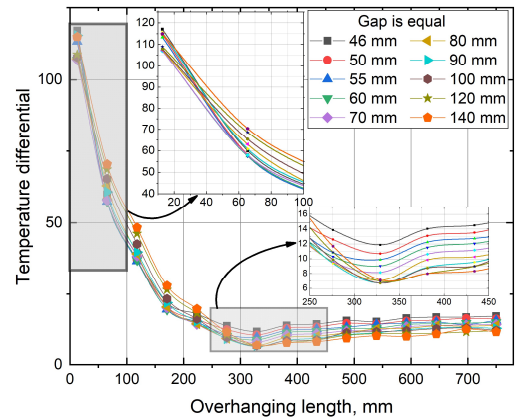


Fig. 4. The temperature difference at the end of heating for the real case

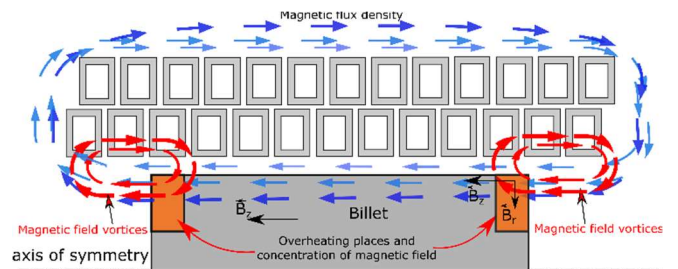


Fig. 5. Explanation of overheating of the marginal zones

IV. CONCLUSION

In the work will be considered approaches how to choose the most appropriate way in order heat up uniformly workpiece. Here, authors show briefly general results as ratio of lengths of inductor and workpiece influence on distribution of temperature along length. In full paper, the result will be added by optimization study and additional parametric explanations.

ACKNOWLEDGMENT

The work was supported by Act 211 Government of the Russia Federation, contract № 02.A03.21.0006.

REFERENCES

- [1] I. A. Smolyanov, V. Kotlan, I. Dozeze, «Optimal heat induction treatment of titanium alloys» COMPEL
- [2] I. Smolyanov F. Sarapulov, S. Sarapulov « Induction Heating Control of Titanium Alloys» Proc. Int. Conf. CSCMP pp. 106-111

Possibilities of Using an Energy Surplus of Photovoltaic Power Plants

Jakub Jiřinec
Department of Electrical Power
Engineering
University of West Bohemia
Pilsen, Czech republic
jjirinec@fel.zcu.cz

Michal Knedlík
Department of Electrical Power
Engineering
University of West Bohemia
Pilsen, Czech republic
mknedlik@fel.zcu.cz

David Rot
Department of Electrical Power
Engineering
University of West Bohemia
Pilsen, Czech republic
rot@fel.zcu.cz

Abstract— Nowadays, the installation of photovoltaic power plants on the roof of houses is becoming more and more common. Compared to earlier times, the surplus electricity to the grid is not well-financed. It leads to increasing pressure to maximize the use of the electricity generated on the premises. Energy storage in batteries is becoming standard but is still insufficient. In most cases, the distribution of the building's consumption does not correspond to the PV generation, and the size of the battery storage would be economically prohibitive to utilize the surplus fully. A solution to this problem can be to control selected appliances depending on the PV production. This paper describes controlling the output of heat pumps, EV chargers, and resistive load. Our goal is to develop a control system for smaller buildings that allows communication between the devices and control their operation depending on the current and future PV production.

Keywords—PV powerplant, heat pump, EV charger, control system, energy management

I. INTRODUCTION

In the Czech Republic, the measurement of the PV surplus electricity is carried out in individual phases. For this reason, it is advantageous to use an asymmetrical inverter, which allows an adequate distribution of power to individual phases according to the actual consumption of the building. The asymmetrical inverter is equipped with a measurement module, which monitors the magnitude and direction of the currents in the individual phases. The whole system can be supplemented with battery storage to increase the share of self-consumption from the PV system.

In order to increase the self-consumption of the PV plant, it is necessary to optimize the operation of individual appliances according to the production of the PV plant. In an air-to-water heat pump operation, the PV production corresponds to the interval of high daily temperatures, making the overall operation even more economical. A requirement for its use is the large storage capacity of the building or storage tanks. For a more precise use of small powers, extending the system with smooth control of the surplus of the generated electricity to the resistance loads is advisable. It includes, for example, the heating of water in tanks or the control of electric heating. Thanks to Solid State Relay (SSR) control, their output can be precisely controlled depending on the flow to the grid.

With the current boom in electromobility, adding an electric car charger to the electrical installation is advisable, especially for new buildings. Using the electric car to accumulate electricity from PV power plants is possible, mainly in summer. In our case, these are mainly AC chargers, which are relatively affordable and can be controlled efficiently.

The possible control of individual appliances during the day depending on the PV production is shown in Fig. 1. The most significant consumption is represented by the heat pump and the electric car charger. These appliances cannot be controlled precisely according to the actual PV production. To minimize the energy surplus to the grid, resistive load control with SSR can be used.

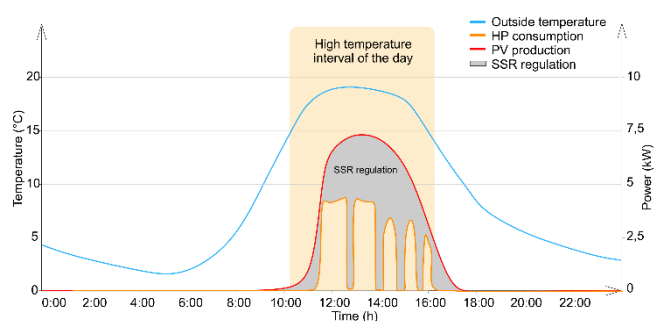


Fig. 1. Control of individual appliances during the day depending on the PV production

II. HEAT PUMP CONTROL

The possibility of controlling an air-to-water heat pump was tested in a building in Domažlice (Czech Republic). The building is equipped with underfloor heating and storage tanks. Due to the large storage capacity of the building, it was possible to shift the operation of the HP to the PV production area.

A comparison of hourly PV generation and HP consumption is shown in Fig. 2. From the course of the HP consumption, it can be seen that most of the electricity consumption was covered by PV production. An undesired start-up of the HP in the morning hours at low outdoor temperature was caused by a drop in room temperature below a set limit. By eliminating this start-up, higher utilization of the electricity produced by the PV plant could be achieved.

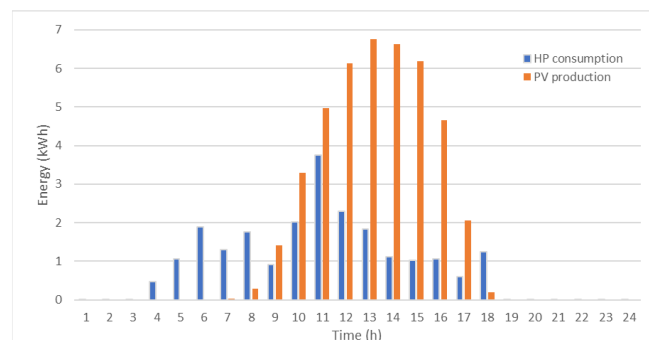


Fig. 2. Coverage of HP consumption from PV in hourly intervals

III. CONTROLLED CHARGING OF ELECTRIC VEHICLES

The proposed system was tested with AC charging station Schneider electric (EVB1A22P4ERI), and TESLA Model S electric vehicle (85 kWh) was charged with an on-board charger of 3x16 A. Based on the observation that EVs have different minimum charging currents, a function for determining the control range of charging was implemented. The system sets the minimum charging current according to the charging station (in our case, 8 A) and then starts increasing the charging current until the EV starts charging. It then considers this current value as the minimum value for the PV surplus control system. If the measured current value does not increase when the maximum charging current is subsequently increased, the system considers this value as the maximum value for surplus control. The measured values for determining the EV charging control range are shown in Table I.

TABLE I. DETERMINING THE CONTROL RANGE OF CHARGING OF AN ELECTRIC VEHICLE

Time (s)	Charging station						PV Power (W)
	Status	Max. current (A)	Power (W)	Current L1 (A)	Current L2 (A)	Current L3 (A)	
0	EV connected	8	5	0,06	0	0	5050
30	EV connected	9	5	0,06	0	0	5050
60	EV connected	10	5	0,06	0	0	5077
120	EV connected	12	5	0,06	0	0	5077
150	EV connected	13	5	0,06	0	0	5077
180	EV charging	14	9183	12,87	12,92	12,86	5127
210	EV charging	15	9960	13,96	14,05	13,86	5127
240	EV charging	16	11282	15,83	15,93	15,78	5127
270	EV charging	17	11282	15,83	15,93	15,78	5127

IV. RESISTIVE LOAD CONTROL

The control system was tested in the same building. There were used 6 kW direct heating elements connected in a star with a neutral conductor N installed in the PHW storage tank (volume 500 l) and the heating system storage tank (total volume 1000 l). The power control could be carried out in each phase separately.

From the temperature waveform in the PHW tank (Fig.3), it can be seen that the surplus from the PV power plant can be accumulated quite well by continuously controlling the power of the resistive loads in the PHW tank. However, there is a cooling of the water due to the inherent heat loss of the tank.



Fig. 3. Resistive load control of surplus from PV for PHW preparation

This cooling is quite significant and therefore ideally the heated water should be used as soon as possible (showing in the evening). In our case, the PHW consumption is minimal, and it can be said that a significant amount of the PV surplus is used for the tank's heat loss. This can be a problem, especially in the summer months when heating the technical room is undesirable.

Fig. 4 presents the electricity surplus to the grid in 2018-2020. The equipment installation took place in May 2020, which is also very clear from the graph, when there was a significant decrease in unconsumed electricity. However, the surplus to the grid persists due to the small volume of water storage tanks for the PWH and heating system. Other limitations are used water heaters, which are fitted with a thermostat, allowing a maximum temperature of 65 °C to be set.

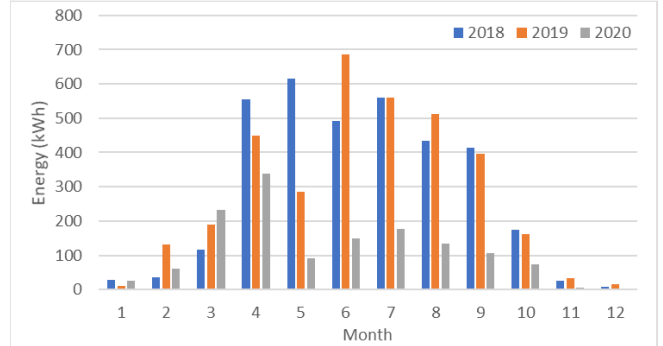


Fig. 4. The energy surplus from PV delivered to the grid.

V. CONCLUSION

The measurements show the suitability of using a heat pump, an electric vehicle, and a controlled resistive load to minimize the PV plant's grid surplus. At the same time, important observations have been made and should be considered for developing a control system that will include all the mentioned components. HP control is suitable in combination with a large storage capacity of a building or water tank. In the context of controlled EV charging, the recognition of the EV charging control range has been implemented in the system. The disadvantage of controlled charging is the relatively high minimum charging current (8 A). Inaccuracies in the HP and EV charging power regulation can be eliminated by continuous regulation of the resistive load using SSR.

A cloud-based application to set up and display the parameters for the user is being prepared, and a microcontroller that would enable the communication and control of the individual parts while making the proposed application cheaper for commercial use is being selected.

ACKNOWLEDGMENT

This paper was supported by the student research project SGS-2021-018.

REFERENCES

- [1] Heat pump system control: the potential improvement based on perfect prediction of weather forecast and user occupancy. In: Proceedings of 12th IEA Heat Pump Conference. Rotterdam, 2017, s. 9. ISBN 978-90-9030412-0.
- [2] C. Ioakimidis, T. Dimitrios, P. Rycerski, and K. Genikomsakis, "Peak shaving and valley filling of power consumption profile in non-residential buildings using an electric vehicle parking lot". Energy [online]. 2018, (148), 148-158 [cit. 2018-06-16]. ISSN 0360-5442. Available: <http://www.sciencedirect.com/science/article/pii/S0360544218301567>
- [3] Schneider Electric [online]. Prague, 2019 [cit. 2019-05-08]. Available: <https://www.se.com/cz/cs/>
- [4] J. Jirinec, "Effective Management of Technical Equipment of Buildings and Renewable Energy Sources for Residential and Commercial Buildings". Doctoral thesis, Pilsen, 2021.

Controlled Ventilation of Interior Spaces Using a Central Recuperation Unit

Jakub Jiřinec
Department of Electrical Power
Engineering
University of West Bohemia
Pilsen, Czech republic
jjirinec@fel.zcu.cz

Lenka Raková
Department of Electrical Power
Engineering
University of West Bohemia
Pilsen, Czech republic
lencar@fel.zcu.cz

David Rot
Department of Electrical Power
Engineering
University of West Bohemia
Pilsen, Czech republic
rot@fel.zcu.cz

Abstract—A common way of ventilating indoor spaces for more significant buildings is to use a central recuperation unit. In contrast to the decentralized recuperation unit, the system must be equipped with a control system that will control the individual parts of the ventilation system. This article describes a designed and implemented control system for commercial, school, or office buildings. The created control system minimizes the operating costs of buildings while adhering to the prescribed limits by effectively controlling the amount of air entering the individual rooms.

Keywords—central recuperation unit, control system, heating, CO₂ concentration, energy management

I. INTRODUCTION

The efficiency of recuperation units is affected by the outdoor air temperature. By operating the equipment at high efficiencies, financial costs can be saved. Standard heating systems only respond to the current outdoor temperature and do not exploit this potential. The solution is predictive control, which would consider the future development of the outdoor temperature and thus optimize the operation of the entire device. Based on the measured data of outdoor temperatures (January 2016 to March 2018), we found that it is possible to compile type courses of outdoor temperatures valid for individual days and months of the year and thus enable an approximate offline prediction. With the help of this prediction, recuperation units can be effectively controlled. Fig. 1 shows an example of outdoor temperatures with marked areas suitable for cooling and heating the building. This control principle was also applied in our designed control system of recuperation units. [1, 2, 3, 4]

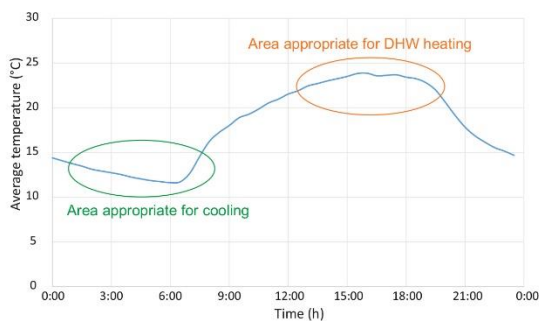


Fig. 1. Average temperatures during the day (August)

II. CONTROL SYSTEM DESIGN OF ACTIVE RECUPERATION UNITS

The proposed system was installed in kindergartens and primary schools for the hearing impaired in Pilsen. The main part of the system is the active recuperation unit NILAN

VPM1000. The control system can be controlled via a web user interface, which is used to control the operation, set working time intervals, and set the required temperatures and CO₂ limits in classrooms. According to the current operating state and system settings, the opening of the ventilation flaps and the radiator actuator is controlled. The WAGO PLC with the appropriate expansion cards was chosen as the core of the control system. Using the Modbus RTU communication protocol, the PLC communicates with individual components (sensors, electricity meter, recuperation unit). A significant advantage of the used hardware is the easy expandability and integration into superior building control systems (via the KNX, LON, etc.). [4, 5]

III. TEST OPERATION RESULTS

The control system was launched in May 2020 and was gradually improved. Interior cooling testing took place in August at outdoor temperatures above 25 °C. The measurement found that if the outdoor temperature is above 30 °C and the interiors are not cooled, then the room temperature is up to 35 °C. With continuous cooling of the whole building, the temperature in the interiors decreases, see the results in Fig. 2.

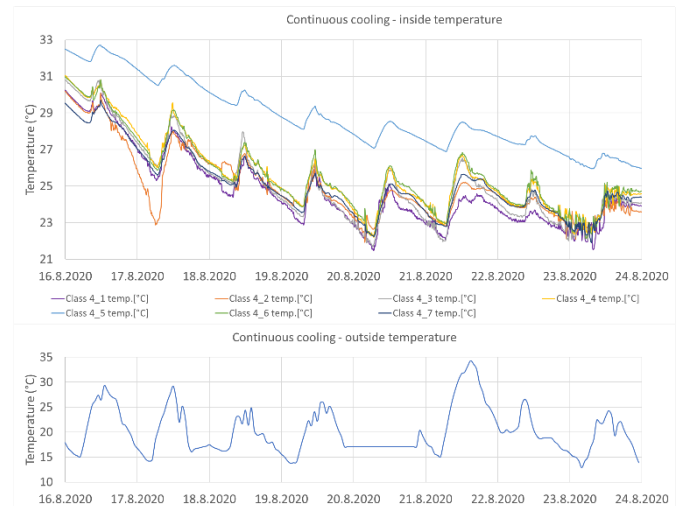


Fig. 2. The course of temperatures with continuous cooling in August 2020

This graph shows that the recuperation unit is not able to cool the entire building space effectively. The temperature in the rooms is decreasing, but very slowly. This is mainly due to the high value of thermal energy, which is accumulated in the concrete structure of the building. However, the maximum temperature was reduced from 32.6 °C to 26.6 °C during the day. During the last tested day, the internal temperature

dropped below the set limit of 23 ° C, and the system began to regulate the opening of the air flaps.

The operation of the proposed system was also monitored in the winter months. The required temperature during working hours was set to 24 ° C and outside working hours to 21 ° C. In the first tests, it was found that at low temperatures, the recuperation unit is not able to sufficiently heat the cold outdoor air to a temperature higher than 24 ° C. For this reason, the recuperation unit was started only according to the current CO₂ concentration in the rooms. The room was heated by radiator bodies equipped with servo drives. The course of the class temperature on the selected day is shown in Fig. 3

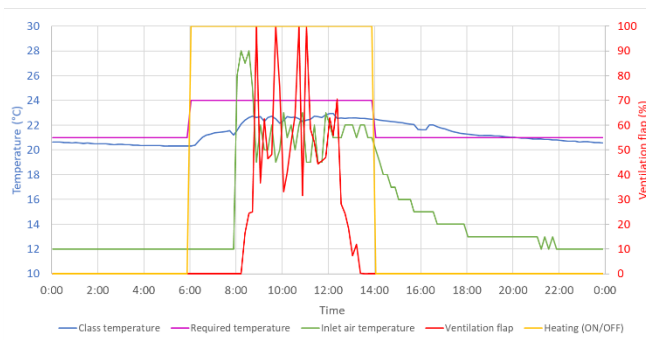


Fig. 3. Temperature course during winter operation in class (8.1.2021)

Fig. 4 shows the course of CO₂ concentration in the selected class. The system starts to regulate the opening of the air flaps from the value of 800 ppm, and at the value of 1,200 ppm, the damper is already fully open.

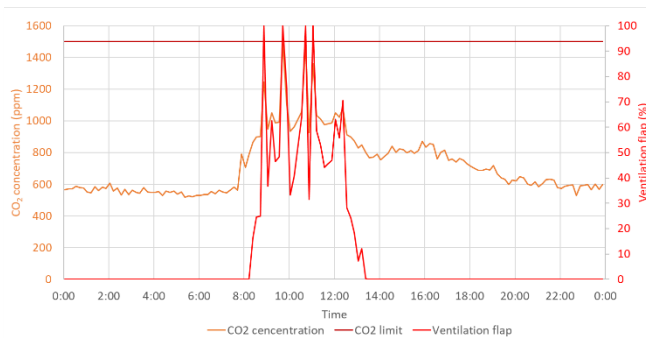


Fig. 4. The course of CO₂ concentration during winter operation in class (8.1.2021)

IV. IMPACT ON ENERGY MANAGEMENT AT SCHOOL

Continuous cooling is very uneconomical, the energy consumption of the primary school building and the curve of the indoor temperature of the selected room is shown in Fig. 5.

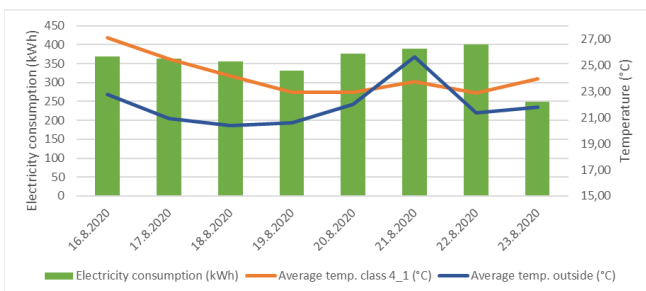


Fig. 5. Energy consumption for continuous cooling

If the recuperation unit is to be used for efficient cooling of the entire building, it would be necessary to increase its cooling capacity. Another important element in reducing cooling consumption would be the effective shading of windows using window blinds, eliminating heat gains from solar radiation. However, the school's energy management evaluation shows that the reconstruction of the building and the proposed controlled air recuperation have significantly improved the energy efficiency of these buildings, see Fig. 6.

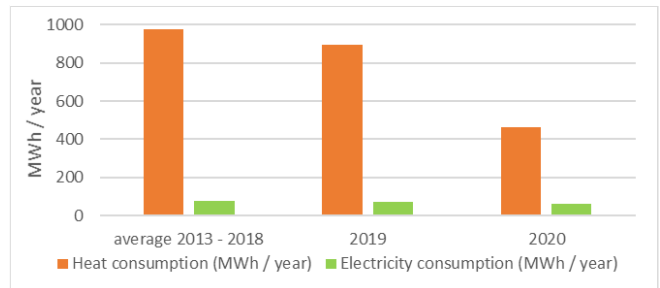


Fig. 6. Results of energy management

V. CONCLUSION

Long-term monitoring of the proposed system proved its suitability for keeping the CO₂ concentration within the required limit. In terms of efficient cooling, the system encounters the limits of the recuperation unit used, which does not have sufficient power to cool the entire building at high outdoor temperatures. However, this unit was not designed to cool the entire building, so we anticipated this in advance. During long-term cooling by the recuperation unit, the indoor temperature can be reduced to a value of around 24 ° C.

A significant result from the analysis of the operation of this system is that the control of night cooling in the summer months was, in many cases, not at the lowest outdoor temperature. The system has therefore been extended with an outdoor temperature forecast. The night cooling interval is controlled so that it always takes place at the lowest night temperatures. The energy analysis results showed that the energy consumption of the buildings was reduced thanks to the proposed controlled recuperation system and building insulation.

ACKNOWLEDGMENT

This paper was supported by the student research project SGS-2021-018.

REFERENCES

- [1] Z. Yang, B. Becerik-Gerber, "How Does Building Occupancy Influence Energy Efficiency of HVAC Systems?" in *energy Procedia*, 2016, pp.775-780. ISSN 1876-6102.
- [2] F. C. Mcquiston, J. D. Parker, J.D. Spitler, "Heating, ventilating, and air conditioning: analysis and design", 6th ed. Hoboken, N.J.: John Wiley, c2005. ISBN 978-0-471-47015-1.
- [3] G. Serale, M. Fiorentini, A. Capozzoli, D. Bernardini, A. Bemporad, "Model Predictive Control (MPC) for Enhancing Building and HVAC System Energy Efficiency: Problem Formulation, Applications and Opportunities." *Energies* [online]. 2018, 11(3) [cit. 2020-03-03]. ISSN 1996-1073. Available: doi:10.3390/en11030631.
- [4] J. Jirinec, "Effective Management of Technical Equipment of Buildings and Renewable Energy Sources for Residential and Commercial Buildings". Doctoral thesis, Pilsen, 2021.
- [5] WAGO, [cit. 2020-03-08]. Available: <https://www.wago.com/cz/>.

Cost reduction opportunities in induction surface hardening processes for smaller diameter cylindrical loads

David Rot
Department of Electrical Power
Engineering
University of West Bohemia
Pilsen, Czech republic
rot@fel.zcu.cz

Michal Knedlík
Department of Electrical Power
Engineering
University of West Bohemia
Pilsen, Czech republic
mknedlik@fel.zcu.cz

Jakub Jiřinec
Department of Electrical Power
Engineering
University of West Bohemia
Pilsen, Czech republic
jjirinec@fel.zcu.cz

Jiří Hajek
COMTES FHT a.s.
Dobřany, Czech republic
jiri.hajek@comtesfht.cz

Jiří Kožený
Department of Electrical Power
Engineering
University of West Bohemia
Pilsen, Czech republic
kozeny@fel.zcu.cz

Antonin Podhrazky
Energetics research center
University of West Bohemia
Pilsen, Czech republic
podhrazk@fst.zcu.cz

Abstract-This article focuses on the possibilities of improving the efficiency of induction surface hardening (ISH) processes using a specialized spray-quench device. This quench is fabricated using 3D printing, and the load is cooled by a quenching spray tangentially fed to its surface. Furthermore, the paper presents the results of several specific experiments which show how the tangential spray-quench device can influence the quenching phase of the ISH process. It is shown that the influence of the surface temperature of the load can be realized not only by the amount and type of quenching medium but also in what way the quenching medium is fed to the surface of the load.

Keywords-induction surface hardening, tangential spray-quench device, 3D print

I. INTRODUCTION

The induction surface hardening (ISH) process aims to achieve the load's desired surface hardness and strength. The load is usually a stressed machine part that must be heated during the first phase of ISH according to the appropriate temperature transformation austenitization diagram (TTA). The load is then quenched according to the (CTT) or (CCT) austenite decay diagram, depending on the specific steel and the desired final hardness during the subsequent ISH phase.

ISH usually involves a low-temperature tempering process to reduce the stresses created within the load in the ISH process. By significantly eliminating the stresses in the load, the tempering process reduces the risk of possible cracks on the load's surface. The tempering process may consist of volumetric heating of the load in the furnace to its tempering temperature or repeated induction heating. This usually results in a reduction in micro-creep and a decrease in the resulting hardness of the load depending on the temperature selected. [1, 2, 3]

II. LOAD

A. Formation of internal tension

A closer look at the ISH shows that the stresses in the load occur when the surface temperature of the load is lowered below the martensitic start temperature of about 300 °C. Since the transformation of the starting austenite to the martensite is the so-called athermal, no intensive cooling of the load is necessary below this temperature. Therefore, it is advisable

and often used in this final stage to reduce the load's cooling rate and thus limit the formation of stresses in the load. It is also possible to take advantage of the internal heat in the load to reduce the stress level and, to some extent, to use the so-called self-tempering. If the cooling rate in the final stage of the ISH process is appropriately controlled, the subsequent tempering process can be omitted.

B. Elimination of tension

When using a conventional spray-quench device in ISH processes (such as in Fig. 1), the load is usually cooled to the temperature of the quenching medium, which is usually water, during quenching. By adding polymers to the water, a favorable modification of the load quenching process in the final stage of ISH can be achieved [4].

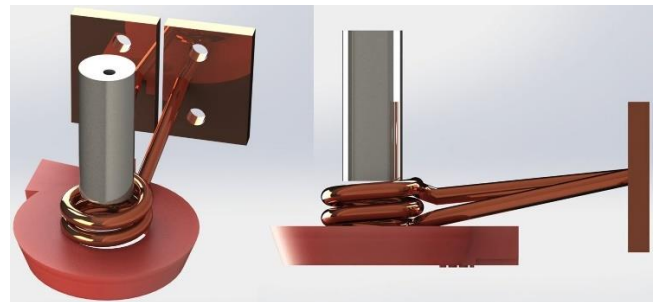


Fig. 1 Standard arrangement of components in ISH process, inductor, load, spray-quench device. [4]

In practice, solutions of polymers based on PAG (polyvinyl alkylene glycol) are most commonly used in the ISH process. Usually in the concentration range of 6% to 20%. However, this solution increases the price of the ISH process and requires higher investment costs for specialized management of quenching media. Quenching bath with polymers must be constantly checked, refilled, swirled, etc. The aerosols released during the ISH process condense on the surrounding surfaces. This phenomenon can subsequently lead to failures of electrical and mechanical components of induction systems. The danger for personnel was that the additives previously used in polymers were considered to be carcinogenic substances. In general, this solution worsens the quality of the environment.

III. EXPERIMENTS

After several experiments carried out using a specialized spray quenching device made by 3D printing (FFF) and a specific method of quenching the load, it turns out that the ISH process can be controlled in the desired way even if the hardening medium is pure water.

The experiments aimed to define the influence of tangential spraying of the deposit on its final temperature after the hardening process, depending on the direction of rotation of the load with respect to the quenching spray and the distance of the spray from the tangent with its surface.

Two quenching media, water and 8% water-polymer (SERVISCOL 98SK-F1) solution were used during the experiments. A high-speed camera was used to study how the water spray behaves on the surface of the load. It captured the ISH processes taking place on the surface of the load as it was being focused. At the same time, the surface temperature after the quenching process was captured by the thermal imaging camera. Subsequently, the maximum, minimum, and average surface temperatures were evaluated to assess the cooling efficiency of the different spraying methods. The following Fig. 2 shows the relative arrangement of the spray-quench device and the load, while the green arrows in the figure show how their manipulation was implemented during the experiments.

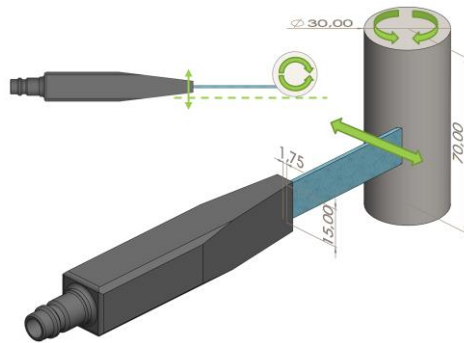


Fig. 2 3D model showing the relative arrangement of the spray quench and the inlet during tangential spraying. All dimensions are in mm.

During the experiments described above, the parameters affecting the ISH process were set identically. The main parameters are listed in TABLE 1.

TABLE 1 ISH process parameters, which are the same for all experiments

Load				Generator		Transformer	S-quench device
steel	diameter (mm)	height (mm)	moving speed (mm/s)	I (A)	fr (kHz)	Conversion (-)	flow rate (kg/m)
EN 34CrAINi7	30	70	2	85	28	16:1	11

IV. RESULTS

Next, Fig 3. shows the temperature field distribution captured by the IR camera on the load's surface after the ISH process. The spray direction in Fig. 3 is opposite to the direction of the rotating load. Spray dimensions 1.75 x 15 mm. The green arrow in Fig. 3 shows the rotation direction of the load. The blue arrow in Fig. 3 shows the spray direction. The situation in Fig. 3 corresponds with the point/variant "W OD" in Fig 4.

This research was funded by the Ministry of Education (Funder ID: 10.13039/501100001823) under the project SGS-2021-018.

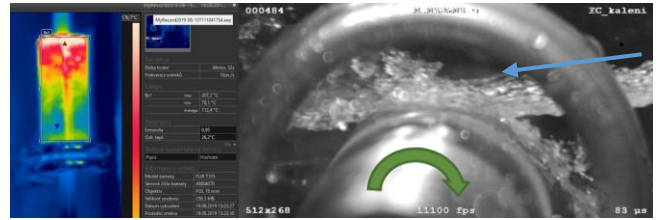


Fig. 3 The left side of the figure shows the temperature distribution in the load surface after the ISH process (front view). Min. temperature on the load surface is, in this case, 70 °C and the max. temperature is 207 °C. Generally, higher differences between min. and max. were in cases when pure water was used. The right side shows a figure from a slow-motion camera during the ISH process (top view).

In summary, the Fig. 4 shows results of the eleven implemented ISH experiments and demonstrates the indicating symbols near the measurement results. The results show the average temperature of the load surface as a function of the distance of the quenching spray from the tangent to its surface.

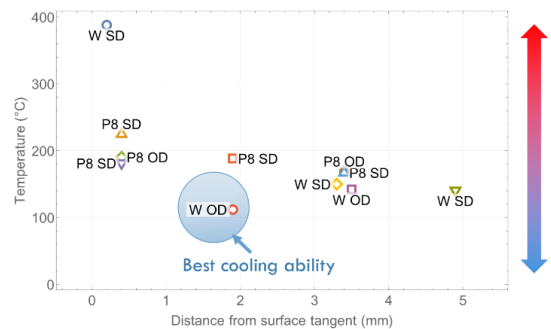


Fig. 4 Experiments results, W means water, P8 means water solution with 8% polymers, SD means the load is rotating in the same direction to the water stream, OD means the load is rotating in the opposite direction to the water stream.

DISCUSSION OF RESULTS

As presented in Fig. 4, the best cooling effect of the quenching medium was found in the case where the distance of the quenching spray was about 2 mm from the tangent with the surface of the load. In this instance, the average surface temperature of the load was the lowest of all experiments. Except for the case where the resulting average surface temperature of the load after ISH process was around 400 °C, all other samples reached the minimum hardness defined in the technical delivery conditions of the respective steel. From the results of the experiments carried out, it is clear that by a suitable configuration of the tangential spray-quench device in relation to the load, the desired load temperature can be achieved after the ISH process. Current experience show that it should be also possible to quench other steels by this ISH method. Further study will confirm these assumptions. A corresponding numerical model is also in preparation.

REFERENCES

- [1] Valery, R., and George, E. T., eds. 2014, *Induction Heating and Heat Treatment 4c*, ASM International.
- [2] Rudnev, V., Loveless, D., and Cook, R., 2017, *Handbook of Induction Heating*, Routledge.
- [3] Totten, G. E., 2002, *Handbook of Residual Stress and Deformation of Steel*, ASM international.
- [4] Hájek, J., Rot, D., and Jiřinec, J., 2019, "Distortion in Induction-Hardened Cylindrical Part," *Defect and Diffusion Forum*, Trans Tech Publ, pp. 30-44.

Modeling of temperature patterns and hardness of surfaces obtained by additive technique

Vaclav Kotlan
Faculty of Electrical Engineering
University of West Bohemia
Pilsen, Czech Republic
vkotlan@fel.zcu.cz

Roman Hamar
Faculty of Electrical Engineering
University of West Bohemia
Pilsen, Czech Republic
hamar@fel.zcu.cz

Karel Slobodnik
Faculty of Electrical Engineering
University of West Bohemia
Pilsen, Czech Republic
karels@fel.zcu.cz

Ivo Dolezel
Faculty of Electrical Engineering
University of West Bohemia
Pilsen, Czech Republic
dolezel@fel.zcu.cz

Abstract—Temperature patterns and hardness of surfaces produced by laser cladding is modeled. The mathematical model includes the description of all important physical phenomena taking part in the process. Experimental values of resultant hardness are also provided.

Keywords—laser cladding, mathematical model, numerical analysis, experimental data, hardness

I. INTRODUCTION

Laser cladding [1] is a modern technology mainly used for improving quality and physical parameters of steel surfaces. The layer of deposited material represents a very good protection against wear, corrosion, fatigue and extends the service life of parts treated in this manner.

The process of cladding is explained in Fig. 1. The laser head moves in the direction perpendicular to the drawing.

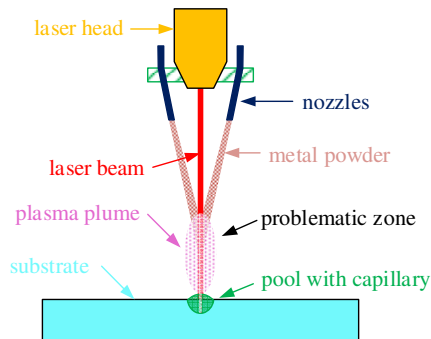


Fig. 1: Basic arrangement of process. Problematic zone denotes area where delivered powder crosses path of laser beam and where also plasma plume occurs.

The substrate is located below the laser head. The beam continuously heats its surface and also the metal powder that is sprayed to the exposed spot using one or more nozzles. At the irradiated spot, the substrate and powder are heated. The heat-affected area is, however, small, so that the power of the laser beam makes fast their temperature high enough for melting both the surface layer of the substrate material and the powder. Subsequently, a pool of melt is formed there with a thin capillary in its center. The capillary contains evaporated particles of metal that form a cloud of plasma above the pool. Its existence may lead to a certain decrease of the power of the laser beam, which may be significant in some cases, when a part of this power is absorbed here and another part is reflected back.

After shifting the substrate (or the laser head), the pool begins to solidify. In this manner, the track is successively formed. Several tracks deposited next to one another then produce the covering layer.

II. MATHEMATICAL MODEL AND ITS SOLUTION

The mathematical models of particular phenomena include:

- The temperature field generated by the laser beam described by the heat transfer equation [2] and supplemented with the correct boundary condition.
- The field of flow providing the distribution of velocities of particles of melt in the pool. During this turbulent process, some ionized particles of material evaporate and penetrate through the thin capillary above the substrate, forming there a plasma plume. The interaction between the temperature and flow fields is here very strong and must be solved in the hard-coupled formulation [3].
- Effects of the plasma plume influencing the power delivered by the laser beam to the irradiated spot. A part of the laser power is absorbed in the plasma plume, another part is reflected back [4].
- Field of mechanical strains and stresses providing the distribution of these quantities in the deposited layer. This model is relatively complicated and must incorporate material nonlinearities, full geometry and works with the theory of large deformations starting from the Green-Lagrange strain equations [5].
- Hardness of the surface. It normally follows from the continuous cooling transformation (CCT) diagram of the deposited material. These diagrams are, however, available mostly for massive hardening (for instance by induction heating), while for laser heating, the final hardness must be found experimentally.

The numerical solution of the model is realized by an own improved algorithm.

III. ILLUSTRATIVE EXAMPLE

As an example, authors present a 3D model of laser cladding of four concentrated circular tracks on a cylindrical substrate. The arrangement is shown in Fig. 2.

The substrate is made of steel S355, while the make of the metal powder is H13. The power delivered by the laser beam to the surface of the substrate was 360 W. The radius of the

laser beam was 2 mm. The velocity of the laser head was 30 mm/s. The injected powder was delivered at a mass rate of 15 g/min. The ambient (initial) temperature was 25 °C and the modified coefficient of convection that includes also the influence of radiation was $\alpha = 25 \text{ W} \cdot \text{m}^{-2} \cdot \text{K}^{-1}$.

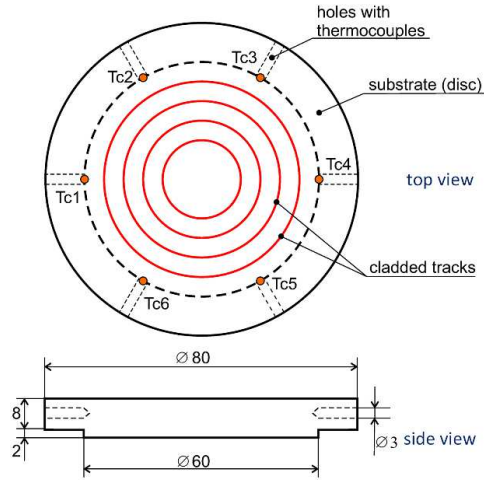


Fig. 2: Solved arrangement: red circles show the axes of four tracks, the positions of thermocouples are marked as Tc1, ..., Tc6. All dimensions are given in mm.

We tested two variants denoted as A and B, see Fig. 3. In variant A, all layers were deposited at once from the outer track towards the center. Therefore, most of the heat was generated in the center of the substrate. In variant B, the layers were also deposited from the largest circle to the inner circle, but only by one. In this way, heat could be distributed to the entire volume.

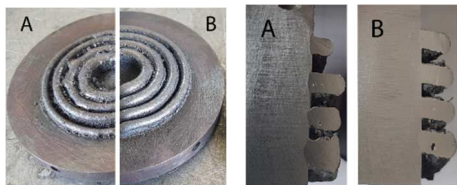


Fig. 3: Two solved variants (left) and cut through particular tracks (right).

Selected results are depicted in the following figures. Figure 4 shows the points where the hardness was measured in case of the variant A. The same was done for the variant B. The distribution of hardness measured in the outermost track for both variants is depicted in Fig. 5. Figure 6 shows the time evolution of temperature at the place of the thermocouple Tc6. The agreement between measurement and modeling is excellent. Finally, Fig. 7 depicts the time evolution of temperature at the measuring point and center of the substrate.



Fig. 4: Points at which hardness was measured.

Based on the model, we can obtain information about the behaviour of the whole system. While at the measured points the temperature waveforms for variants A and B are almost identical and do not indicate any problem, the temperatures in the center of the substrate (generally anywhere in the system), which cannot be easily measured, already show a clear problem. For variant A, there is clearly a problem in heat

build-up leading to poor quality and softer filaments, as can be seen in Fig. 7.

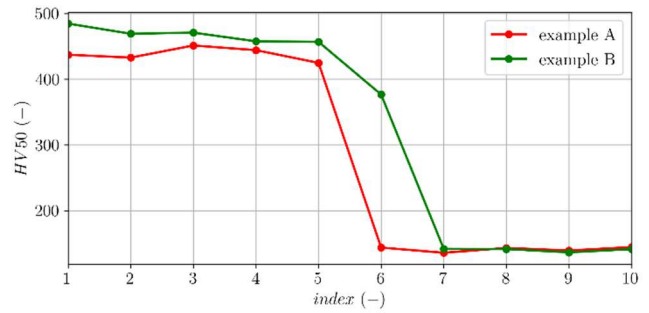


Fig. 5: Hardness measurements - hardness curve for ten measuring points in the outermost track for variants A and B.

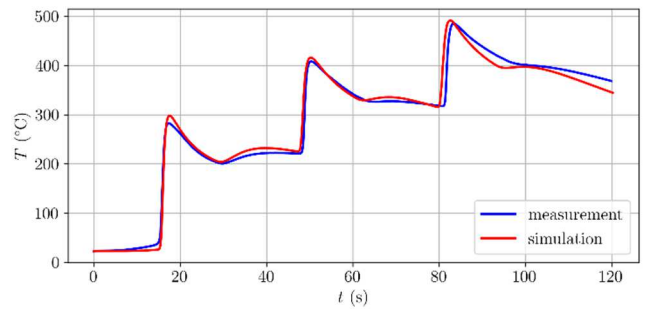


Fig. 6: Time evolution of temperature at thermocouple Tc6 for variant B (see Fig. 2).

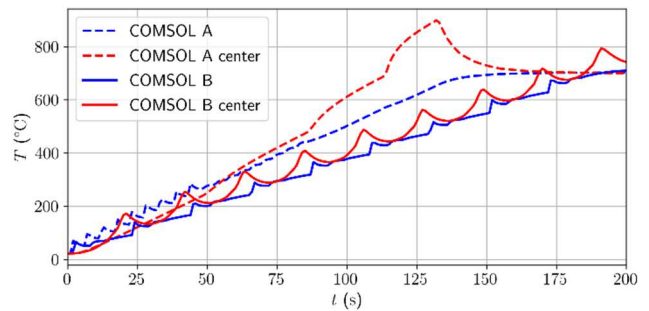


Fig. 7: Temperature waveforms obtained from model at measurement point and at center of substrate.

ACKNOWLEDGMENT

This research has been supported by the Technological Agency of the Czech Republic, project No. TH03020130.

REFERENCES

- [1] A. von Starck, A. Mühlbauer and C. Kramer, "Handbook of Thermo-processing Technologies: Fundamentals, Processes, Components, Safety," Vulkan: Essen, Germany, 2005.
- [2] P. Yi, Y. Liu, C. Fan, X. Zhan, P. Xu, and T. Liu, "Impact analysis of the thermal mechanical coupling characteristics of graphite morphologies during laser cladding of gray cast iron," *Opt. Laser Technol.*, vol. 90, pp. 52–64, 2017.
- [3] Y. Lee and D. F. Farson, "Simulation of transport phenomena and melt pool shape for multiple layer additive manufacturing," *J. Laser Appl.*, vol. 28 (1), paper 012006, 2016.
- [4] M. Courtois, M. Carin, P. Le Mason, S. Gaided, and M. Balabane "A complete model of keyhole and melt pool dynamics to analyze instabilities and collapse during laser welding," *J. Laser Appl.*, vol. 26, paper 042001, 2014.
- [5] Z. Zhang and R. Kovacevic, "A thermo-mechanical model for simulating the temperature and stress distribution during laser cladding process," *Int. J. Adv. Manuf. Technol.*, vol. 102 (1–4), pp. 457–472, 2019.

Modeling of the heat transfer in the switchboard cabinet

1st Jan Kohout

Department of electrical and computational engineering
University of West Bohemia
Pilsen, Czech Republic
kohoutj@students.zcu.cz

2nd Lenka Šroubová

Department of electrical and computational engineering
University of West Bohemia
Pilsen, Czech Republic
lsroubov@fel.zcu.cz

Abstract—This paper deals with the modeling of a heat transfer in the switchboard cabinet by using the COMSOL Multiphysics software. The heat transfer field distribution can be seen from a typical example and discussion of its results. Furthermore, the results of simulations and performed measurements are compared for the selected cooling variant.

Index Terms—switchboard cabinet, heat transfer, simulation

I. INTRODUCTION

Currently, work on the paragliding flight simulator is in progress. The project fundamentally changes the possibilities of paragliding training, increases safety and reduces the risks of paraglider pilot's injuries. It can faithfully simulate conditions caused by pilot's mistakes. This simulator requires a special switchboard. One of the important issues was the cooling system of the switchboard cabinet design. For this purpose, the main heat sources were found in the switchboard and the cooling system was simulated. The aim of this paper is to replace time consuming switchboard testing with an effective simulation of the temperature field.

II. SWITCHBOARD CABINET CONSTRUCTION

The switchboard is designed for operation under normal ambient conditions for the temperature range -20 °C and 70 °C [1]. To protect the components and the correct operation of the device, it is important to maintain the internal switchboard temperature in the range of 20 °C to 25 °C by correctly sizing the switchboard during design and adjusting the temperature using appropriate means. The main heat sources are converters, which task is to control the servo motors. There are also the smaller sources of heat and those are two direct voltage sources. They are used for supplying microcontrollers with electric energy. The heat, that arises due to microcontrollers, is in simulations neglected. The issue of the cooling system is shown in Fig. 1.

The switchboard cabinet consists of two main parts. In the bottom part, converters, control circuits for controlling servo motors, are situated. In the upper part are located voltage sources, circuit breakers, and other protective elements. The air flows through the grill, which is placed in the bottom part, to the ventilators in the upper part. The dimensions, of one switchboard cabinet, are 800 x 600 x 300 mm [1].

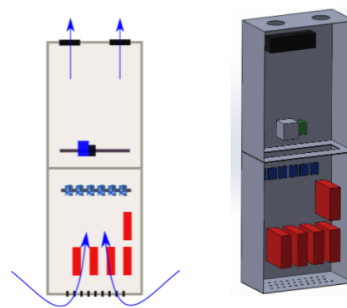


Fig. 1. Switchboard cabinet cooling choice (left) and model of switchboard cabinet (right)

III. HEAT TRANSFER FIELD SIMULATION

The mathematical model of the temperature field is described by the Fourier-Kirchhoff's partial differential equation (1).

$$-div\lambda \cdot gradT + \rho \cdot c_p \cdot \frac{\delta T}{\delta t} = p \quad (1)$$

where λ is a thermal conductivity, T is the temperature, ρ is a specific weight of the material, c_p is a heat capacity and p represents external the heat sources.

The airflow in the switchboard is described by the Navier-Stokes's partial differential equation (2).

$$\rho \frac{\delta \vec{u}}{\delta t} - \eta \cdot \nabla^2 \vec{u} + \rho(\vec{u} \cdot \nabla) \vec{u} + \nabla p = \vec{F}, \quad (2)$$

$$\nabla \cdot \vec{u} = 0,$$

where ρ is density, η is dynamic viscosity, \vec{u} is field of the velocities, p is pressure and \vec{F} is force field intensity.

The temperature distribution in the switchboard is influenced by the air flow. The computer model was solved in the COMSOL Multiphysics software [2] and consists of two coupled physical fields. Heat transfer depends on the flow of the surrounding air.

The heat distribution in the switchboard cabinet without air flow is depicted in Fig. 2.

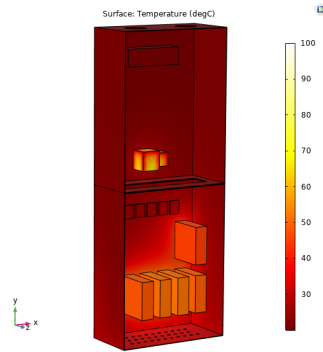


Fig. 2. Distribution of the temperature without air flow

In the next part, we considered the value of the heat transfer coefficient $\alpha = 20 \text{ W}\cdot\text{m}^{-2}\cdot\text{K}^{-1}$, which represents natural cooling. The initial temperature was $20 \text{ }^\circ\text{C}$. The temperature distribution in the switchboard cabinet is shown in the Fig. 3. The converters, as the temperature sources, worked only a partial power during the simulation.

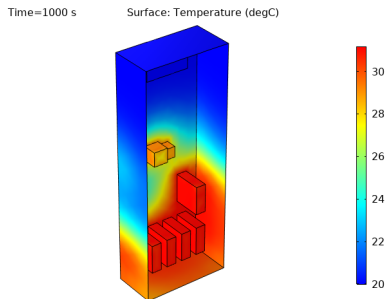


Fig. 3. Temperature distribution with natural cooling

Fig. 4 shows the temperatures obtained from the simulation. These temperatures are compared with the temperature values from the measurements. The initial temperature for the simulation was $29 \text{ }^\circ\text{C}$ as well as the temperature in our laboratory during the experiment.

The EasyLog Dual Channel Thermocouple Data Logger was used to measure the temperature. This device was put into the switchboard. During the measurement, the maximum load was applied to the servo motors. The peak current value that the converters received was approximately 2.5 A .

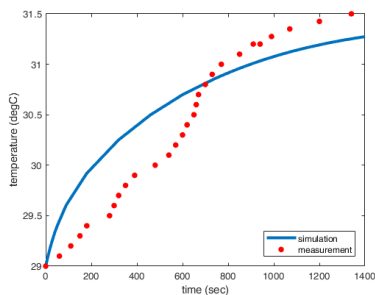


Fig. 4. Temperature in the switchboard cabinet with nature cooling.

During real operation of the simulator, the individual converters become more hot due to switching losses, current consumption and dynamic braking. All these aspects will be included in the model according to the measurements during the operation of the simulator.

There are a number of ways to dissipate heat from the switchboard. The internal temperature was calculated and it was found that the thermal limits of some devices were exceeded. Natural ventilation is not sufficient. During the simulation the value of the heat transfer coefficient $\alpha = 150 \text{ W}\cdot\text{m}^{-2}\cdot\text{K}^{-1}$ is used. This value of coefficient α represents forced cooling. The initial temperature is $29 \text{ }^\circ\text{C}$. All other variables were the same as in the previous simulation with the nature cooling. For the forced cooling, two ventilators are used, which are located on the upper part of the switchboard cabinet. The input power of those ventilators is 5W and they are supplied by 24 V DC .

The temperature of this simulation is shown in the Fig. 5 together with the measured values. During the measurements in our laboratory, the temperature was $29 \text{ }^\circ\text{C}$, so the temperature inside the switchboard was lower than the initial value due to forced cooling.

The steady state value we obtained from the forced cooling simulation is approximately $21.9 \text{ }^\circ\text{C}$. The same value was obtained during the measurement when two ventilators were used. This temperature is suitable for the operation of all devices in the switchboard cabinet.

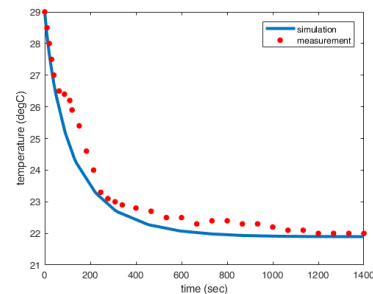


Fig. 5. Temperature in the switchboard cabinet with forced cooling.

IV. CONCLUSION

This paper presents a simulation of heat transfer in a switchboard. Illustrative examples show that we are able to simulate the heat transfer behavior inside a switchboard cabinet. Different types of simulators will be constructed, a special switchboard will be designed for each simulator and the simulation will save time with testing these switchboards.

REFERENCES

- [1] Schrack technik. Datasheet for WST8060300. Online: <https://www.schrack.cz/eshop/rozvadec-wst-ip66-800x600x300mm-1kridle-dvere-vcetne-md-wst8060300.html>
- [2] J. P. Holman., "Heat Transfer," in McGraw-Hill, New York, 2002.
- [3] COMSOL Multiphysics Reference Manual